

PHOSPHATE (U-TH)/HE THERMOCHRONOLOGY OF ZAGAMI AND ALHA77005
MARTIAN METEORITES

By

ANNETTE EMILY FARAH

A THESIS PRESENTED TO THE GRADUATE SCHOOL
OF THE UNIVERSITY OF FLORIDA IN PARTIAL FULFILLMENT
OF THE REQUIREMENTS FOR THE DEGREE OF
MASTER OF SCIENCE

UNIVERSITY OF FLORIDA

2011

© 2011 Annette Emily Farah

To my family for their love and support

ACKNOWLEDGMENTS

I extend a heartfelt thank you to Kyoungwon Kyle Min, my advisor, for his trust, patience, and guidance while I worked with him throughout the past three years. I would also like to thank my committee members, Paul Mueller and David Foster, for their advice and support. Thank you to Ann Heatherington, George Kamenov, Ray Thomas, and Dow Van Arnam for their help with equipment and software for my research. Thank you to Sergio Restrepo and Antonios Marsellos for their assistance and kind words, and to Annie Wintzer for her work and contribution to this project. I am especially grateful to Bo Gustafson from the Department of Astronomy and professors and students from the Department of Geological Sciences at the University of Florida for their cooperation and support towards the completion of my project. I offer a special thank you to the Ladies of the Office (Nita Fahm, Susan Lukowe, Pamela Haines, and Carrie Williams) for their help with countless things and taming of the copy machine.

This research was performed by the generous support of the Korean Institute of Geoscience and Mineral Resources (KIGAM). I would like to thank KIGAM for supplying a sample of Zagami, and to the National Aeronautics and Space Administration (NASA) for providing a sample and thin section of ALHA77005. I would also like to acknowledge the curators from the Smithsonian Institution, Washington, D.C. and the American Museum of Natural History, New York, NY for supplying Zagami thin sections USNM6545-4 and 4709-1, respectively. I also recognize and greatly appreciate the assistance of Peter W. Reiners and Stefan Nicolescu from the University of Arizona Department of Geosciences for their expertise and handling of my first set of samples.

TABLE OF CONTENTS

	<u>page</u>
ACKNOWLEDGMENTS.....	4
LIST OF TABLES.....	7
LIST OF FIGURES.....	8
ABSTRACT	10
CHAPTER	
1 INTRODUCTION	12
Background of Methodology	12
Purposes of This Study.....	15
2 BACKGROUND	16
Types of Meteorites	16
Martian Meteorites	17
Two Minerals Unique in Meteorites: Maskelynite and Merrillite	21
Martian Meteorites of This Study	22
Zagami	22
ALHA77005.....	24
3 (U-TH)/HE THERMOCHRONOLOGY.....	30
4 ANALYTICAL METHODS	33
5 (U-TH)/HE RESULTS	59
Cosmogenic ⁴ He Correction	59
(U-Th)/He Ages.....	59
6 DISCUSSION	66
Alpha-Recoil	66
Diffusion Behavior.....	69
Diffusion Domain	70
Diffusion Parameters.....	72
Fractional Loss	73
Peak Shock Temperatures	76
Zagami	77
ALHA77005.....	79
Post-shock versus peak shock temperatures	81

Future Studies	82
7 CONCLUSIONS	87
APPENDICES A-H: ZAGAMI AND ALHA77005 IMAGES.....	90
A SEM CHEMICAL MAPS FOR ZAGAMI PHOSPHATE AGGREGATES	91
B SEM CHEMICAL MAPS FOR ALHA77005 PHOSPHATE AGGREGATES.....	128
C TRACED ZAGAMI MERRILLITE PHOSPHATES	149
D TRACED ALHA77005 MERRILLITE PHOSPHATES	161
E ZAGAMI MICROFRACTURES	179
F ALHA77005 MICROFRACTURES.....	184
G ZAGAMI THERMAL MODELS.....	187
H ALHA77005 THERMAL MODELS	198
LIST OF REFERENCES	207
BIOGRAPHICAL SKETCH.....	218

LIST OF TABLES

<u>Table</u>		<u>page</u>
2-1	Mineralogical composition for Zagami.	27
2-2	Radiometric ages for Zagami and ALHA77005.	28
4-1	List of 80 out of 165 Zagami aggregates.	37
4-2	List of 85 out of 165 Zagami aggregates.	38
4-3	List of 56 out of 83 ALHA77005 aggregates.	39
4-4	List of 27 out of 83 ALHA77005 aggregates.	40
5-1	(U-Th)/He results, fractional loss, and age calculations.	62
5-2	Aggregate fraction data and cosmogenic contribution calculations.	63
5-3	Average ages and fractional loss calculations per grouped fractions.	64
6-1	Zagami shock temperatures from thermal modeling.	83
6-2	ALHA77005 shock temperatures from thermal modeling.	84

LIST OF FIGURES

<u>Figure</u>	<u>page</u>
2-1 Two pieces of Zagami.	29
2-2 ALHA77005 <i>in-situ</i> on Antarctica ice.	29
4-1 Zagami rock chip sample.....	41
4-2 ALHA77005 samples.....	41
4-3 Zagami single phosphate aggregate.	42
4-4 ALHA77005 single phosphate aggregate.	42
4-5 Zagami aggregates for group Z103-113.	43
4-6 ALHA77005 aggregates for group A41-56	44
4-7 Zagami aggregates for group Z01-20.	45
4-8 Zagami BSE image fld005_img02 and histogram.....	46
4-9 ALHA77005 BSE image fld003_img01 and histogram.	47
4-10 SEM composite image of thin section Zagami 4709-1.....	48
4-11 SEM composite image of thin section ALHA77005 120.	49
4-12 Zagami aggregates for group Z21-40.	50
4-13 Zagami aggregates for group Z41-60.	51
4-14 Zagami aggregates for group Z61-80.	52
4-15 Zagami aggregates for group Z81-92.	53
4-16 Zagami aggregates for group Z93-102.	53
4-17 Zagami aggregates for group Z114-123.	54
4-18 Zagami aggregates for group Z124-134.	54
4-19 Zagami aggregates for group ZAG01.	55
4-20 Zagami aggregates for group ZAG234.....	55
4-21 Zagami aggregates for group ZAG05.	55

4-22	ALHA77005 aggregates for group A01-20.	56
4-23	ALHA77005 aggregates for group A21-40.	57
4-24	ALHA77005 aggregates for group AHp123.	58
4-25	ALHA77005 aggregates for group AHp45.	58
5-1	Helium-4 versus Age plots for Zagami and ALHA77005.	65
6-1	Thermal Modeling for Zagami.....	85
6-2	Thermal Modeling for ALHA77005	86

Abstract of Thesis Presented to the Graduate School
of the University of Florida in Partial Fulfillment of the
Requirements for the Degree of Master of Science

PHOSPHATE (U-TH)/HE THERMOCHRONOLOGY OF ZAGAMI AND ALHA77005
MARTIAN METEORITES

By

Annette Emily Farah

August 2011

Chair: Kyoungwon Kyle Min
Major: Geology

Martian meteorites bring a wealth of information pertaining to the evolution of the Martian lithosphere and atmosphere, as well as the ejection of meteorites from Mars and their delivery to Earth. Zagami and ALHA77005 are two Martian meteorites (shergottites) with similar compositions and crystallization ages, yet different thermal histories. To better constrain the shock history of Zagami and ALHA77005, I applied (U-Th)/He thermochronology to multiple aggregates of merrillite (phosphate) from both Martian meteorites. After identifying phosphate aggregates using SEM (Scanning Electron Microscopy), the samples were divided into groups consisting of 5-20 grains per group based on their size. The (U-Th)/He data obtained from these groups yield ages that range between 19.8 Ma and 202.4 Ma for Zagami, and 5.9 Ma to 78.2 Ma for ALHA77005. For Zagami, the ages from groups of larger aggregates (~111-202 Ma) are older than the ages from groups of smaller ones (~20-200 Ma). To understand the age distribution, the textures of phosphate aggregates were investigated using SEM, BSE (Back-Scattered Electron) imaging, and compositional (chemistry) maps. The phosphate aggregates used for (U-Th)/He dating have similar 2D surface areas of phosphate, but the larger aggregates have thicker attached, non-phosphatic phases.

The observed textures and age-size relationship suggest that the large phosphate aggregates experienced the least amount of alpha recoil loss and yield the most reliable ages.

To estimate the peak shock temperatures reached by these meteorites during their ejection from Mars, a simple volume diffusion model was applied. The most reliable ages of Zagami and ALHA77005 are converted to helium fractional losses (f_{He}) of 0.17 and 0.94, respectively, with an assumption that the ejection-related shock is completely responsible for the observed He loss. The diffusion domain radii, a , of Zagami and ALHA77005 were estimated at 0.05-6 μm , and 5-15 μm , respectively, through detailed image analysis of 56 phosphate grains in two thin sections. For the volume diffusion modeling, these estimates (f_{He} , a) as well as other physical parameters related to the parent meteoroids were combined with general He diffusion properties in merrillite. For Zagami, average peak shock temperatures of 213°C and 407 °C were obtained at a diffusion domain radius of 0.05 μm and 6 μm , respectively. The results are comparable to, or slightly higher, than previous values of $220 \pm 50^\circ\text{C}$ (Nyquist *et al.*, 2001) when converted using the average temperature of space (-70°C) at the time of ejection from Mars. However, the new estimates are apparently higher than the converted estimates of $70 \pm 5^\circ\text{C}$ (Fritz *et al.*, 2005). For ALHA77005, the models produced average peak temperatures of 520°C and 615°C given a diffusion domain size of 5 μm and 15 μm , respectively. These peak shock temperatures are consistent with previous suggestions of 450-600°C (Nyquist *et al.*, 2001) and $800 \pm 200^\circ\text{C}$ (Fritz *et al.*, 2005).

CHAPTER 1 INTRODUCTION

Martian meteorites are known to have experienced shock metamorphism during their ejection from Mars. The ejection dynamics of Martian meteorites have been studied through petrologic investigations (McSween, 1984, 1985; Meyer, 2003), shock experiments (Stöffler *et al.*, 1986; Stöffler, 2000; El Goresy *et al.*, 2000a, 2000b), numerical simulations (Melosh, 1985; Hartmann and Neukum, 2001; Head *et al.*, 2002; Artemieva and Ivanov, 2004), cosmic ray exposure ages (Eugster *et al.*, 1997; Eugster, 2003) and thermochronologic constraints (Weiss *et al.*, 2002; Shuster and Weiss, 2005; Min and Reiners, 2007). Ejection processes and delivery mechanisms of meteorites from Mars, through space, to Earth have also been discussed (Melosh, 1985, 1995; Gladman, 1997; Nyquist *et al.*, 2001; Fritz *et al.*, 2005). To better constrain the timing of such events and understand their dynamic processes, (U-Th)/He thermochronology was applied to phosphates from rock chip samples of Martian meteorites Zagami and ALHA77005.

Background of Methodology

Thermal histories of meteorites provide a basis for further comprehending the origin and heat radiation of the early solar system as performed through various studies including interstellar grains and Pb isotope ages from chondrites (Alexander, 2001; Hutchison *et al.*, 2001; Hutchison, 2004), accretion processes of the planets through Rb-Sr and U-Pb systems (Hutchison, 2004) as well as shock impact dynamics (Melosh, 1985) and evidence of early hypervelocity impacts (Shu *et al.*, 2001; Hutchison, 2004). The most widely used thermochronometers are K/Ar and $^{40}\text{Ar}/^{39}\text{Ar}$ which can constrain cooling histories in the range of $\sim 550^\circ\text{C}$ down to $\sim 200^\circ\text{C}$ (McDougall *et al.*, 1999).

These methods have been applied to a range of meteorites including chondrites (Turner *et al.*, 1978; Bogard *et al.*, 1987; Trierloff *et al.*, 2003), lunar samples (Turner *et al.*, 1971), and Martian meteorites (Ash *et al.*, 1996; Turner *et al.*, 1997; Bogard and Park, 2008; Bogard, 2009; Bogard *et al.*, 2009; Cassata *et al.*, 2010) mainly to document cooling from formation or shock metamorphism. In contrast, (U-Th)/He methods have been widely applied to terrestrial samples to constrain thermal histories below $\sim 200^{\circ}\text{C}$, which are directly related to exhumation histories (Reiners and Ehlers, 2005). With relatively low closure temperatures of $\sim 70^{\circ}\text{C}$ for apatite (Farley, 2002; Wolf *et al.*, 1996), $\sim 190^{\circ}\text{C}$ for zircon (Reiners, 2005), and $\sim 200^{\circ}\text{C}$ for titanite (Reiners *et al.*, 1999) at typical grain dimensions and terrestrial cooling rates, the (U-Th)/He methods can provide important information on the relatively low-temperature thermal histories of terrestrial and extraterrestrial samples.

Another important application of the (U-Th)/He thermochronometer is to constrain transient thermal events such as wildfire (Mitchell and Reiners, 2003) or shock metamorphism on meteorites (Min, 2005). In fire-prone or wildfire areas, (U-Th)/He methods applied to apatite and zircon minerals can determine thermal histories of exposed bedrocks (Mitchell and Reiners, 2003) or detached rock fragments (Reiners *et al.*, 2007). Evidence of shock registered in meteorites and impact craters can be further supported through the study of their (U-Th)/He systems (Min and Reiners, 2007).

Although the (U-Th)/He thermochronometer has been widely applied to terrestrial samples for their low-temperature thermal histories, its applications to meteorites are limited probably due to the traditional concept that ^4He can easily diffuse out of the system resulting in unreasonably young (U-Th)/He ages. This concept is mainly from

whole-rock data requiring more thorough examination. Single- and multi-grain analysis, contrary to the whole-rock method, focuses on selected minerals of similar physical dimensions, producing more consistent (U-Th)/He ages. The contribution of radiogenic ^4He to the total measured ^4He is much larger for mineral-based methods than for whole rock dating, thus yielding significantly more precise ages (Min, 2005a, 2005b). Some examples of (U-Th)/He dating applied to meteorites include (1) whole-rock age calculations based on published U, Th and ^4He concentrations of ordinary chondrites (Watson and Wang, 1991), (2) single-grain phosphate ages on Acapulco, an achondritic meteorite with a chondritic texture (Min *et al.*, 2003), (3) single-grain phosphate data of Martian meteorite Los Angeles (Min *et al.*, 2004) and ALH 84001 (Min and Reiners, 2007), (4) He loss data for whole-rock and mineral separates from a suite of Martian meteorites (Schwenzer *et al.*, 2008), and (5) single-grain phosphate ages from St. Severin LL6 chondrite (Min *et al.*, 2011).

The (U-Th)/He methods can be efficiently applied to Martian meteorites because the He concentration in the Martian atmosphere is low, causing only a limited amount of ^4He to be injected into Martian meteorites during shock events. However such contamination of atmospheric gas has been a serious issue for $^{40}\text{Ar}/^{39}\text{Ar}$ dating for Martian meteorites (Bogard and Garrison, 1999). Multiple radiogenic and cosmogenic isotope systems of Martian meteorites can provide a chronological sequence of events on Mars. For example, ALH 84001 formed at ~ 4.5 Ga (from Sm/Nd system: Jagoutz *et al.*, 1994; Nyquist *et al.*, 1995), experienced a severe shock at ~ 4.0 Ga (from $^{40}\text{Ar}/^{39}\text{Ar}$ system: Treiman, 1995), and ejected from Mars at ~ 15 Ma (from cosmogenic isotope systems: Treiman, 1998). Furthermore, implications such as timing of impact

metamorphism and maximum shock temperatures can be evaluated to better understand their thermal histories.

Purposes of This Study

The goals of this research are to (1) improve fundamental aspects of the (U-Th)/He thermochronometer in application to shocked meteorites and (2) constrain temperature conditions of shock metamorphism for two Martian meteorites, Zagami and ALHA77005. For these goals, I performed (U-Th)/He analysis on a few hundred phosphate grains, estimated their diffusion domain, and generated thermal models to infer thermal histories. For thermal modeling, I examined the sensitivity of the final results and compared them with previously reported parameters.

CHAPTER 2 BACKGROUND

Types of Meteorites

Meteorites are classified into *iron*, *stony*, or *stony-iron* groups based on their metallic iron-nickel (Fe-Ni) and silicate (silicon-oxygen, Si-O) contents. *Iron* meteorites are made primarily of iron-nickel metal alloy; *stony* meteorites consist primarily of silicate minerals; and *stony-iron* meteorites contain roughly a mixture of equal proportions of iron-nickel metal and silicates. A brief explanation of each classification follows.

Iron meteorites contain two major minerals: kamacite (nickel-poor iron of 5-15% Ni) and taenite (nickel-rich iron, >15-20% Ni). Trace amounts of other elements are also present in *iron* meteorites measuring below 500 ppm (Shirley and Fairbridge, 1997). *Iron* meteorites are further classified in two ways: the appearance of a Widmannstätten pattern and concentrations of gallium (Ga), germanium (Ge), and iridium (Ir). The presence or absence of a Widmannstätten pattern is used as an older structural classification method depending on varying amounts of nickel; a meteorite with no pattern and low nickel content is identified as a hexahedrite, and one with no pattern and high nickel content is known as an ataxite. However, a meteorite with an average to high amount of nickel (kamacite) separated by varying lamellae of taenite will exhibit a Widmannstätten pattern. The second classification method is based on trace element concentrations of Ni, Ga, Ge, and Ir. The amount of these trace elements, and other diagnostic features, present in the meteorite determines further class divisions, i.e. IIAB, IVB, etc. For example, iron meteorites from group IVB are Ir-rich and Ga- and Ge-poor (less volatile) while group IIAB is Ga- and Ge-rich (more

volatile) with a negative correlation between Ir and Ni reflecting fractional crystallization (Hutchison, 2004). Both classification schemes relate to the chemistry of iron meteorites and whether an element prefers to occur as a metal (siderophile elements) versus a silicate (lithophile elements) or sulfide (chalcophile elements).

Stony meteorites are the most common class of meteorites and consist principally of silicate minerals and are divided into chondrites and achondrites depending on the presence of chondrules (near spherical masses of silicates: Hutchison, 2004). Chondrites have chemical compositions closely resembling the atmosphere of the Sun and exhibit textures indicating no melting has occurred since their formation (Hutchison, 2004). Achondrites lack chondrules and are generally different in chemical composition than chondrites. However, a group of rare meteorites, known as primitive achondrites, have chondritic mineralogies and resemble chondritic chemical compositions suggesting minimal melting (Hutchison, 2004), yet are free of chondrules.

Stony-iron meteorites are the least common type of meteorites and consist roughly of a mixture of equal proportions of iron-nickel metal and rock (silicates), commonly referred as siderolites. *Stony-iron* meteorites composed of a continuous matrix of Fe-Ni metal with crystal fragments of olivine are pallasites. And those composed of brecciated mixtures of metal plus olivine and recrystallized silicates are mesosiderites.

Martian Meteorites

Martian meteorites are achondritic *stony* igneous rocks originally categorized into one of three classes: Shergottite, Nakhlite, and Chassignite (SNC). The SNC meteorites are named after their discovery from locations in Shergotty (in the Gaya district of Bihar, India), Nakhla (Nakhla region of Abu Hommos in Alexandria, Egypt),

and Chassigny (Chassigny, Haute Marne in France). They are categorized based on their petrologic and chemical characteristics: shergottites are basalts and lherzolites, nakhlites are olivine clinopyroxenites, and chassignites are dunites (McSween, 1985, 1994; Hutchison, 2004). Currently there are 24 shergottites, 7 nakhlites, and 2 chassignites known. One other Martian meteorite, ALH 84001, is an orthopyroxenite with its own category.

Basaltic shergottites are composed primarily of pyroxene and maskelynite (shocked plagioclase) with accessory olivine, sulfides, phosphates and oxides (McSween, 1985, 1994; Hutchison, 2004). The appearance of fine-grain textures and aligned pyroxene crystals suggests that these rocks have magmatic compositions and formed from quickly cooled lava (McSween, 1994; Treiman *et al.*, 2000). Lherzolic shergottites are rich in olivine and composed of chromite surrounded by orthopyroxene crystals with interstitial maskelynite, phosphate and other accessory oxides (McSween, 1985; Treiman *et al.*, 2000). These rocks originate from a plutonic environment (McSween, 1994) based on early formation of (olivine cumulate) crystals (Hutchison, 2004), which slowly settled and cooled in a deep magma chamber (Treiman *et al.*, 2000). Early Sm-Nd studies produced an isochron age of ~ 1.3 Ga (Wooden *et al.*, 1982; Shih *et al.*, 1982) interpreted as the time of formation. Recent isotopic data provide a younger age of ~180 Ma as the time of shock metamorphism from an explosive event.

Nakhlites are cumulate rocks from basaltic magma consisting of magnesian augite with less abundant Fe-rich olivine (McSween, 1994; Treiman, 2005). Inclusions in olivine and augites suggest trapped magma, and deposits of iddingsite and salt

minerals indicate the presence of water (Treiman, 2005). These rocks may have formed from a lava flow, shallow intrusion or subsurface sill (Hutchison, 2004; Treiman, 2005). Chassignites are predominantly olivine cumulates abundant in Mg for NWA 2737 and Fe for Chassigny (Meyer, 2003; Beck *et al.*, 2006). Both exhibit similar petrographic and chemical compositions to suggest their parental melts are related, although the melt from NWA 2737 is less evolved (Beck *et al.*, 2006).

Following these types of identifications, Martian meteorites continue to be scrutinized and re-examined. While many Martian meteorites fall within the existing SNC groups, others exhibit characteristics where the SNC classification may no longer apply. ALH 84001 and ALHA77005 are two examples where their association to other Martian meteorites may not exactly fit the SNC classification. For example, ALH 84001 was originally classified as a diogenite, for its orthopyroxenite cumulate composition with minor chromite, Na-rich plagioclase, and Fe-Mg-Ca carbonates (MacPherson, 1985; Mittlefehldt, 1994). Subsequently, ALH 84001 was categorized into the HED (howardites, eucrites, and diogenites) group most likely originating from the asteroid Vesta. However later mineralogic and petrologic studies showed that the existence of these carbonates, along with the presence of pyrite, Na-rich plagioclase (and maskelynite), and an enrichment in Fe^{3+} , distinguish it from diogenites (Mittlefehldt, 1994). Furthermore, other features in ALH 84001 such as oxygen isotopic composition (Clayton, 1993), maskelynite composition, and shock textures closely resemble those of Martian meteorites, albeit not necessarily belonging to any one of the SNC groups (Mittlefehldt, 1994; Swindle, 1995). Therefore, this one meteorite is classified into a

separate group of Orthopyroxenite and contributes another addition to the group: SNCO.

Another example is ALHA77005, the parent body of one of the samples used for this research. ALHA77005 is a member of the shergottite group. Mineral and chemical compositions in ALHA77005 are similar to the other shergottites, however its cumulate texture and plutonic origin make it noticeably different from the basaltic shergottites. Since its crystallization and cosmic ray exposure ages are comparable to basaltic shergottites, ALHA77005 was classified a lherzolithic shergottite.

SNCO are believed to be the only Martian meteorites. While grouping Martian meteorites emphasizes their similarities, it may also ignore qualities that make them different, i.e. ALHA77005 as a shergottite. In this report, I use the SNC nomenclature when discussing the parent bodies of my samples to remain consistent with their definitions from books and published articles. Following the naming convention, the rock chip samples in this research are from two shergottites: basaltic shergottite Zagami and lherzolithic shergottite ALHA77005. However after the introduction of this report, I will refer to them as Martian meteorites.

In general, Martian meteorites closely resemble terrestrial igneous rocks. Their crystallization ages are significantly younger (~180 Ma to 1250 Ma) than most other meteorites. The only exception is ALH 84001 with a very old crystallization age of ~ 4.5 Ga (Jagoutz *et al.*, 1994). Martian meteorites share similar properties that are highly distinctive from other meteorites in terms of their mineral chemistry, redox state, and radiometric ages (McSween, 1985). They consist of mafic and ultramafic cumulate rocks with petrologic features such as poikilitic texture in olivine and chromite, and

glassy rims around plagioclase crystals (McSween, 1985). Such characteristics suggest relatively rapid formation from a large parent body (McSween, 1985, 1994). Their oxygen isotope composition (Clayton and Mayeda, 1996), trapped gases (Bogard and Johnson, 1983) matching the Martian atmosphere, and young formation ages (Treiman *et al.*, 2000) indicate their origin to be from Mars (McSween, 1985).

To date, 99 Martian meteorite pieces have been discovered (Meteoritical Bulletin Database from the Meteoritical Society: <http://www.lpi.usra.edu/meteor/index.php>) including 57 fragments from 34 identified parent meteorites (NASA's Mars Meteorites website: <http://www2.jpl.nasa.gov/snc/>; Baalke, 2006). Many of these meteorites were discovered as broken pieces of a single stone and naturally paired through petrologic and chemical investigations.

Two Minerals Unique in Meteorites: Maskelynite and Merrillite

Maskelynite and merrillite are two minerals frequently identified in extraterrestrial samples. Maskelynite has been naturally detected on terrestrial samples collected from impact craters (Lambert and Grieve, 1984) showing that these Earth rocks experienced severe shock leading to the formation of the mineral (Milton and Carli, 1963). Petrologic evidence has presented maskelynite as a glassy form of plagioclase resulting from strong shock metamorphism below pressures of 45 GPa (Stöffler, 2000; Nyquist *et al.*, 2001; Fritz *et al.*, 2005). Pressures in excess of 45 GPa would cause plagioclase to recrystallize (Fritz *et al.*, 2005b) and experience shock-induced fusion (Stöffler, 2000) thereby exhibiting flow structures and vesiculation consistent with normal glass instead of diaplectic glass (shocked isotropic plagioclase) associated with maskelynite (Stöffler, 1988). Excessive pressure would require extreme post-shock temperatures causing

plagioclase to mix with melt (Stöffler, 1988, 2000). Maskelynite is considered a main characteristic in all Iherzolitic shergottites.

Another mineral commonly found in extraterrestrial rocks is merrillite. The name was assigned to hydrogen-free whitlockite to differentiate it as a separate mineral from terrestrial whitlockite (Jolliff, 2006). The chemical composition of whitlockite is $\text{Ca}_{18}(\text{Mg,Fe})_2(\text{PO}_4)_{12}[\text{PO}_3(\text{OH})]_2$ and that of merrillite is $\text{Ca}_{18}\text{Na}_2\text{Mg}_2(\text{PO}_4)_{14}$ (Jolliff, 2006; Hughes *et al.*, 2008). Throughout the remainder of this report, the term “merrillite” will be used to describe phosphates having this chemical composition. Merrillite can be distinguished from whitlockite by two important chemical signatures: (1) lack of (OH) and (2) existence of Na (Hughes *et al.*, 2008). Merrillite occurs only in extraterrestrial material, although synthetic merrillite has been grown for crystallographic studies (Hughes, 2008).

Martian Meteorites of This Study

Zagami

Zagami was discovered immediately after landing on Earth by a farmer on October 3, 1962 at Zagami, Katsina Province, Nigeria (Meyer, 2003). The sample weighed approximately 18.1 kg with a suggested minimum radius of ~11.3 cm (Schwenzer *et al.*, 2008). Figure 2-1 shows a portion of Zagami as acquired by a private collector (Haag, 2010). Zagami is a basaltic shergottite with a main lithology (“Normal Zagami”, NZ) consisting mostly of pyroxenes (pigeonite and augite) and maskelynite. Approximately 20% of the rock is comprised of a dark-mottled lithology (DML) with heterogeneously distributed iron-oxide enriched pyroxenes, maskelynite, and melt pockets. Accessory minerals of sulfides, oxides, merrillite and other phosphates are also identified (Vistisen *et al.*, 1992; McCoy *et al.*, 1993; Wang *et al.*, 1999). Zagami consists of fine-grained

(average grain dimension of 0.24 mm) and coarse-grained (0.36 mm) portions (Meyer, 2003). Table 2-1 lists mineralogic modes of the two Zagami lithologies and their grain size portions (McCoy *et al.*, 1991, 1999; Meyer, 2003).

The grain size variations of Zagami suggest a complex series of crystallization processes (Nyquist *et al.*, 2006) possibly involving a two-stage magmatic history (McCoy *et al.*, 1991). The first stage can be represented by the (1) presence of homogeneous Mg-rich, amphibole-bearing melt inclusions in pyroxene crystals and (2) development of fine lamellae in pyroxene indicating slow cooling within a magma chamber (McCoy *et al.*, 1991; Nyquist *et al.*, 2001). The second stage can be characterized by (1) Fe-rich rims in pyroxene crystals and (2) overall fine-grained textures in Zagami, both suggesting rapid cooling in a moderately thick lava flow (McCoy *et al.*, 1991; McCoy *et al.*, 1999; Langenhorst and Poirier, 2000a). Zagami is given a cooling rate $< 0.5^{\circ}\text{C/hr}$ (McCoy *et al.*, 1992; McCoy *et al.*, 1999). In summary, the two-stage magmatic history starts with an initial slow crystallization within a magma chamber followed by a rapid cooling during a magma flow near the surface (McCoy *et al.*, 1999).

Shock conditions were estimated to include pressures of 31 ± 2 GPa (Stöffler *et al.*, 1986) using refractive index data of maskelynite (Binns, 1967) and a post-shock temperature of $220 \pm 50^{\circ}\text{C}$ (Stöffler, 2000; Nyquist *et al.*, 2001). From analyses of black glassy veins, the appearance of high-pressure phases (Malavergne *et al.*, 2001) such as stishovite and KAlSi_3O_8 hollandite (Langenhorst and Poirier, 2000a, b) suggest a minimum pressure and temperature of ~ 30 GPa and $2400\text{-}2500^{\circ}\text{C}$ (Langenhorst and Poirier, 2000b), respectively. Furthermore, Langenhorst and Poirier (2000a, b)

concluded the black glassy veins indicate rapid shear melting during shock. From petrographic studies and refractive index data, Fritz *et al.* (2005) deduced shock pressures of 29.5 ± 0.5 GPa and post-shock temperature of $70 \pm 5^\circ\text{C}$ (70 ± 5 K, ΔT).

Zagami yielded relatively consistent radiometric ages (Table 2-2). Borg *et al.* (2003) determined U-Th-Pb ages from whole-rock samples and mineral separates, and concluded that the parent body magma formed during the early stage of planet formation (~ 4550 Ma) followed by differentiation at a much younger period (163 ± 4 Ma). Bouvier *et al.* (2005) reported a Sm-Nd mineral isochron age of 155 Ma and Lu-Hf isochron age of 185 Ma from analyses performed on Zagami whole-rock, maskelynite and pyroxene separates. Whole-rock Pb isotope analyses applied to Zagami resulted in an older isochron age of 4.048 ± 0.017 Ga, while $^{207}\text{Pb}/^{206}\text{Pb}$ and $^{204}\text{Pb}/^{206}\text{Pb}$ compositions of other shergottites including Zagami resulted in a crystallization age of 4.0 Ga (Bouvier *et al.*, 2005). Nyquist *et al.* (2006) reported Rb-Sr isochron ages of 166 ± 12 Ma for coarse-grained and 177 ± 9 Ma for fine-grained lithologies of Zagami.

ALHA77005

ALHA77005 (Figure 2-2) was discovered in Victoria Land, Allan Hills of Antarctica in 1977 (Yanai, 1981; Meyers, 2003; Harvey, 2003) weighing approximately 0.483 kg and measuring 9.5 cm \times 7.5 cm \times 5.25 cm (Score *et al.*, 1981; Nishiizumi *et al.*, 1986). ALHA77005 is classified as a lherzolithic shergottite with a gabbroic, olivine-rich composition. It mainly consists of olivine ($\sim 52\%$), low-Ca pyroxene ($\sim 26\%$), high-Ca pyroxene ($\sim 11\%$), maskelynite ($\sim 8\text{-}9\%$), and other accessory minerals ($\sim 2\%$) including chromite, ilmenite, merrillite, and troilite (McSween *et al.*, 1979a, b; Ma *et al.*, 1981; Mason, 1981; Meyer, 2003). The mode of merrillite is only $\sim 0.4\%$ (Treiman *et al.*,

1994). The olivine is anhedral and commonly occurs in poikilitic texture with pyroxene (Shearer *et al.*, 2009).

Veins and melt pockets, commonly found in olivine crystals, show wide compositional variations for P₂O₅ (0-8 wt%), SiO₂ (35-71 wt%), and REE (e.g., Nd = 0.1 to 26 ppm) suggesting a variable contribution of merrillite within the impact melt (Edmunson *et al.*, 2005). Trace element patterns analyzed for maskelynite and plagioclase suggest fractional crystallization occurred in a closed-system environment (Wadhwa *et al.*, 1994).

Petrographic features observed in ALHA77005 have been considered particularly interesting with respect to shock metamorphism. Most of the olivine in ALHA77005 has a yellowish-brown discoloration exhibiting homogeneous chemical compositions within each grain as a result of re-equilibration upon cooling (Ikeda, 1994) and shock-induced oxidation (Beech *et al.*, 2008). From textural observations in olivine, pyroxene and maskelynite, McSween *et al.* (1980) suggested shock pressures of 35 - 50 GPa. Based on re-evaluation of the textures, Fritz *et al.* (2005) suggested peak shock pressures of ~45-55 GPa with post-shock temperatures of 800 ± 200°C (Fritz *et al.*, 2005). Shock experiments combined with observed refractive indices for maskelynite suggest a peak shock pressure of 43 ± 2 GPa (Stöffler, 2000; Nyquist *et al.*, 2001) and post-shock temperature of 450-600°C (Nyquist *et al.*, 2001). Such high pressure and temperature conditions of shock can also be assumed from evidence of partial recrystallization (Fritz *et al.*, 2005) along the rim of shock-induced plagioclase melt pockets (Beech *et al.*, 2008). These observations suggest temperatures were above ~726.85°C (~1000 K) lasting for 0.5 h as illustrated from annealing experiments (Ostertag, 1982; Beech *et al.*,

2008). Strongly vesiculated plagioclase melt suggests shock pressures were in excess of 45 GPa (Fritz *et al.*, 2005). Even higher shock pressure conditions of 45-80 GPa were proposed based on deformation features in olivine and pyroxene, skeletal crystals of pigeonite with residual glass, and common occurrence of melt veins (Boctor *et al.*, 1999). Based on these shock features, ALHA77005 has been considered the most heavily shocked Martian meteorite (McSween and Stöffler, 1980; Ikeda, 1994; Nyquist *et al.*, 2001; Fritz *et al.*, 2005).

Radiometric ages of this meteorite are scattered (Table 2-2). Among these, modern Rb-Sr and Sm-Nd studies indicate a preferred crystallization age of 179 ± 5 Ma (Nyquist *et al.*, 2001; Schwenger *et al.*, 2008). The apparently older K-Ar and $^{40}\text{Ar}/^{39}\text{Ar}$ ages are likely caused by (1) incorporation of a sufficient amount of unsupported ^{40}Ar from the Martian atmosphere or mantle and (2) excessive production of cosmogenic ^{36}Ar and ^{40}Ar (Nyquist *et al.*, 2001; Bogard and Garrison, 1999).

Table 2-1. Mineralogical composition for Zagami.

	Normal Zagami		Dark-mottled Lithology	
	Fine-grain	Coarse-grain	Fine-grain	Coarse-grain
Pyroxene	74-78	80	71	77-80
Maskelynite	18-21	10	22	9-14
Oxides	2	2	1	3
Sulfides	< 1	< 1	< 1	< 1
Phosphates	1	1	1	2

Mineralogical composition (in vol. %) for Normal Zagami and Dark-mottled lithologies of Zagami. Sources: McCoy *et al.*, 1991; McCoy *et al.*, 1999; and Meyer 2010.

Table 2-2. Radiometric ages for Zagami and ALHA77005.

Radiometric Ages (Ma)	$^{40}\text{Ar}/^{39}\text{Ar}$	K-Ar	Rb-Sr	Sm-Nd	$^{232}\text{Th}-^{208}\text{Pb}$	$^{238}\text{U}-^{206}\text{Pb}$	Preferred Age
Zagami	209 ^[1]		166 ± 6 ^[3]	166 ± 12 ^[3]	229 ± 8 ^[6]	156 ± 6 ^[3]	177 ± 3 ^[7]
	242 ^[2]		180 ± 4 ^[4]	180 ± 37 ^[5]		230 ± 5 ^[6]	
			183 ± 6 CG ^[5]				
			186 ± 5 FG ^[5]				
ALHA77005	1100 ± 100 ^[8]	1330 ± 130 ^[9]	154 ± 6 ^[10]	135 ± 40 ^[10]			179 ± 5 ^[7]
	3500 ^[2]		185 ± 11 ^[11]	173 ± 6 ^[11]			
			185 ± 12 ^[4]				

CG=coarse-grained and FG=fine-grained. [1] Bogard and Park (2008). [2] Bogard and Garrison (1999). [3] Borg *et al.* (2005). [4] Shih *et al.* (1982). [5] Nyquist *et al.* (1995) [6] Chen and Wasserburg (1986). [7] Nyquist *et al.* (2001). [8] Schaeffer *et al.* (1981). [9] Miura *et al.* (1995). [10] Jagoutz (1989). [11] Borg *et al.* (2002).

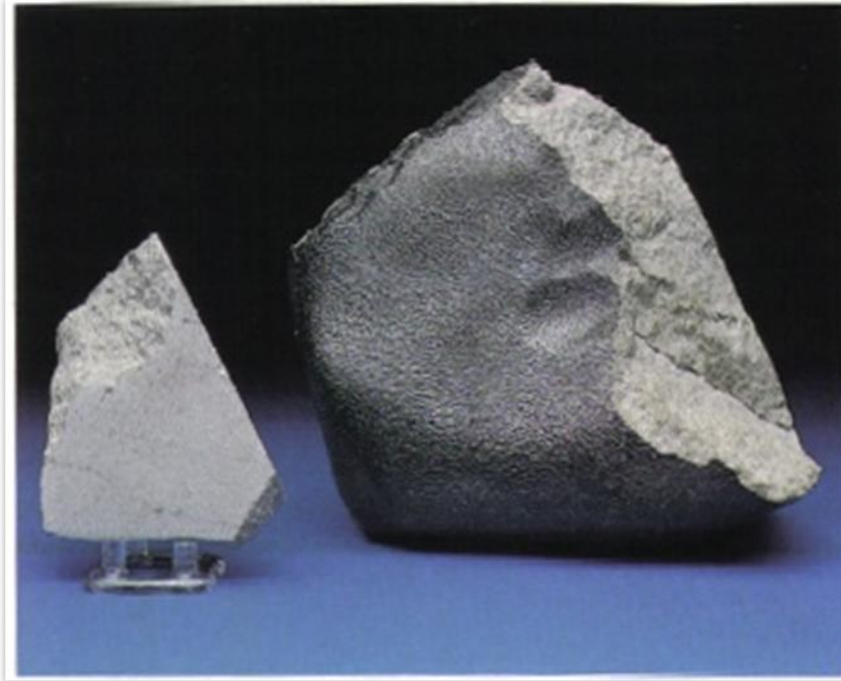


Figure 2-1. Two pieces of Zagami with a combined weight of 2,794 grams (~6.2 lbs) and measuring 158 x 165 x 70 mm. Source: Haag (1991).



Figure 2-2. ALHA77005 *in-situ* on Antarctica ice. Source: Yanai (1981).

CHAPTER 3 (U-TH)/HE THERMOCHRONOLOGY

(U-Th)/He thermochronology relies on the accumulation of radiogenic ^4He produced from radioactive decay of parent isotopes ^{238}U , ^{235}U , and ^{232}Th . Although ^{147}Sm also experiences α -decay producing ^4He atoms, its contribution to the total radiogenic ^4He is less significant than U and Th for most samples. U and Th follow a series of natural radioactive decays (α - and β -decays) producing multiple intermediate daughter isotopes. The decay from one intermediate isotope to the next is performed through the release of alpha or beta particles, and in some cases gamma particles. For instance, the parent isotope ^{238}U has 8 alpha decay steps in its decay chain, with a final step to the stable isotope ^{206}Pb . During the alpha decay, one alpha particle (^4He nucleus: 2 protons and 2 neutrons) is emitted from the nucleus of the parent atom. The produced He nucleus couples with electrons becoming a ^4He atom. A similar process occurs for ^{235}U and ^{232}Th with 7 and 6 alpha decays, respectively. In contrast, ^{147}Sm yields only one alpha particle during its decay to stable ^{143}Nd .

In various types of meteorites, U and Th are mainly concentrated in phosphate minerals such as merrillite and apatite. Once the U-Th-Sm- ^4He abundances are determined from a sample, an age can be determined from the following equation: $^4\text{He} = 8 \times ^{238}\text{U} [\exp(t \times \lambda_{238}) - 1] + 7 \times ^{235}\text{U} [\exp(t \times \lambda_{235}) - 1] + 6 \times ^{232}\text{Th} [\exp(t \times \lambda_{232}) - 1] + ^{147}\text{Sm} [\exp(t \times \lambda_{147}) - 1]$.

If the produced ^4He atoms are completely preserved in the system, the resulting (U-Th)/He age should indicate the timing of crystallization. However, ^4He can easily diffuse out of the system because of (1) its nature as a noble gas being inert and not bound in crystal structures, and (2) its small atomic size allowing it to pass through

crystal structures. To account for the amount of remaining ^4He present in a system, the mineral must remain below a certain “closure temperature” to encounter little or no diffusion. The rate of diffusion varies depending on the mineral’s properties and temperatures. Because the diffusion rate increases with temperature, (U-Th)/He ages represent the timing when the mineral passed through its closure temperature. This point in time is the “apparent age” of the mineral with its respective closure temperature, T_c (McDougall and Harrison, 1999). The closure temperature can be expressed by the following equation (Dodson, 1973): $T_c = R / [E \ln (A \tau D_0/a^2)]$, where R is the gas constant, E is the activation energy, τ is the time constant as diffusion coefficient D diminishes, a is the diffusion domain size, A is the geometry factor, and D_0 is the pre-exponential factor (Dodson, 1973). Following this equation, the closure temperature is sensitive to various factors such as the diffusion domain size, crystal geometry, and cooling rate. To estimate the closure temperature of terrestrial apatite, Farley (2000) performed high-precision stepped-heating experiments on Durango apatite which is the best understood standard for (U-Th)/He dating. From these experiments, Farley (2000) calculated a closure temperature of approximately 68°C assuming a cooling rate of $10^\circ\text{C}/\text{Ma}$ for a diffusion domain radius of $100 \mu\text{m}$.

If a rock is exposed to sufficiently high temperatures, the diffusion rate of daughter elements would be larger than the production rate of radioactive decay, resulting in essentially no accumulation of the daughters (open system). If a rock is at sufficiently low temperatures, the system almost completely retains the daughter products (closed system). Between these two end member conditions, the thermochronometer would experience a gradual transition from one to the other, resulting in partial retention of the

daughters (McDougall and Harrison, 1999). The temperature range of such a transition (or converted depth range at assumed geothermal gradient) is known as a partial retention zone (PRZ) (McDougall and Harrison, 1999; Reiners, 2002). In a transition from an open system to a closed system, an apparent age can be extrapolated showing a point in time when the daughter product begins to accumulate at a constant rate.

Other U and Th carriers such as titanite and zircon function as good (U-Th)/He thermochronometers characterized by their helium diffusion properties and well-defined closure temperatures (Reiners and Farley, 1999; Reiners, 2005). As a result, a wider range of low-temperature (40°C – 240°C) thermal histories of terrestrial rocks were constrained using (U-Th)/He as a thermochronometer (Reiners, 2002; Stockli, 2005). For meteorites, low-temperature thermal histories are poorly constrained mainly due to the lack of He diffusion data for extraterrestrial merrillite, a major reservoir of U and Th in meteorites. However, a recent study on He diffusion properties in merrillite and apatite (Min *et al.*, 2011) may provide a basis for more reliable constraints on low-temperature thermal histories for meteorites. According to the study (Min *et al.*, 2011), a closure temperature for merrillite is calculated as ~104°C (at an assumed cooling rate of 2°C/Ma and a diffusion domain radius of 59 µm), which is significantly higher than that of apatite. These new diffusion properties are used in this study for thermal modeling of Zagami and ALHA77005.

CHAPTER 4 ANALYTICAL METHODS

Thin sections and rock fragments were examined with optical and stereo microscopes and a scanning electron microscope (SEM). To obtain precise (U-Th)/He ages, phosphate-bearing aggregates were separated from meteorite rock fragments, degassed using a helium extraction line, dissolved and analyzed using inductively coupled plasma mass spectrometry (ICP-MS) for U-Th-Sm-⁴He measurements. Below is a detailed account of the methods.

Small rock chips of Zagami (~15 mm × 10 mm × 2 mm, Figure 4-1) and ALHA77005 (~9 mm × 7 mm × 2 mm, 0.27 gram, Figure 4-2) were carefully crushed, and the resulting fragments were sieved. The final separates were scanned using SEM in order to identify phosphate-bearing separates. Since these separates are pieces of the rock (or meteorite), they consist of other minerals, including phosphate grains. Throughout this report, I will refer to these phosphate-bearing separates as aggregates or phosphate aggregates. A total of 248 phosphate aggregates were selected: 165 from Zagami and 83 from ALHA77005 (Tables 4-1, 4-2, 4-3, and 4-4). Each phosphate aggregate was scanned to reveal the chemical composition of each sample. The chemical data from the scans are displayed as 2-dimensional images (or chemical maps) and used to determine morphological relationships between phosphates and other phases included in the same aggregate.

Chemistry maps and results from energy dispersive spectroscopy (EDS) spot analyses for two phosphate aggregates are shown in Figure 4-3 for Zagami and Figure 4-4 for ALHA77005. The aggregates from Figures 4-3 and 4-4 measure between 150-250 μm (Figure 4-5) and 63-150 μm (Figure 4-6), respectively. Chemistry maps for all

selected aggregates in this study are found in Appendix A for Zagami and Appendix B for ALHA77005. Regional and spot analyses from chemical mapping detect high P and Ca peaks strongly associated with phosphates, and moderate signals of S, O, Al, and Mg suggest the existence of other phases (e.g., silicate) in these aggregates (Figures 4-3 and 4-4). From the presence of Na with Mg, together with high signals of P and Ca, these phosphates are identified as merrillite $[\text{Ca}_{18} \text{Na}_2 \text{Mg}_2 (\text{PO}_4)_{14}]$. From the analyses of the 248 phosphate aggregates, the majority of the identified phosphates are classified as merrillite.

After petrographic examinations, one to twenty phosphate aggregates were wrapped in Pt or Nb tubes and subsequently sealed to avoid any sample loss during analytical procedures. A total of 17 packets were arranged: twelve for Zagami and five for ALHA77005. Three Zagami samples (ZAG01, ZAG234, ZAG05: Table 4-2) and two ALHA77005 samples (AHp123, AHp45: Table 4-4) were wrapped in Pt tubes. The remaining nine Zagami samples (Z01-20, Z21-40, Z41-60, Z61-80, Z81-92, Z93-102, Z103-113, Z114-123, Z124-134, Tables 4-1 and 4-2) and three ALHA77005 (A01-20, A21-40, A41-56, Table 4-3) were wrapped in Nb tubes. Size fractions, number of aggregates, and names corresponding to each packet are listed in Tables 4-1 and 4-2 for Zagami and Tables 4-3 and 4-4 for ALHA77005. As indicated in these tables, phosphate aggregates were grouped based on their sizes and measured based on their overall ^4He and U-Th-Sm concentrations (Table 5-1).

The sample packets were loaded in a stainless steel planchette and degassed under high vacuum using a diode laser. The extracted gas was purified using a cryotrap and NP-10 getter for 3 Zagami (ZAG01, ZAG234, ZAG05: Table 4-2) and 2

ALHA77005 (AHP123, AHP45: Table 4-4) packets. For all the remaining samples, only NP-10 getter was used. The $^4\text{He}/^3\text{He}$ ratios of blanks with and without the cryogenic trap are essentially identical. Extracted gas from each of the 17 packets was then spiked with ^3He and analyzed using a quadrupole mass spectrometer. Each of the 17 packets was dissolved in 5% nitric acid, spiked, and its U-Th-Sm abundances were determined using ICP-MS.

Originally each phosphate aggregate was to be analyzed separately (single-grain instead of multi-grain analysis) to gain high spatial resolution. However, preliminary ^4He analyses for 33 ALHA77005 single aggregates at the University of Arizona yielded very low signals, commonly less than 150% of procedural blanks. Based on these preliminary data, the analyses in this study consist of groups of multiple grains (aggregates). Therefore the resulting ages represent pooled ages of the groups of aggregates.

Phosphorus chemistry maps for grouped aggregates Z103-113, A41-56, and Z01-20 are shown in Figures 4-5, 4-6, and 4-7, respectively. For the remaining grouped aggregates, phosphorus chemistry maps are shown in Figures 4-12 to 4-21 for Zagami and Figures 4-22 to 4-25 for ALHA77005. Each figure represents one packet of samples used for (U-Th)/He analysis. For three more packets (ZAG05, ZAG234 and ZAG01, Figures 4-19, 4-20, and 4-21), chemistry mapping was not performed and only back-scattered electron (BSE) images are displayed. From these chemistry maps, the two-dimensional distribution of phosphate grains was deduced in each aggregate. It is noteworthy that aggregates of different sizes may have similar dimensions as the phosphate grains. In this case, the large aggregates have other phases attached to

phosphates, thus more efficiently capturing radiogenic ^4He atoms, which were energetic immediately after radioactive decay.

Two Zagami and one ALHA77005 thin sections were examined under a stereo microscope for basic petrography and fracture-free areas. BSE images and chemical scans were produced using SEM. For examples of BSE images of merrillite from thin sections, refer to Figure 4-8 for Zagami and Figure 4-9 for ALHA77005. For composite views of full thin section scans, refer to Figures 4-10 and 4-11 for Zagami and ALHA77005, respectively. More BSE images of merrillite are presented in Appendix C for Zagami and Appendix D for ALHA77005.

Table 4-1. List of 80 out of 165 Zagami aggregates used in this study.

ZAGAMI packets	75-125 μm	125-150 μm	150-250 μm	
Z01-20	06 grn01	26 grn01		
	14 grn01	27 grn01		
	15 grn01	30 grn01		
	16 grn01	31 grn01		
	18 grn01	33 grn01		
	18 grn02	33 grn02		
	22 grn01	33 grn03		
	22 grn02	36 grn01		
	22 grn03	38 grn01		
	23 grn01	41 grn01		
Z21-40	42 grn01	52 grn02		
	43 grn01	54 grn01		
	45 grn01	55 grn01		
	45 grn02	58 grn01		
	46 grn01	58 grn02		
	47 grn01	60 grn01		
	47 grn02	64 grn01		
	48 grn01	65 grn01		
	51 grn01	65 grn02		
	52 grn01	65 grn03		
Z41-60	67 grn01	20 grn01	44 grn01	
	68 grn01	25 grn01	51 grn01	
	68 grn02	25 grn02	51 grn02	
	69 grn01	28 grn01	51 grn03	
	71 grn01	29 grn01	64 grn01	
	72 grn01	39 grn01	64 grn02	
	72 grn02	39 grn02		
Z61-80		63 grn01	75 grn01	4 grn01
		63 grn02	75 grn02	4 grn02
		63 grn03	86 grn01	5 grn01
		66 grn01	86 grn02	8 grn01
		66 grn02	106 grn01	
		68 grn01	112 grn01	
		68 grn02	116 grn01	
	72 grn01	117 grn01		

Each group (Z01-20, Z21-40, Z41-60, and Z61-80) consists of aggregates listed in each corresponding row by their fraction size.

Table 4-2. List of 85 out of 165 Zagami aggregates used in this study.

ZAGAMI packets	150-250 μm		125-150 μm	
			packets	
Z81-92	14 grn01	20 grn01	ZAG01	Zag0011-001
	15 grn01	21 grn01		Zag0022-001
	16 grn01	21 grn02		Zag0023-002
	17 grn01	21 grn03		Zag0026-001
	17 grn02	22 grn01		Zag0038-002
	18 grn01	23 grn01		
Z93-102	24 grn01	31 grn01	ZAG234	Zag0040-001
	27 grn01	31 grn02		Zag0041-001
	28 grn01	31 grn03		Zag0042-001
	30 grn01	31 grn04		Zag0046-001
	30 grn02	32 grn01		Zag0047-001
				Zag0047-002
Z103-113	37 grn01	42 grn02		Zag0047-003
	37 grn02	43 grn01		Zag0047-004
	39 grn01	43 grn02		Zag0049-001
	41 grn01	45 grn01		Zag0052-001
	41 grn02	45 grn02		Zag0059-001
	42 grn01			Zag0059-002
Z114-123	46 grn01	52 grn01		Zag0059-003
	47 grn01	52 grn02		Zag0060-002
	48 grn01	52 grn03	ZAG05	Zag0060-001
	48 grn02	54 grn01		Zag0004-001
	50 grn01	54 grn02		Zag0011-002
				Zag0022-001
		Zag0022-002		
		Zag0065-001		
Z124-134	56 grn01			Zag0069-001
	56 grn02			Zag0070-001
	57 grn01			Zag0083-001
	58 grn01			Zag0083-002
	58 grn02			Zag0093-001
	58 grn03			Zag0100-001
	59 grn01			
	59 grn02			
	61 grn01			
	61 grn02			
61 grn03				

Each group (Z81-92, Z93-102, 103-113, Z114-123, Z124-134, ZAG01, ZAG234, and ZAG05) consists of aggregates listed in each corresponding row by their fraction size.

Table 4-3. List of 56 out of 83 ALHA77005 aggregates used in this study.

ALHA77005 packets	63-150 μm		>180 μm	
A01-20	02 grn01	15 grn02		
	03 grn01	15 grn03		
	03 grn02	16 grn01		
	04 grn01	16 grn02		
	04 grn02	17 grn01		
	08 grn01	17 grn02		
	08 grn02	18 grn01		
	09 grn01	19 grn01		
	11 grn01	20 grn01		
	15 grn01	20 grn02		
A21-40	21 grn01	29 grn03		
	22 grn01	39 grn01		
	22 grn02	39 grn02		
	23 grn01	42 grn01		
	27 grn01	45 grn01		
	27 grn02	46 grn01		
	28 grn01	46 grn02		
	28 grn02	47 grn01		
	29 grn01	51 grn01		
	29 grn02	51 grn02		
A41-56	49 grn01	64 grn01	32 grn01	51 grn01
	53 grn01	66 grn01	36 grn01	55 grn01
	59 grn01	66 grn02	37 grn01	55 grn02
	60 grn01	66 grn03	44 grn01	56 grn01

Each group (A01-20, A21-40, and A41-56) consists of aggregates listed in each corresponding row by their fraction size.

Table 4-4. List of 27 out of 83 ALHA77005 aggregates used in this study.

ALHA77005 packets	63-150 μm	150-180 μm	
AHp123	Cu0010130-01	Cu0020039-01	Cu0030008-01
	Cu0010046-02	Cu0020006-01	Cu0030012-01
	Cu0010042-01	Cu0030005-01	Cu0030020-01
	Cu0010027-03	Cu0030006-01	Cu0030022-01
	Cu0010030-02	Cu0030007-01	Cu0030023-01
AHp45		Cu0030030-01	Cu0030048-01
		Cu0030032-01	Cu0030052-01
		Cu0030039-01	Cu0030060-01
		Cu0030040-01	Cu0030062-01
		Cu0030045-01	Cu0030067-02
		Cu0030046-01	Cu0030075-01

Each group (AHp123 and AHp45) consists of aggregates listed in each corresponding row by their fraction size.

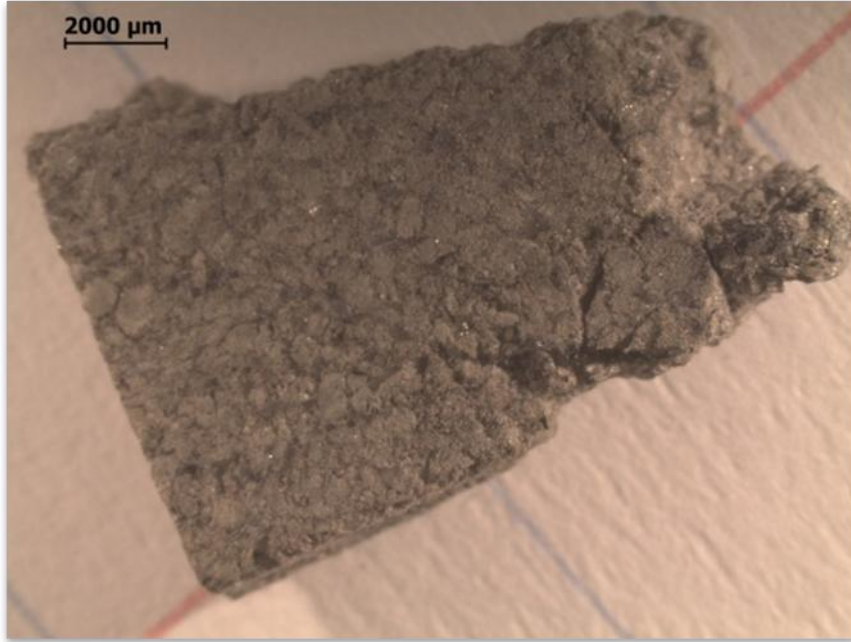


Figure 4-1. Zagami rock chip sample used for this research. Scale: 2000 μm.



Figure 4-2. ALHA77005 samples used for this research. Scale: 1500 μm.

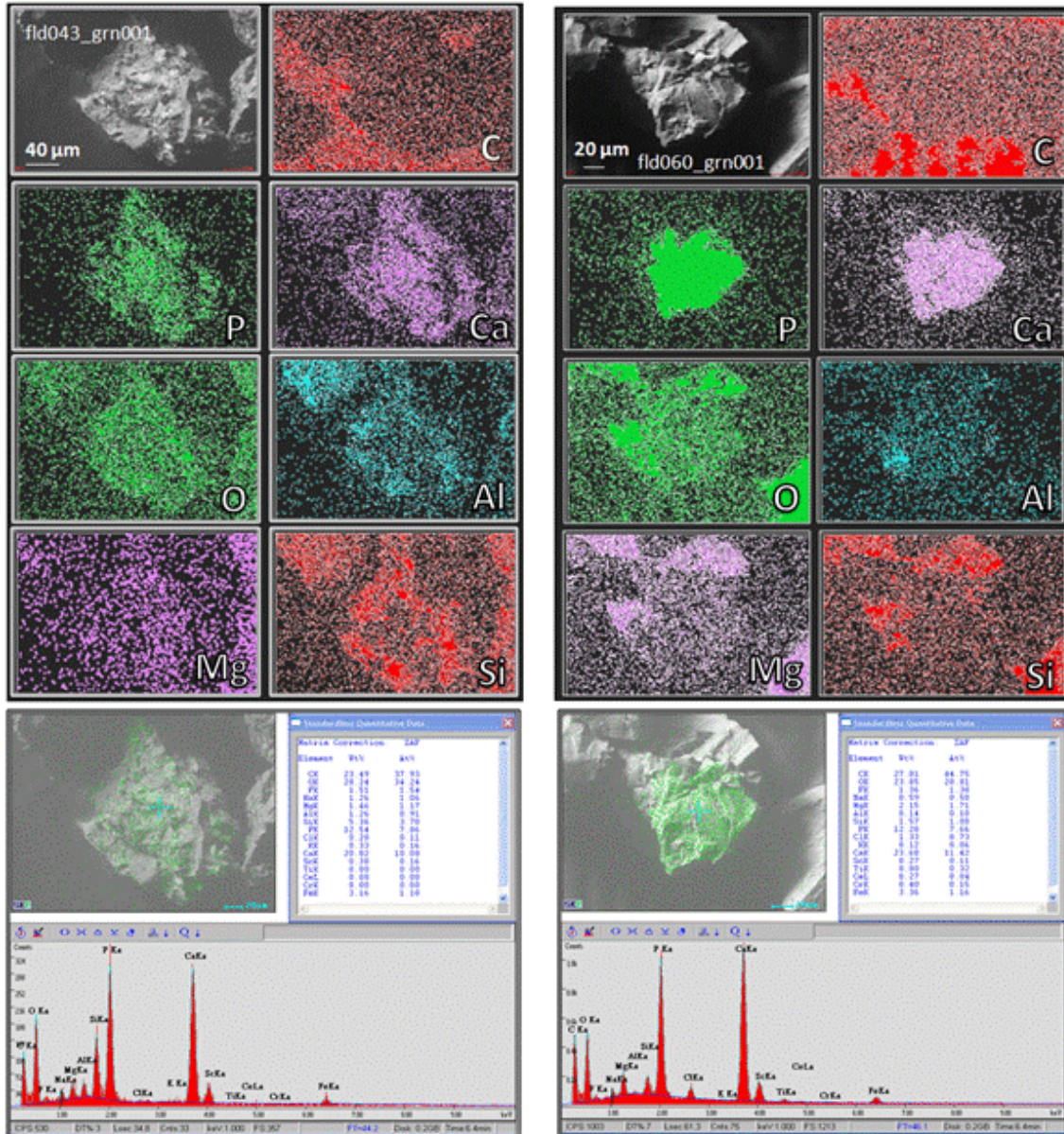


Figure 4-3. Zagami single phosphate aggregate. SEM chemical maps (top left) illustrate very good P, Ca, and O coverage with fair amounts of Al, Mg, Si and very low C. EDS spot analyses (bottom left) show very high P and Ca peaks with moderate Mg, Na, and Si signals.

Figure 4-4. ALHA77005 single phosphate aggregate. SEM chemical maps (top right) illustrate very good P and Ca coverage with fair amounts of O, Mg, Si and very low C and Al. EDS spot analyses (bottom right) show very high P and Ca peaks with moderate Mg and Na signals.

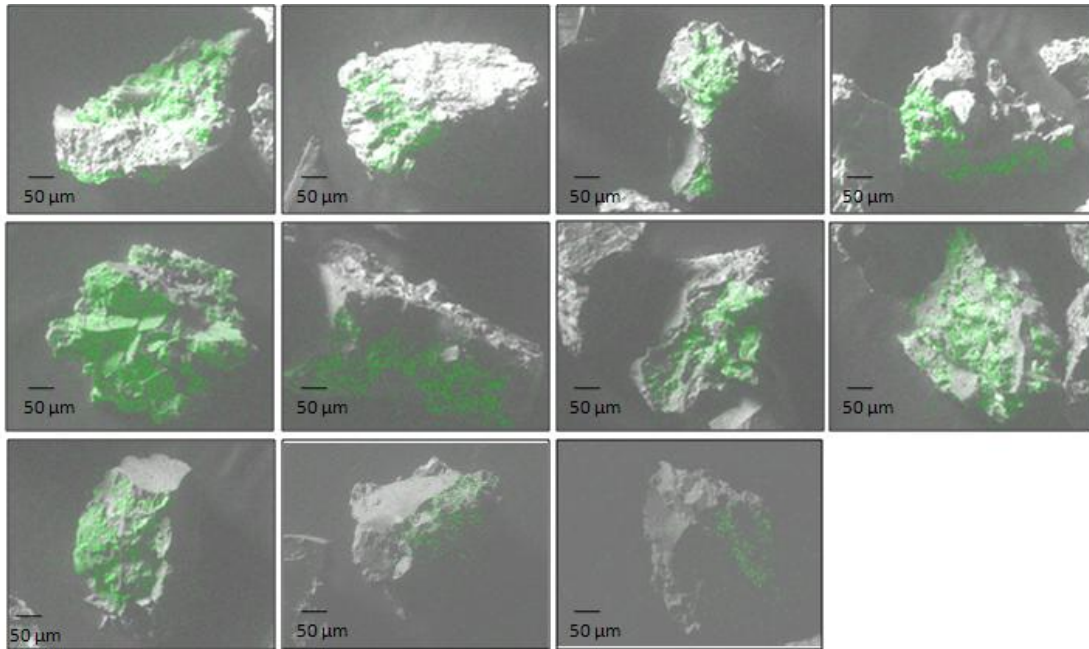


Figure 4-5. Zagami aggregates displaying phosphorus SEM scans for group Z103-113 measuring 150-250 μm . Most larger fractions illustrate partial phosphorus coverage relative to smaller aggregates. Counting from top left to right, the eighth image is chemically mapped in Figure 4-3.

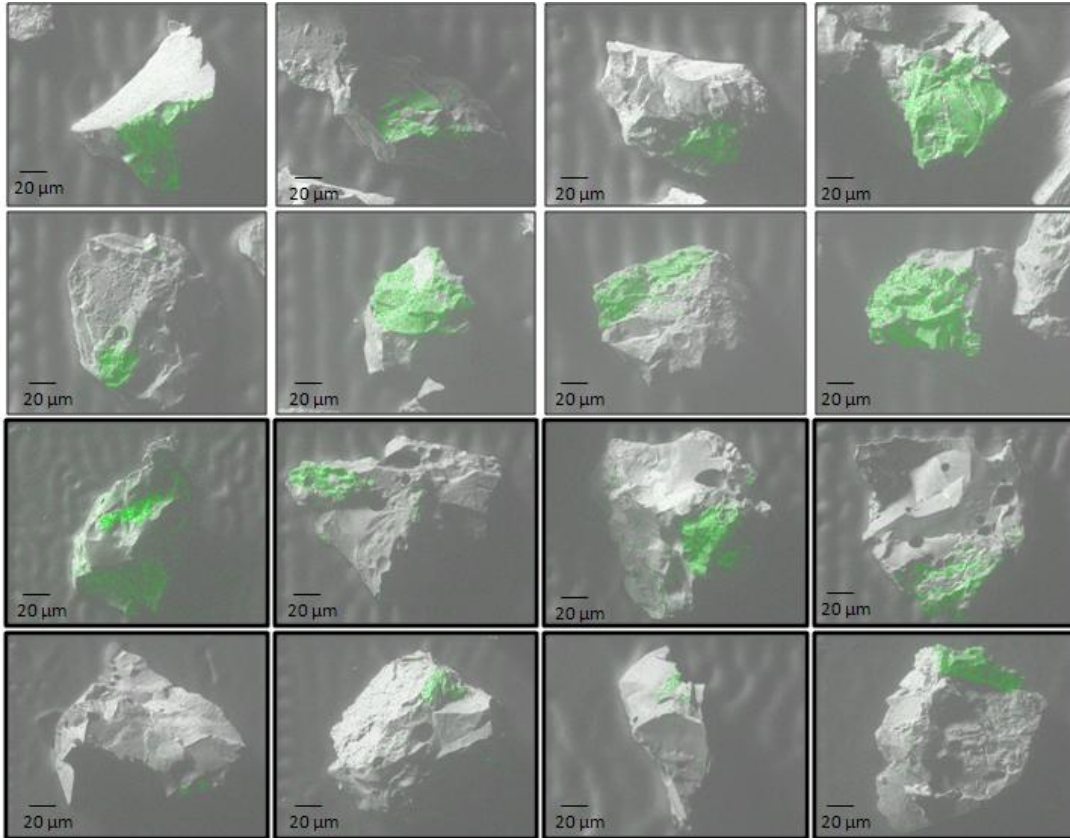


Figure 4-6. ALHA77005 aggregates displaying phosphorus SEM scans for group A41-56 measuring 63-150 μm for the top eight and $> 180 \mu\text{m}$ for the bottom eight aggregates (black bold borders). Counting from top left to right, the fourth image is chemically mapped in Figure 4-4.

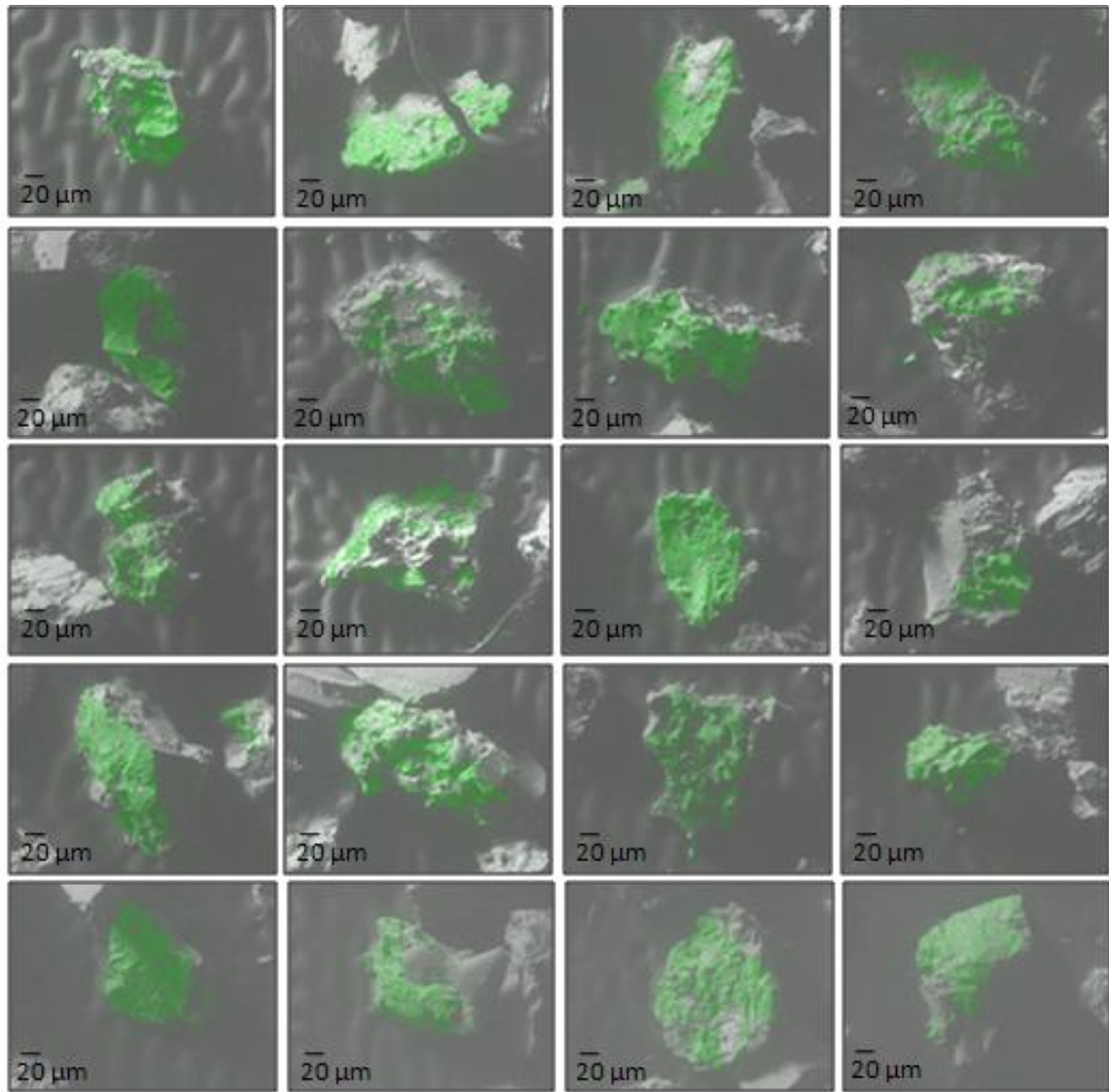


Figure 4-7. Zagami aggregates displaying phosphorus SEM scans for group Z01-20 measuring 75-125 μm . Note that these smaller fractions have almost complete phosphorus coverage radially extending to the rim of the grain when compared to the larger fractions.

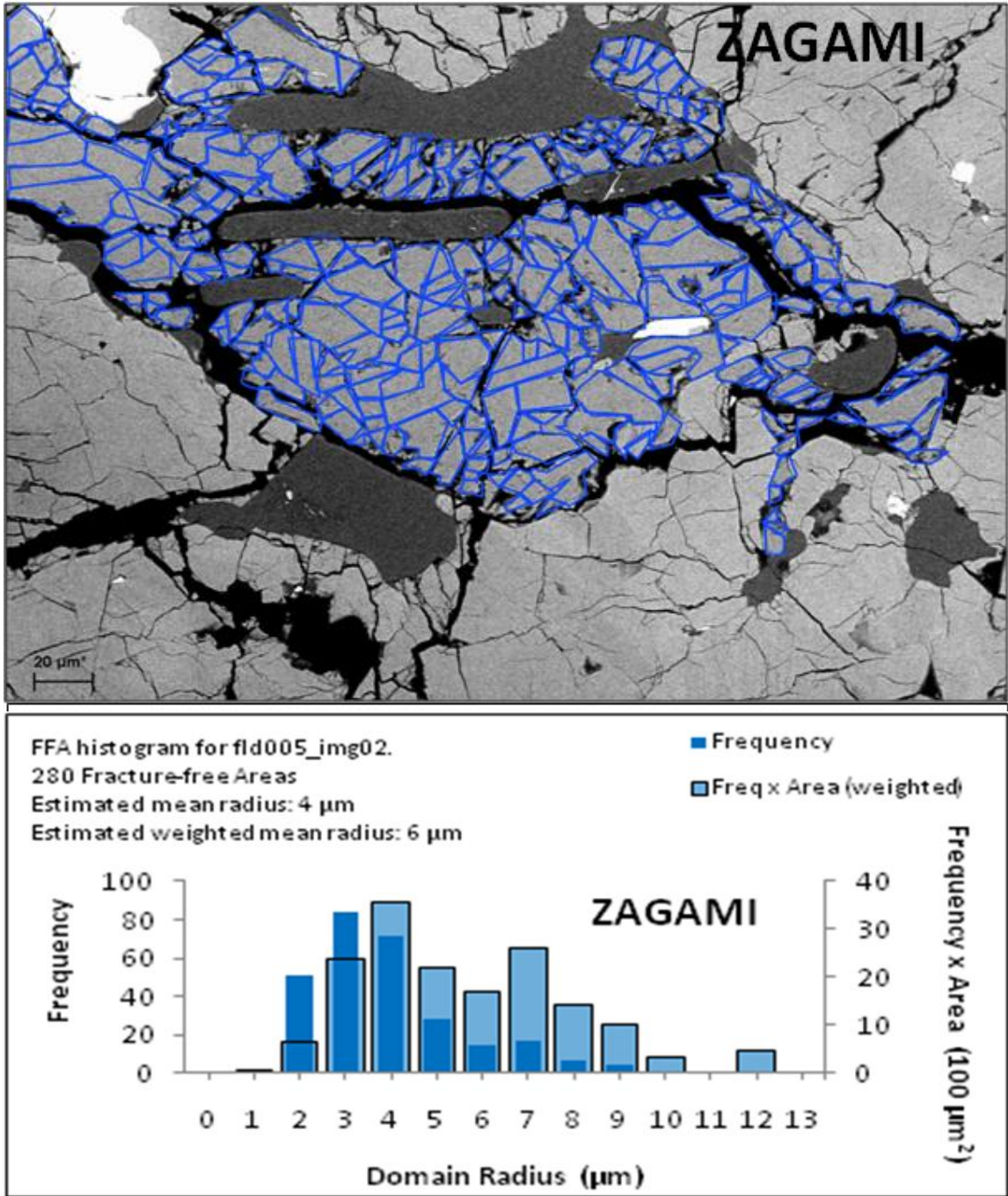


Figure 4-8. Zagami BSE image fld005_img02 and histogram. Blue traces on thin section of merrillite (top) mark fracture-free areas (FFA). Radius distribution (bottom histogram) is defined by FFAs from the merrillite thin section. Left axis represents the raw frequency of each radius (blue solid bars), right axis illustrates the weighted frequency (pale blue bars with borders) of the larger FFAs. Thin section (Zagami 4709-1) supplied by the American Museum of Natural History, New York, NY.

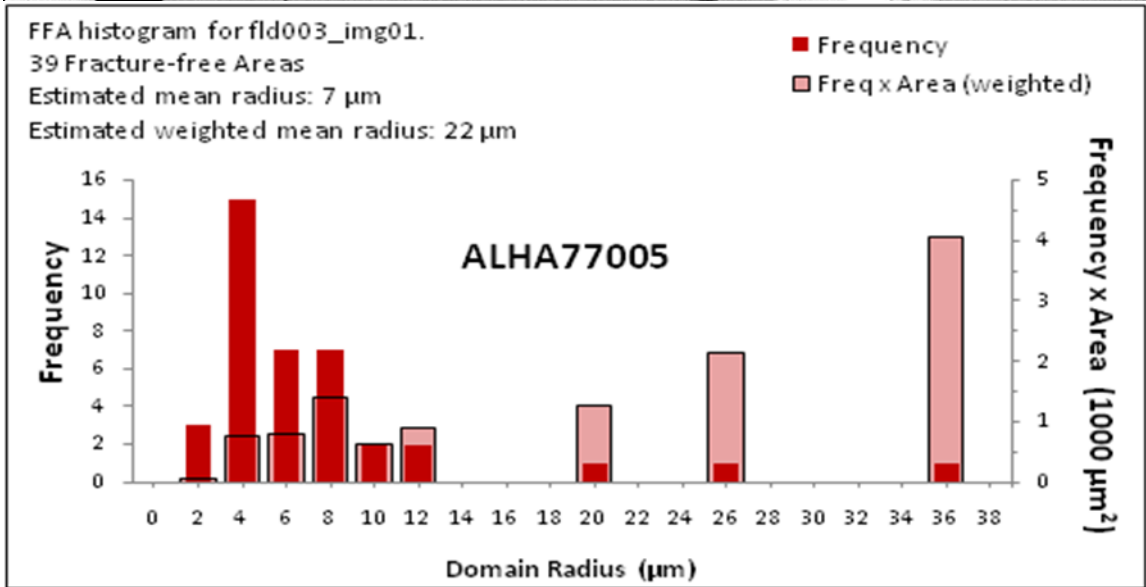
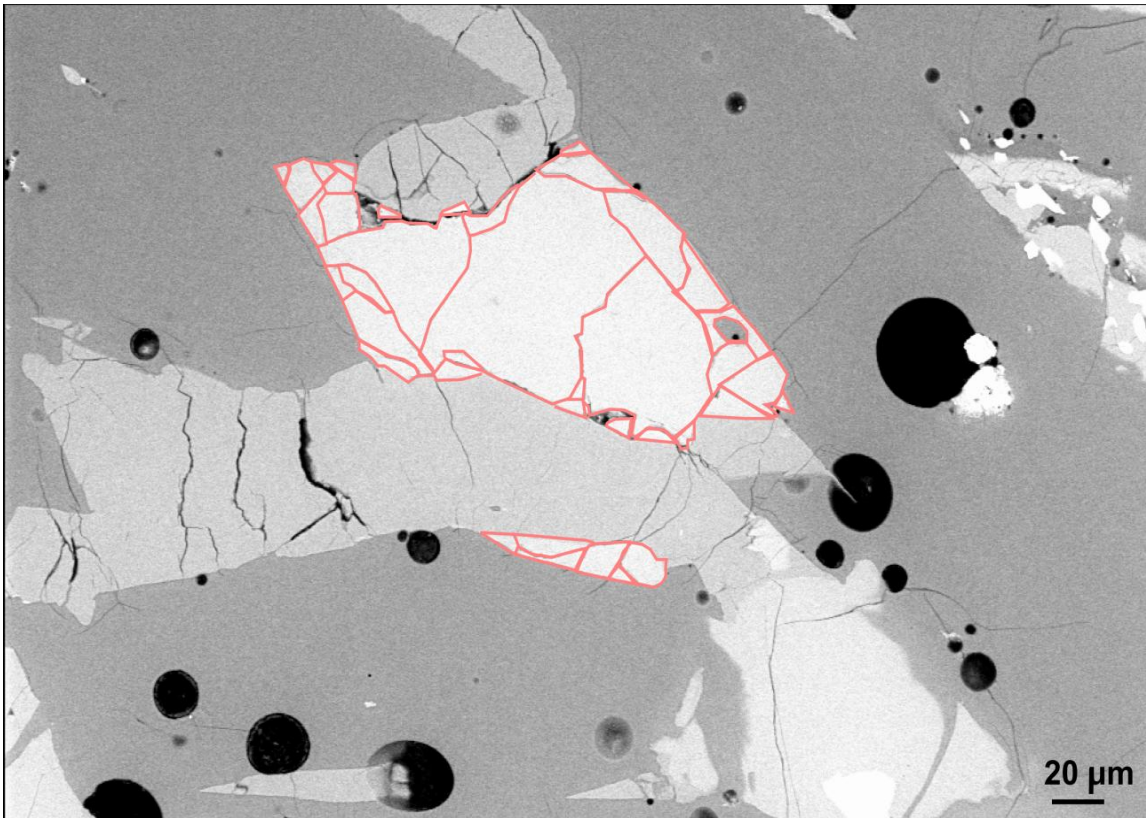


Figure 4-9. ALHA77005 BSE image fld003_img01 and histogram. Red traces on this section of merrillite (top) mark fracture-free areas (FFA). Radius distribution (bottom histogram) is defined by FFAs from the merrillite thin section. Left axis represents the raw frequency of each radius (red solid bars), right axis illustrates the weighted frequency (pale red bars with borders) of the larger FFAs. Thin section (ALHA77005 120) supplied by NASA.

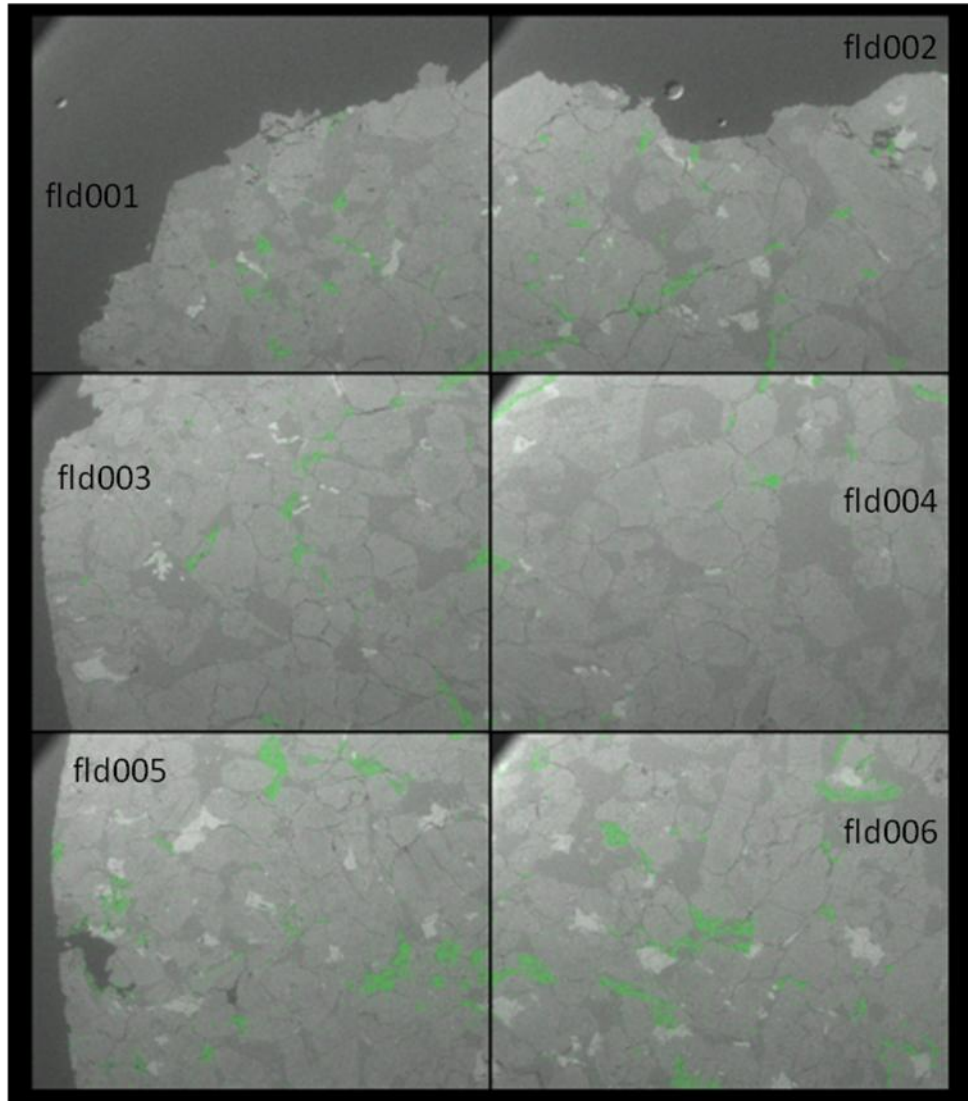


Figure 4-10. SEM composite image of thin section Zagami 4709-1. Green areas are merrillite (phosphate) minerals.

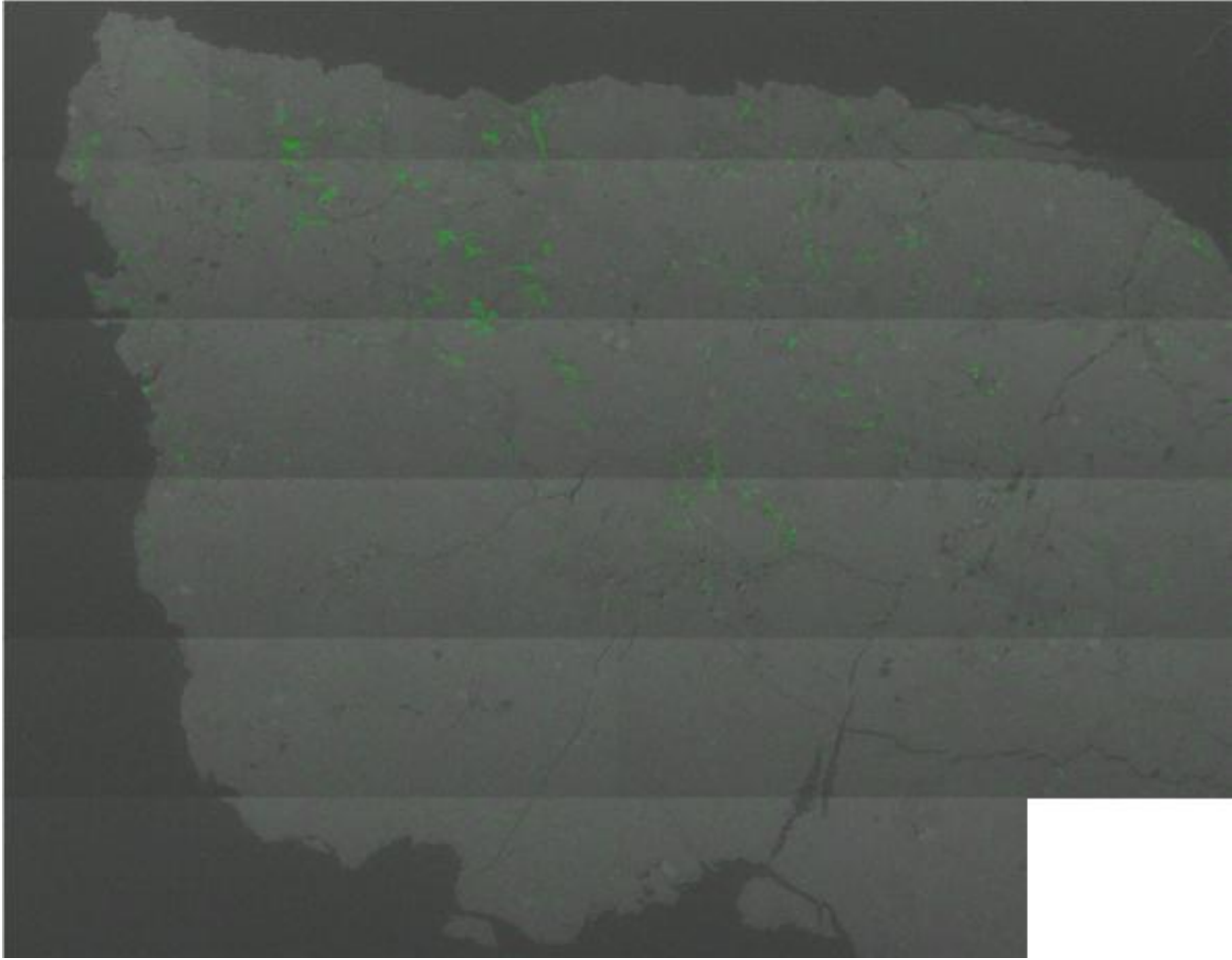


Figure 4-11. SEM composite image of thin section ALHA77005 120. Green areas are merrillite (phosphate) minerals.

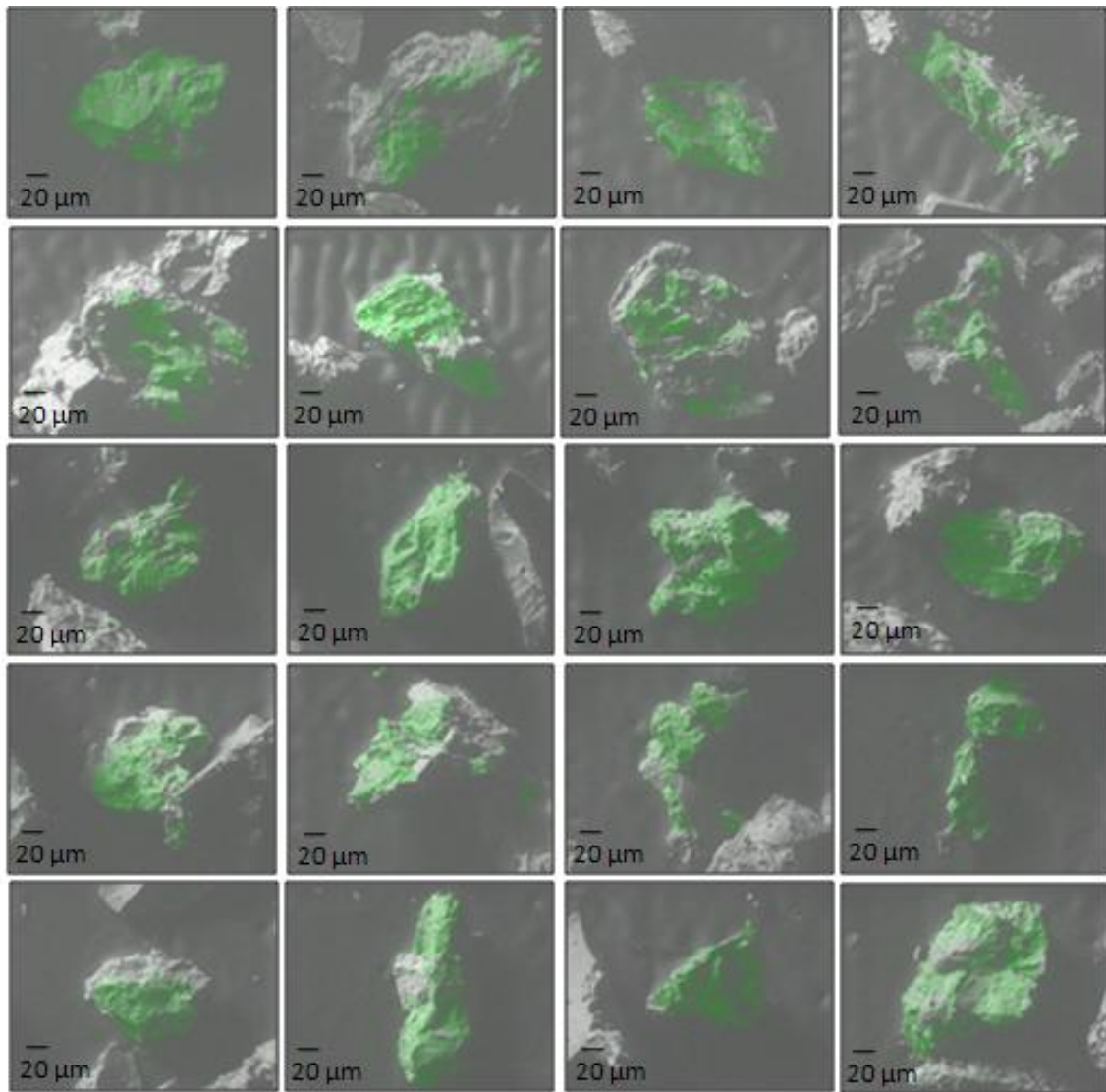


Figure 4-12. Zagami aggregates displaying phosphorus SEM scans for group Z21-40 measuring 75-125 μm.

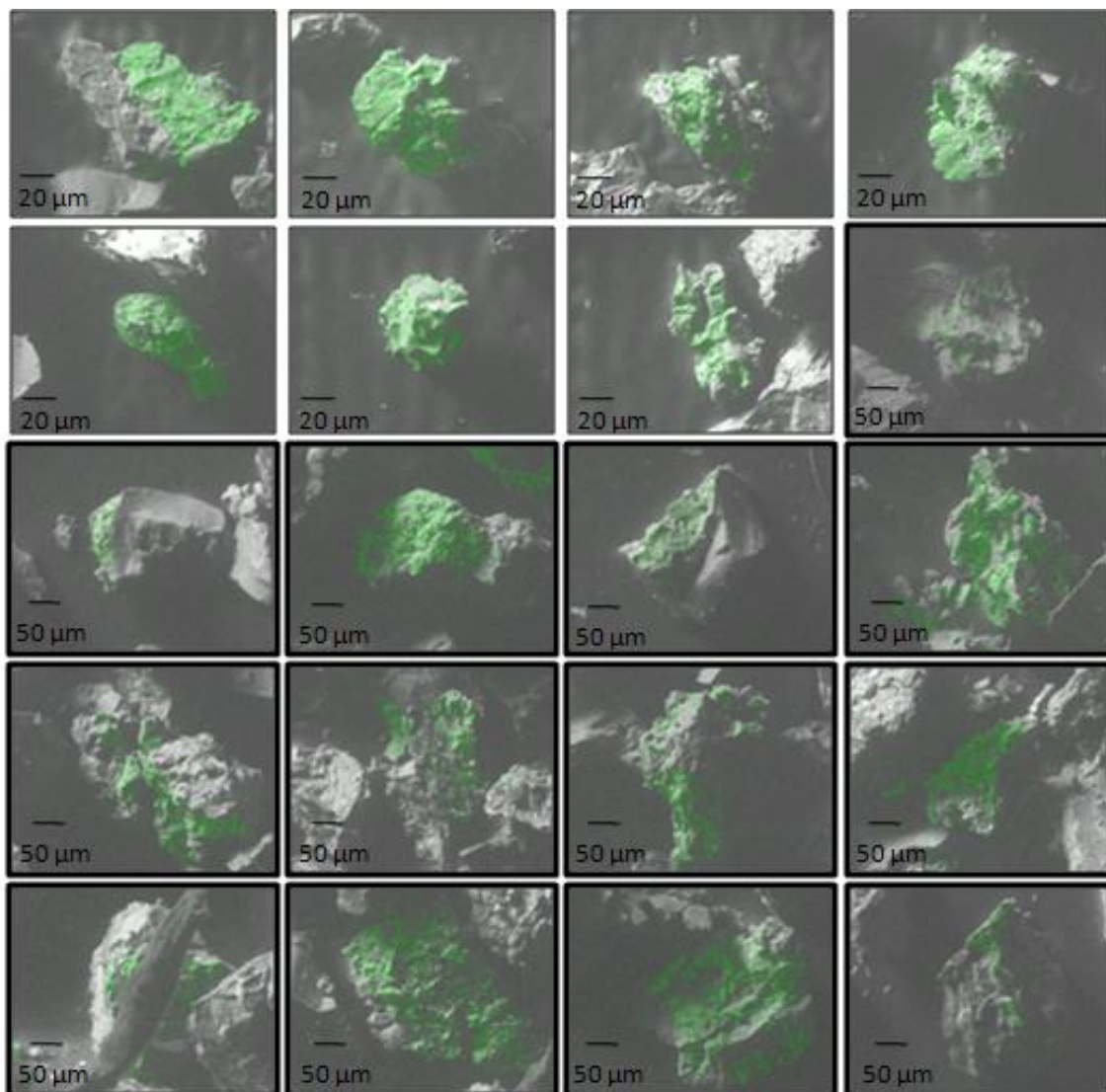


Figure 4-13. Zagami aggregates displaying phosphorus SEM scans for group Z41-60 measuring 75-125 μm for the top seven aggregates and 125-150 μm for the bottom thirteen aggregates (black bold borders).

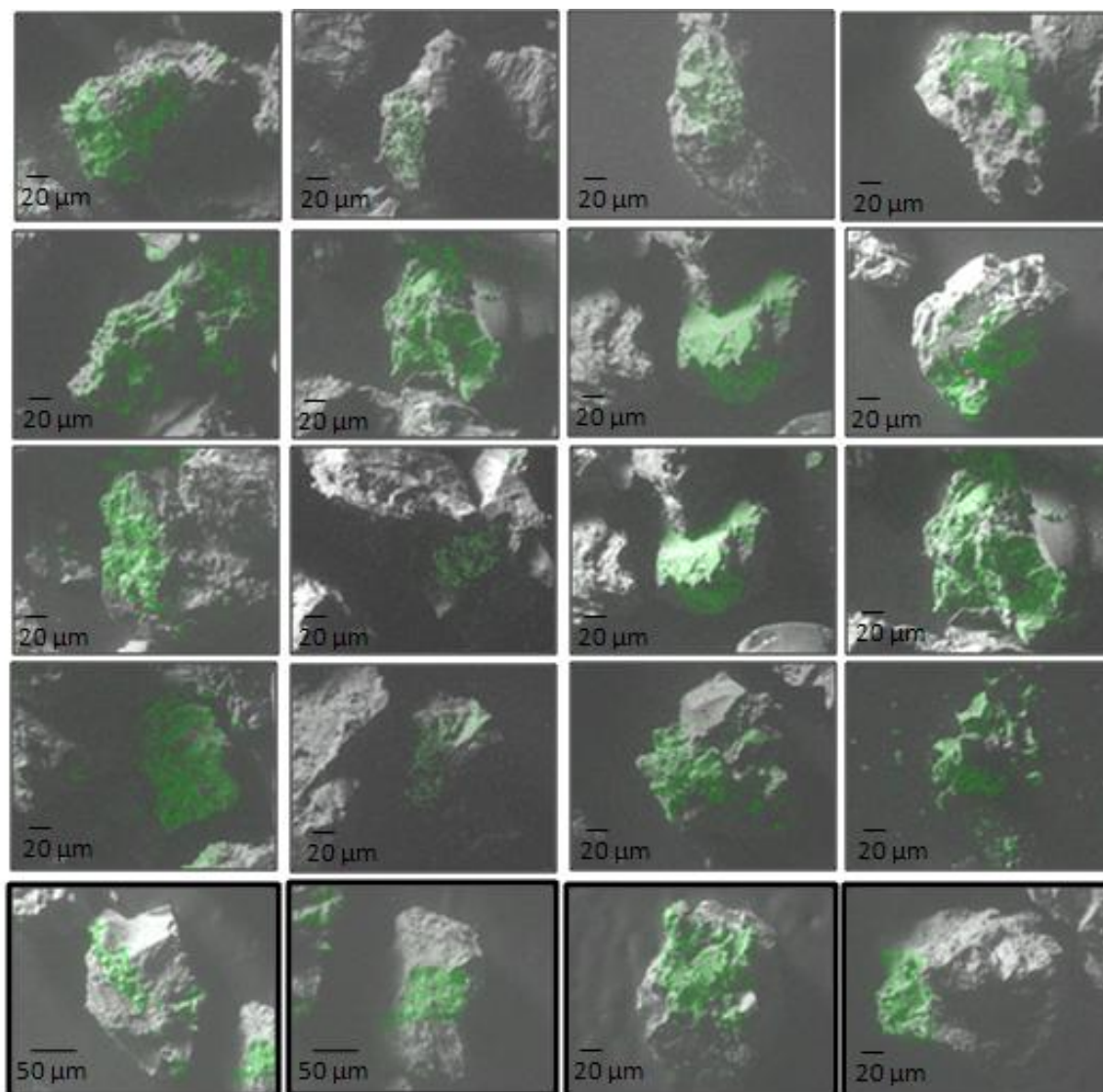


Figure 4-14. Zagami aggregates displaying phosphorus SEM scans for group Z61-80 measuring 125-150 μm for the top sixteen aggregates and 150-250 μm for the bottom four aggregates (black bold borders).

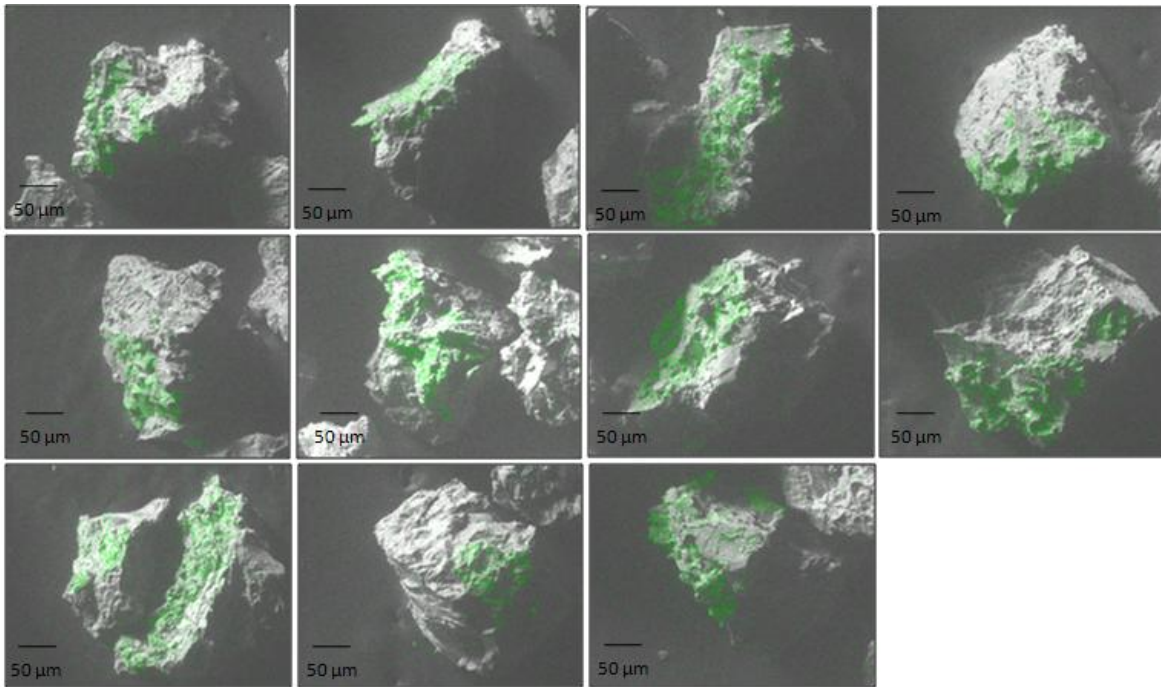


Figure 4-15. Zagami aggregates displaying phosphorus SEM scans for group Z81-92 measuring 150-250 μm.

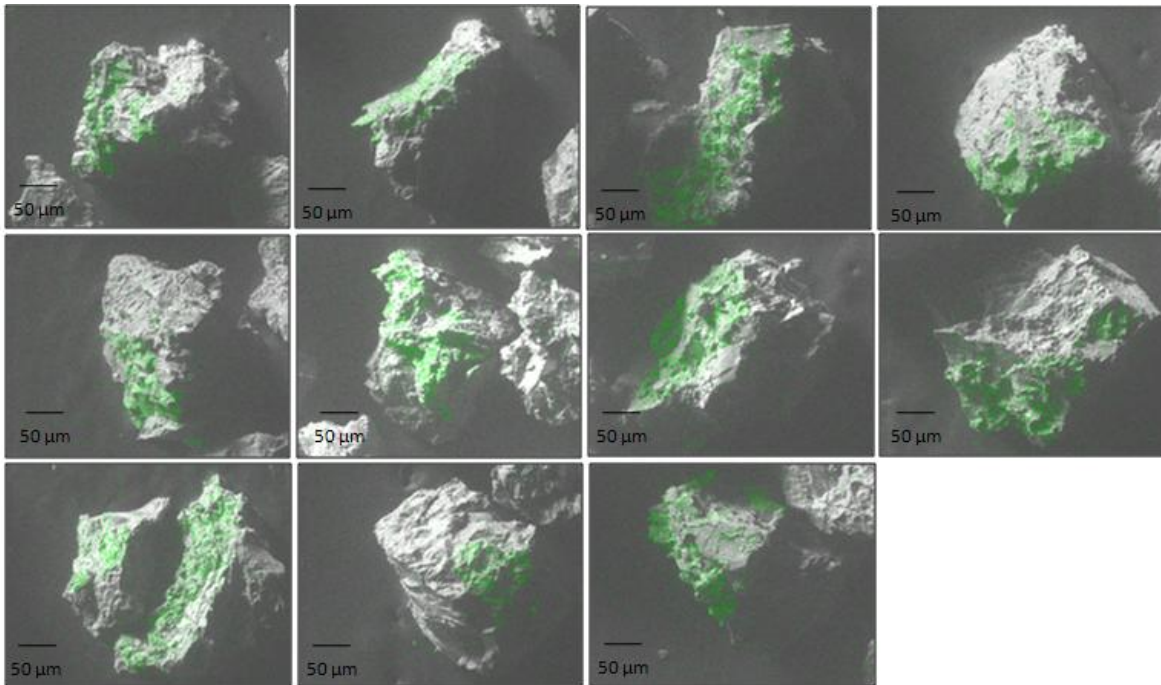


Figure 4-16. Zagami aggregates displaying phosphorus SEM scans for group Z93-102 measuring 150-250 μm.

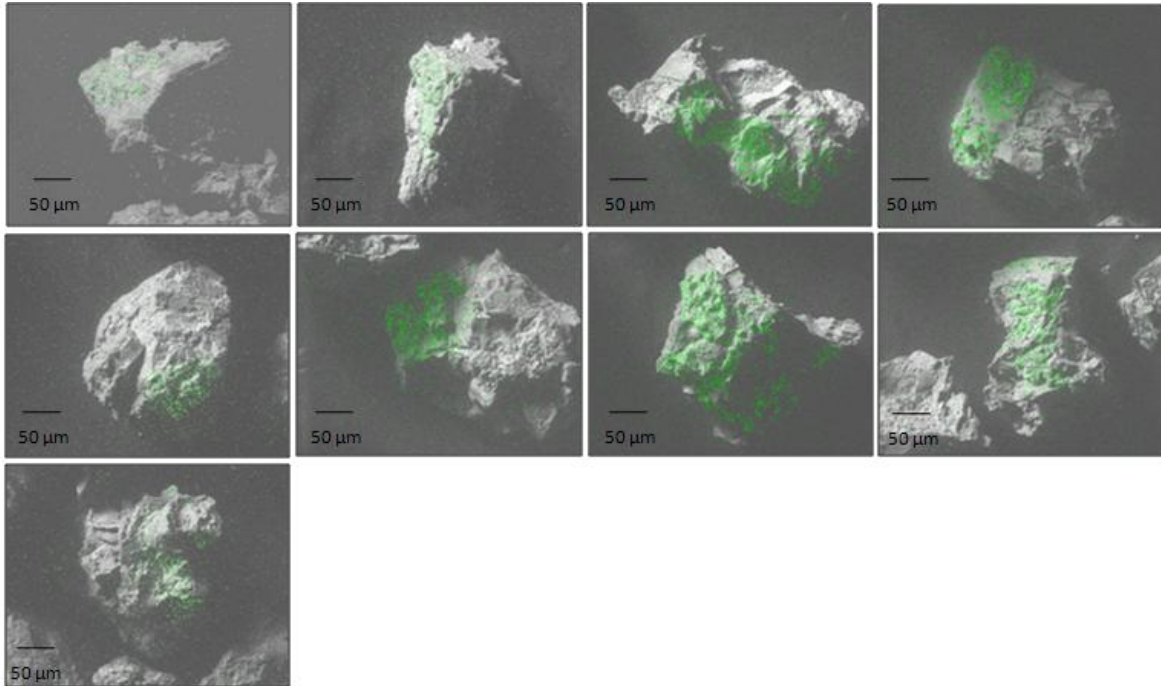


Figure 4-17. Zagami aggregates displaying phosphorus SEM scans for group Z114-123 measuring 150-250 μm .

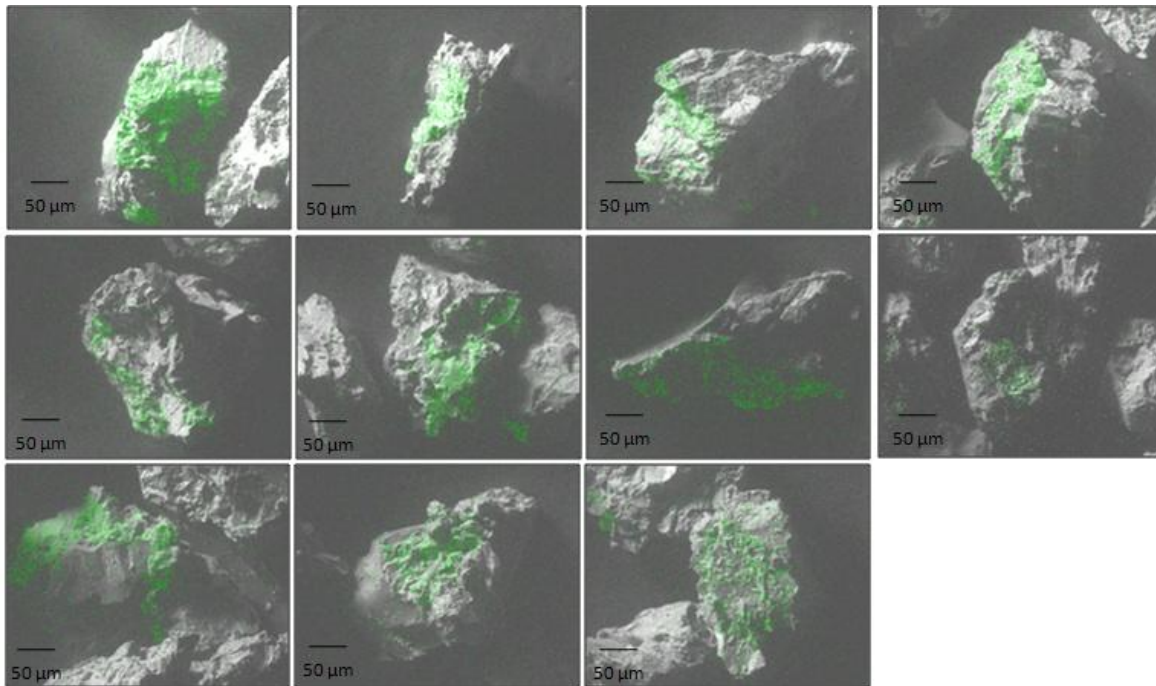


Figure 4-18. Zagami aggregates displaying phosphorus SEM scans for group Z124-134 measuring 150-250 μm .

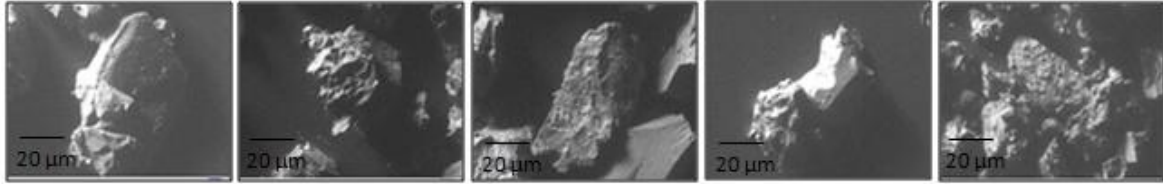


Figure 4-19. Zagami aggregates displaying SEM scans for group ZAG01 measuring 125-150 μm.

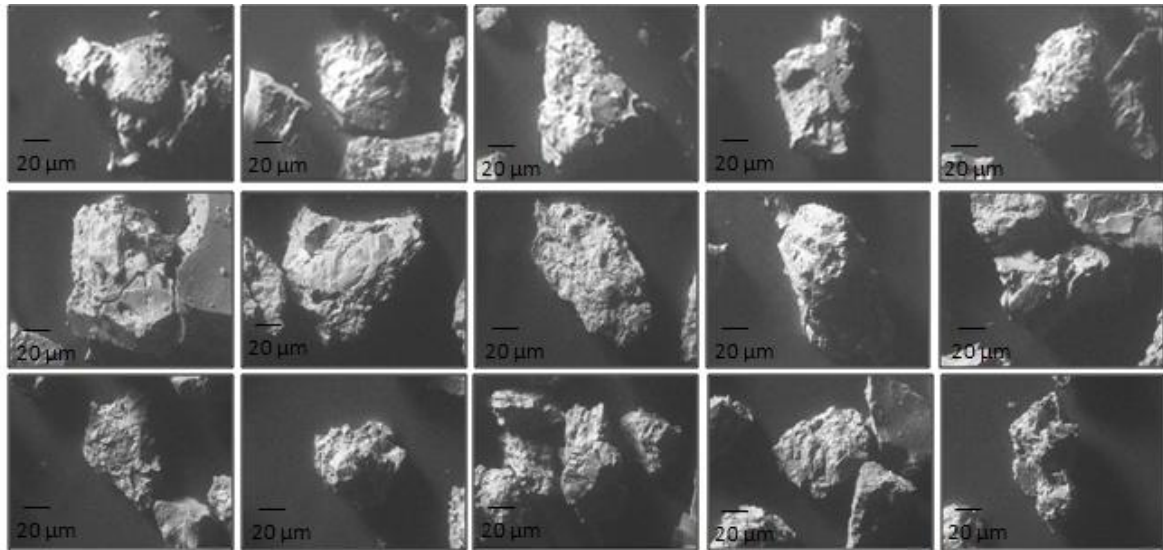


Figure 4-20. Zagami aggregates displaying SEM scans for group ZAG234 measuring 125-150 μm.

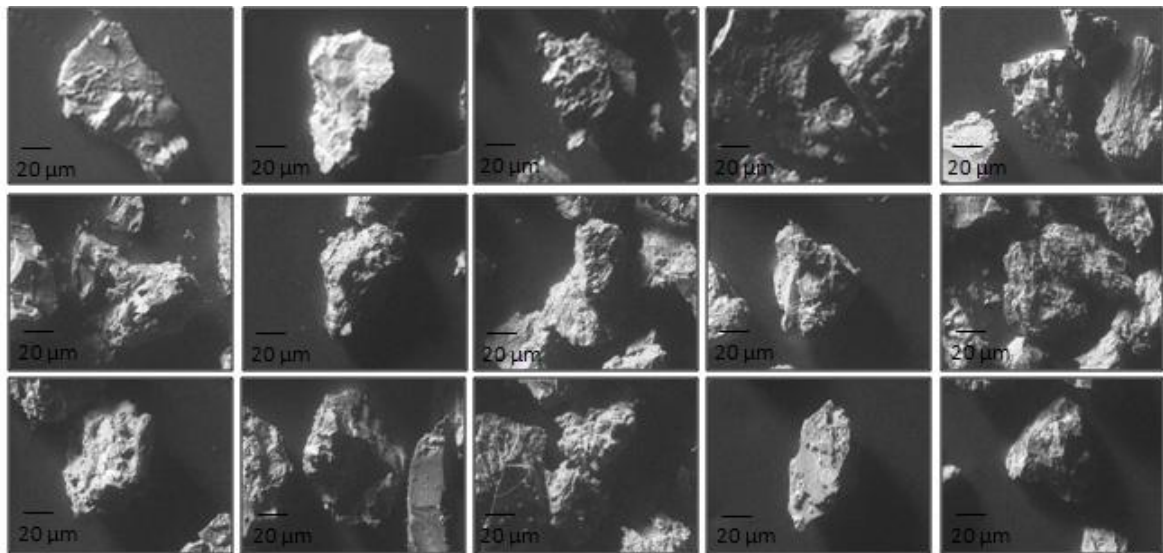


Figure 4-21. Zagami aggregates displaying SEM scans for group ZAG05 measuring 125-150 μm.

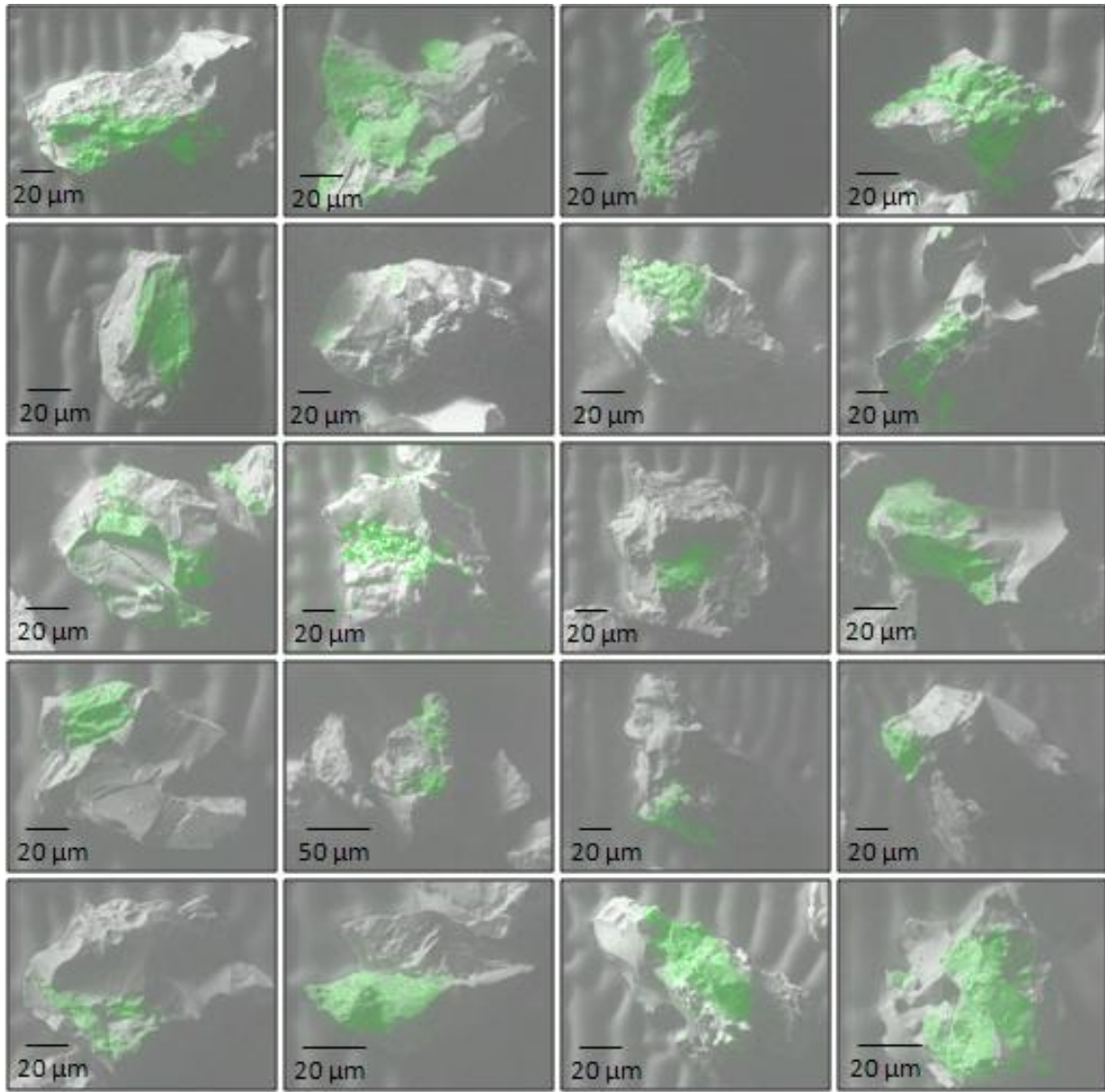


Figure 4-22. ALHA77005 aggregates displaying phosphorus SEM scans for group A01-20 measuring 63-150 μm .

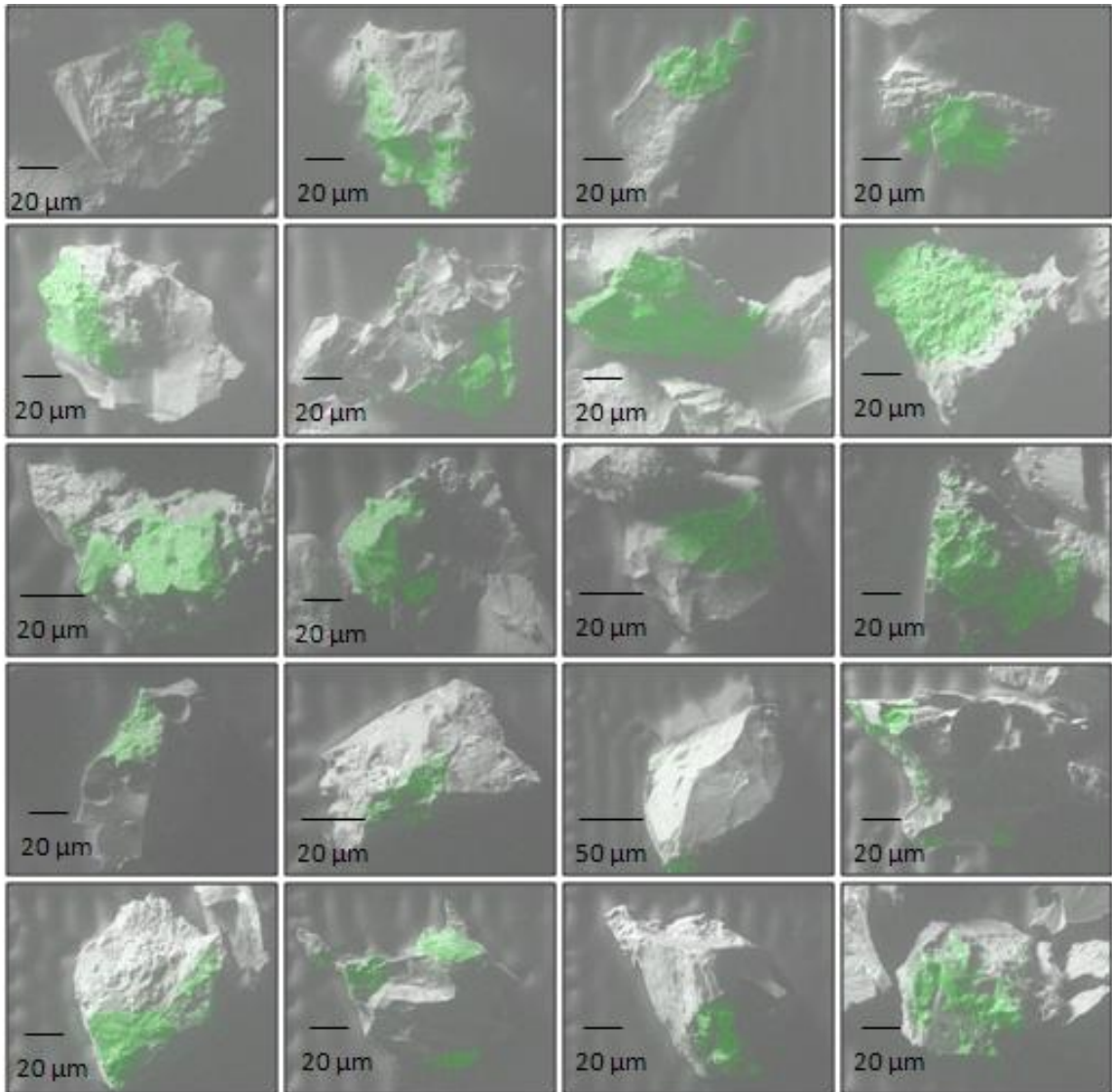


Figure 4-23. ALHA77005 aggregates displaying phosphorus SEM scans for group A21-40 measuring 63-150 μm.

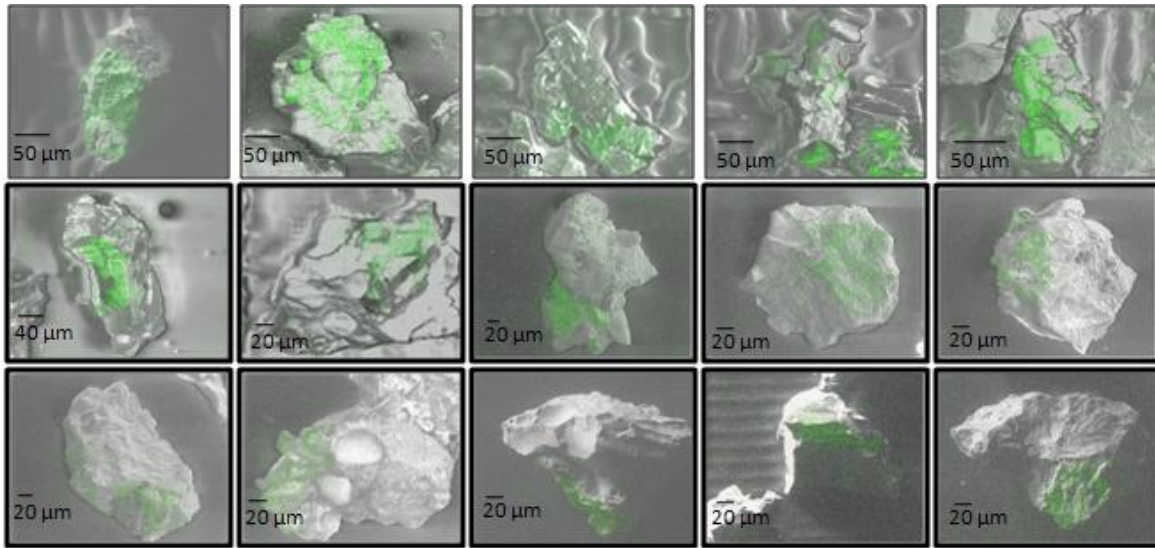


Figure 4-24. ALHA77005 aggregates displaying phosphorus SEM scans for group AHp123 measuring 63-150 μm for the top five aggregates and 150-180 μm for the bottom ten (black bold borders).

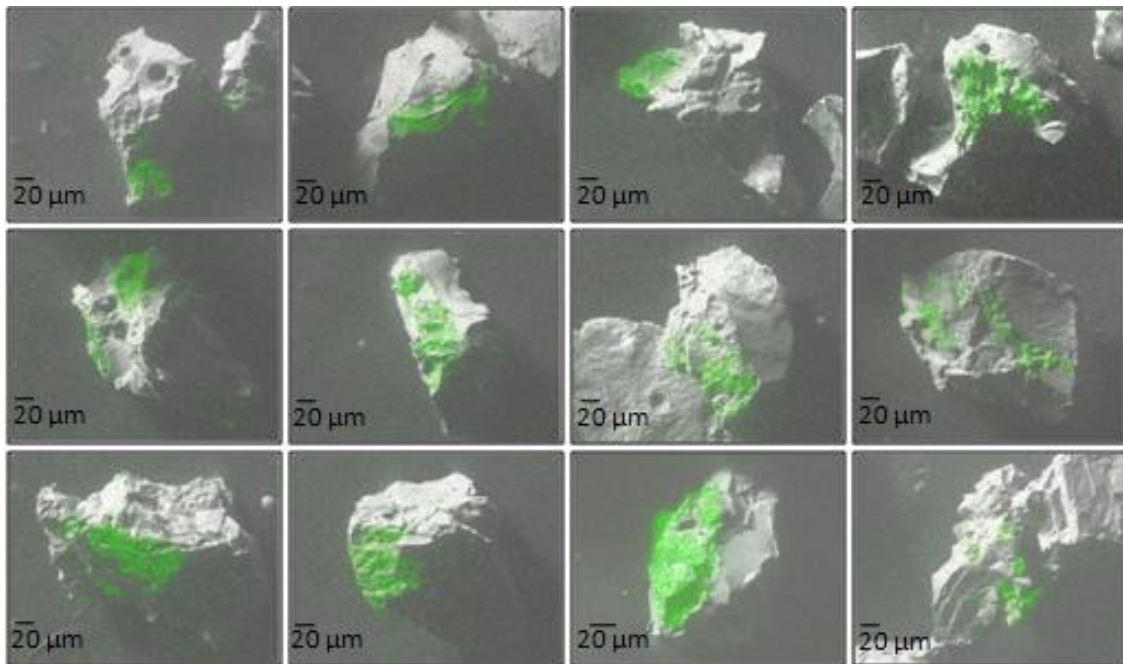


Figure 4-25. ALHA77005 aggregates displaying phosphorus SEM scans for group AHp45 measuring 150-180 μm .

CHAPTER 5 (U-TH)/HE RESULTS

Cosmogenic ^4He Correction

To accurately calculate (U-Th)/He ages, radiogenic ^4He abundances need to be estimated. Because ^4He can be also produced through interactions with cosmic rays, cosmogenic ^4He needs to be subtracted from the measured ^4He . The common way to correct this effect is based on the production rate of cosmogenic ^4He calculated from an isotopic ratio of $^4\text{He}/^3\text{He}$ (Paneth and Reasbeck, 1952; Shuster and Farley, 2003; Min, 2005). The following parameters are used for cosmogenic ^4He correction: (1) the estimated mass of each sample (using density values from Schwenger *et al.*, 2008), (2) the cosmogenic ^4He production rate of 8.05×10^{-8} (Eugster, 1988; Lorenzetti *et al.*, 2003), and (3) exposure ages of 3.2 Ma and 2.7 Ma for ALHA77005 and Zagami, respectively (Eugster *et al.*, 1997; Schwenger *et al.*, 2008). For Zagami, the contribution of cosmogenic ^4He to the total ^4He is generally in the range of 0.46% - 6.08%. For ALHA77005, however, the cosmogenic ^4He contribution is in the range of 10.36% - 44.02% (Tables 5-1 and 5-2).

(U-Th)/He Ages

The twelve Zagami packets yielded widely scattered (U-Th)/He ages ranging from 19.8 Ma to 202.4 Ma with an average of 107.3 Ma and a standard deviation of 61.0 Ma (Table 5-1 and Figure 5-1). Among these twelve packets, five contained large aggregate fractions measuring between 150-250 μm (Z81-92, Z93-102, Z103-113, Z114-123, Z124-134, Table 4-2) resulting in ages ranging from 110.7 Ma to 202.4 Ma (average = 146.6 Ma, standard deviation = 34.8 Ma, Table 5-3). The average age corresponds to a fractional loss (f_{He}) of 0.17 (Table 5-3) when a reset of the helium

system was assumed at 177 Ma (summarized in Nyquist *et al.*, 2001; Schwenger *et al.*, 2008). These ages are fairly consistent with a calculated (U-Th)/He age of 113 Ma by using U and Th concentrations analyzed by Schwenger *et al.* (2008) from whole rock samples of Zagami.

Five groups consist of mixed aggregates measuring between 75-250 μm : Z41-60 measures between 75-150 μm and Z61-80 measures between 125-250 μm ; ZAG01, ZAG234, and ZAG05 each consists of aggregates measuring between 125-150 μm (Tables 4-1 and 4-2). These five mixed aggregate groups yielded ages in the range of 19.8 Ma to 93.6 Ma (average = 51.2 Ma, standard deviation = 31.4 Ma, $f_{\text{He}} = 0.71$, Table 5-3). The remaining two groups consist of aggregates measuring between 75-125 μm (Z01-20, Z21-40, Table 4-1) with ages ranging from 99.6 Ma and 199.9 Ma (average = 149.7 Ma, standard deviation = 70.9 Ma, $f_{\text{He}} = 0.15$, Table 5-3).

For ALHA77005, four out of the five groups yielded tightly clustered (U-Th)/He ages ranging from 5.9 Ma to 17.9 Ma, with the fifth one producing an older age of 78.2 Ma (Table 5-1, 5-3, and Figure 5-1). A fractional loss (f_{He}) of 0.94 (Table 5-3) corresponds to the younger ages (5.9-17.9 Ma) when the helium system was reset at an assumed crystallization age of 179 Ma (summarized in Nyquist *et al.*, 2001; Schwenger *et al.*, 2008). The estimated fractional loss is consistent with a whole rock value of $94 \pm 3\%$ calculated by Schwenger *et al.* (2008) using their U-Th data combined with the mean He concentration from Schultz and Franke (2004). Schwenger *et al.* (2008) applied this same U-Th data combined with He concentration, both obtained from a whole rock sample (43.2 mg), and calculated a fractional loss of $100 \pm 30\%$.

No apparent correlation is observed between the ages and aggregate sizes for the ALHA77005 groups. For Zagami, aggregates from the five large groups (150-250 μm) show a positive correlation between its (U-Th)/He ages and size of phosphate aggregate. The scattered age-distribution may suggest either (1) differentiated sampling of multiple diffusion domains (Min and Reiners, 2007) or (2) heterogeneous heating during or immediately after shock impact (Cassata *et al.*, 2010).

Table 5-1. (U-Th)/He results, fractional loss, and age calculations.

Packet name	U (mg)	Th (mg)	Sm (mg)	⁴ He (fmol)	⁴ He per aggregate [fmol]	f _{He} (%)	Age (Ma)
ZAGAMI							
ZAG234*	3.57E-08	2.11E-07	2.82E-07	9.17	0.61	90.44	19.77
Z41-60*	9.59E-08	2.98E-07	1.09E-06	27.39	1.37	84.74	30.20
Z61-80*	6.99E-08	3.14E-07	1.39E-06	29.74	1.49	80.37	37.73
ZAG05	7.61E-10	8.01E-08	1.97E-07	8.05	0.73	59.53	74.53
ZAG01	-6.31E-10	3.85E-08	1.39E-08	4.31	0.86	48.72	93.61
Z01-20	3.38E-08	2.03E-07	8.19E-07	44.74	2.24	45.49	99.56
Z103-113	5.31E-08	3.16E-07	1.58E-06	78.03	7.09	39.17	110.73
Z124-134	5.31E-08	2.36E-07	1.13E-06	75.84	6.89	30.27	126.48
Z114-123	3.92E-08	1.78E-07	9.18E-07	64.30	6.43	20.63	143.44
Z81-92	5.94E-08	3.04E-07	1.41E-06	108.32	9.03	17.09	149.65
Z21-40*	2.19E-08	1.58E-07	8.33E-07	65.64	3.28	-11.53	199.86
Z93-102*	2.75E-08	1.47E-07	6.53E-07	69.68	6.97	-13.03	202.44
ALHA77005							
A41-56	1.91E-08	6.05E-08	4.87E-07	1.08	0.07	98.52	5.88
AHp123	1.16E-08	1.69E-07	1.70E-07	1.99	0.13	97.84	7.10
A21-40	1.84E-09	2.47E-08	2.71E-07	0.64	0.03	93.58	14.77
AHp45	3.82E-09	1.30E-07	3.07E-07	3.37	0.28	91.86	17.85
A01-20*	2.89E-09	2.40E-08	2.82E-07	3.77	0.19	58.30	78.19

Ages consist of corrected radiogenic, ⁴He(rad), values from cosmogenic contribution. f_{He} is helium fractional loss since crystallization. Crystallization ages: ALHA77005 = 179 Ma and Zagami = 177 Ma (Nyquist *et al.*, 2001; Schwenger *et al.*, 2008). Exposure ages: ALHA77005 = 3.2 Ma and Zagami = 2.7 Ma (Eugster *et al.*, 1997; Schwenger *et al.*, 2008). Outliers, marked with (*), yielded ages one standard deviation away from the mean age. Table sorted by age.

Table 5-2. Aggregate fraction data and cosmogenic contribution calculations.

Packet name	Aggregate Fractions	Aggregates per packet	⁴ He(cos) [fmol]	⁴ He(rad) (fmol)	⁴ He(cos / cos+rad)	Age (Ma)
ZAGAMI						
ZAG234*	125-150	15	0.5940	9.1711	0.0608	19.77
Z41-60*	75-125, 25-150	20	0.5861	27.3870	0.0210	30.20
Z61-80*	125-150, 150-250	20	1.0282	29.7444	0.0334	37.73
ZAG05	125-150	11	0.4356	8.0537	0.0513	74.53
ZAG01	125-150	5	0.1980	4.3124	0.0439	93.61
Z01-20	75-125	20	0.3046	44.7360	0.0068	99.56
Z103-113	150-250	11	1.3404	78.0348	0.0169	110.73
Z124-134	150-250	11	1.3404	75.8411	0.0174	126.48
Z114-123	150-250	10	1.2186	64.2967	0.0186	143.44
Z81-92	150-250	12	1.4623	108.3196	0.0133	149.65
Z21-40*	75-125	20	0.3046	65.6377	0.0046	199.86
Z93-102*	150-250	10	1.2186	69.6782	0.0172	202.44
ALHA77005						
A41-56	63-150, >180	16	0.8491	1.0796	0.4402	5.88
AHp123	63-150, 150-180	15	0.8375	1.9865	0.2966	7.10
A21-40	63-150	20	0.4361	0.6403	0.4052	14.77
AHp45	150-180	12	0.9731	3.3741	0.2239	17.85
A01-20*	63-150	20	0.4361	3.7749	0.1036	78.19

⁴He(cos): amount of cosmogenic ⁴He per packet. ⁴He(rad): [measured amount of ⁴He per packet] - [⁴He(cos) per packet].
⁴He(cos / cos+rad): ratio of cosmogenic contribution. Ages consist of corrected radiogenic, ⁴He(rad), values from cosmogenic contribution. Outliers, marked with (*), yielded ages one standard deviation away from the mean age. Table sorted by age.

Table 5-3. Average ages and fractional loss calculations per grouped fractions.

Ages (Ma) and f_{He} per Fraction	Average	Standard Deviation
ZAGAMI		
All Fractions		
Age	107.33	60.95
f_{He}	39.47	34.51
Excluding Outliers (*)		
Age	114.00	27.34
f_{He}	35.76	15.44
Smaller Fractions		
Age	149.71	70.92
f_{He}	15.47	40.32
Mixed Fractions		
Age	51.17	31.44
f_{He}	71.22	17.78
Larger Fractions		
Age	146.55	34.75
f_{He}	17.32	19.78
ALHA77005		
All Fractions		
Age	24.76	30.29
f_{He}	86.24	16.85
Excluding Outlier (*)		
Age	11.40	5.83
f_{He}	93.67	3.25

f_{He} : helium fractional loss since crystallization. Smaller, mixed, and larger fractions measure between 75-125 μm , 75-250 μm , and 150-250 μm , respectively.

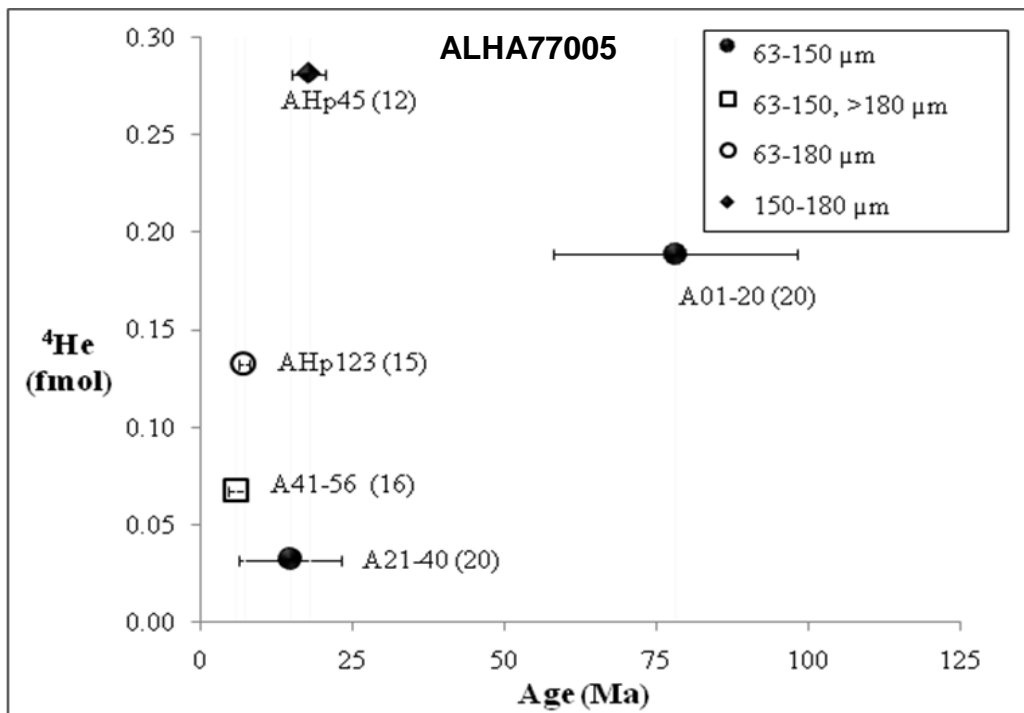
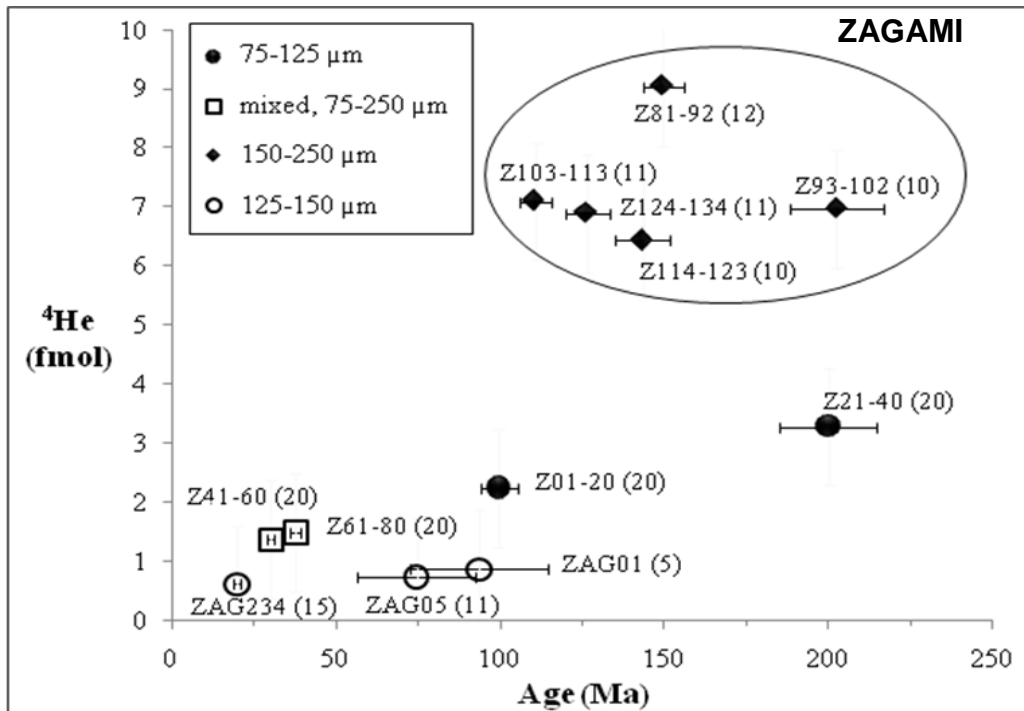


Figure 5-1. Helium-4 versus Age plots for Zagami and ALHA77005 phosphate aggregates. Data points with error bars are labeled by sample group name. Number in parenthesis is the number of aggregates in each group.

CHAPTER 6 DISCUSSION

Alpha-Recoil

Alpha-particles (^4He atoms) are emitted from the decay of parent nuclides and tend to move away from its initial position before coming to rest. This motion occurs from the kinetic energy created during the decay process. The moving or recoil distance is generally between 10-30 μm for common target minerals (Farley *et al.*, 1996), but depends on density and chemical composition of the host mineral as well as the parent nuclides. For apatite and zircon, the recoil distance is known to be approximately 20 μm (Farley *et al.*, 1996). A portion of alpha-particles may be ejected from the host mineral resulting in too young apparent ages. The most common way to correct for this effect is based on the morphology of the grain and the distribution of parent nuclides in the grain (Farley *et al.*, 1996; Hourigan *et al.*, 2005). Such alpha-recoil correction is routinely done for terrestrial samples, in many cases with an assumption that U and Th are homogeneously distributed in the grains.

For meteorites, however, it is almost impossible to retrieve phosphate grains without modification of their original morphologies. They are small, cracked, and irregularly shaped hampering the application of the morphology-based alpha recoil correction for these samples. By not applying the alpha recoil correction, the procedure assumes that the extracted phosphate grains are from inner parts of originally larger grains (Min *et al.*, 2003), or the phosphate aggregates can efficiently capture the recoiled alphas within the attached phases (Min *et al.*, 2004; Min and Reiners, 2007). The former approach is based on morphological modifications (abrasion of marginal parts of phosphate grains) during sample preparation procedures, as well as the

reasonably good (U-Th)/He ages without alpha recoil correction. The latter approach is from the observation of the final phosphate aggregates and from the fact that the alpha-recoil uncorrected ages are consistent with other isotopic systems (Min *et al.*, 2004; Min *et al.*, 2011). As alpha atoms are ejected into these attached phases, the majority of ejected alphas may remain in these neighboring grains requiring minimal alpha-recoil correction and efficiently capturing radiogenic ^4He atoms. Nevertheless, these neighboring phases may also lose ejected alphas or contain trapped alpha particles from another system. How much is lost or retained is a direct consequence of the density and chemical structures of the attached phases. In this study, I followed the second approach, which requires collection of phosphate aggregates to avoid alpha recoil correction.

According to SEM examination on aggregates from Zagami and ALHA77005, the dimensions of phosphates themselves are similar for the different size groups, but the large groups (150-250 μm) contain more attached phases around phosphates increasing the size of the aggregate. Therefore, the aggregates in the smaller groups have higher phosphate to aggregate volume ratios than the larger aggregates (Figures 4-5, 4-6, and 4-7). Such morphological differences in phosphate aggregates are likely related to the (U-Th)/He ages. The (U-Th)/He ages of Zagami show a tendency to increase as a function of size of phosphate aggregate (Figure 5-1). Although this relationship does not hold for all size fractions, it is obvious that the largest size fractions (150-250 μm ; samples Z81-92, Z93-102, Z103-113, Z114-123, and Z124-134, Table 4-2) yielded consistently higher (U-Th)/He ages than the remaining samples. The most plausible explanation of such age-size relationships is that the attached phases in

the largest groups are thick enough ($> \sim 40 \mu\text{m}$) to preserve most of the recoiled alphas, whereas the smaller samples have thinner ($< \sim 20 \mu\text{m}$) attached phases and too thin a veneer to completely capture recoiled alphas yielding apparently younger (U-Th)/He ages (Figure 4-7). Because the small aggregate groups may have experienced incomplete shielding of recoiled alphas at different degrees, depending on the thickness and morphology of the attached phases, they show younger and more scattered ages than the large-group samples. Therefore, the ages from the larger Zagami aggregates ($147 \pm 35 \text{ Ma}$, Table 5-3) are believed to be more reliable than the remaining aggregates ($79 \pm 62 \text{ Ma}$). Comparing these ages to previous studies, whole rock (U-Th)/He age of $\sim 113 \text{ Ma}$ calculated from data by Schwenger *et al.* (2008) corresponds to the lower limit estimates from the large phosphate aggregates.

An alternative explanation for the age-size relationship is that these larger Zagami aggregates have larger diffusion domains, thus less sensitive to thermal disturbance and yielding older ages. However, for shocked meteorites, diffusion domains are believed to be much smaller than the grain itself because of many fractures developed inside the grain. Therefore, it is necessary to examine these fractures in phosphate grains to constrain the diffusion domain size, which affects the resulting (U-Th)/He ages.

ALHA77005 shows no consistent relationship between size and age (Figure 5-1). In reviewing the thickness and morphology of the attached phases in these groups, the majority of the phases had a thickness $> \sim 40 \mu\text{m}$ and a few of them were $< \sim 20 \mu\text{m}$, regardless of their fraction size (Figures 4-6, 4-22 to 4-25). In fact, sample A41-56 produced the youngest (U-Th)/He age of 5.9 Ma (Table 5-1) with aggregates measuring between $63\text{-}150 \mu\text{m}$ and $>180 \mu\text{m}$ (Table 4-3) and most attached phases having a

thickness > ~ 40 μm . However sample A01-20, measuring between 63-150 μm (Table 4-3) and with most of the attached phases also exhibiting a thickness > ~ 40 μm , produced an age of 78.2 Ma much older than A41-56 (Table 5-1), but relatively young compared to its crystallization age (179 Ma). Based on these observations and (U-Th)/He age results (Figure 5-1), if the attached phases are efficiently capturing recoiled alphas, then these samples must have experienced an extensive loss of helium to yield young ages. Since these ages are a result of only five samples or data points as seen in Figure 5-1, more analyses are required to determine a precise distribution of (U-Th)/He ages for ALHA77005.

Diffusion Behavior

The high diffusivity of helium at relatively low temperatures allows for (U-Th)/He dating to act as a powerful tool in studying shallow crustal exhumation or transient thermal events of various samples. The volume diffusion can be best described by the Arrhenius equation which relates the temperature to diffusion properties: $D/a^2 = D_0/a^2 \exp(-E_a/RT)$ where D is the diffusion coefficient, a is the diffusion domain radius, E_a is the activation energy, R is the gas constant, and T is the temperature (McDougall and Harrison, 1999). From previous studies, Arrhenius plots showed a consistent linear relationship between $\log(D)$ and $1/T$, and the regressed line defines the diffusion parameters (E_a and D_0) from its slope and y-intercept (Zeitler *et al.*, 1987; Farley, 2000). However, models implemented on Durango fluorapatite showed a change in the rate of diffusion at temperatures greater than 300°C (Wolf *et al.*, 1996; Farley, 2000) digressing from the linear regression model. Although physical or chemical changes such as the loss of a volatile did not demonstrate a change in diffusion behavior, Wolf *et al.* (1996) concluded that the presence of multiple diffusion domains and subtle changes in crystal

structure within the mineral may be responsible for variations in helium diffusivity. According to a range of studies on (U-Th)/He systems, variations of helium retentivity suggest that a number of factors may be involved: (1) radiation damage induced by the ejection of high-energy alpha particles (as explained in the previous section) may modify the diffusion properties, (2) the system may be experiencing a complex thermal history, and (3) the presence of structural defects such as cracks may act as fast pathways enhancing the rate of diffusive loss.

Diffusion Domain

In order to constrain the physical dimensions of diffusion domains, 22 phosphate grains in two thin sections of Zagami (“4709-1” from the American Museum of Natural History; “USNM6545-4” from the Smithsonian Institution) and 34 phosphate grains in one thin section of ALHA77005 (“ALHA77005 120” from NASA) were carefully examined using SEM and an optical microscope. Phosphates present in Zagami and ALHA77005 samples exhibit numerous fractures acting as good pathways for helium diffusion, thus the diffusion domain dimensions are likely smaller than the grain size of phosphates. According to our detailed image processing of multiple BSE images, all of the analyzed phosphate grains in Zagami contain numerous fractures. ALHA77005 also exhibits fractures but the population is much lower than in Zagami. To quantitatively estimate the diffusion domain size, I defined fracture-free areas (FFA) represented by areas bounded by visible fractures.

FFAs were determined by tracing fractures for each of the 56 (22 from Zagami and 34 from ALHA77005) total phosphate grains examined from thin sections. Afterwards, the two-dimensional area of each FFA was converted to a hypothetical circle with the same surface area, and the radius of this circle was calculated. This

“diffusion domain radius” is used to demonstrate the distribution of FFA sizes. Based on these calculations, it is clear that smaller FFAs are more dominant than larger ones. Because the contributions of the smaller FFAs to the final (U-Th)/He age are less significant than those of the larger ones, the data were weighted based on the surface areas of each FFA.

Figures 4-8 and 4-9 are two examples (out of the 56 total phosphate grains) for Zagami and ALHA77005, respectively, showing traced fractures in one phosphate grain (top) and their corresponding histogram (bottom). The histograms in Figure 4-8 (blue solid bars) and Figure 4-9 (red solid bars) show the distribution of diffusion domain radii defined from the respective traced fractures as illustrated on the top images of each figure. The weighted data from Figures 4-8 (pale blue bars with borders) and 4-9 (pale red bars with borders) yield an estimated diffusion domain radius of ~6 μm for Zagami and ~22 μm for ALHA77005, respectively. Traced fractures for each of the 56 phosphate grains with their corresponding histograms are found in Appendices C and D for Zagami and ALHA77005, respectively.

From measurements of 3861 FFAs from the 22 phosphates in Zagami, the most representative average diffusion domain radius falls in the range of 4 - 6 μm (Appendices C and G). From measurements of 1130 FFAs from 34 phosphates in ALHA77005, the most representative average diffusion domain radius falls in the range of 9 - 15 μm (Appendices D and H). It is clear that FFAs for ALHA77005 are apparently larger than those for Zagami. The estimated diffusion domain radii represent the maximum diffusion domain sizes for these phosphates because of the potential existence of microfractures within the FFAs. Although these microfractures (blurry,

fairly indistinguishable fractures) were more noticeable when we increased the magnification in the SEM, they remained indistinct and too faint to trace (Appendices E and F).

Zagami evidently contained far more microfractures (Appendix E), reducing the practical diffusion domain radius by a factor of one (or two) orders of magnitude. Therefore, these are conservative estimates of diffusion domain radii, and the true domain size is probably close to $0.05\ \mu\text{m}$ with a large error. Peak shock temperatures at each of these estimates are shown in Figure 6-1. At $a = 0.05\ \mu\text{m}$, the peak shock temperature is estimated at $\sim 213^\circ\text{C}$. More on peak shock temperatures is discussed later in this chapter.

In contrast, ALHA77005 had far fewer microfractures (Appendix F), where many of the FFAs are “clean” and void of microfractures. From the 34 thin section images of ALHA77005, five are classified as “dirty” because of dark spots and imperfections (distinct from microfractures) that may also contribute to helium diffusion. Therefore the true domain size is probably close to $5\ \mu\text{m}$ with a large uncertainty. Referring to Figure 6-2, a peak shock temperature is estimated at $\sim 525^\circ\text{C}$ when $a = 5\ \mu\text{m}$.

Diffusion Parameters

During shock metamorphism, an increase in temperature occurs instantaneously followed by rapid cooling to the meteoroid’s ambient temperature in space. Diffusive loss of helium from phosphates varies as a function of diffusion domain size and thermal history related to the shock event. By understanding diffusion properties of extraterrestrial phosphates, it is possible to constrain the maximum temperature experienced during shock metamorphism. For terrestrial apatites, their He diffusion behavior is relatively well understood through stepped heating experiments for (1) ^4He

from untreated apatites (Zeitler *et al.*, 1987; Farley, 2000; Wolf *et al.*, 1996), (2) ^4He and ^3He produced by proton bombardment (Shuster and Farley, 2003) and (3) ^4He artificially implanted along the c-axis and perpendicular direction of apatite (Cherniak *et al.*, 2009). However diffusion properties for extraterrestrial merrillite are poorly understood because they have (1) generally a small size, therefore having a small amount of radiogenic ^4He , and (2) irregular shapes often with many cracks hampering precise determination of diffusion parameters. Nevertheless, $^3\text{He}/^4\text{He}$ diffusion experiments were conducted on large apatite and merrillite crystals from an unshocked chondrite (Min *et al.*, 2011). From the linear relationship in the Arrhenius plot, Min *et al.* (2011) determined diffusion parameters for merrillite: $E_a = 135.1 \pm 2.5$ kJ/mol and $\ln(D_0/a^2) = 5.73 \pm 0.37$ s $^{-1}$. These values were used in this study for thermal modeling to show a relationship between helium fractional loss (f_{He}) and maximum shock temperature based on diffusion domain size (Figures 6-1 and 6-2; Appendices G and H).

Fractional Loss

The age equation allows for calculating the time over which helium has accumulated within the sample. If the timing of initial inception of radiogenic ^4He accumulation is known, it would be possible to estimate the effect of secondary thermal events. For example, from the known crystallization ages of Martian meteorites and the abundances of parent nuclides of U-Th-Sm, the expected radiogenic ^4He can be calculated. If the measured ^4He is lower than the expected value, it means the meteorite experienced post-crystallization degassing. Fractional loss (f_{He}), which simply represents the ratio between the measured to the expected ^4He , provides important constraints on the nature of thermal events experienced by the meteorites.

Other neighboring phases in the aggregates have very low U and Th, thus their contributions are expected to be very minor. If there are some radiogenic ^4He in the neighboring phases, most likely in silicates of pyroxene and olivine, they would cause slow He diffusion. However, because this amount of He diffusion is expected to be very small, I concentrated on phosphates only for thermal modeling.

Fractional losses of ^4He were calculated using preferred crystallization ages of 177 Ma for Zagami and 179 Ma for ALHA77005 (Nyquist *et al.*, 2001; Schwenger *et al.*, 2008). For example, if no helium fractional loss ($f_{\text{He}} = 0$) occurred for a certain sample, the (U-Th)/He age should be the same as the crystallization age. If a complete loss ($f_{\text{He}} = 1$) of ^4He occurred during the ejection-related shock event, the resulting (U-Th)/He age should be identical to its cosmic ray exposure age.

One of the five sample groups of ALHA77005 yielded a low f_{He} of 0.57 (Tables 5-1 and 5-3). The remaining four groups of ALHA77005 produced f_{He} values greater than 0.9 (average $f_{\text{He}} = 0.94$) and are consistent with calculated losses by Schwenger *et al.* (2008). The twelve Zagami sample groups have f_{He} ranging from 0.9 (for the youngest age at 19.8 Ma) to -0.15 for the oldest age at 202 Ma (Table 5-1). The average fractional loss for all twelve groups is $f_{\text{He}} = 0.39$ ($39 \pm 35\%$) and has a larger error when compared with whole rock loss values of $36 \pm 6\%$ and $56 \pm 18\%$ (Schwenger *et al.*, 2008). A breakdown of these losses by fraction size for Zagami are as follows (Table 5-3): (1) the five large groups (150-250 μm) have an average $f_{\text{He}} = 0.17$ ($17 \pm 20\%$), (2) the five mixed groups (75-250 μm) have an average $f_{\text{He}} = 0.71$ ($71 \pm 18\%$), and (3) the two remaining groups (75-125 μm) have an average $f_{\text{He}} = 0.15$ ($15 \pm 40\%$).

Two samples of Zagami yielded ages older than its crystallization age, thus producing fractional loss values less than zero. This may (1) suggest the existence of an unidentified source of ^4He or (2) offer some evidence that the crystallization age of Zagami may be close to or slightly greater than 200 Ma. If the former is true, the calculated f_{He} values are likely to have uncertainties at least the level of offset (by 15%). If the latter is correct, this is consistent with previous studies on U-Th-Pb radiometric ages of approximately 229 - 230 Ma (Chen and Wasserburg, 1986; Nyquist *et al.*, 2001) and ^{39}Ar - ^{40}Ar age of about 242 Ma (Bogard and Garrison, 1999). Bogard and Park (2008) calculated a radiometric ^{39}Ar - ^{40}Ar age of ~209 Ma and proposed that excess ^{40}Ar may have contributed to ages older than previously reported. In this case, the calculated f_{He} overestimated the true values requiring systematic modification.

The larger f_{He} values for ALHA77005 than Zagami suggest that either (1) the shock temperature conditions of ALHA77005 are higher, or (2) the diffusion domain size of phosphates in ALHA77005 is smaller. According to our preliminary studies on the textures of merrillite, the dimensions of fracture-free areas are not much different for these two meteorites. Therefore, the shock temperature of ALHA77005 is expected to be much higher than Zagami, which is qualitatively consistent with previous studies (Nyquist *et al.*, 2001; Fritz *et al.*, 2005).

The relationship between helium fractional loss and maximum shock temperatures can be established with an assumption of volume diffusion and represented through thermal modeling (Figures 6-1 and 6-2; Appendices G and H). An assumed parent body radius (A) calculated from previous estimates, ambient temperature of Mars (T_s), and depth of the sample from the surface of the parent body (d) are applied to the

model at varying temperatures until helium fractional loss (f_{He}) reaches a value of 1. For fractional loss values close to or equal to 1 (complete helium loss), f_{He} becomes less dependent on the radius of the body (A) and diffusion domain size (a) and an initial temperature based on diffusion parameters can be inferred from the model. Given f_{He} and diffusion domain values, a maximum peak shock temperature can also be implied.

Peak Shock Temperatures

A shock event causes an instantaneous temperature increase to a peak shock temperature followed by conductive cooling. During this thermal event, a portion of radiogenic ^4He (accumulated since crystallization) diffuses out of the grain, and the degree of diffusive loss (or fractional loss) can be used to estimate peak shock temperatures and temperature variations at different conditions. Peak shock temperatures in this study are calculated and modeled by using helium diffusion parameters of merrillite, ambient temperatures on Mars, and parameters related to the parent body of Zagami and ALHA77005. Specifically from Zagami and ALHA77005, their respective helium fractional losses (f_{He}) and estimated maximum and minimum diffusion domain sizes are also applied in the models.

The helium diffusion parameters of merrillite used in this study are $E_a = 135.1 \pm 2.5$ kJ/mol (32.28 kcal/mol) and $D_o = 0.01$ cm²/s (Min *et al.*, 2011). Ambient surface temperatures for Mars include very a cold ($T_s = -148^\circ\text{C}$: Soffen, 1976) and hot ($T_s = 22^\circ\text{C}$: Spanovich *et al.*, 2006) temperature, and the average space temperature at Mars distance from the Sun, $T_s = -70^\circ\text{C}$ (Butler, 1966). Remaining parameters used to calculate peak shock temperatures are described in the sections below for each Martian meteorite, Zagami and ALHA77005.

Thermal modeling created from these parameters are displayed in Figures 6-1 and 6-2 and Appendices G and H. These models illustrate maximum (or peak) shock temperatures as a function of helium fractional loss and diffusion domain size. From the models for Zagami with $f_{\text{He}} = 0.17$, peak shock temperatures are calculated at 213°C for $a = 0.05 \mu\text{m}$ and 407°C for $a = 6 \mu\text{m}$. And for ALHA77005 with $f_{\text{He}} = 0.94$, peak shock temperatures are calculated at 520°C for $a = 5 \mu\text{m}$ and 615°C for $a = 15 \mu\text{m}$.

Zagami

In addition to diffusion properties and ambient temperatures, the following parameters related to the parent meteoroid (body) and diffusion domain size of Zagami were also applied: radius of parent body (A) = 23 cm (Eugster *et al.*, 2002), 25 cm (Schnabel *et al.*, 2001), and 35 cm (Artemieva and Ivanov, 2004); diffusion domain radii, $a = 0.0005 \mu\text{m}$ to $50 \mu\text{m}$; and depth from parent body surface, $d = 15 \text{ cm}$ and 18 cm . Calculating the depth from parent body surface specifies the location of my sample with respect to the Zagami parent meteorite. The rock chip sample for this study was retrieved approximately 5 to 8 cm (personal communication with Michael Farmer who provided the Zagami sample to KIGAM) below the fusion crust of the recovered Zagami meteorite. Because the parent body should have experienced physical ablation during its entry into Earth's atmosphere, the original parent body at the time of ejection from Mars is expected to be larger. The depth from parent body surface was then calculated by using the approximate minimum radius (Schwenzer *et al.*, 2008) of the recovered Zagami meteorite and estimating a minimum parent body radius of 23 cm. The samples were retrieved at a depth approximately 15 to 18 cm below the surface of the pre-atmospheric parent body of Zagami before undergoing ablation as it passes through the atmosphere of Earth.

According to the thermal modeling for Zagami phosphate aggregates with $f_{\text{He}} = 0.17$, average peak shock temperatures of approximately 213°C and 407°C are calculated for a diffusion domain size of $a = 0.05 \mu\text{m}$ and $a = 6 \mu\text{m}$ (from FFA data), respectively. These shock temperatures may be sensitive to other factors such as parent body size (A), depth from surface of parent body (d), and ambient temperatures (T_s) of Mars. More specifically, the following was also determined from thermal modeling (Table 6-1): (1a) for $a = 0.05 \mu\text{m}$ and $d = 15 \text{ cm}$, the calculated shock temperatures deviate by 6°C (211°C to 217°C) for $A = 23, 25, \text{ and } 35 \text{ cm}$ at $T_s = 22^\circ\text{C}, -70^\circ\text{C}, \text{ and } -148^\circ\text{C}$. (1b) At $a = 0.05 \mu\text{m}$ and $d = 18 \text{ cm}$, the calculated shock temperatures also deviate by 6°C (207°C to 213°C) for the same values as A and T_s . (2a) At $a = 6 \mu\text{m}$ and $d = 15 \text{ cm}$, the calculated peak shock temperatures deviate by 9°C (405°C to 414°C). (2b) And at $a = 6 \mu\text{m}$ and $d = 18 \text{ cm}$, the shock temperatures deviate by 10°C (397°C to 407°C) for the same A and T_s values as (1). From these models, peak shock temperatures for Zagami are fairly robust against extreme temperatures and minimally affected by the body size and sample surface depth of the parent meteoroid.

Post-shock temperatures describe the temperature increase produced from a shock wave as it propagates through a material. Immediately after a shock event, the temperature of Martian rocks (ambient temperature) increases by the post-shock temperature. Therefore, 'previously published post-shock temperatures + ambient Mars temperatures' are used for comparison with peak shock temperatures in this study. For Zagami, previous estimates of post-shock temperature are used from Nyquist *et al.* (2001) and Fritz *et al.* (2005).

Peak shock temperatures from this study (213°C and 407°C) are evidently higher than those from Fritz *et al.* (2005) at $70 \pm 5^\circ\text{C}$ ($70 \pm 5\text{ K}$, ΔT). However from the models, a post-shock temperature of $70 \pm 5^\circ\text{C}$ (Fritz *et al.* 2005) may be achieved with a diffusion domain size, $a < 0.0005\ \mu\text{m}$. Therefore, Zagami would need to have innumerable amounts of fractures, far more than the ones seen in this study, to reach a diffusion domain size less than $0.0005\ \mu\text{m}$. If future analyses show that Zagami may possess this many fractures for $a < 0.0005\ \mu\text{m}$, then a post-shock temperature of $70 \pm 5^\circ\text{C}$ (Fritz *et al.* 2005) may be likely for Zagami.

In contrast, the Zagami peak shock temperature of 213°C falls within range of post-shock temperature $220 \pm 50^\circ\text{C}$ (Nyquist *et al.*, 2001) only when the ambient surface temperature of Mars reaches 22°C . However from the models, this same temperature of $220 \pm 50^\circ\text{C}$ (Nyquist *et al.*, 2001) may also be achieved with an ambient temperature in space of -70°C and $a = 0.005\ \mu\text{m}$. This diffusion domain size is one order of magnitude smaller than the suggested $a = 0.05\ \mu\text{m}$ in this study. This setting is likely if further studies demonstrate the diffusion domain size may be less than or equal $0.005\ \mu\text{m}$ for Zagami.

ALHA77005

To create thermal models for ALHA77005, the same diffusion properties ($E_a = 135.1 \pm 2.5\ \text{kJ/mol}$, $D_o = 0.01\ \text{cm}^2/\text{s}$: Min *et al.*, 2011) and ambient temperatures ($T_s = -148^\circ\text{C}$: Soffen, 1976; $T_s = 22^\circ\text{C}$: Spanovich *et al.*, 2006; $T_s = -70^\circ\text{C}$: Butler, 1966) used for Zagami are applied for ALHA77005. In addition, the following parameters are used for ALHA77005 thermal modeling: radius of parent body (A) = 25 cm (Artemieva and Ivanov, 2004; Fritz *et al.*, 2005), 30 cm (Artemieva and Ivanov, 2004; Fritz *et al.*, 2005),

and 35 cm (Artemieva and Ivanov, 2004); sample depth from parent body surface, $d = 24$ cm and 28 cm; and diffusion domain radii, $a = 0.0005$ μm to 50 μm .

In calculating the depth from parent body surface for ALHA77005, the same steps were followed as described above for Zagami. No current data is available to report from where in the recovered meteorite the rock chip samples were retrieved. Based on dimensions of the recovered meteorite, 9.5 cm \times 7.5 cm \times 5.25 cm (Nishiizumi *et al.*, 1986), the rock chip samples in this study may have been retrieved no more than possibly 2 to 3 cm from the fusion crust of ALHA77005. Selecting a parent body radius of 30 cm, the rock chip samples may have been retrieved approximately 24 to 28 cm from the surface of the parent body of ALHA77005 before passing through the atmosphere of Earth.

From the thermal modeling for ALHA77005 phosphate aggregates with $f_{\text{He}} = 0.94$, average peak shock temperatures are estimated at approximately 520°C and 615°C for $a = 5$ μm and 15 μm (from FFA data), respectively. Similar to Zagami, these shock temperatures may be affected by parent body size (A), depth from surface of parent body (d), and ambient temperatures (T_s) of Mars. From these models, the following was determined (Table 6-2): (1) for $a = 5$ μm and 15 μm , the calculated shock temperatures deviate by 17°C (516°C to 533°C) and 22°C (609°C to 631°C), respectively, for $d = 24$ cm, $A = 25, 30,$ and 35 cm, and $T_s = 22^\circ\text{C}, -70^\circ\text{C},$ and -148°C . (2) For $a = 5$ μm and 15 μm , the calculated shock temperatures deviate by 11°C (509°C to 520°C) and 13°C (601°C to 614°C), respectively, for $d = 28$ cm, $A = 30$ and 35 cm, and T_s values same as in (1). Based on these values, peak shock temperatures for ALHA77005 are slightly

more sensitive than Zagami but somewhat resilient against extreme temperatures and slightly affected by the depth from surface and body size of the parent meteoroid.

In comparing ALHA77005 results with previous estimates from Nyquist *et al.* (2001), the following was determined. (1) Both peak shock temperatures (520°C and 615°C) fall well within range of post-shock temperature 450 - 600°C (Nyquist *et al.*, 2001) when the ambient surface temperature of Mars is 22°C. (2) For an average temperature in space, -70°C, the peak shock temperature of 520°C also falls within this range (450 - 600°C: Nyquist *et al.*, 2001).

When comparing these peak shock temperatures with values from Fritz *et al.* (2005), (1) the peak shock temperature of 615°C falls within post-shock temperature $800 \pm 200^\circ\text{C}$ ($800 \pm 200\text{ K}$, ΔT : Fritz *et al.*, 2005) during an average temperature in space of -70°C. (2) For an ambient surface temperature of -148°C, both peak shock temperatures fall within this same range $800 \pm 200^\circ\text{C}$ (Fritz *et al.*, 2005). In contrast to Zagami, peak shock temperatures for ALHA77005 are more favorable with previous values from Nyquist *et al.* (2001) and Fritz *et al.* (2005).

Post-shock versus peak shock temperatures

Post-shock temperatures describe the temperature increase produced from a shock wave as it propagates through a material. To calculate post-shock temperatures, a thermodynamic equation of state (EOS) is applied using a Hugoniot model relating particle velocity, shock wave velocity, and energy released during decompression after a shock event (Stöffler *et al.*, 1988; Sharp *et al.*, 2006). Experimental EOS has been derived for terrestrial geologic materials and used on meteorites with similar composition to determine their post-shock temperatures (Stöffler *et al.*, 1986; Artemieva and Ivanov, 2004; Fritz *et al.*, 2005). In contrast, peak shock temperatures in this study

are calculated through thermal modeling using several factors related directly to the meteorite: diffusion properties from a meteorite mineral (merrillite), characteristics from Martian meteorite samples, and parameters from the parent planet, Mars. In this case, peak shock temperatures offer an absolute temperature (versus relative temperature) for the ejected meteorite upon impact.

Future Studies

Future (U-Th)/He studies on Martian meteorites are required to complement the results from this study and subsequently obtain discrete peak shock temperatures. Items to consider: (a) select phosphate aggregates with thicker attached phases measuring between 40 μm to 50 μm to evaluate grain size control on maximum temperatures, (b) analyze aggregates with mineral phases other than phosphates such as pyroxene- or plagioclase-bearing aggregates to determine and compare their U, Th, Sm, and He abundances with phosphate aggregates, and (c) separate more ALHA77005 phosphate samples to better define (U-Th)/He ages with those from this study. Other important studies may include analyzing whole rock samples to compare with these results, applying the use of SEM with a stronger magnification to constrain diffusion domain size, and possibly determining a method to perform single-grain analyses on merrillite crystals from meteorites.

Table 6-1. Zagami shock temperatures from thermal modeling simulations at $d = 15$ cm and $d = 18$ cm.

$d=15$ cm	$T_s = 22^\circ\text{C}$		$T_s = -70^\circ\text{C}$		$T_s = -148^\circ\text{C}$		
	A	$0.05 \mu\text{m}$	$6 \mu\text{m}$	$0.05 \mu\text{m}$	$6 \mu\text{m}$	$0.05 \mu\text{m}$	$6 \mu\text{m}$
23		214	410	216	413	217	414
25		213	409	215	411	216	413
35		211	405	213	407	215	409
avg		212.67	408	214.67	410.33	216	412
std dev		1.53	2.65	1.53	3.06	1	2.65

$d=18$ cm	$T_s = 22^\circ\text{C}$		$T_s = -70^\circ\text{C}$		$T_s = -148^\circ\text{C}$		
	A	$0.05 \mu\text{m}$	$6 \mu\text{m}$	$0.05 \mu\text{m}$	$6 \mu\text{m}$	$0.05 \mu\text{m}$	$6 \mu\text{m}$
23		211	404	213	406	213	407
25		211	404	212	404	213	406
35		207	397	209	399	210	400
avg		209.67	401.67	211.33	403	212	404.33
std dev		2.31	4.04	2.08	3.61	1.73	3.79

d = depth from surface of parent body. T_s = ambient surface temperature of Mars. A = parent body size. Overall shock temperature averages: $\sim 213^\circ\text{C}$ at $0.05 \mu\text{m}$ and $\sim 407^\circ\text{C}$ at $6 \mu\text{m}$.

Table 6-2. ALHA77005 shock temperatures from thermal modeling simulations at $d = 24$ cm and $d = 28$ cm.

$d=24\text{cm}$	$T_s = 22^\circ\text{C}$		$T_s = -70^\circ\text{C}$		$T_s = -148^\circ\text{C}$		
	A	$5\ \mu\text{m}$	$15\ \mu\text{m}$	$5\ \mu\text{m}$	$15\ \mu\text{m}$	$5\ \mu\text{m}$	$15\ \mu\text{m}$
25		531	628	532	630	533	631
30		520	616	522	617	524	619
35		516	609	517	611	519	613
avg		522.33	617.67	523.67	619.33	525.33	621
std dev		7.77	9.61	7.64	9.71	7.09	9.17

$d=28\text{cm}$	$T_s = 22^\circ\text{C}$		$T_s = -70^\circ\text{C}$		$T_s = -148^\circ\text{C}$		
	A	$5\ \mu\text{m}$	$15\ \mu\text{m}$	$5\ \mu\text{m}$	$15\ \mu\text{m}$	$5\ \mu\text{m}$	$15\ \mu\text{m}$
30		517	610	518	612	520	614
35		509	601	511	603	512	604
avg		513	605.5	514.5	607.5	516	609
std dev		5.66	6.36	4.95	6.36	5.66	7.07

d = depth from surface of parent body. T_s = ambient surface temperature of Mars. A = parent body size. Overall shock temperature averages: $\sim 520^\circ\text{C}$ at $5\ \mu\text{m}$ and $\sim 615^\circ\text{C}$ at $15\ \mu\text{m}$.

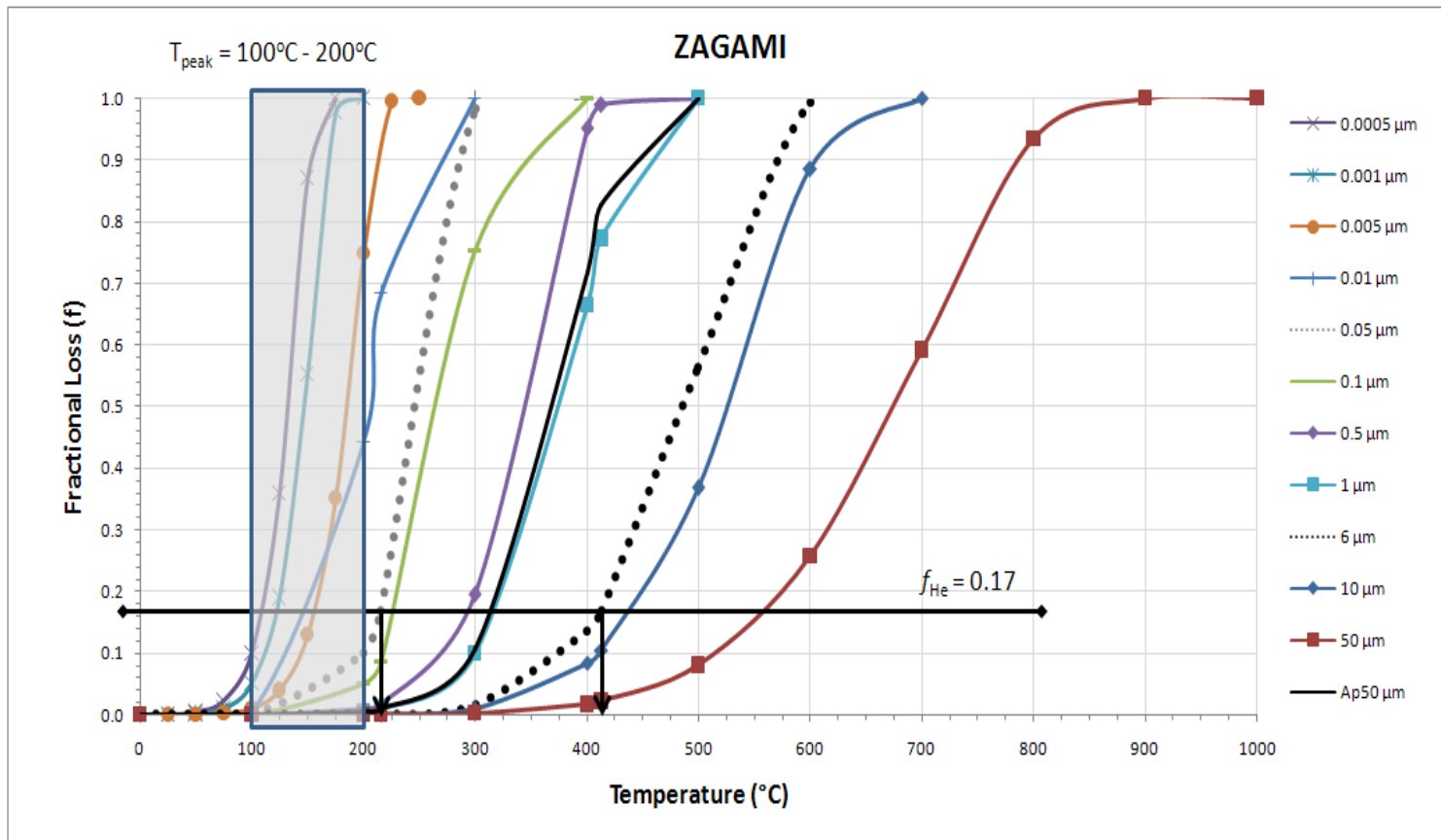


Figure 6-1. Thermal Modeling for Zagami. $T_s = -70^{\circ}\text{C}$, $d = 15 \text{ cm}$, and $A = 23 \text{ cm}$. Diffusion properties of merrillite: $E_a = 32.28 \text{ kcal/mol}$, $\ln(D_0/a^2) = 5.73/\text{s}$, and $D_0 = 0.01 \text{ cm}^2/\text{s}$. Diffusion properties of apatite (Ap): $E_a = 32.9 \text{ kcal/mol}$, $\ln(D_0/a^2) = 13.44/\text{s}$, and $D_0 = 50 \text{ cm}^2/\text{s}$ (Farley, 2000). Post-shock temperature calculated by Nyquist *et al.* (2001) is displayed as a converted peak shock temperature range (light gray box with blue border). Each curve represents the diffusion profile per diffusion domain size (refer to legend for range of radii). For this study, $a = 0.05 \mu\text{m}$ (gray dotted line) and $a = 6 \mu\text{m}$ (black dotted line).

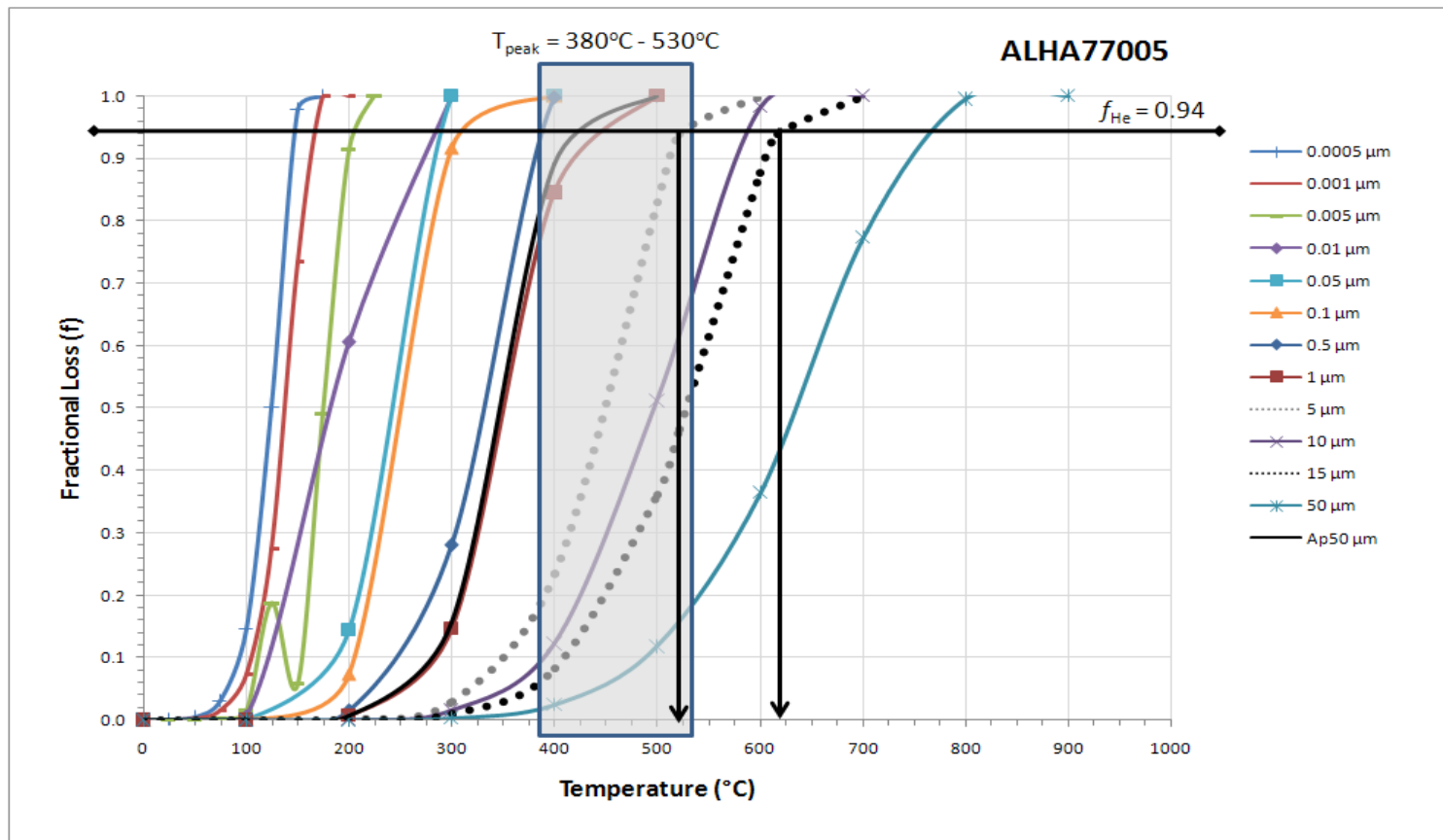


Figure 6-2. Thermal Modeling for ALHA77005. $T_s = -70^\circ\text{C}$, $d = 24$ cm, and $A = 30$ cm. Diffusion properties of merrillite: $E_a = 32.28$ kcal/mol, $\ln(D_o/a^2) = 5.73/\text{s}$, and $D_o = 0.01$ cm^2/s . Diffusion properties of apatite (Ap): $E_a = 32.9$ kcal/mol, $\ln(D_o/a^2) = 13.44/\text{s}$, and $D_o = 50$ cm^2/s (Farley, 2000). Post-shock temperature calculated by Nyquist *et al.* (2001) is displayed as a converted peak shock temperature range (light gray box with blue border). Each curve represents the diffusion profile per diffusion domain size (refer to legend for range of radii). For this study, $a = 5$ μm (gray dotted line) and $a = 15$ μm (black dotted line).

CHAPTER 7 CONCLUSIONS

(1) Semi-quantitative chemical analyses using EDS (Energy Dispersive Spectroscopy) suggest high P and Ca concentrations along with moderate Mg and Na signals. These chemical analyses are consistent for almost the entire population of phosphates identified in Zagami and ALHA77005 Martian meteorites. The results indicate that the phosphates in these meteorites are exclusively merrillite. The detection of merrillite in these phosphates is consistent with the composition of these meteorites from previous studies for Zagami (Vistisen *et al.*, 1992; McCoy *et al.*, 1993; Wang *et al.*, 1999; Meyer, 2003) and ALHA77005 (McSween *et al.*, 1979a, b; Mason, 1981; Treiman *et al.*, 1994; Meyer, 2003).

(2) (U-Th)/He ages were obtained from multiple phosphate aggregates in Zagami and ALHA77005. Because single-grain analysis did not yield enough ^4He , multiple-grain (5-20 grains per packet) analysis was performed. The ages of all size groups are in the range of 19.8 Ma - 202.4 Ma for Zagami and 5.9 Ma - 78.2 Ma for ALHA77005. The widely scattered ages are probably due to different degrees of alpha-recoil loss.

(3) For Zagami, the (U-Th)/He ages from the five large phosphate aggregate groups (~111-202 Ma; 150-250 μm) are systematically older than the small and mixed groups (~20-200 Ma; 75-250 μm). According to the chemical maps of the individual aggregates obtained using SEM, the 2D areas of phosphate grains are almost identical for large and small aggregates, and the aggregate size difference is mainly from the attached phases. Phosphate aggregates from the five large groups typically contain thick layers (> 40 μm) of attached phases, efficiently capturing recoiled alphas within the aggregates. In contrast, most of the aggregates from the small groups have relatively

thin layers ($< 20 \mu\text{m}$ in many cases) of other phases around phosphate grains, potentially allowing partial recoil loss from the system. Based on the textural observations and age-size relationship, I conclude that the uncorrected (U-Th)/He ages from the five large groups ($150\text{-}250 \mu\text{m}$, $\sim 111\text{-}202 \text{ Ma}$, average = $147 \pm 35 \text{ Ma}$) are more reliable than those from the remaining groups ($75\text{-}250 \mu\text{m}$, $\sim 20\text{-}200 \text{ Ma}$, average = $79 \pm 62 \text{ Ma}$).

(4) For ALHA77005, areas of phosphate grains observed with the SEM are similar between large and small aggregates. The major size differences within these areas in ALHA77005 phosphate grains may come from attached phases, just like in Zagami. However unlike Zagami, ALHA77005 produced young ages regardless of the size of the aggregate showing no immediate relationship between age, thickness of attached phases, and fraction size.

(5) Based on detailed examination of thin sections, numerous fractures are identified in the phosphate crystals. To constrain the diffusion domain size, I analyzed fracture patterns in 56 phosphate crystals and defined 4991 fracture-free areas (FFAs). The distribution of FFAs shows weighted average radii of $6 \mu\text{m}$ and $15 \mu\text{m}$ for Zagami and ALHA77005, respectively. However, these estimates only provide the upper limits of diffusion domain radius because these FFAs contain microfractures, which can be only observed at high SEM magnifications. Based on the distribution of such microfractures, I conclude that the practical diffusion domain radii are in the range of $0.05 - 6 \mu\text{m}$ for Zagami and $5 - 15 \mu\text{m}$ for ALHA77005.

(6) Peak shock temperatures in this study are determined from thermal modeling using helium diffusion properties of merrillite, ambient temperatures of Mars, and

parameters related to the parent meteoroid of Zagami and ALHA77005. Fractional losses (f_{He}) and estimated maximum and minimum diffusion domain sizes, a , for Zagami and ALHA77005 are also considered for these models.

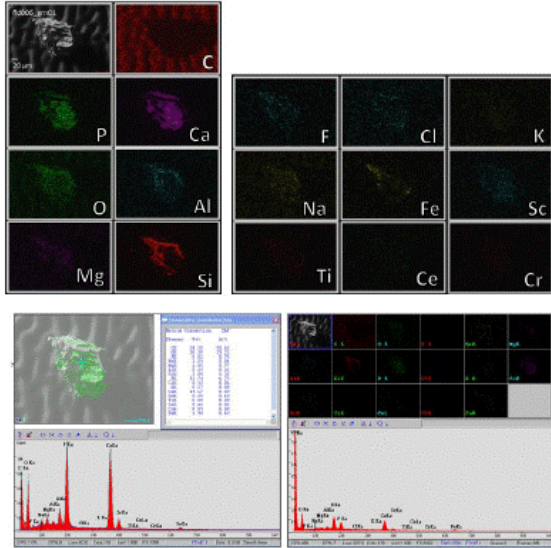
From thermal modeling for Zagami with $f_{\text{He}} = 0.17$, peak shock temperatures are calculated to be 213°C for $a = 0.05 \mu\text{m}$ and 407°C for $a = 6 \mu\text{m}$. For ALHA77005 with $f_{\text{He}} = 0.94$, peak shock temperatures are calculated to be 520°C for $a = 5 \mu\text{m}$ and 615°C for $a = 15 \mu\text{m}$. At these temperatures, Zagami and ALHA77005 show very little variation at different ambient conditions and regardless of the size of the meteoroid. Based on these models, peak shock temperatures for ALHA77005 are slightly more sensitive than Zagami, but both are fairly robust against extreme ambient temperatures, parent body size, and depth from surface of the parent meteoroid. To complement reported post-shock temperatures based on shock conditions, peak shock temperatures for Martian meteorites after ejection offer absolute temperatures built directly on their attributes.

APPENDICES A-H: ZAGAMI AND ALHA77005 IMAGES

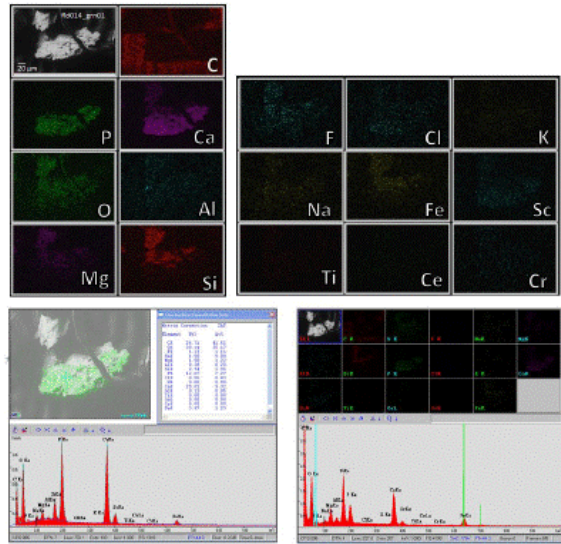
The images in the following appendices can be viewed individually and at a larger scale. Requests can be made by contacting Kyoungwon Kyle Min at kmin@ufl.edu or Annette Emily Farah at afarah@ufl.edu.

APPENDIX A
SEM CHEMICAL MAPS FOR ZAGAMI PHOSPHATE AGGREGATES

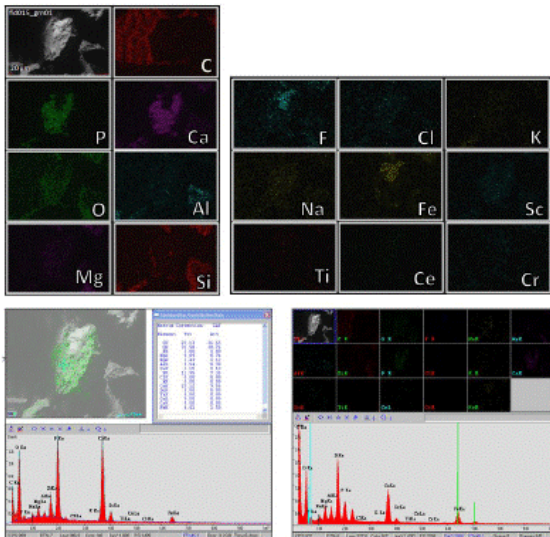
Z01-20: fld006_grn01, 75-125 μm



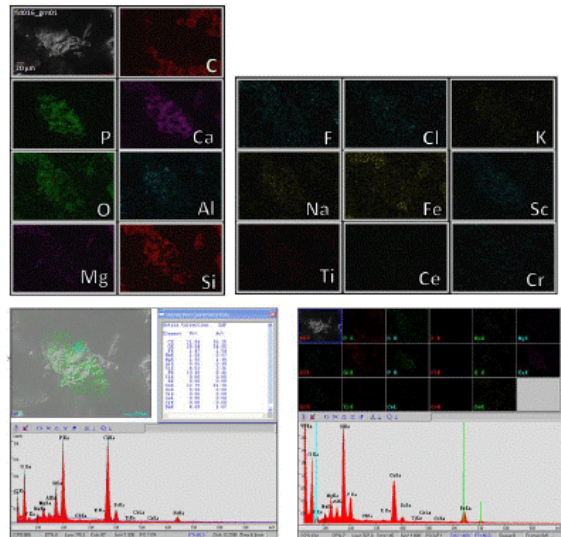
Z01-20: fld014_grn01, 75-125 μm



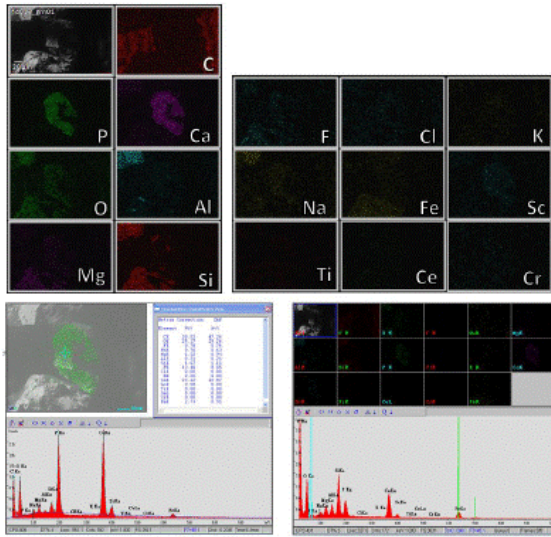
Z01-20: fld015_grn01, 75-125 μm



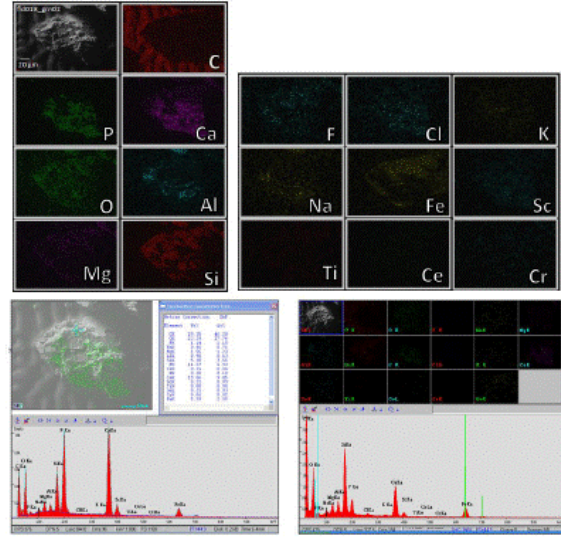
Z01-20: fld016_grn01, 75-125 μm



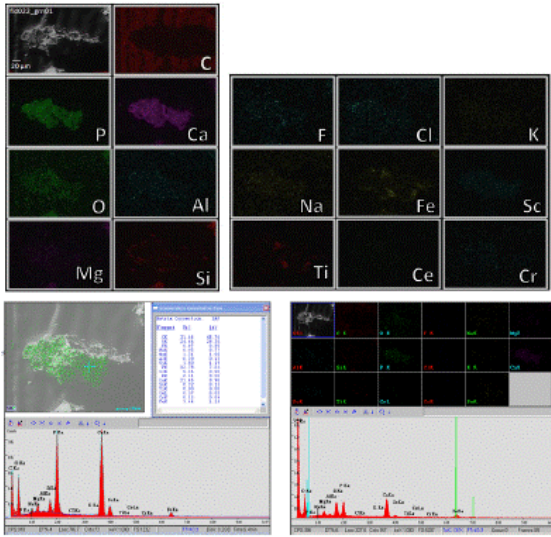
Z01-20: fld018_grn01, 75-125 μm



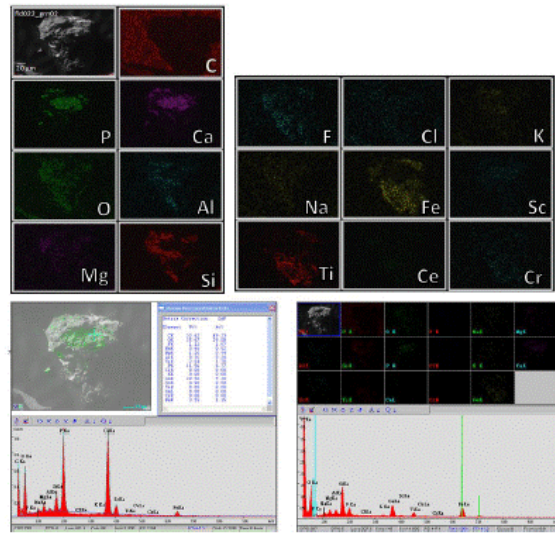
Z01-20: fld018_grn02, 75-125 μm



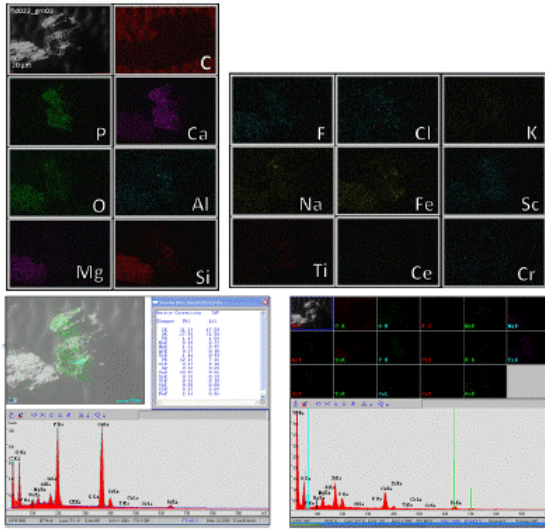
Z01-20: fld022_grn01, 75-125 μm



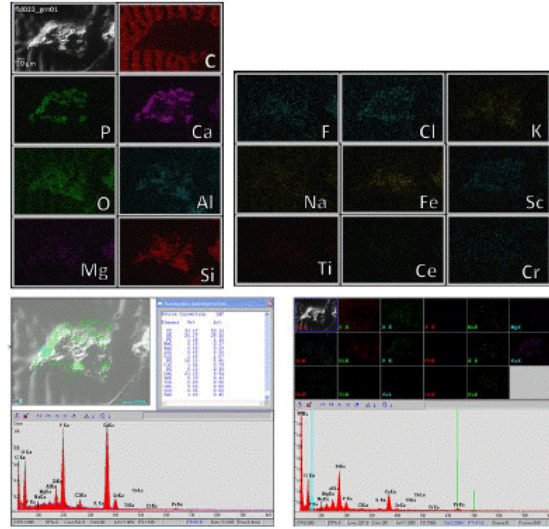
Z01-20: fld022_grn02, 75-125 μm



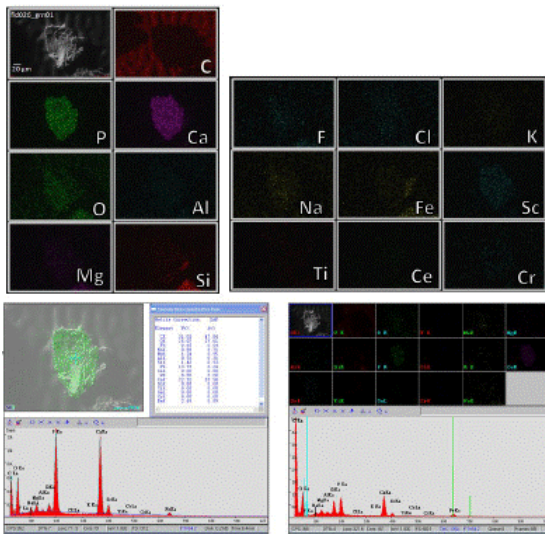
Z01-20: fld022_grn03, 75-125 μm



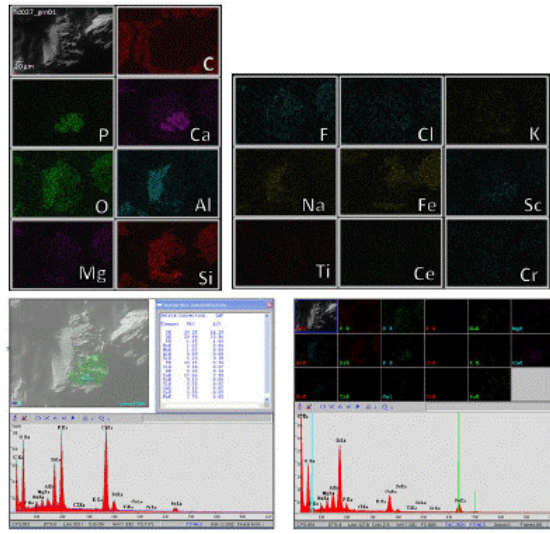
Z01-20: fld023_grn01, 75-125 μm



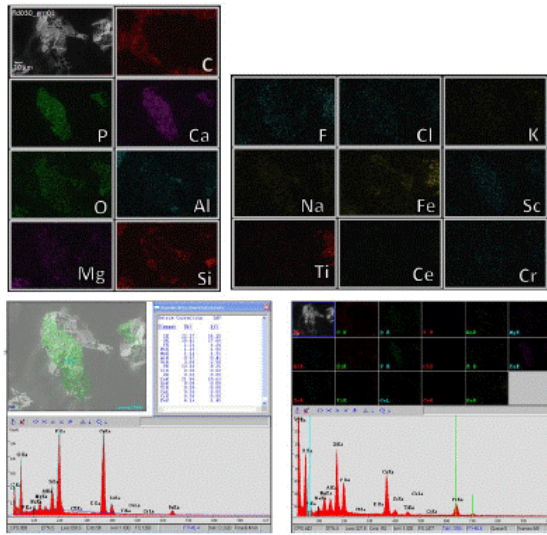
Z01-20: fld026_grn01, 75-125 μm



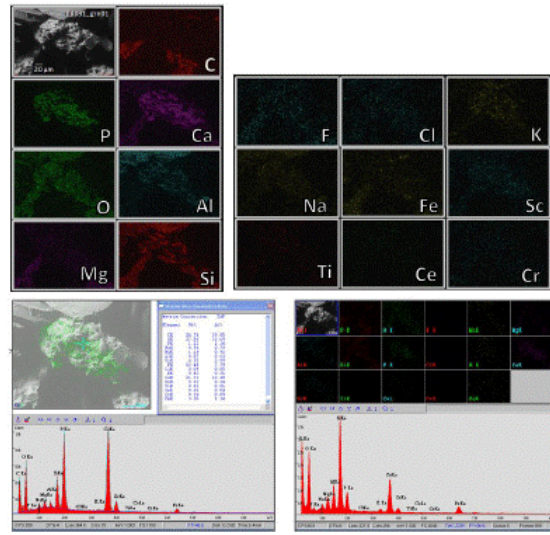
Z01-20: fld027_grn01, 75-125 μm



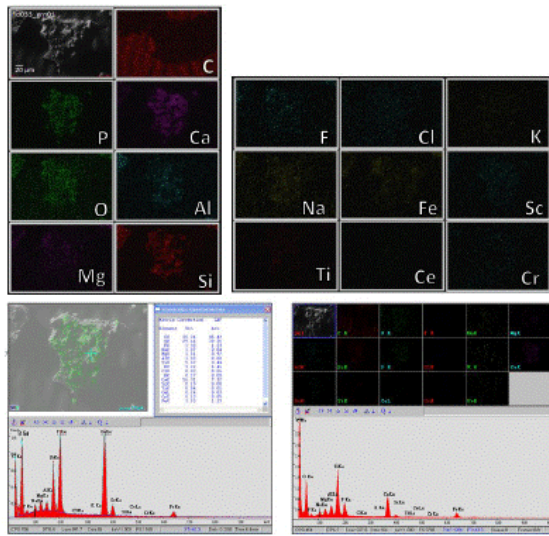
Z01-20: fld030_grn01, 75-125 µm



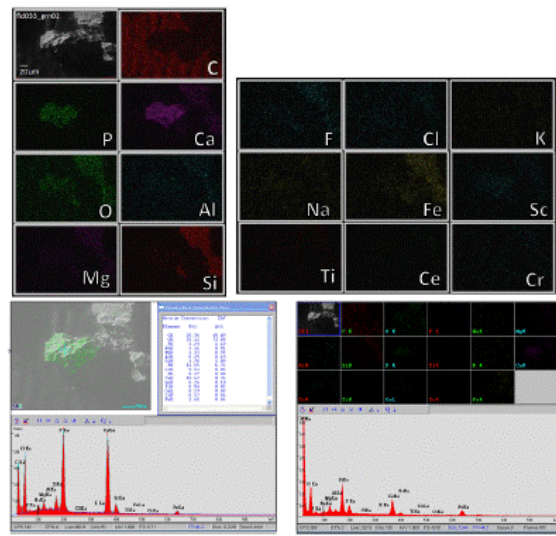
Z01-20: fld031_grn01, 75-125 µm



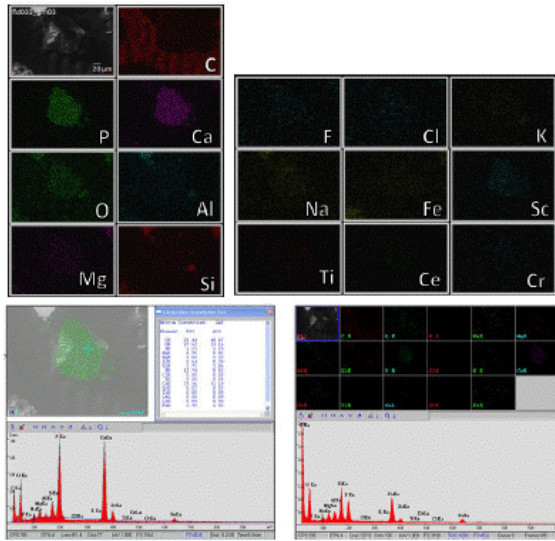
Z01-20: fld033_grn01, 75-125 µm



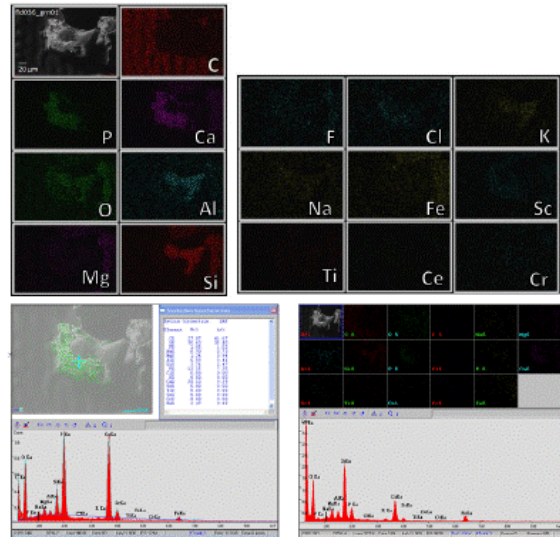
Z01-20: fld033_grn02, 75-125 µm



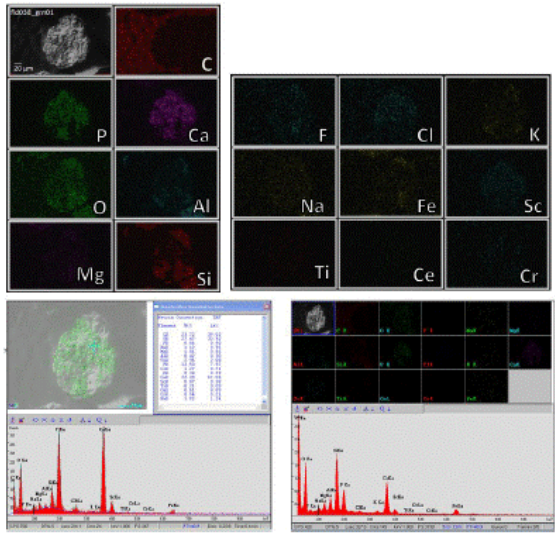
Z01-20: fld033_grn03, 75-125 μm



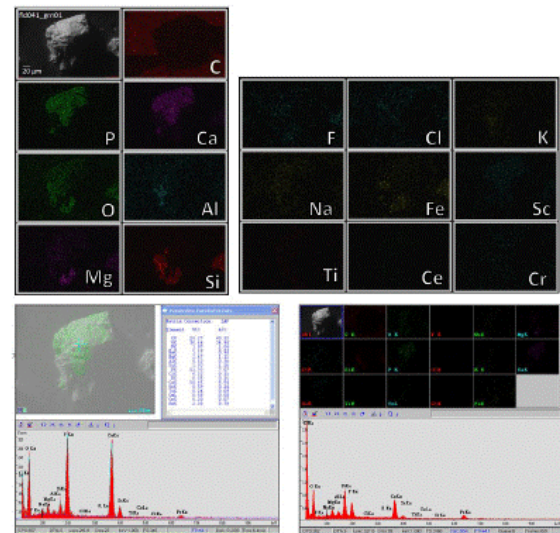
Z01-20: fld036_grn01, 75-125 μm



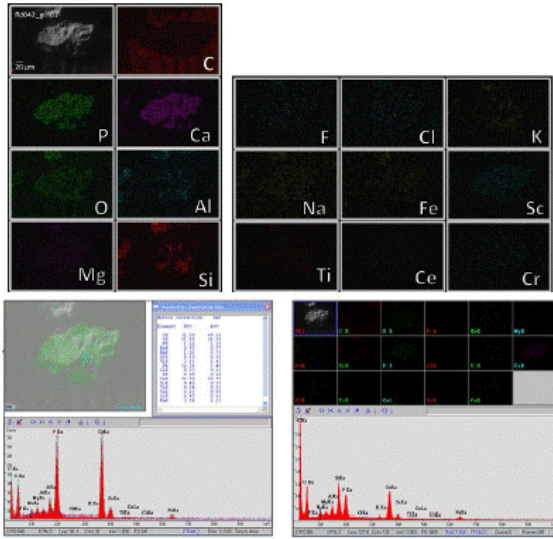
Z01-20: fld038_grn01, 75-125 μm



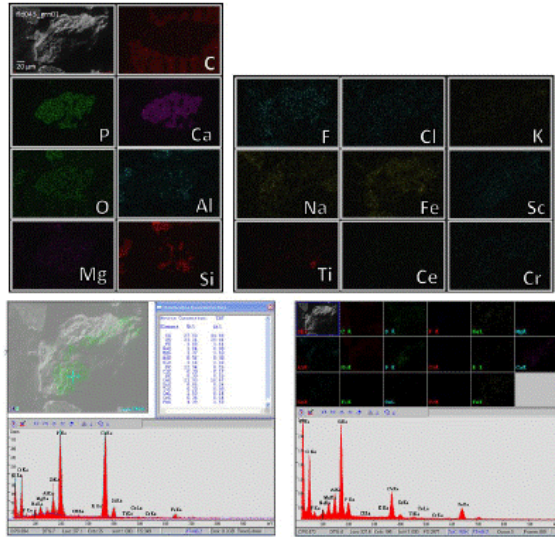
Z01-20: fld041_grn01, 75-125 μm



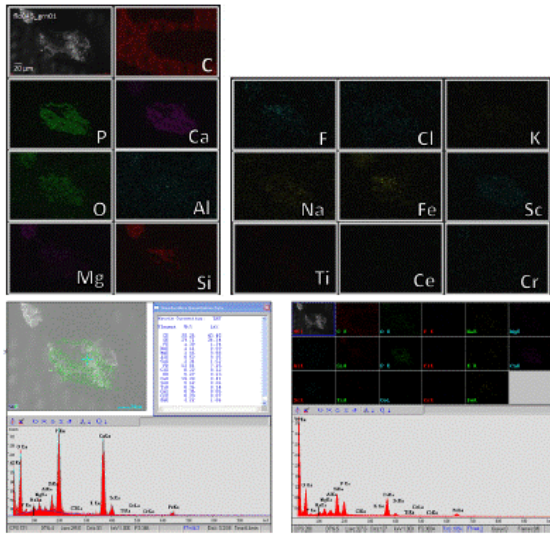
Z21-40: fld042_grn01, 75-125 μm



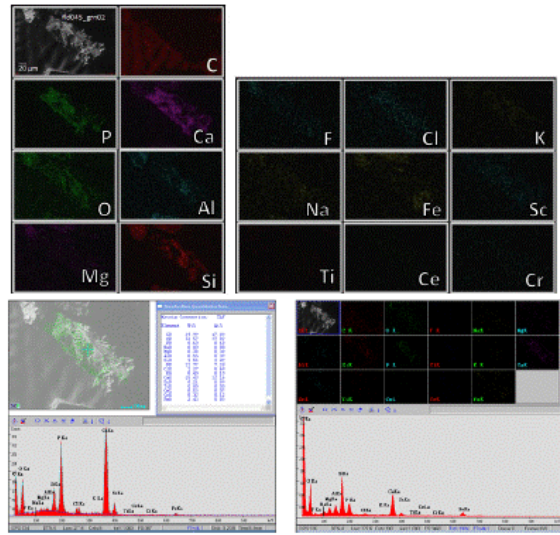
Z21-40: fld043_grn01, 75-125 μm



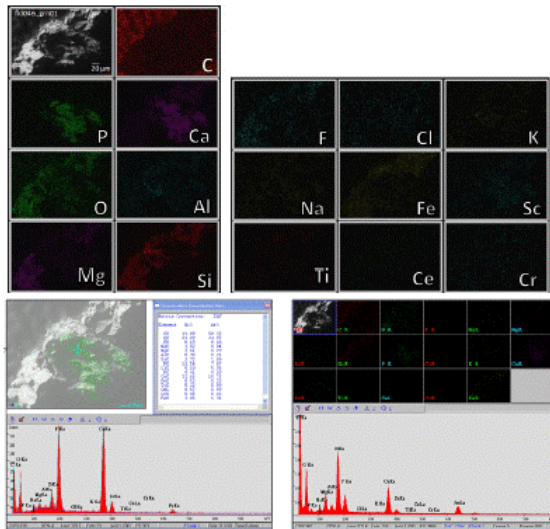
Z21-40: fld045_grn01, 75-125 μm



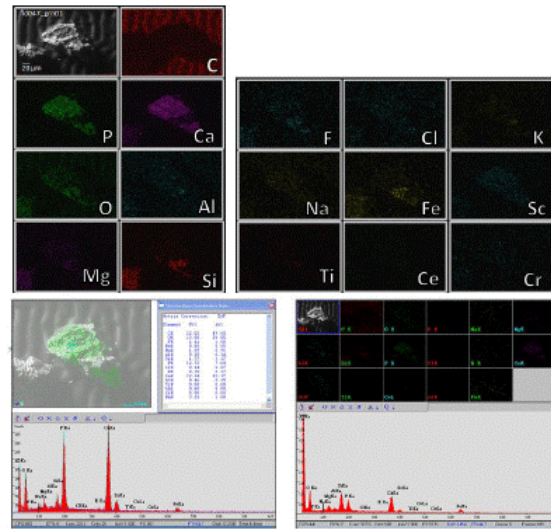
Z21-40: fld045_grn02, 75-125 μm



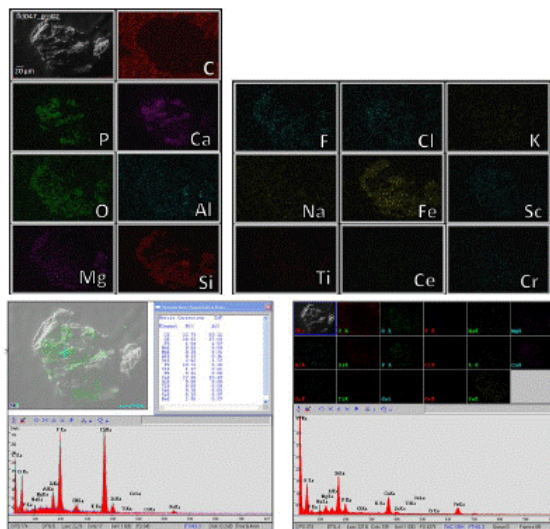
Z21-40: fld046_grn01, 75-125 μm



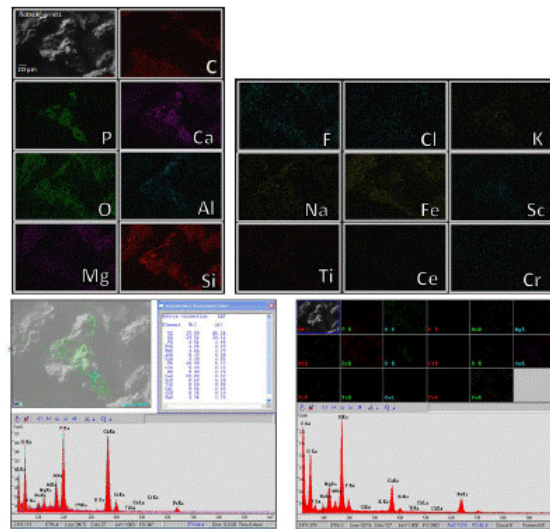
Z21-40: fld047_grn01, 75-125 μm



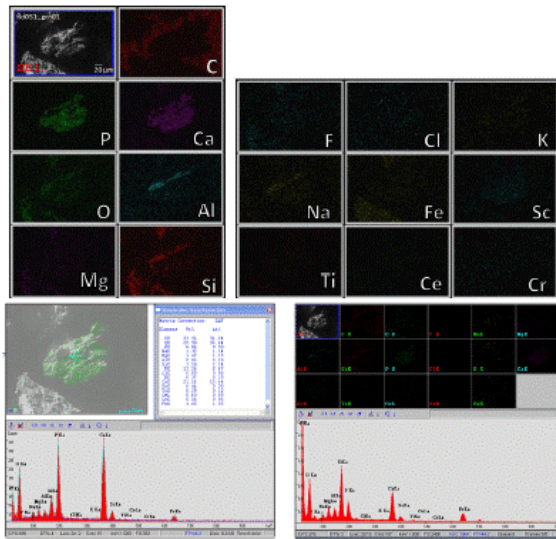
Z21-40: fld047_grn02, 75-125 μm



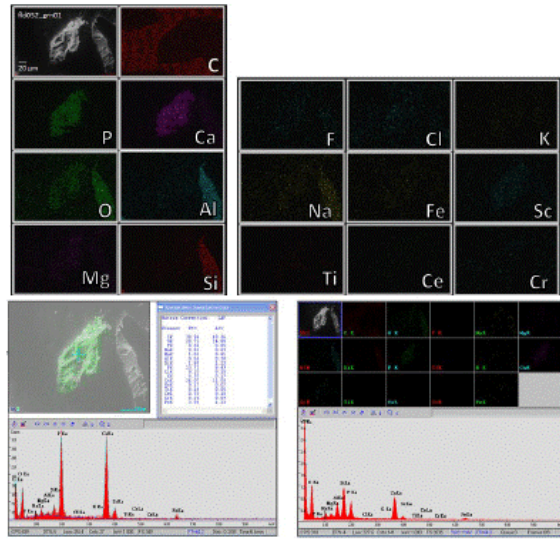
Z21-40: fld048_grn01, 75-125 μm



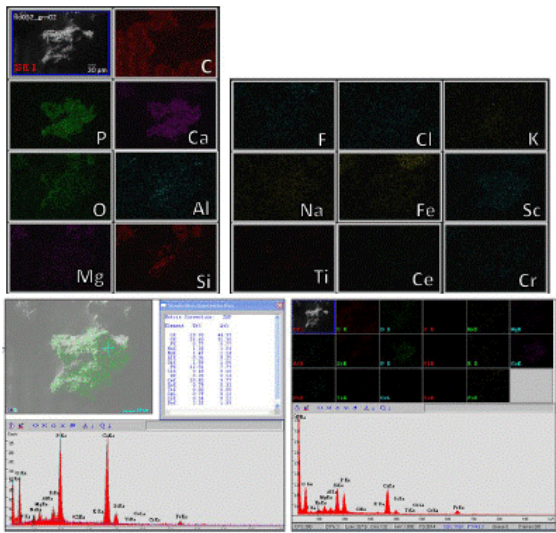
Z21-40: fld051_grn01, 75-125 μm



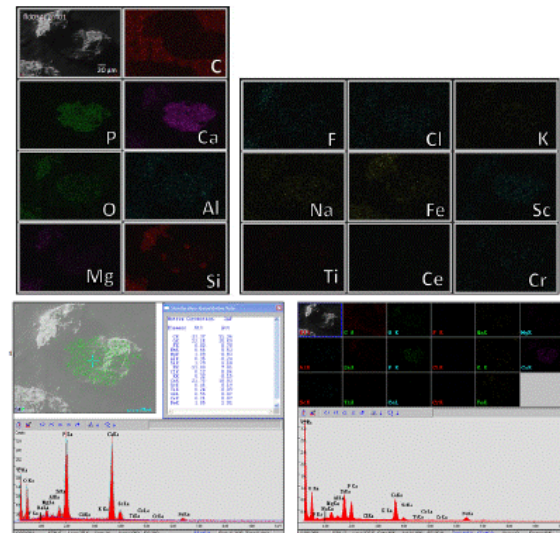
Z21-40: fld052_grn01, 75-125 μm



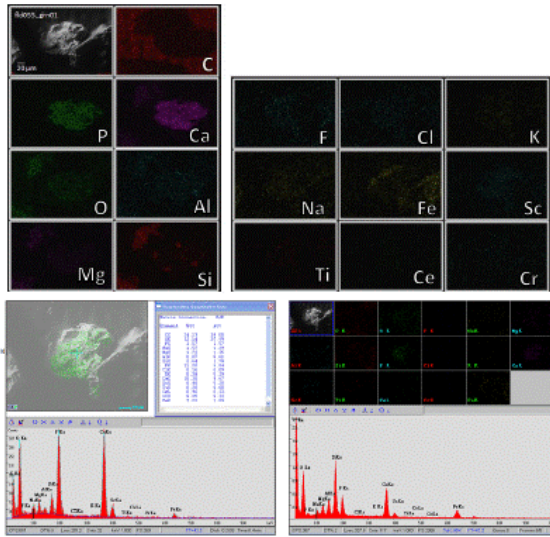
Z21-40: fld052_grn02, 75-125 μm



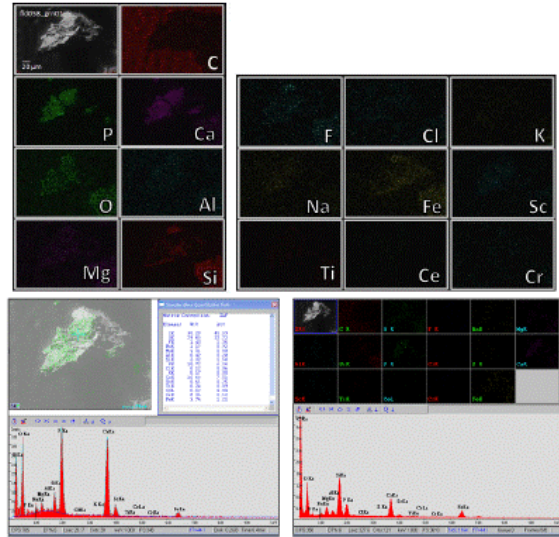
Z21-40: fld054_grn01, 75-125 μm



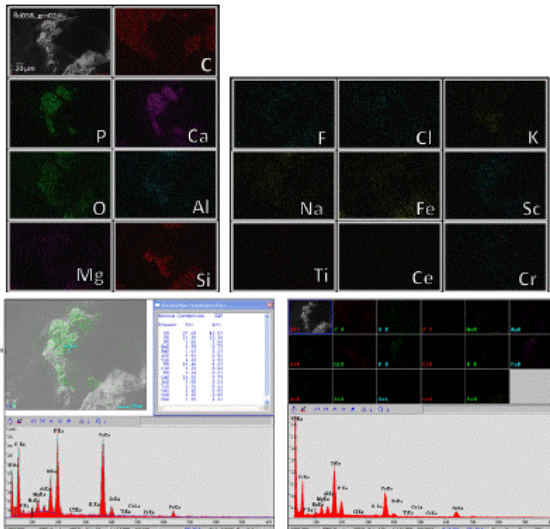
Z21-40: fld055_grn01, 75-125 μm



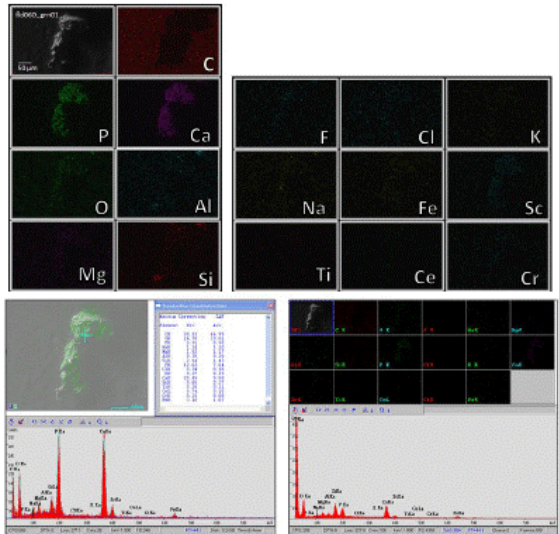
Z21-40: fld058_grn01, 75-125 μm



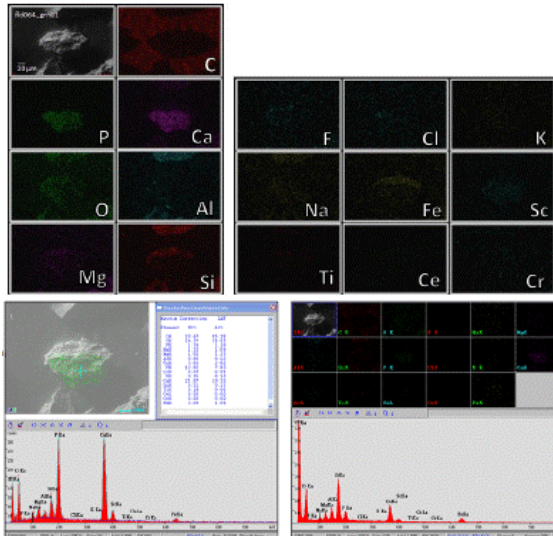
Z21-40: fld058_grn02, 75-125 μm



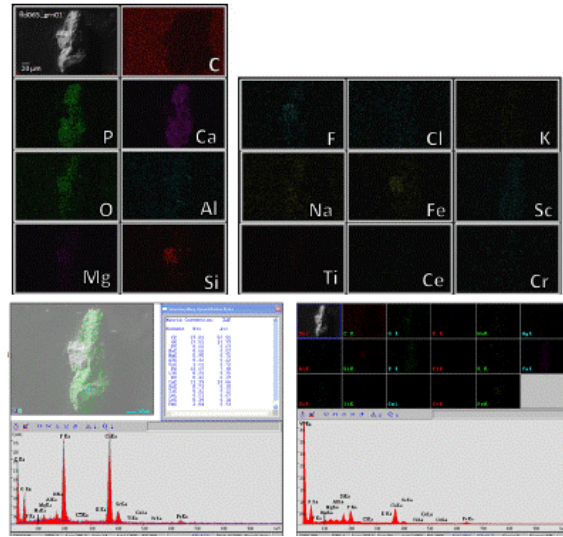
Z21-40: fld060_grn01, 75-125 μm



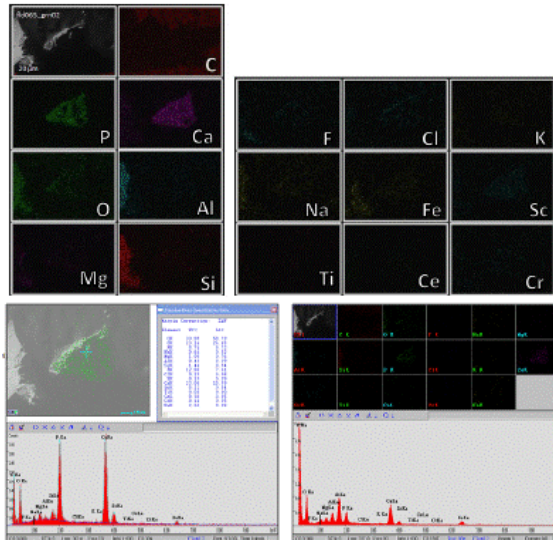
Z21-40: fld064_grn01, 75-125 μm



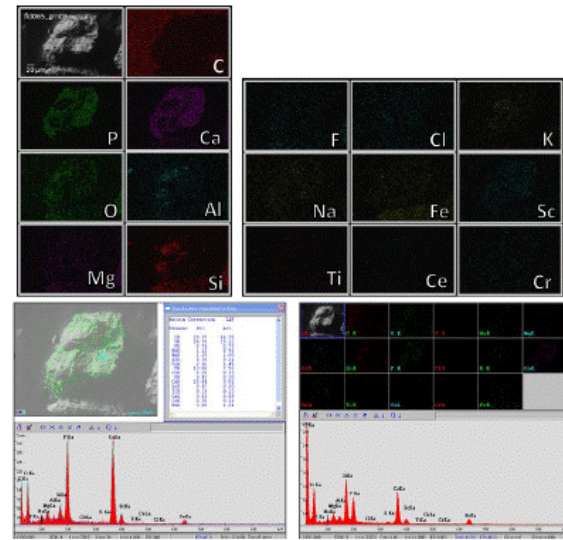
Z21-40: fld065_grn01, 75-125 μm



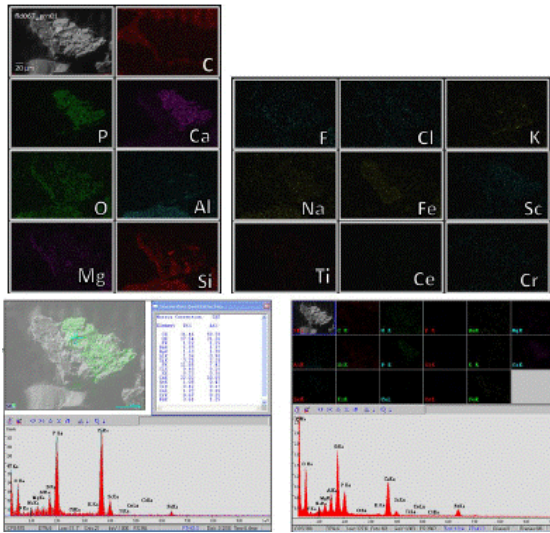
Z21-40: fld065_grn02, 75-125 μm



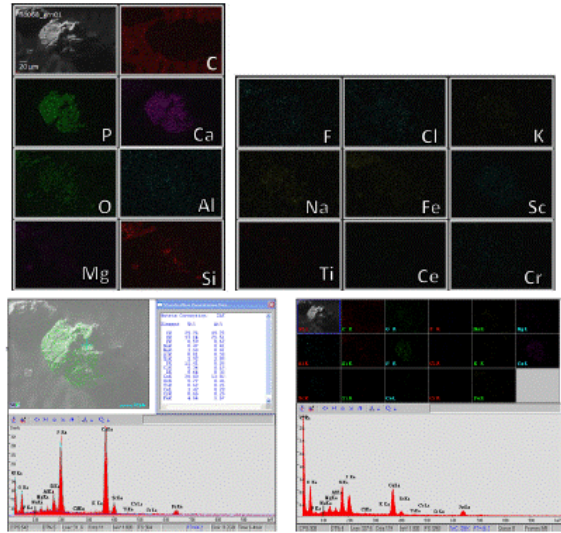
Z21-40: fld065_grn03, 75-125 μm



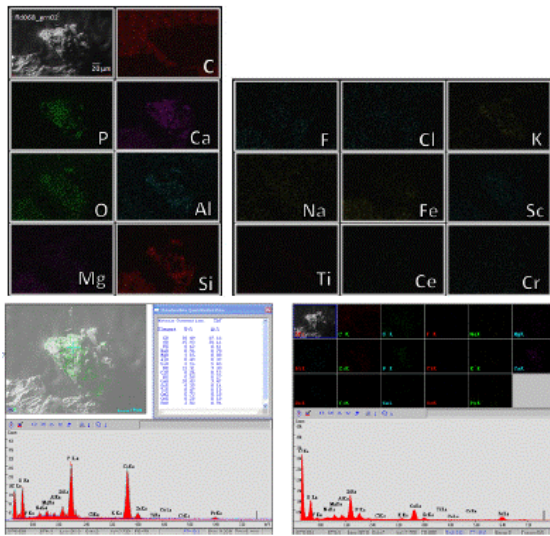
Z41-60: fld067_grn01, 75-125 μm



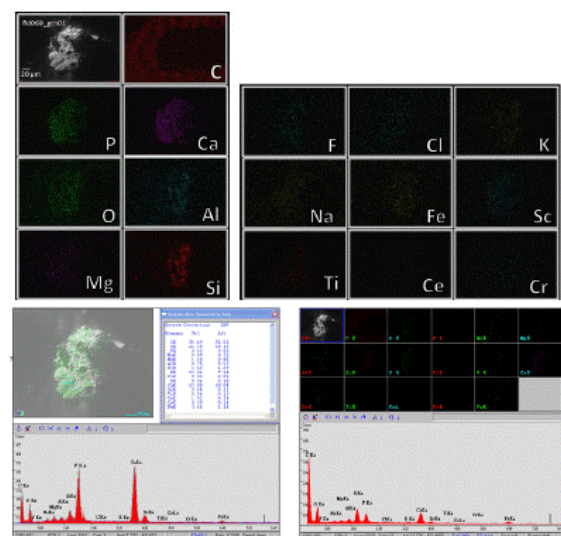
Z41-60: fld068_grn01, 75-125 μm



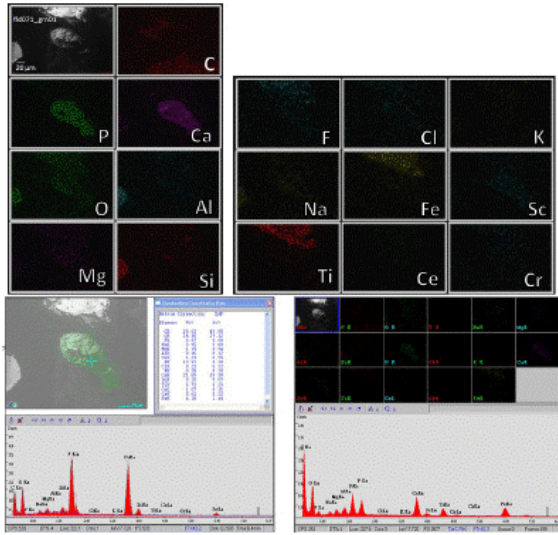
Z41-60: fld068_grn02, 75-125 μm



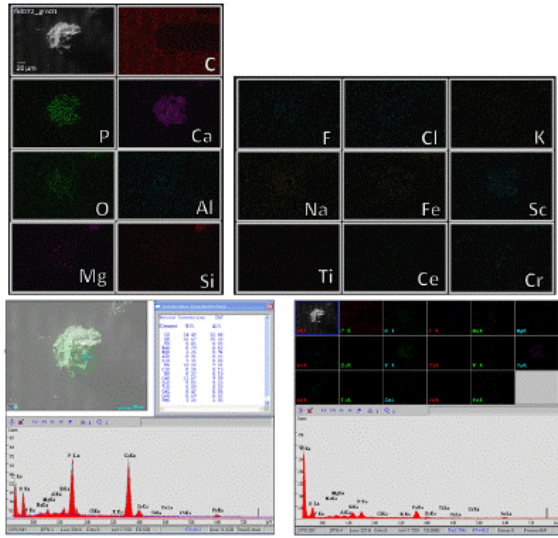
Z41-60: fld069_grn01, 75-125 μm



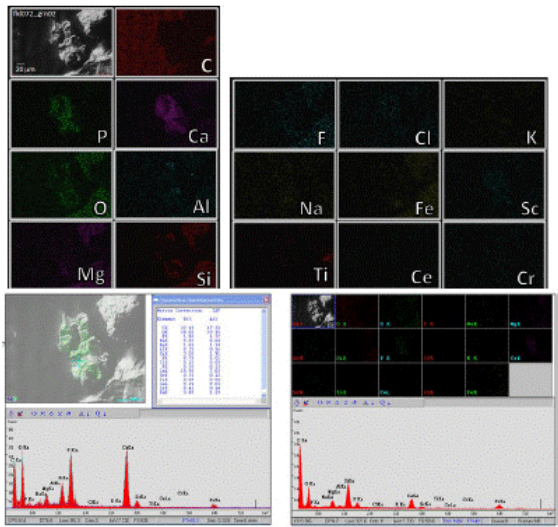
Z41-60: fld071_grn01, 75-125 μm



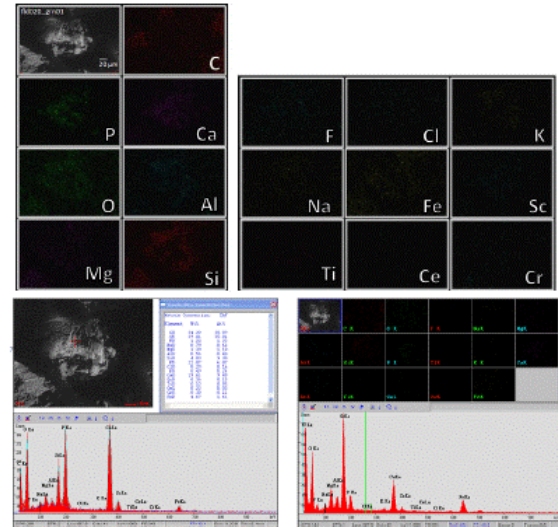
Z41-60: fld072_grn01, 75-125 μm



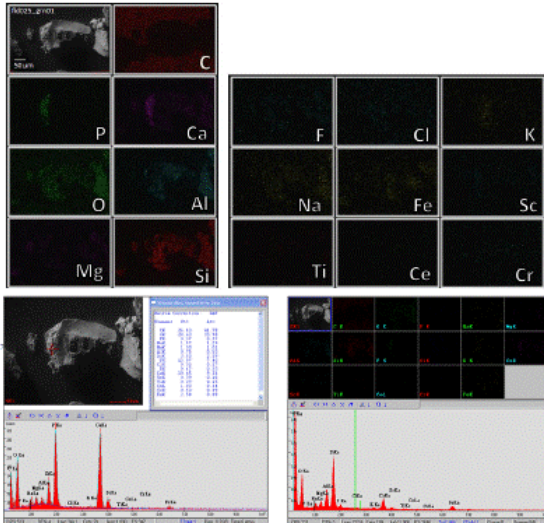
Z41-60: fld072_grn02, 75-125 μm



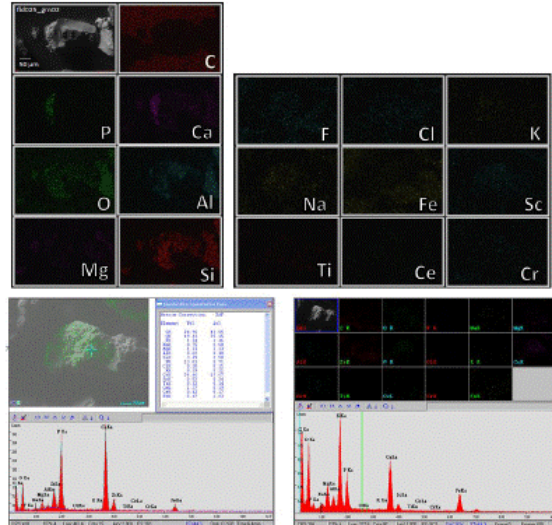
Z41-60: fld020_grn01, 125-150 μm



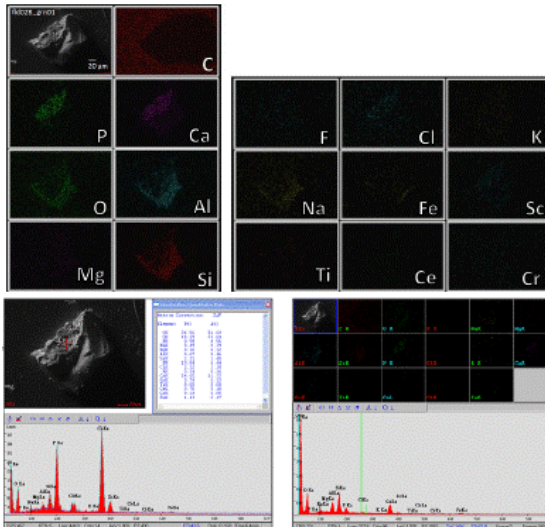
Z41-60: fld025_grn01, 125-150 μm



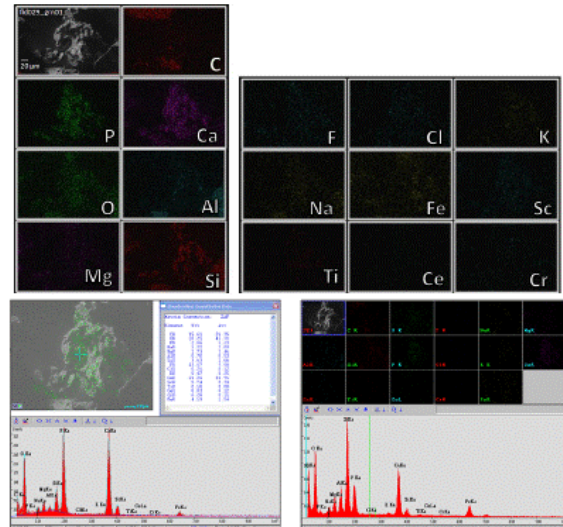
Z41-60: fld025_grn02, 125-150 μm



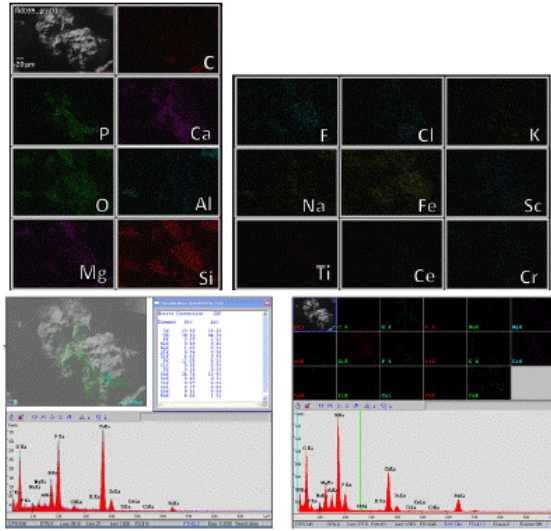
Z41-60: fld028_grn01, 125-150 μm



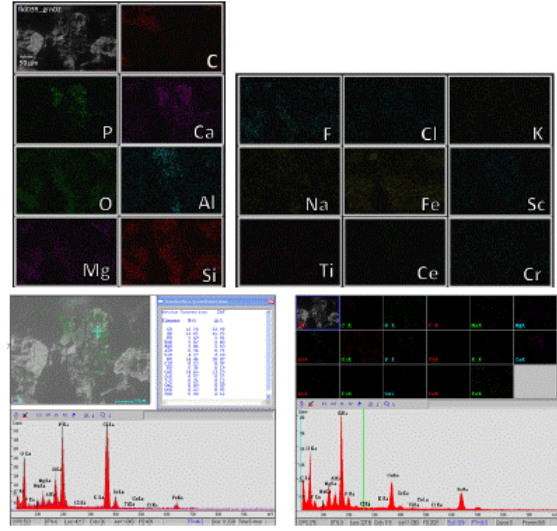
Z41-60: fld029_grn01, 125-150 μm



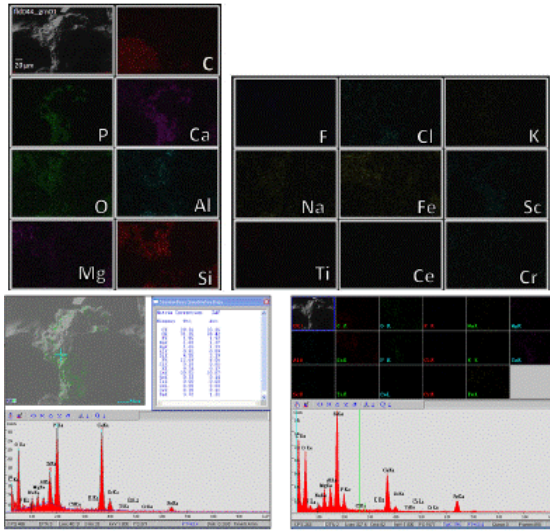
Z41-60: fld039_grn01, 125-150 μm



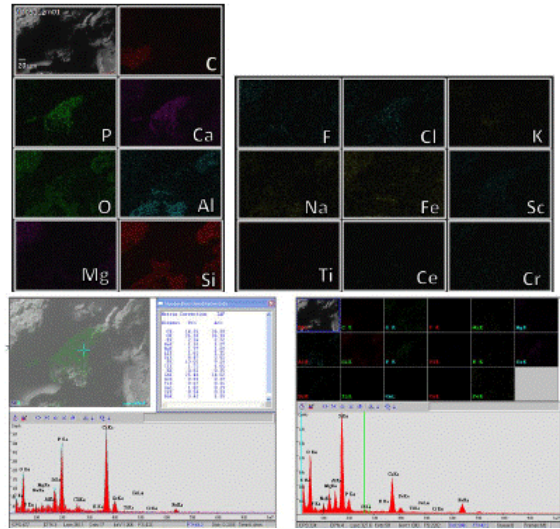
Z41-60: fld039_grn02, 125-150 μm



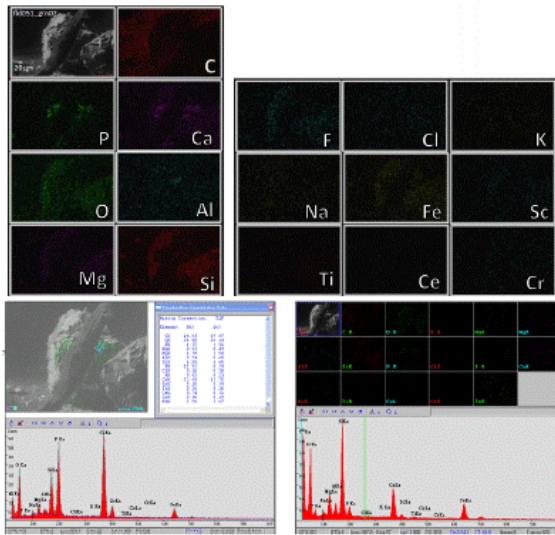
Z41-60: fld044_grn01, 125-150 μm



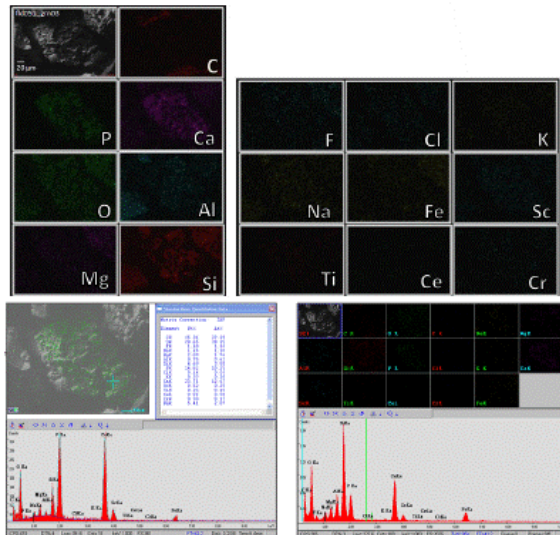
Z41-60: fld051_grn01, 125-150 μm



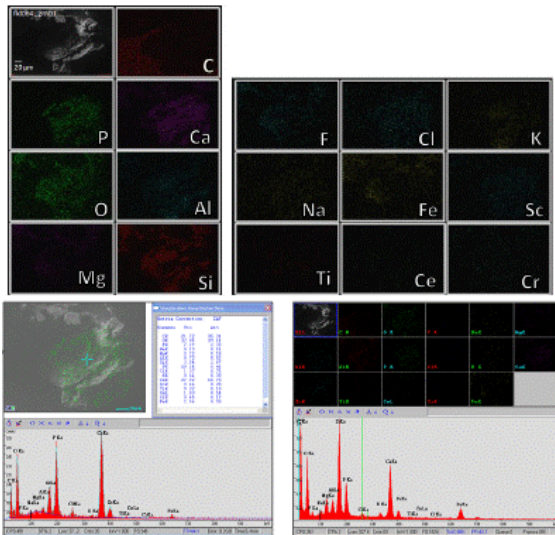
Z41-60: fld051_grn02, 125-150 μm



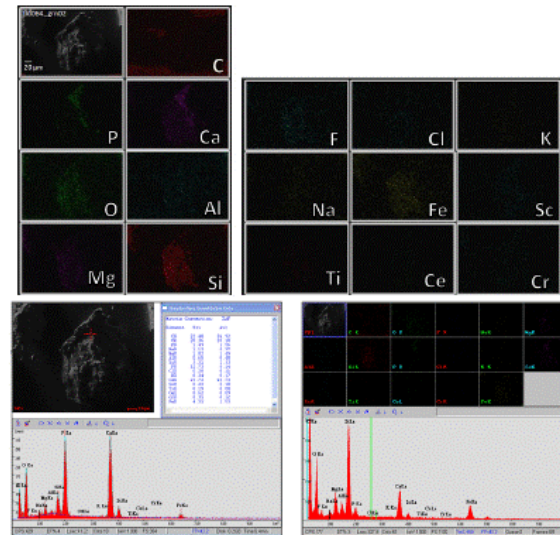
Z41-60: fld051_grn03, 125-150 μm



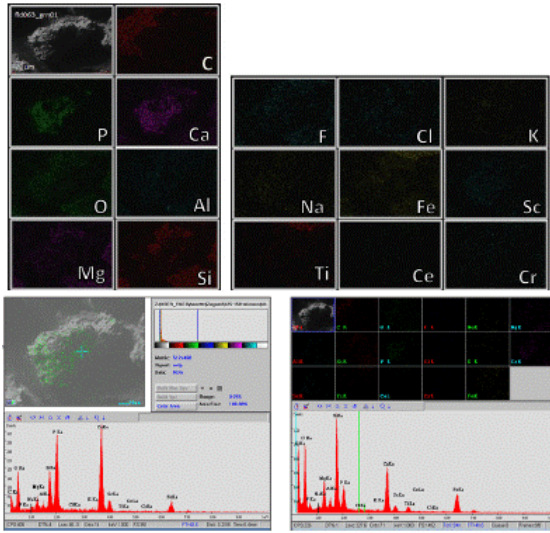
Z41-60: fld064_grn01, 125-150 μm



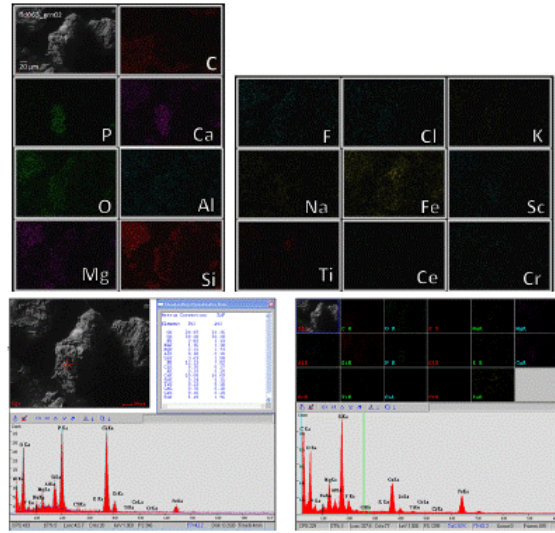
Z41-60: fld064_grn02, 125-150 μm



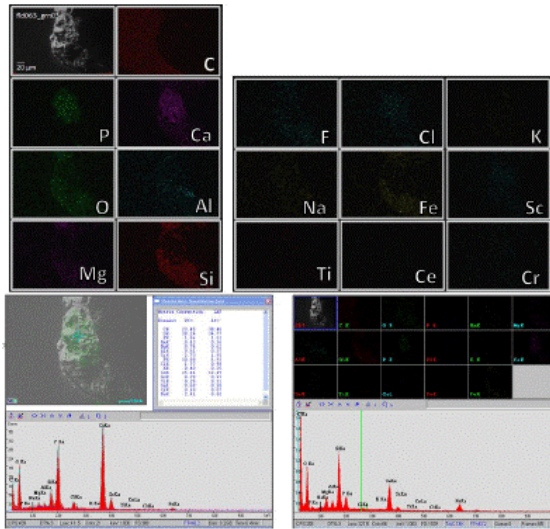
Z61-80: fld063_grn01, 125-150 µm



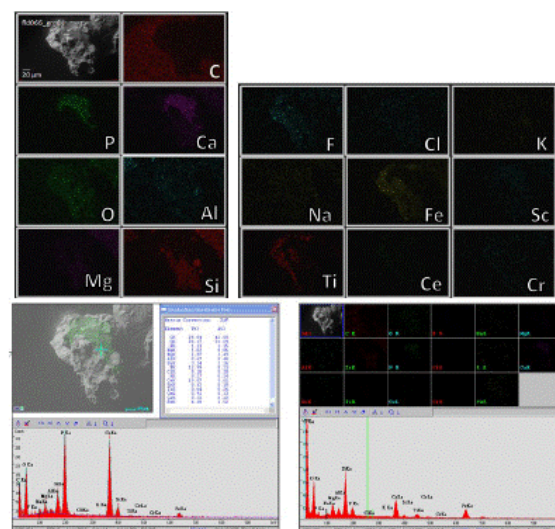
Z61-80: fld063_grn02, 125-150 µm



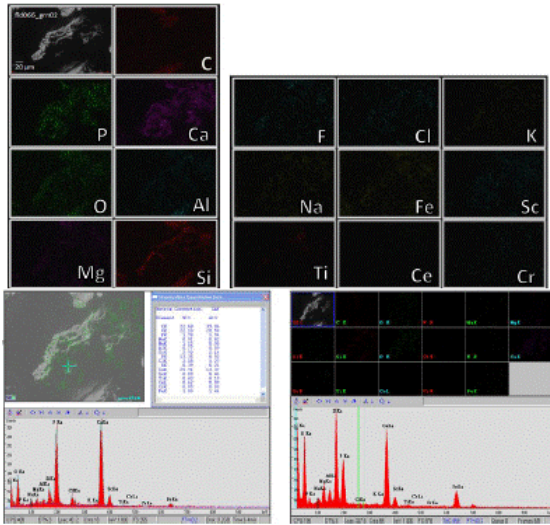
Z61-80: fld063_grn03, 125-150 µm



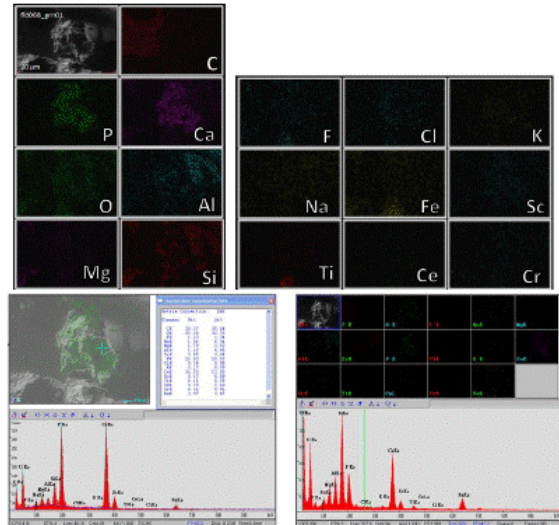
Z61-80: fld066_grn01, 125-150 µm



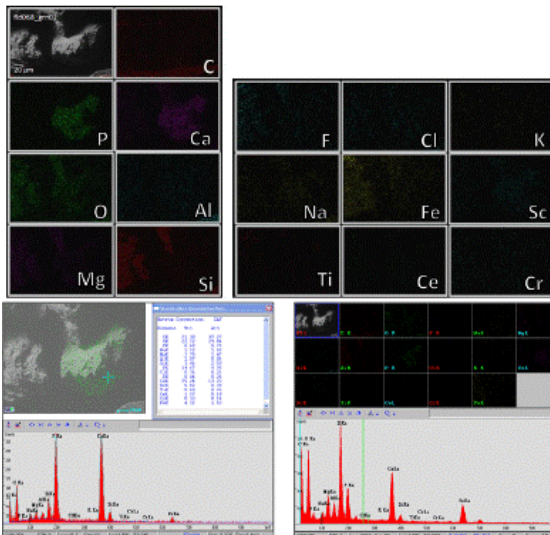
Z61-80: fld066_grn02, 125-150 μm



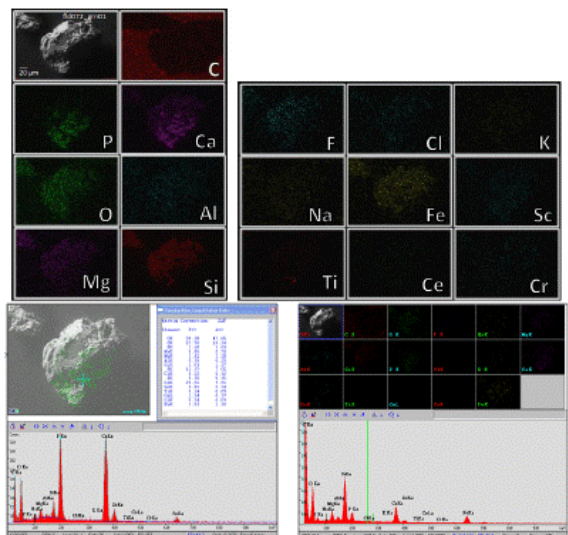
Z61-80: fld068_grn01, 125-150 μm



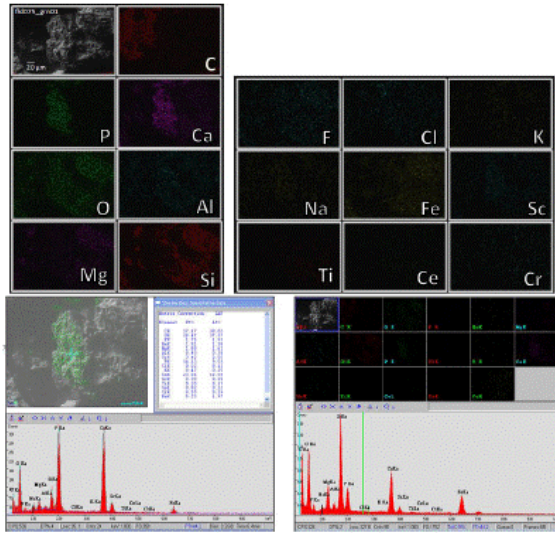
Z61-80: fld068_grn02, 125-150 μm



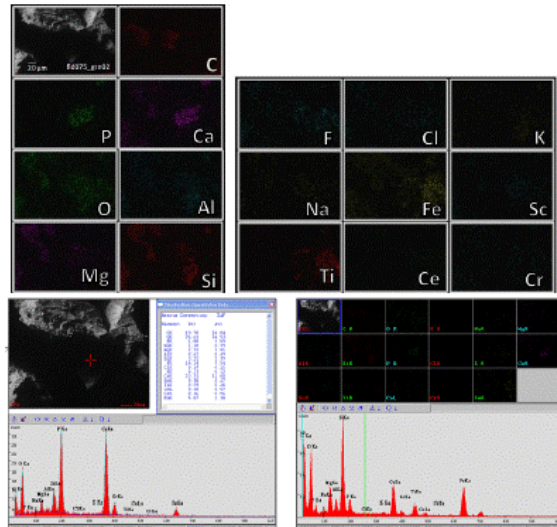
Z61-80: fld072_grn01, 125-150 μm



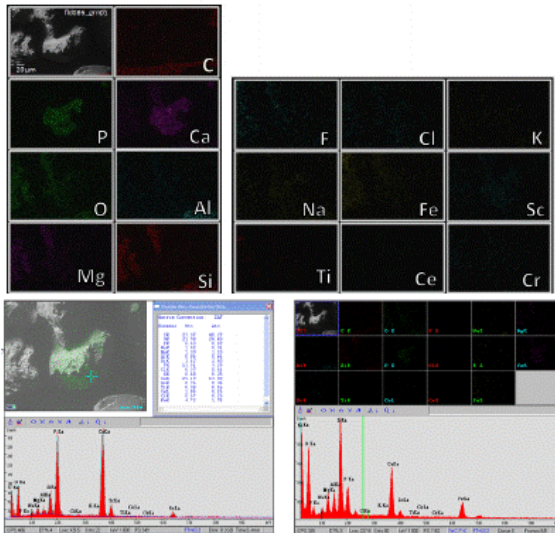
Z61-80: fld075_grn01, 125-150 μm



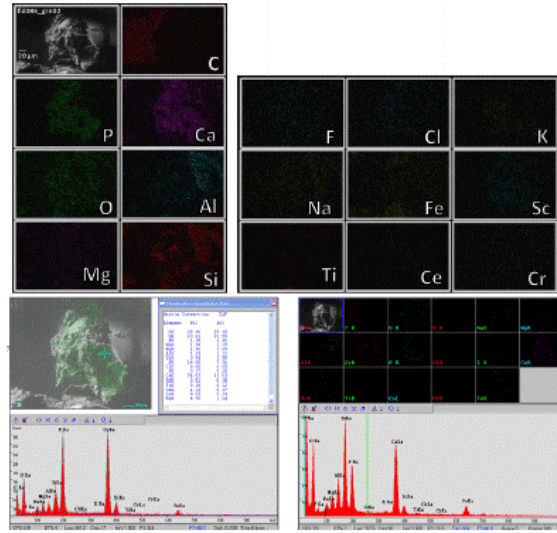
Z61-80: fld075_grn02, 125-150 μm



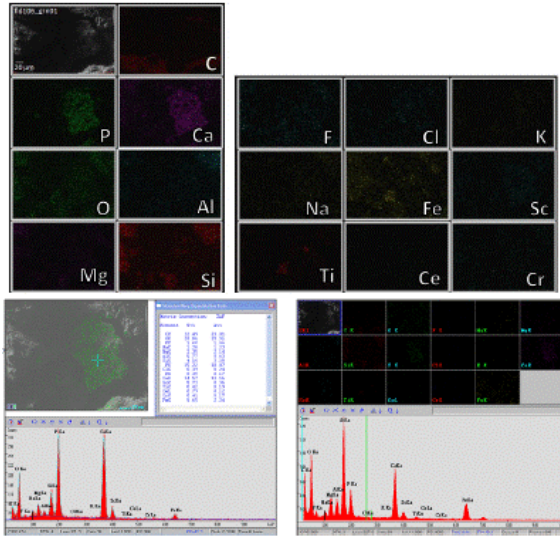
Z61-80: fld086_grn01, 125-150 μm



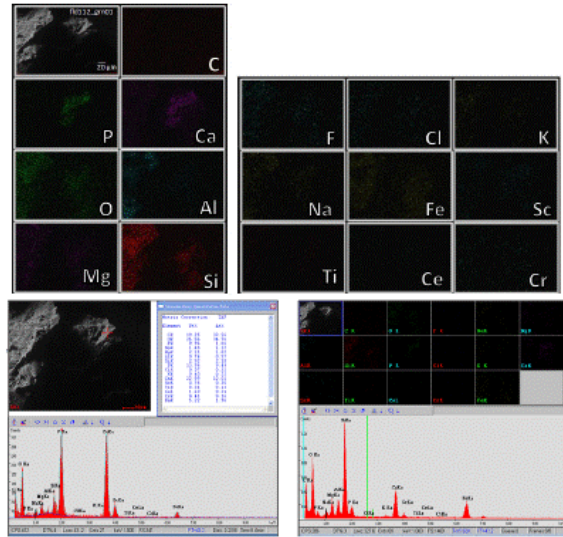
Z61-80: fld086_grn02, 125-150 μm



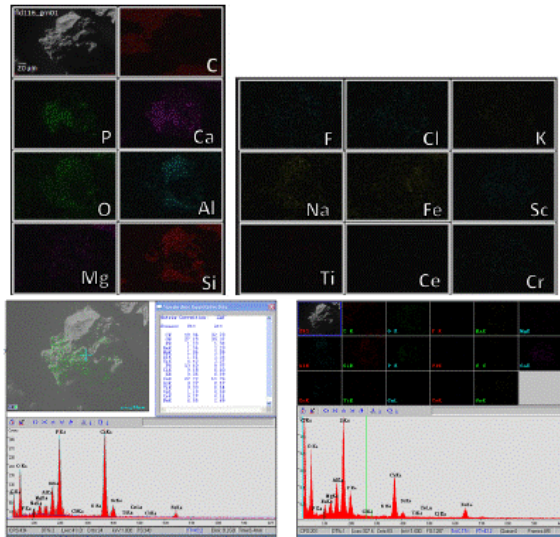
Z61-80: fld106_grn01, 125-150 μm



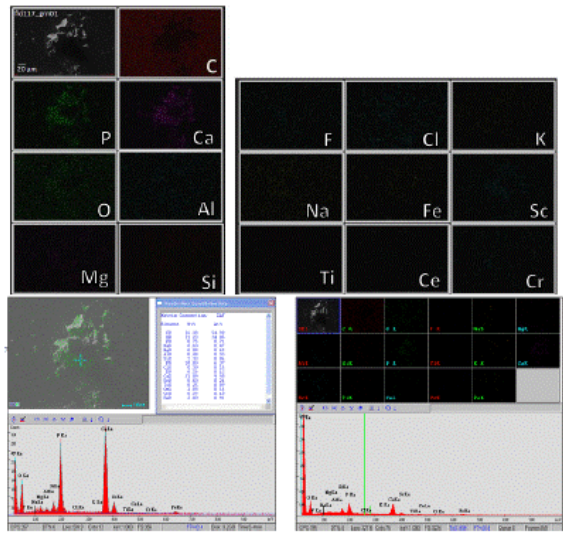
Z61-80: fld112_grn01, 125-150 μm



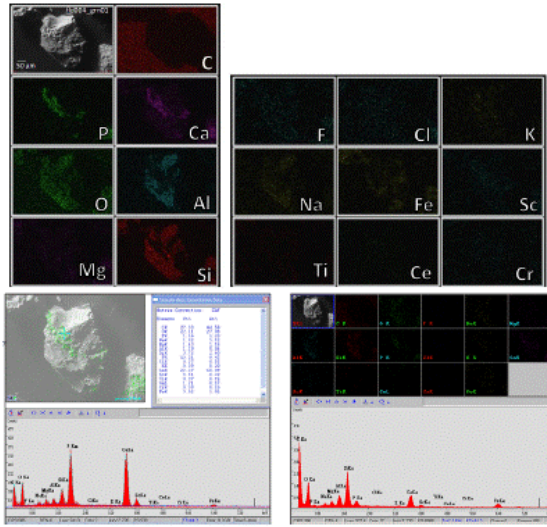
Z61-80: fld116_grn01, 125-150 μm



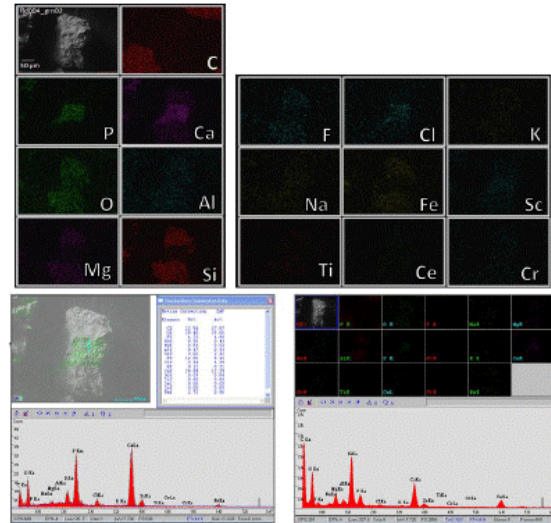
Z61-80: fld117_grn01, 125-150 μm



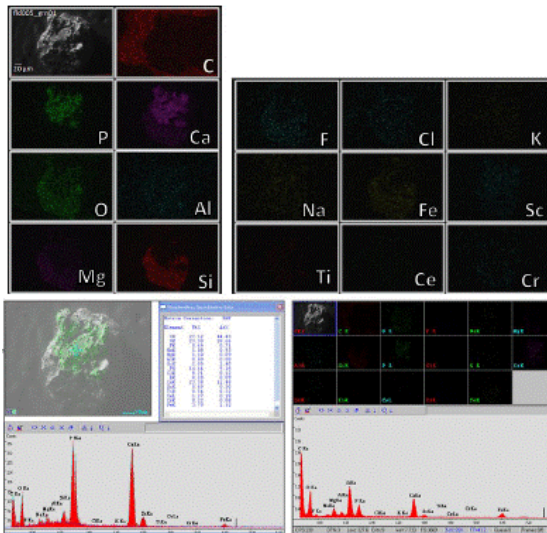
Z61-80: fld004_grn01, 150-250 μm



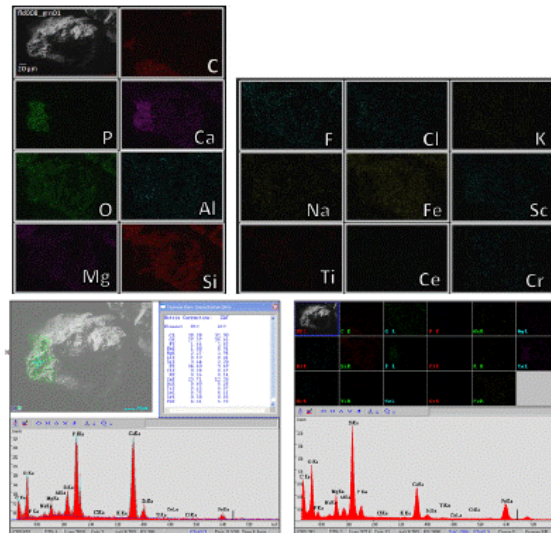
Z61-80: fld004_grn02, 150-250 μm



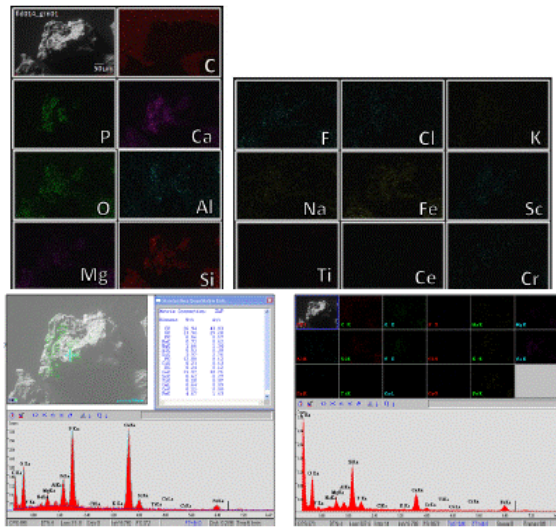
Z61-80: fld005_grn01, 150-250 μm



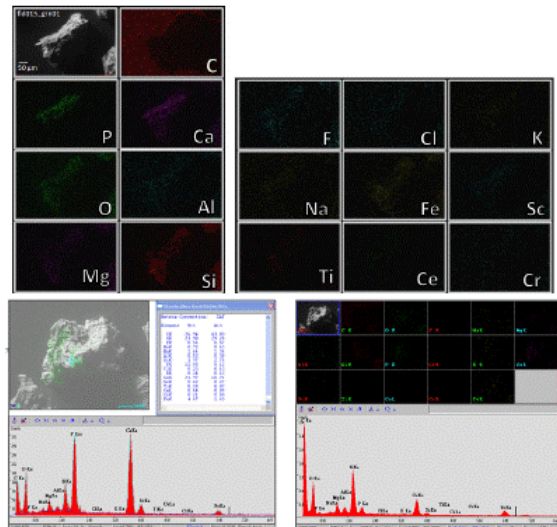
Z61-80: fld008_grn01, 150-250 μm



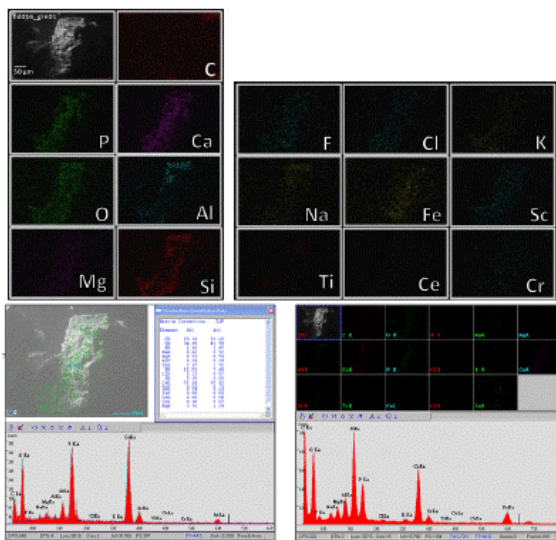
Z81-92: fld014_grn01, 150-250 μm



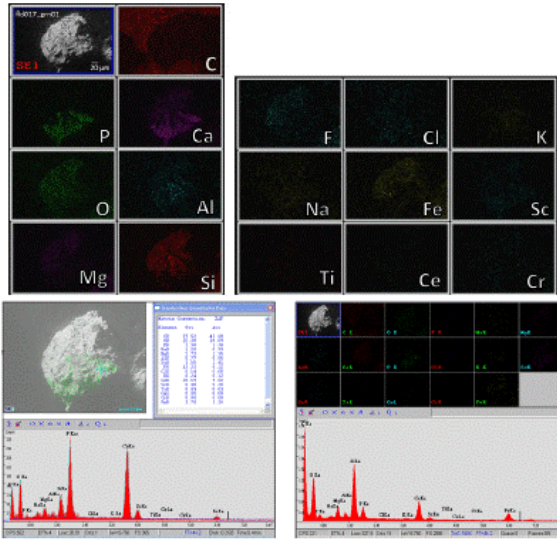
Z81-92: fld015_grn01, 150-250 μm



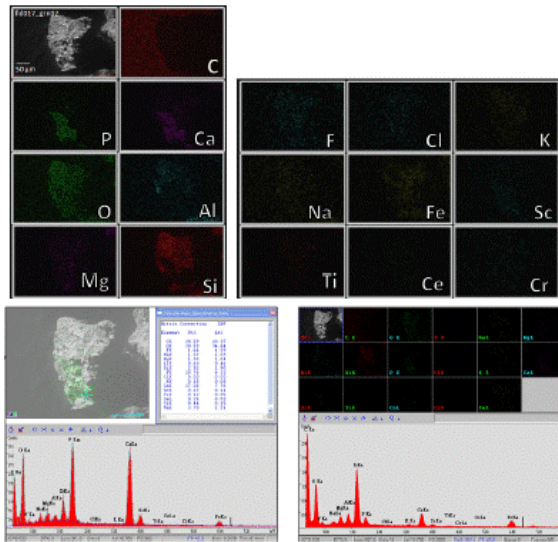
Z81-92: fld016_grn01, 150-250 μm



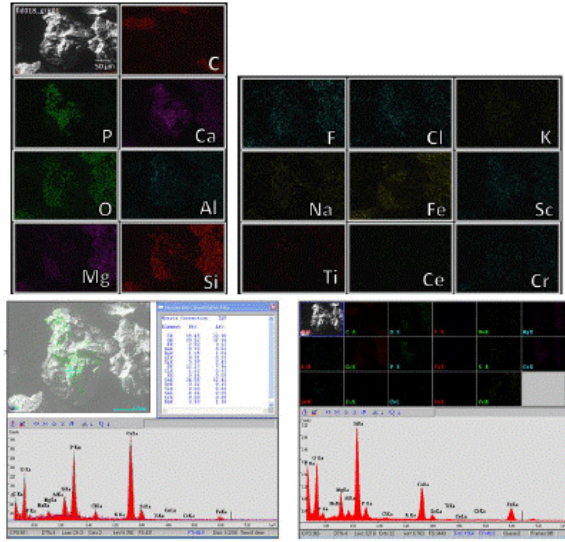
Z81-92: fld017_grn01, 150-250 μm



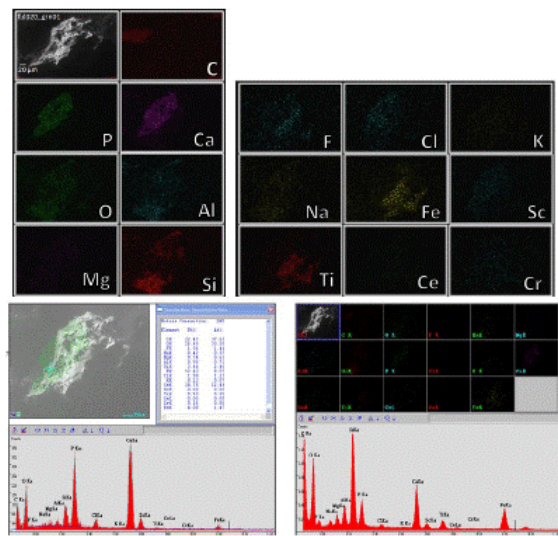
Z81-92: fld017_grn02, 150-250 μm



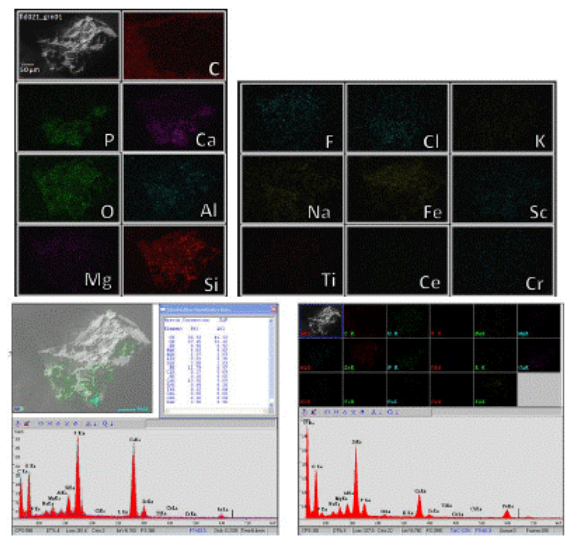
Z81-92: fld018_grn01, 150-250 μm



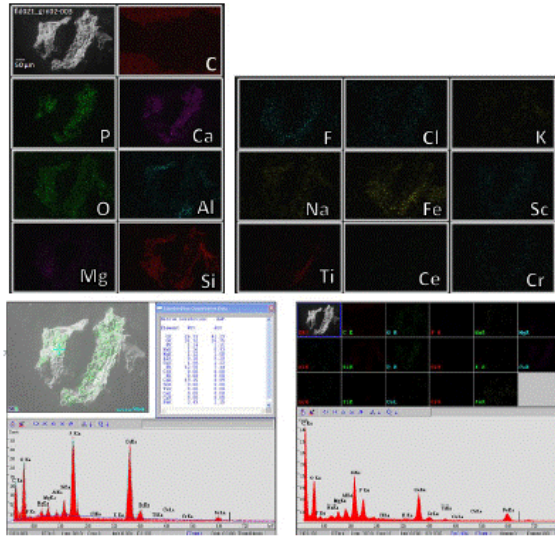
Z81-92: fld020_grn01, 150-250 μm



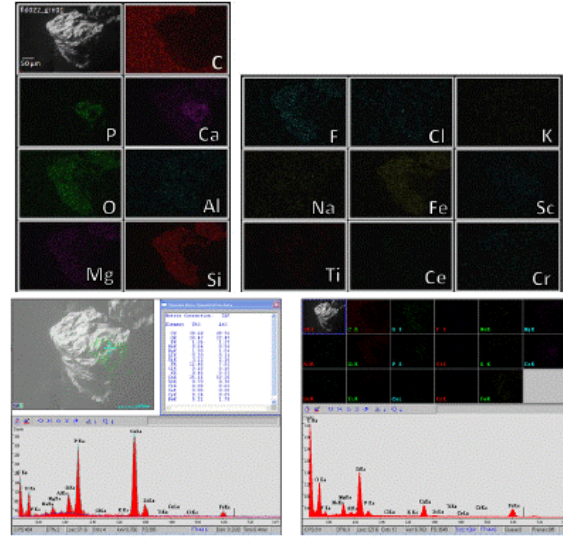
Z81-92: fld021_grn01, 150-250 μm



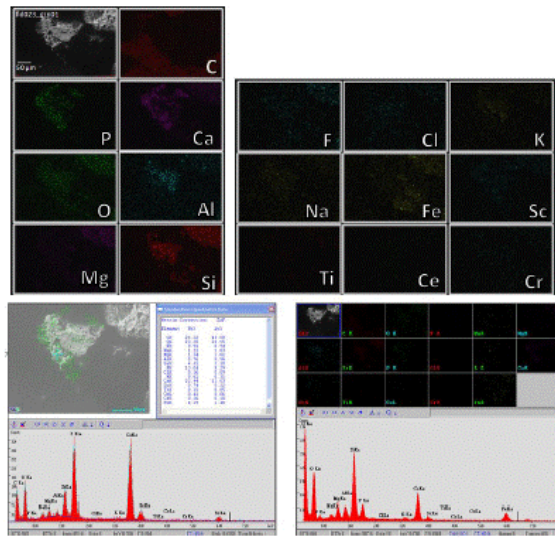
Z81-92: fld021_grn02-03, 150-250 μm



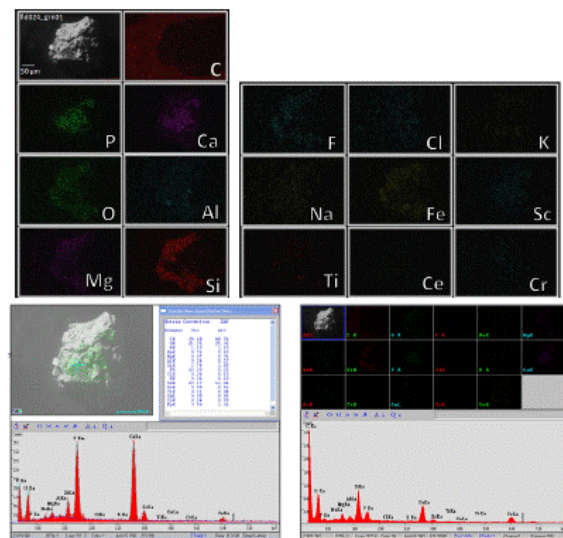
Z81-92: fld022_grn01, 150-250 μm



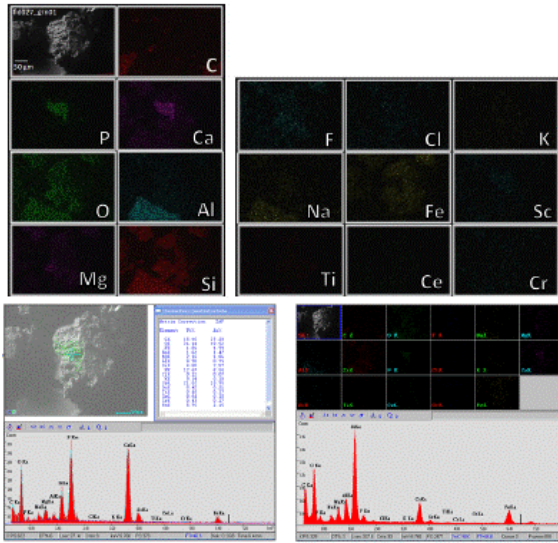
Z81-92: fld023_grn01, 150-250 μm



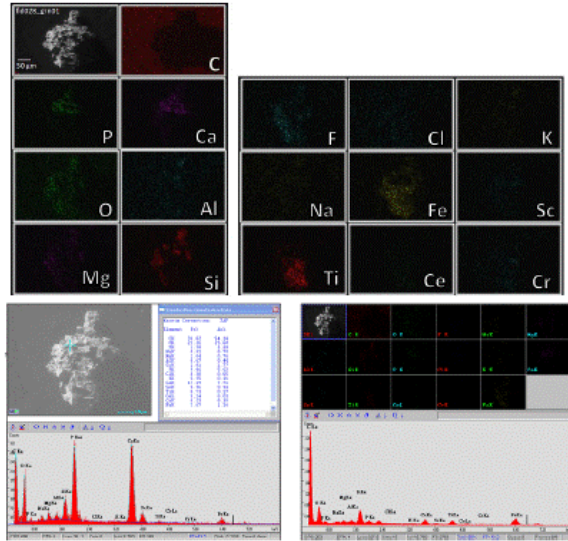
Z93-102: fld024_grn01, 150-250 μm



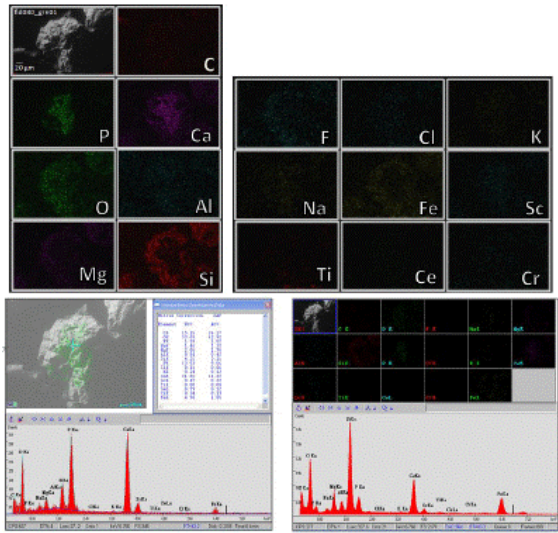
Z93-102: fld027_grn01, 150-250 μm



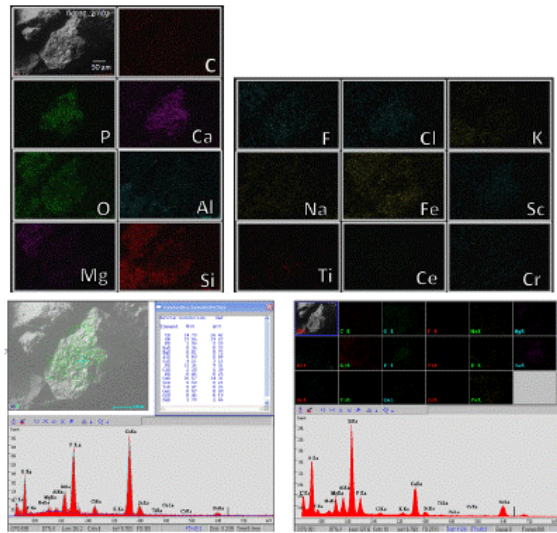
Z93-102: fld028_grn01, 150-250 μm



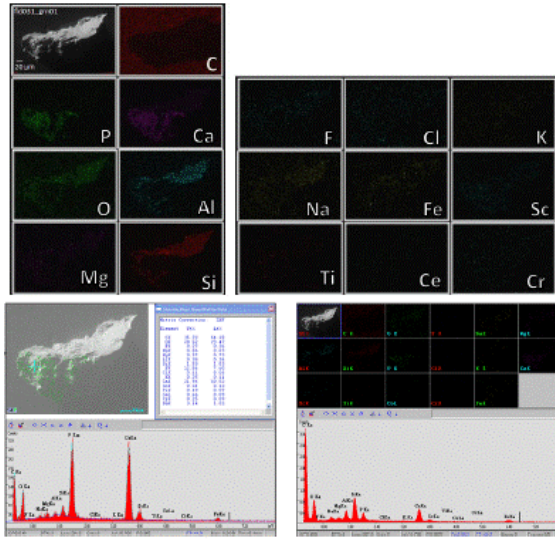
Z93-102: fld030_grn01, 150-250 μm



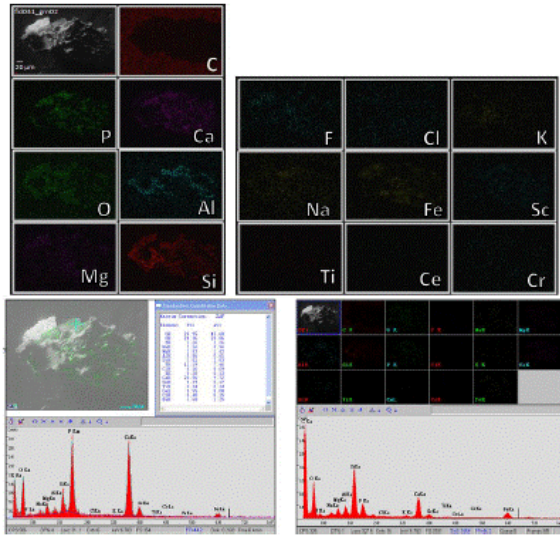
Z93-102: fld030_grn02, 150-250 μm



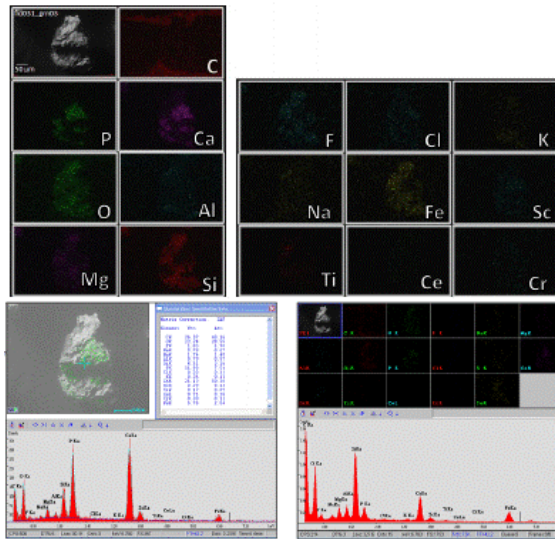
Z93-102: fld031_grn01, 150-250 μm



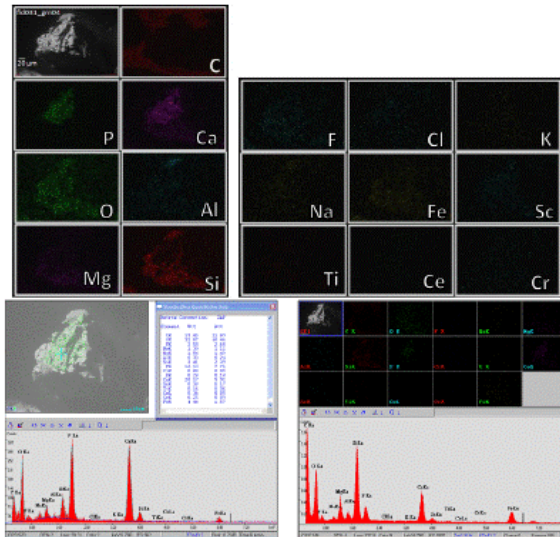
Z93-102: fld031_grn02, 150-250 μm



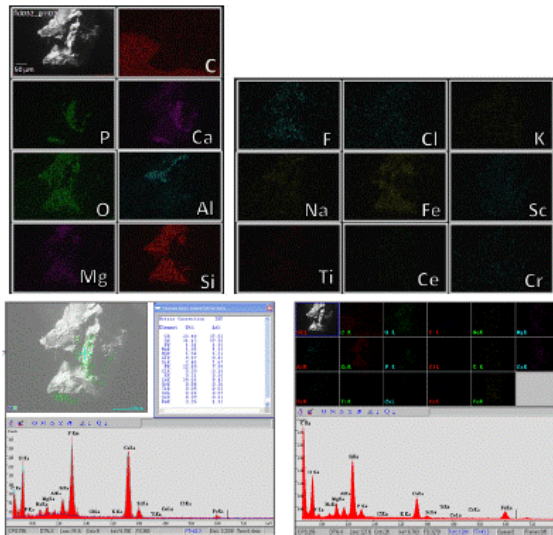
Z93-102: fld031_grn03, 150-250 μm



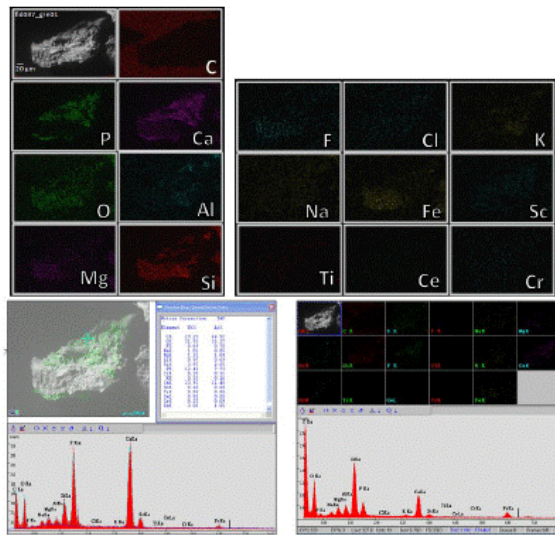
Z93-102: fld031_grn04, 150-250 μm



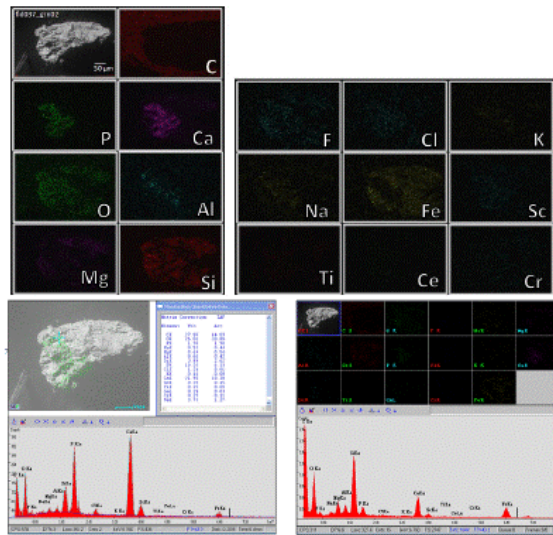
Z93-102: fld032_grn01, 150-250 µm



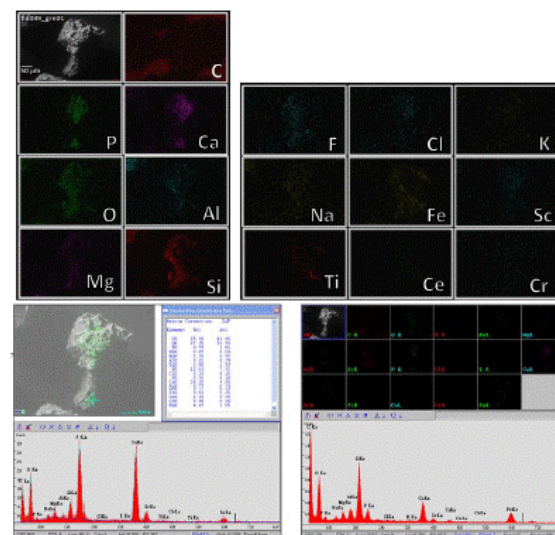
Z103-113: fld037_grn01, 150-250 µm



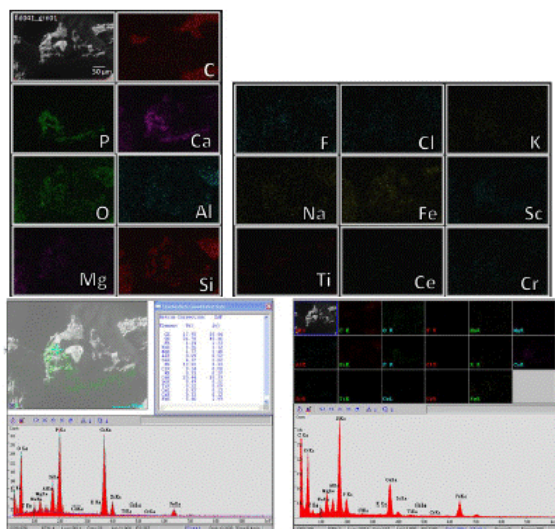
Z103-113: fld037_grn02, 150-250 µm



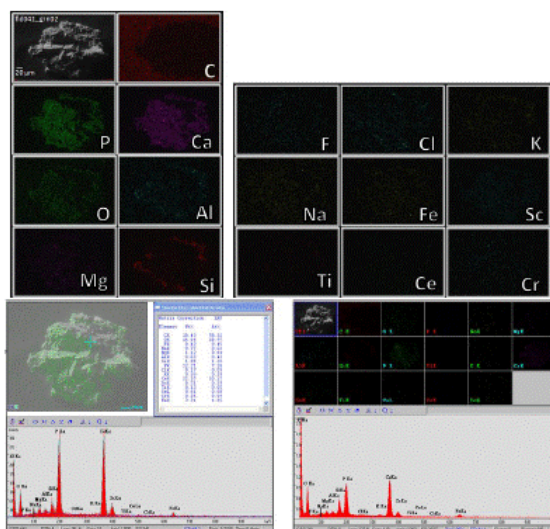
Z103-113: fld039_grn01, 150-250 µm



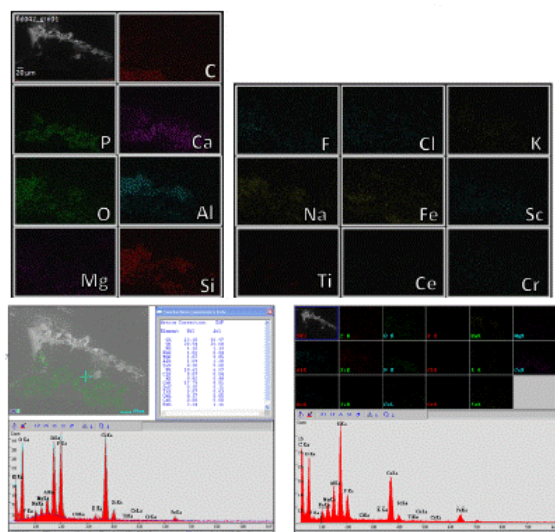
Z103-113: fld041_grn01, 150-250 μm



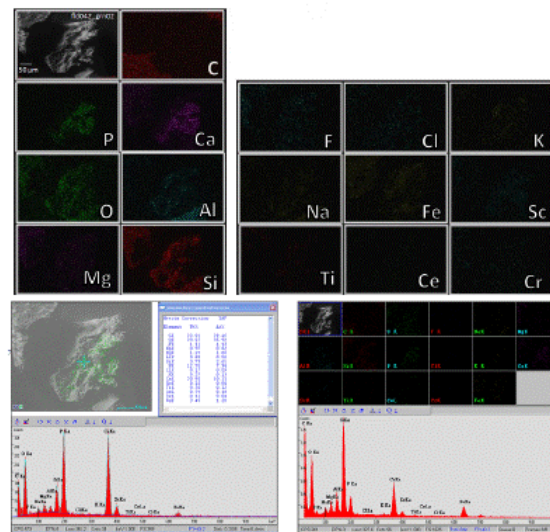
Z103-113: fld041_grn02, 150-250 μm



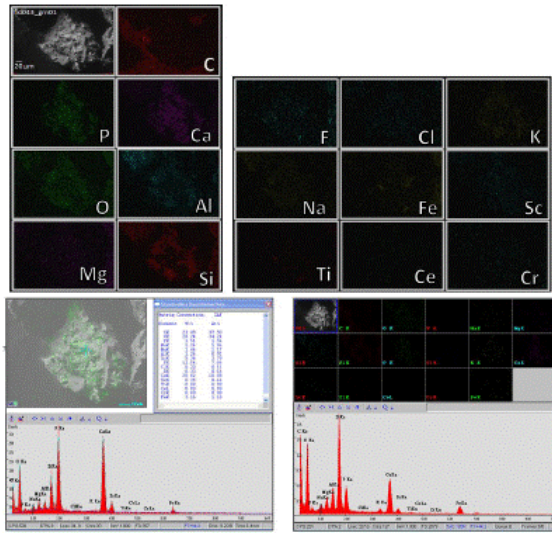
Z103-113: fld042_grn01, 150-250 μm



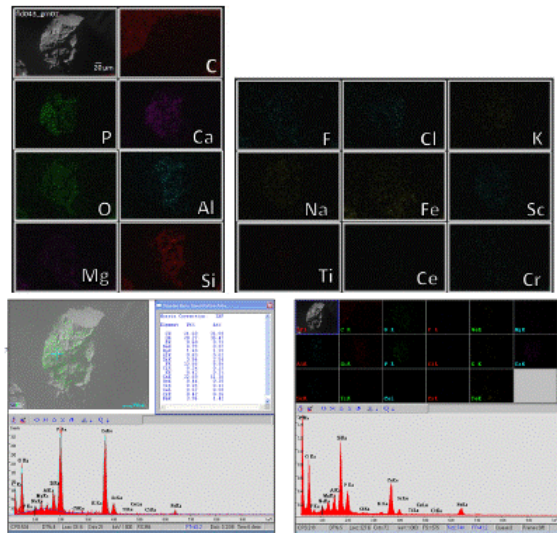
Z103-113: fld042_grn02, 150-250 μm



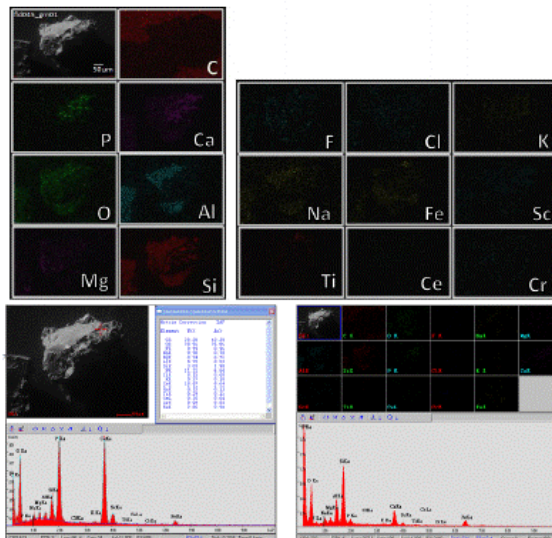
Z103-113: fld043_grn01, 150-250 μm



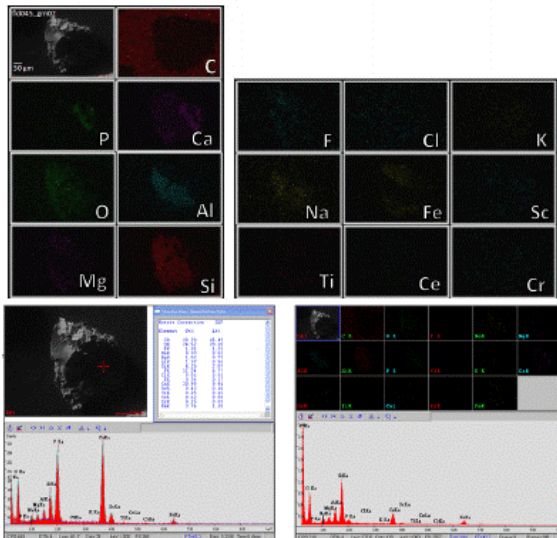
Z103-113: fld043_grn02, 150-250 μm



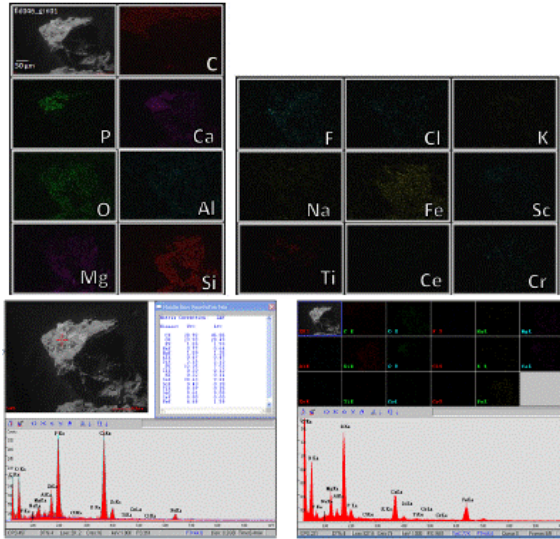
Z103-113: fld045_grn01, 150-250 μm



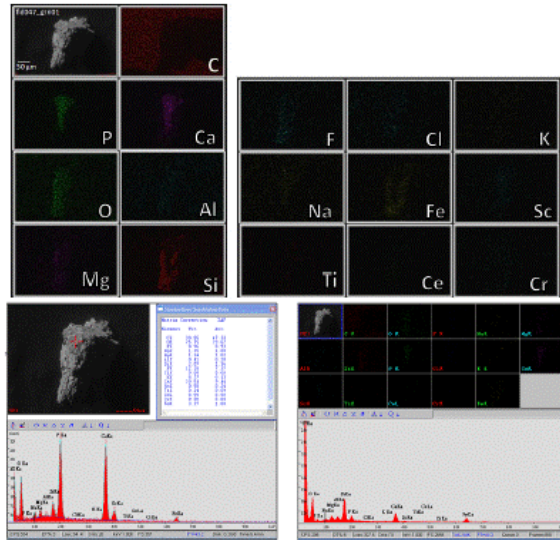
Z103-113: fld045_grn02, 150-250 μm



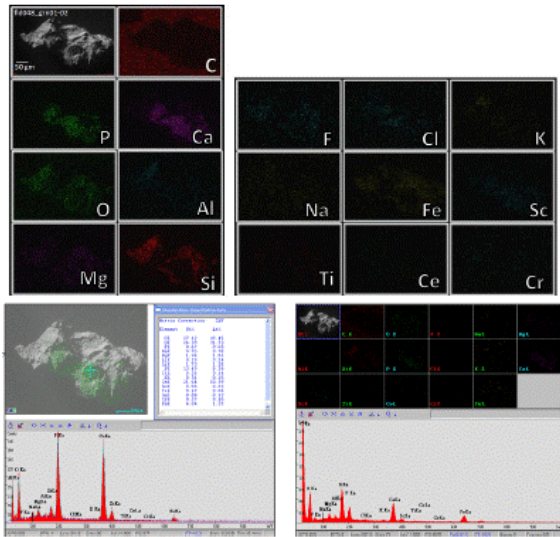
Z114-123: fld046_grn01, 150-250 μm



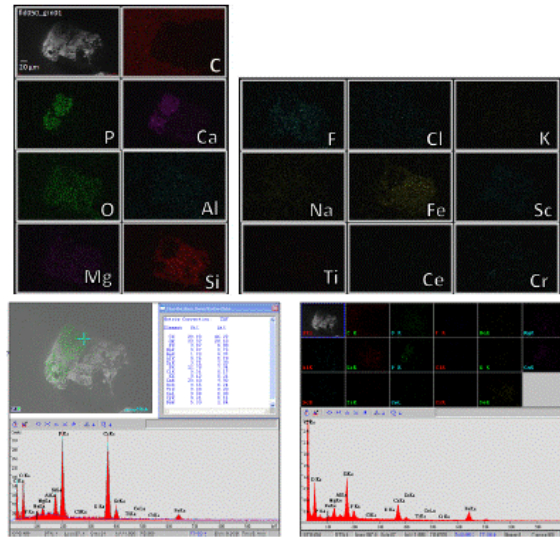
Z114-123: fld047_grn01, 150-250 μm



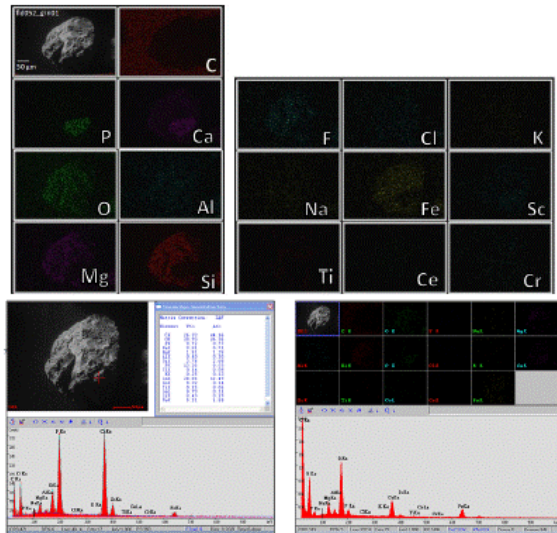
Z114-123: fld048_grn01-02, 150-250 μm



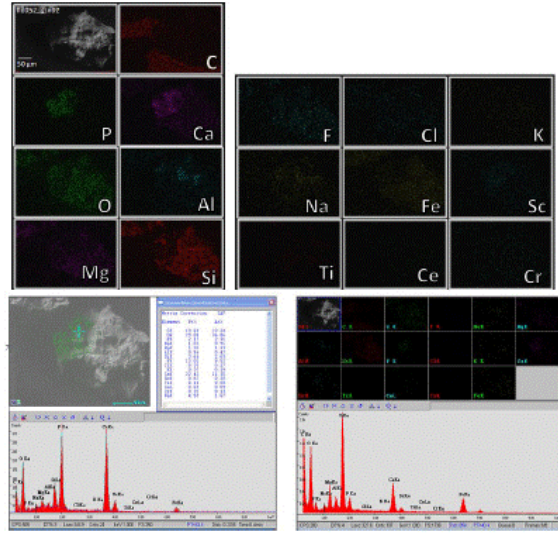
Z114-123: fld050_grn01, 150-250 μm



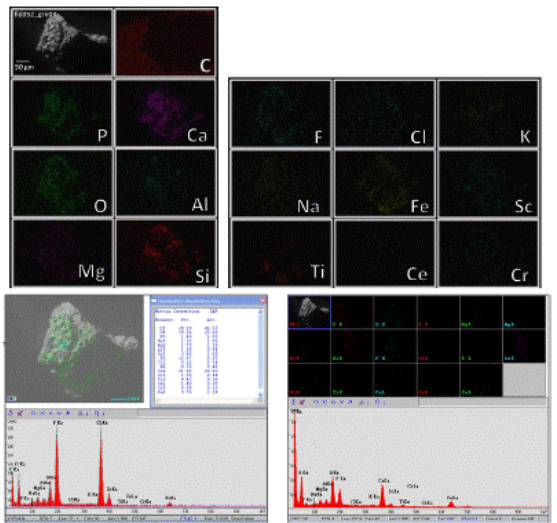
Z114-123: fld052_grn01, 150-250 μm



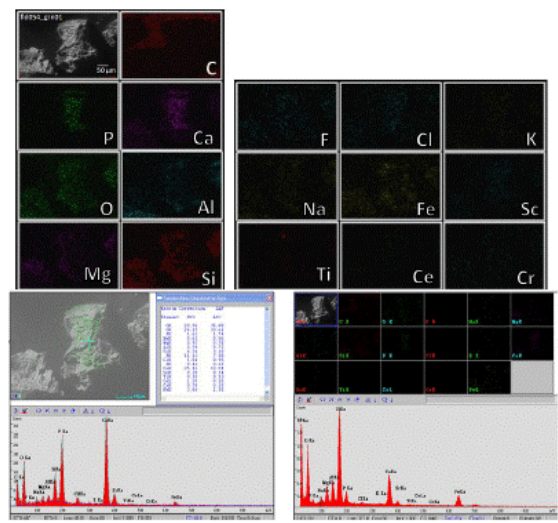
Z114-123: fld052_grn02, 150-250 μm



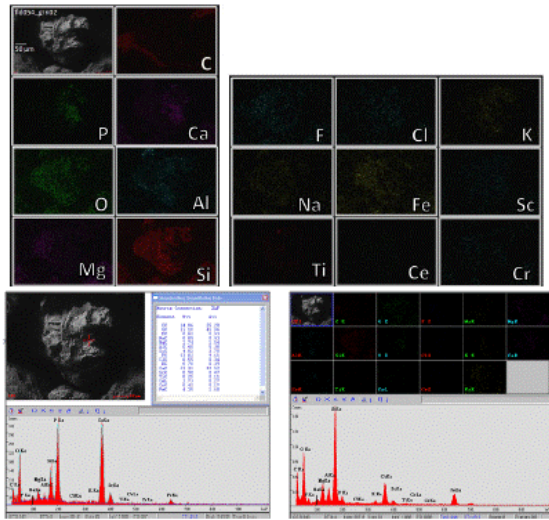
Z114-123: fld052_grn03, 150-250 μm



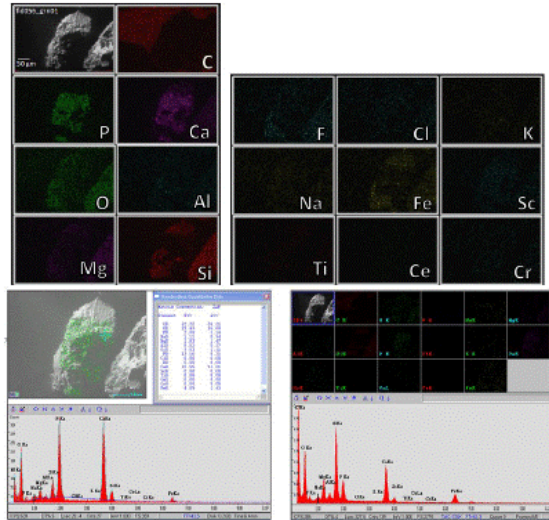
Z114-123: fld054_grn01, 150-250 μm



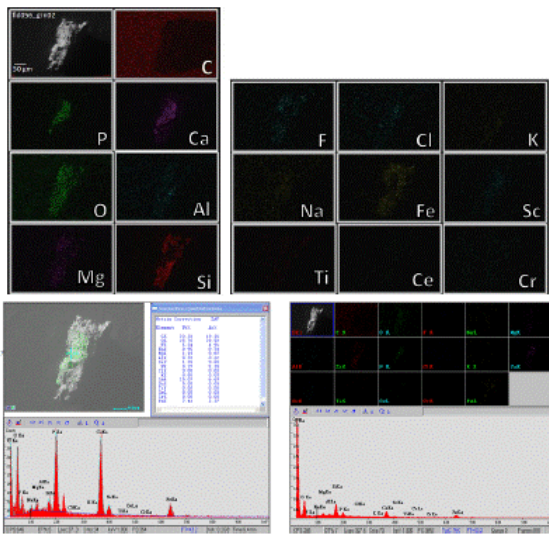
Z114-123: fld054_grn02, 150-250 μm



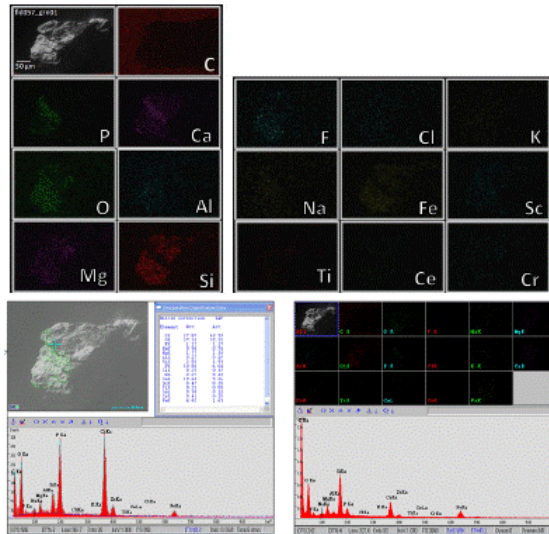
Z124-134: fld056_grn01, 150-250 μm



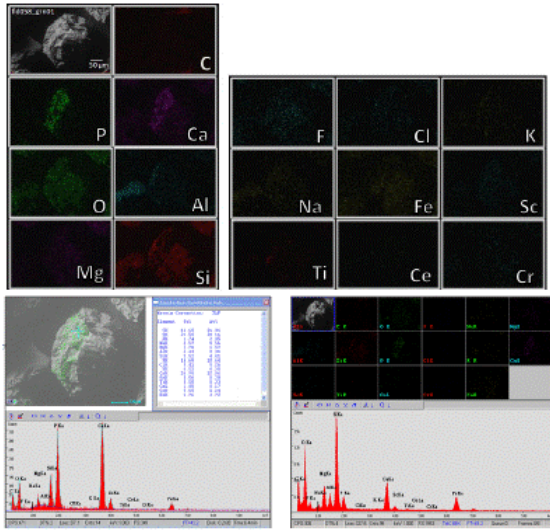
Z124-134: fld056_grn02, 150-250 μm



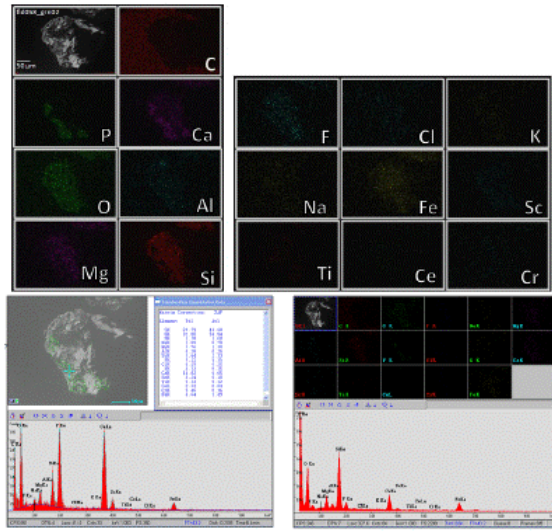
Z124-134: fld057_grn01, 150-250 μm



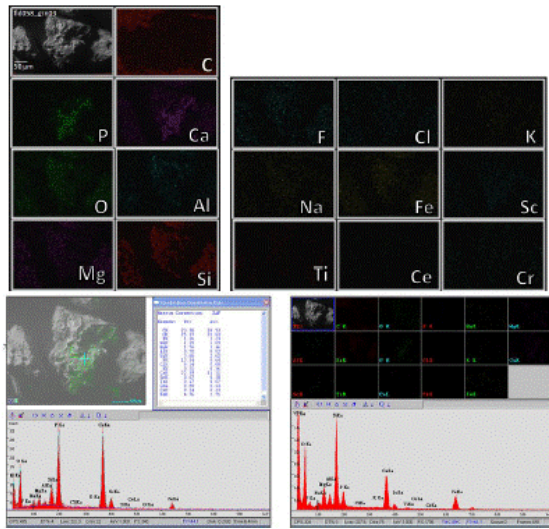
Z124-134: fld058_grn01, 150-250 μm



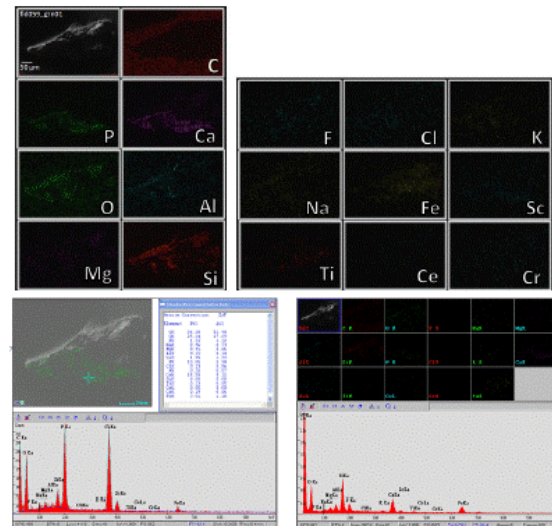
Z124-134: fld058_grn02, 150-250 μm



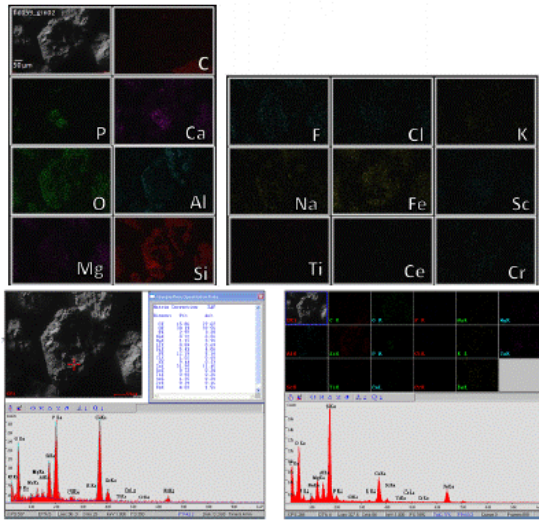
Z124-134: fld058_grn03, 150-250 μm



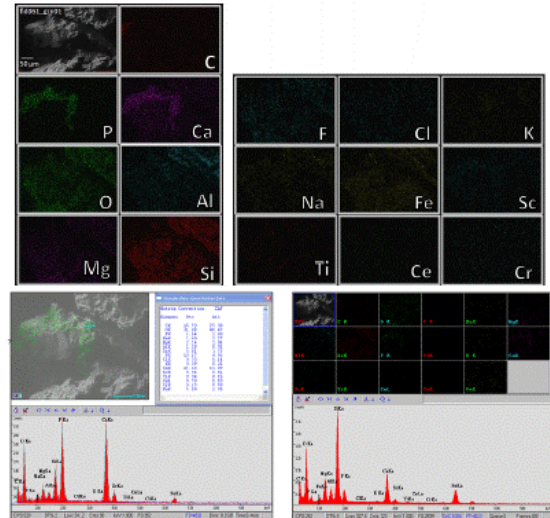
Z124-134: fld059_grn01, 150-250 μm



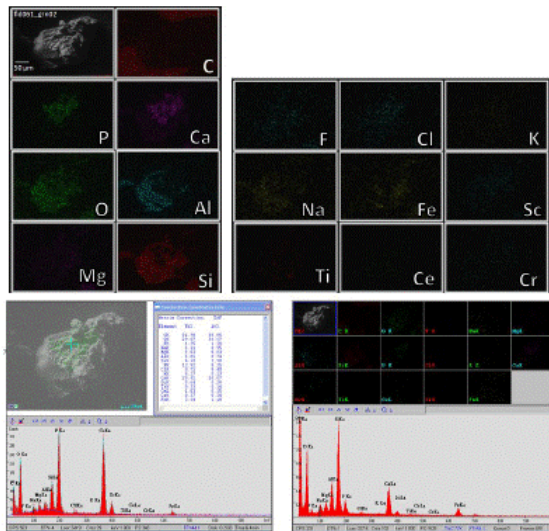
Z124-134: fld059_grn02, 150-250 μm



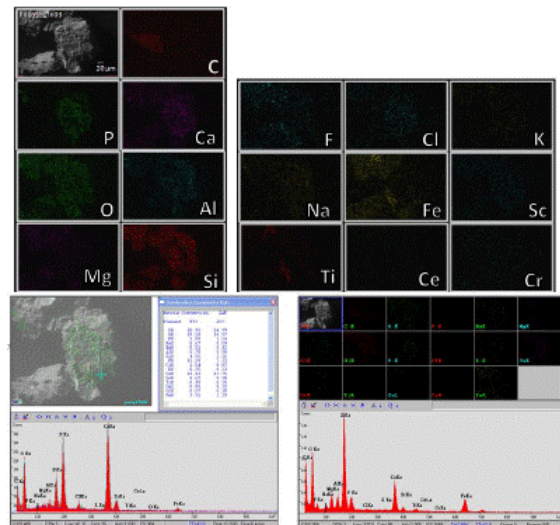
Z124-134: fld061_grn01, 150-250 μm



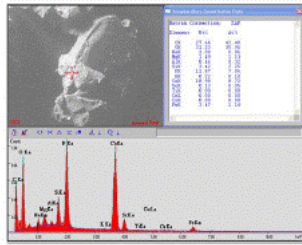
Z124-134: fld061_grn02, 150-250 μm



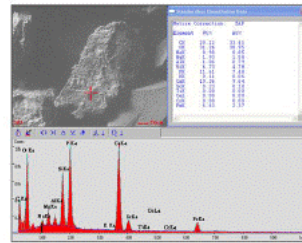
Z124-134: fld061_grn03, 150-250 μm



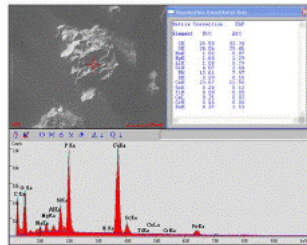
ZAG01: Zag0011_grn01, 125-150 μm



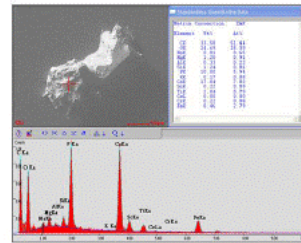
ZAG01: Zag0023_grn02, 125-150 μm



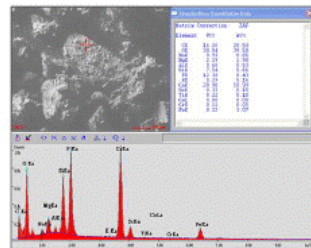
ZAG01: Zag0022_grn01, 125-150 μm



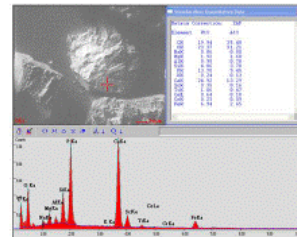
ZAG01: Zag0026_grn01, 125-150 μm



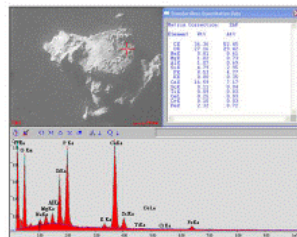
ZAG01: Zag0038_grn02, 125-150 μm



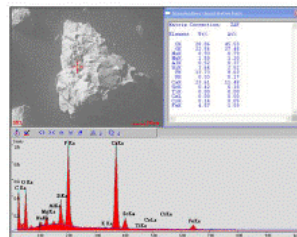
ZAG234: Zag0041_grn01, 125-150 μm



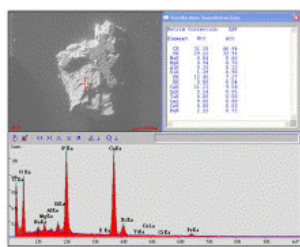
ZAG234: Zag0040_grn01, 125-150 μm



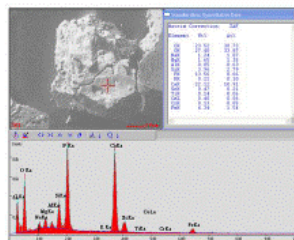
ZAG234: Zag0042_grn01, 125-150 μm



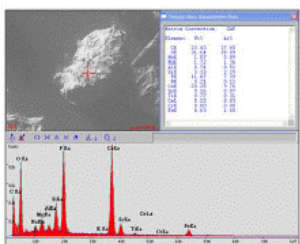
ZAG234: Zag0046_grn01, 125-150 μm



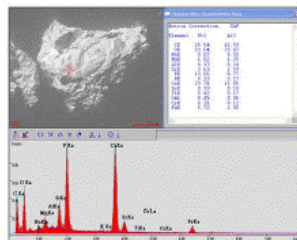
ZAG234: Zag0047_grn02, 125-150 μm



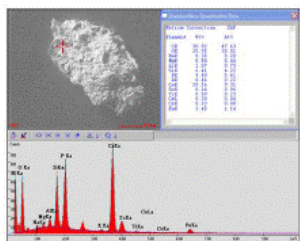
ZAG234: Zag0047_grn01, 125-150 μm



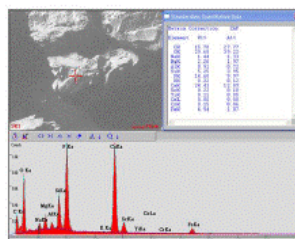
ZAG234: Zag0047_grn03, 125-150 μm



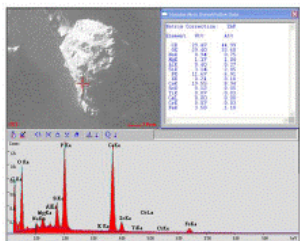
ZAG234: Zag0047_grn04, 125-150 μm



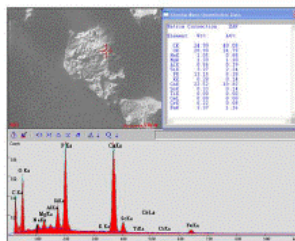
ZAG234: Zag0052_grn01, 125-150 μm



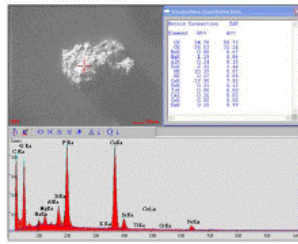
ZAG234: Zag0049_grn01, 125-150 μm



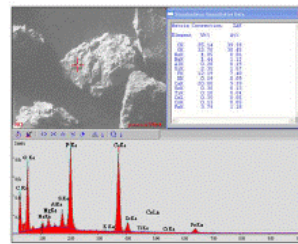
ZAG234: Zag0059_grn01, 125-150 μm



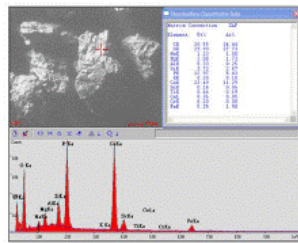
ZAG234: Zag0059_grn02, 125-150 μm



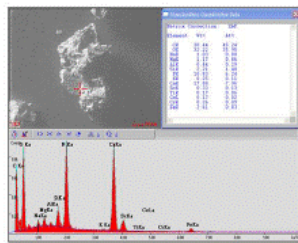
ZAG234: Zag0060_grn01, 125-150 μm



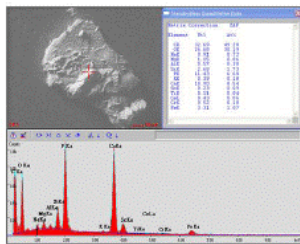
ZAG234: Zag0059_grn03, 125-150 μm



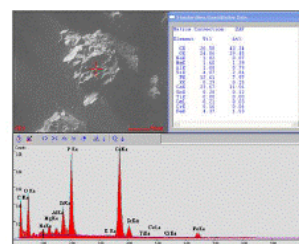
ZAG234: Zag0060_grn02, 125-150 μm



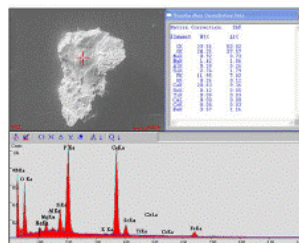
ZAG05: Zag0004_grn01, 125-150 μm



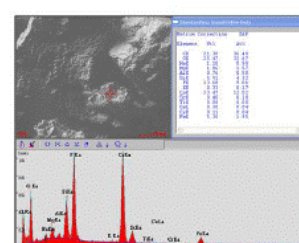
ZAG05: Zag0022_grn01, 125-150 μm



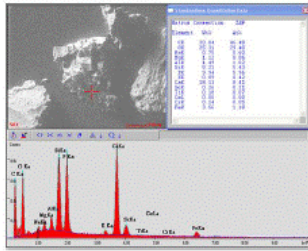
ZAG05: Zag0011_grn02, 125-150 μm



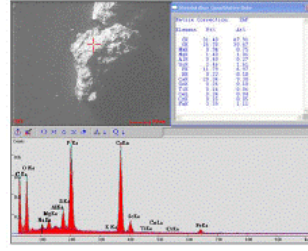
ZAG05: Zag0022_grn02, 125-150 μm



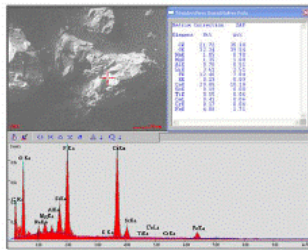
ZAG05: Zag0065_grn01, 125-150 μm



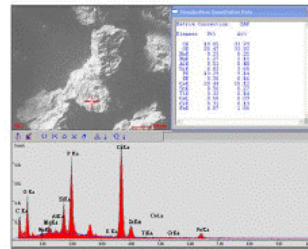
ZAG05: Zag0070_grn01, 125-150 μm



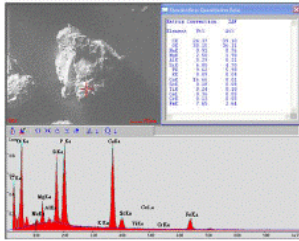
ZAG05: Zag0069_grn01, 125-150 μm



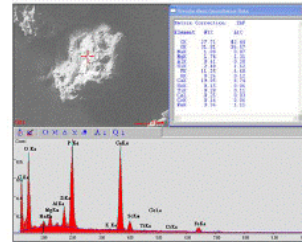
ZAG05: Zag0083_grn01, 125-150 μm



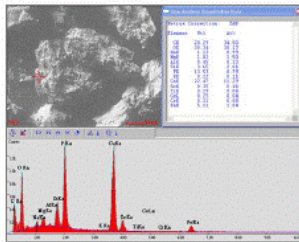
ZAG05: Zag0083_grn02, 125-150 μm



ZAG05: Zag0100_grn01, 125-150 μm



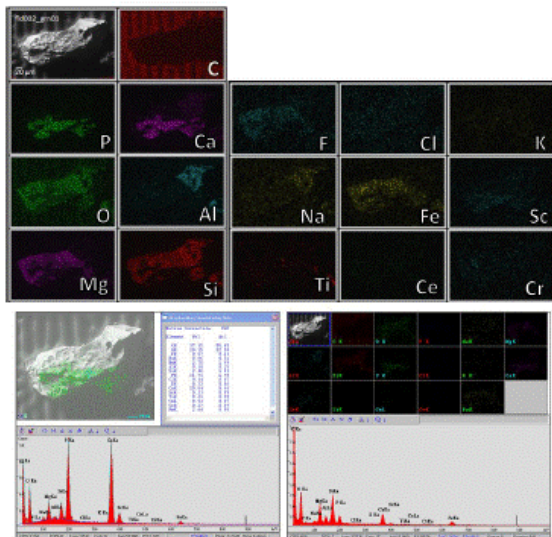
ZAG05: Zag0093_grn01, 125-150 μm



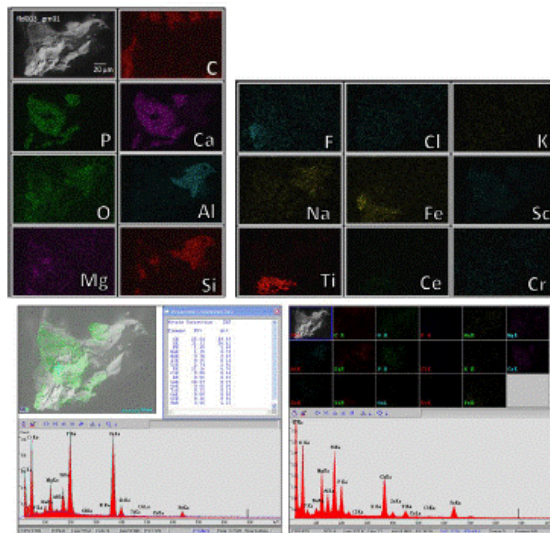
APPENDIX B

SEM CHEMICAL MAPS FOR ALHA77005 PHOSPHATE AGGREGATES

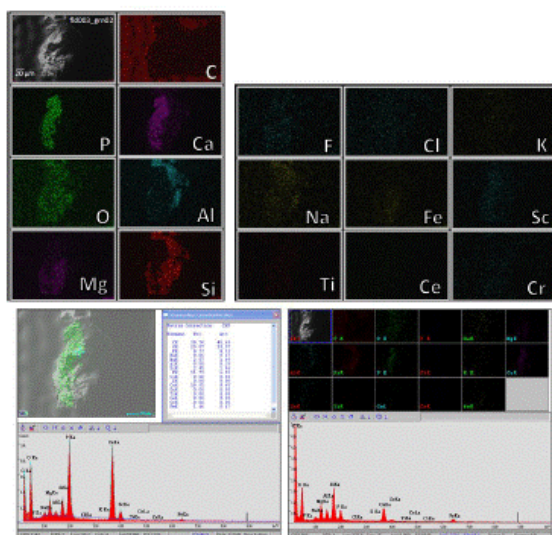
A01-20: fld002_grn01, 63-150 μm



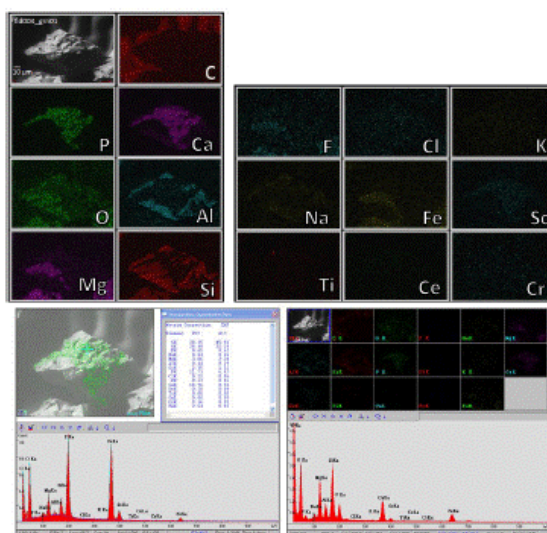
A01-20: fld003_grn01, 63-150 μm



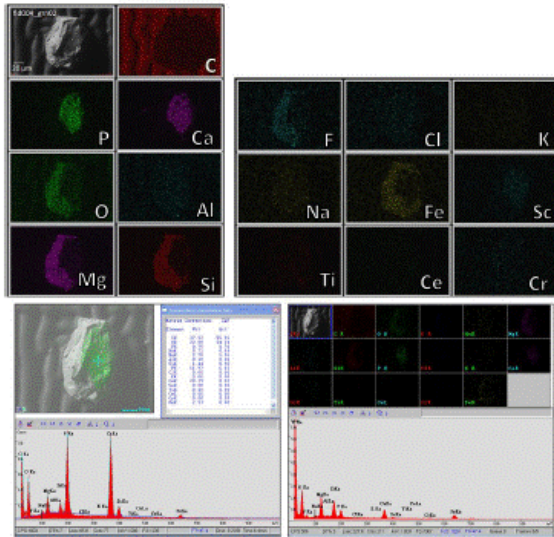
A01-20: fld003_grn02, 63-150 μm



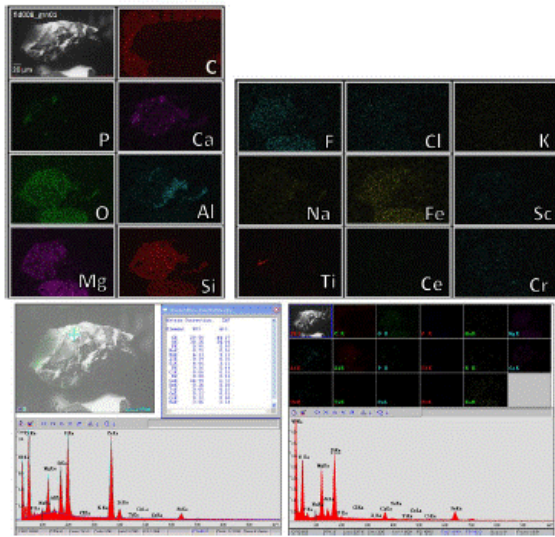
A01-20: fld004_grn01, 63-150 μm



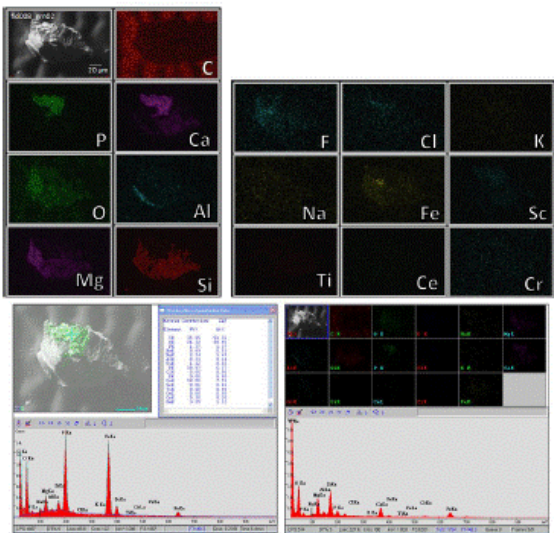
A01-20: fld004_grn02, 63-150 μm



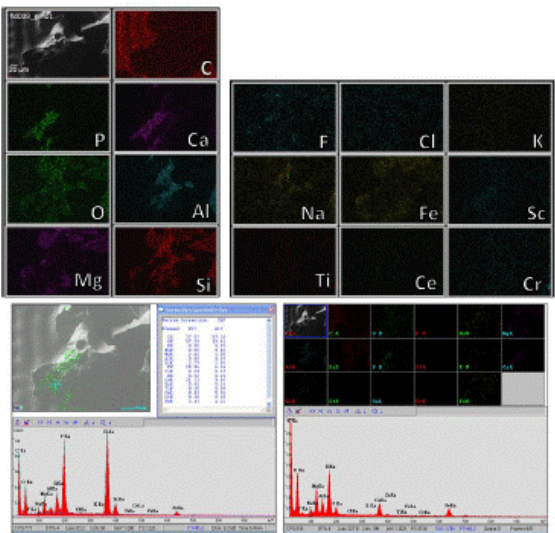
A01-20: fld008_grn01, 63-150 μm



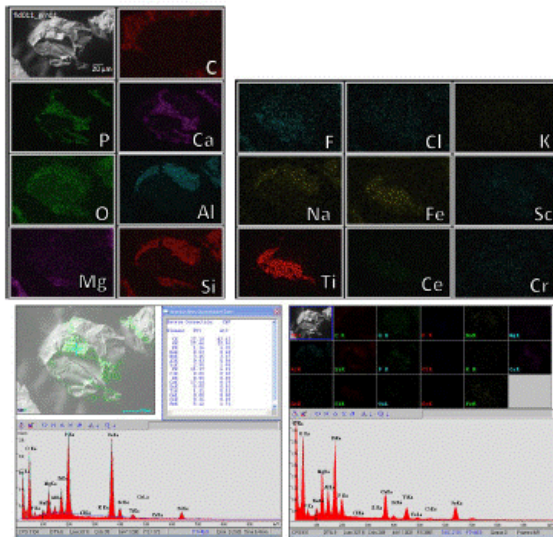
A01-20: fld008_grn02, 63-150 μm



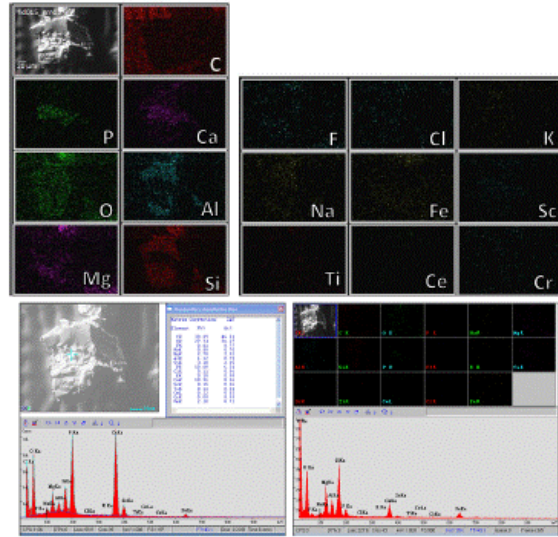
A01-20: fld009_grn01, 63-150 μm



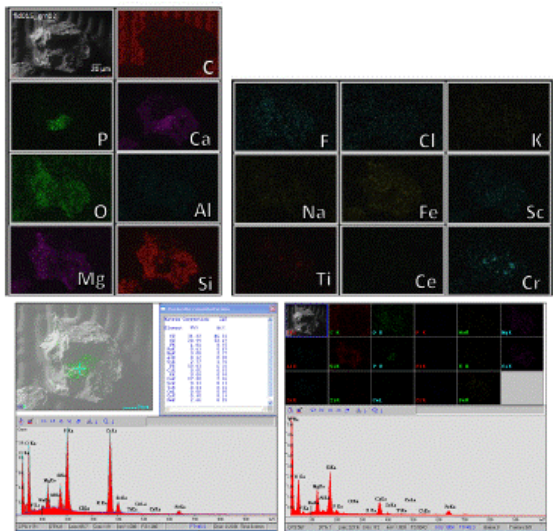
A01-20: fld011_grn01, 63-150 μm



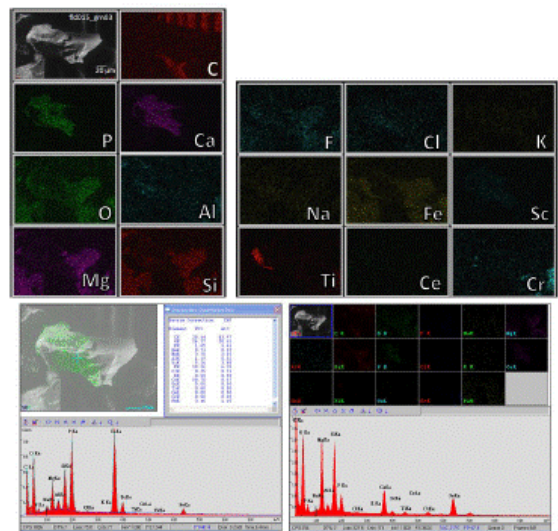
A01-20: fld015_grn01, 63-150 μm



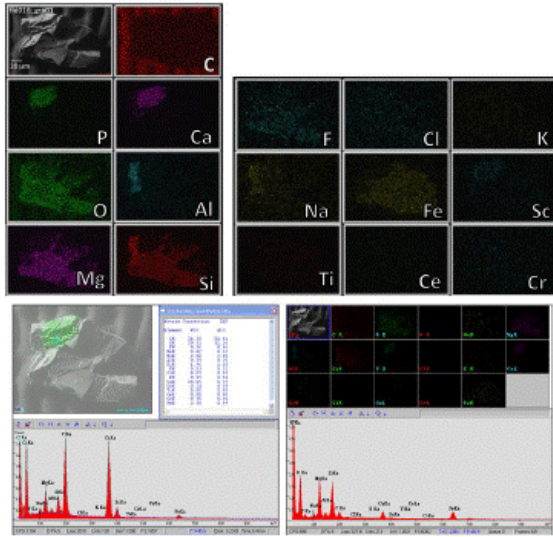
A01-20: fld015_grn02, 63-150 μm



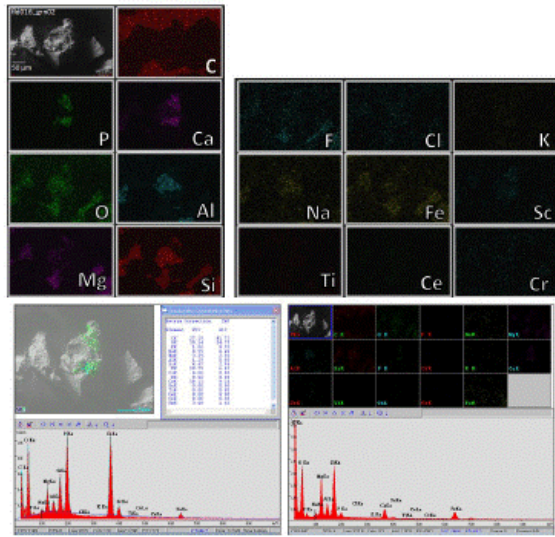
A01-20: fld015_grn03, 63-150 μm



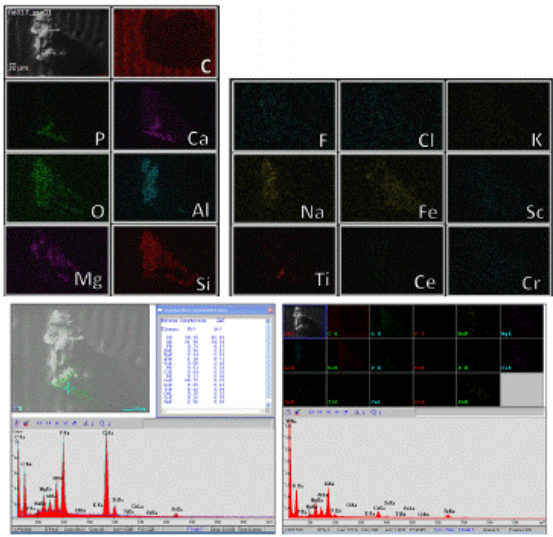
A01-20: fld016_grn01, 63-150 μm



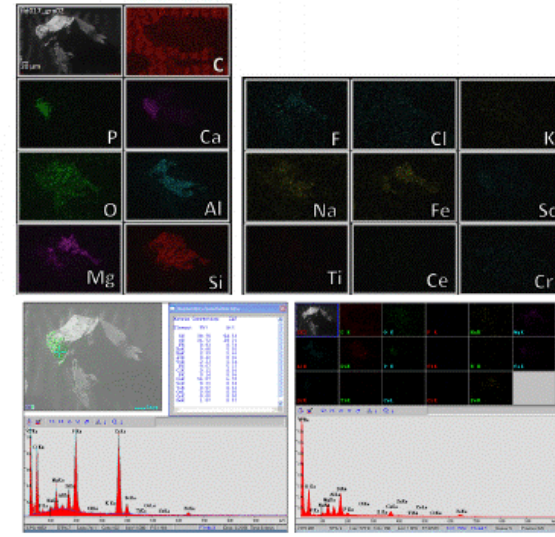
A01-20: fld016_grn02, 63-150 μm



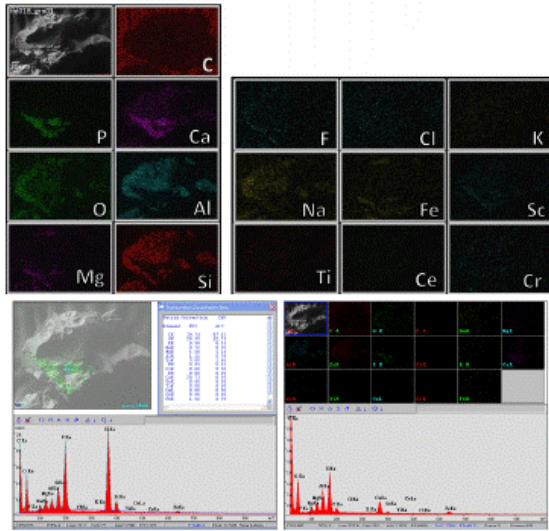
A01-20: fld017_grn01, 63-150 μm



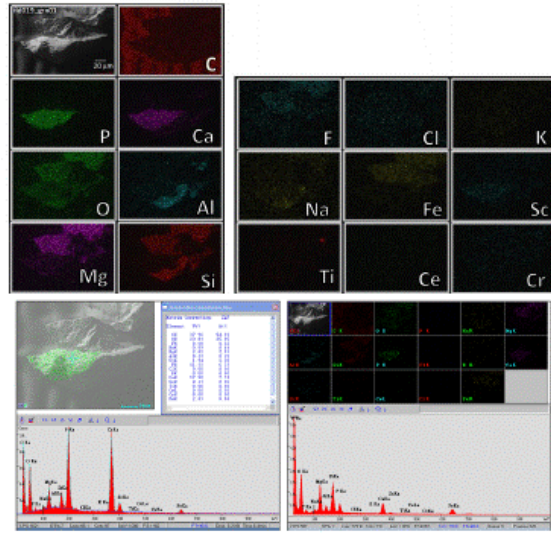
A01-20: fld017_grn02, 63-150 μm



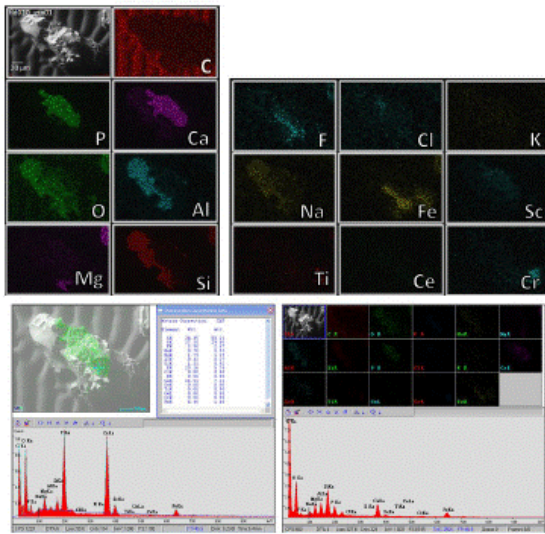
A01-20: fld018_grn01, 63-150 μm



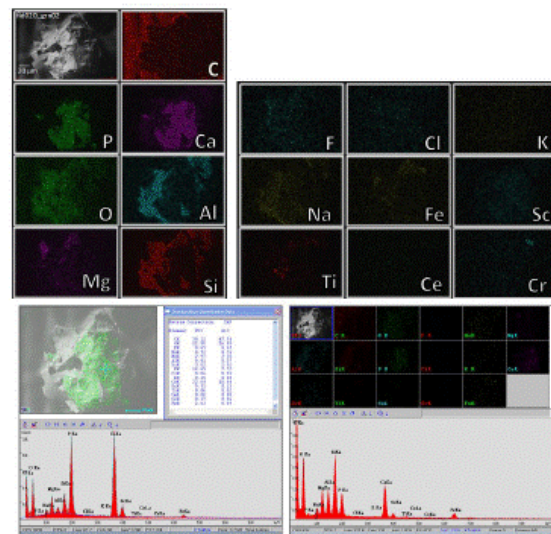
A01-20: fld019_grn01, 63-150 μm



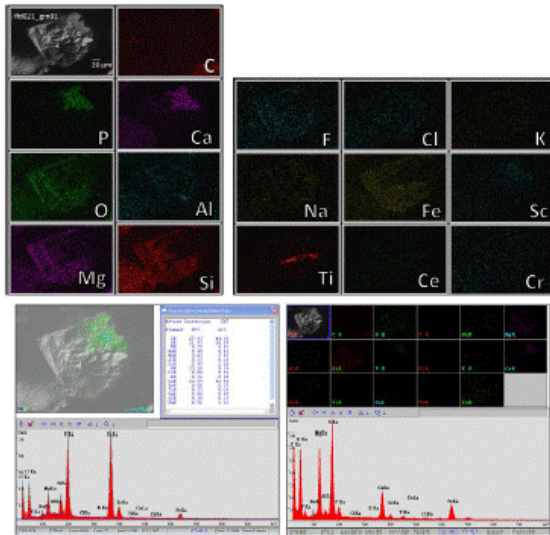
A01-20: fld020_grn01, 63-150 μm



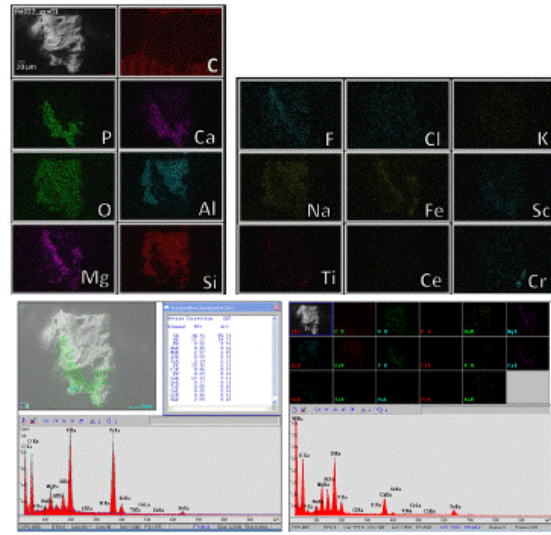
A01-20: fld020_grn02, 63-150 μm



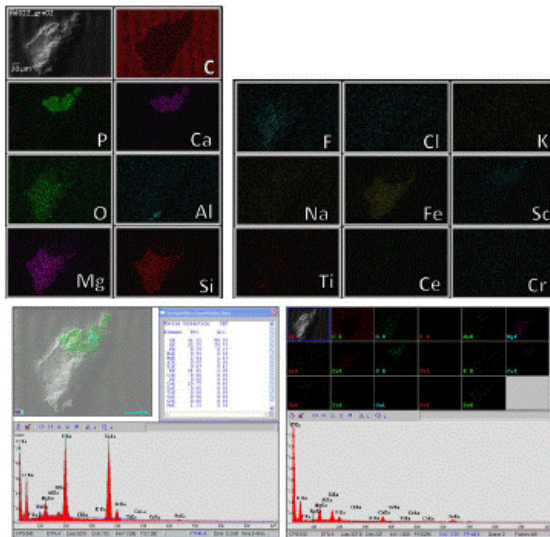
A21-40: fld021_grn01, 63-150 μm



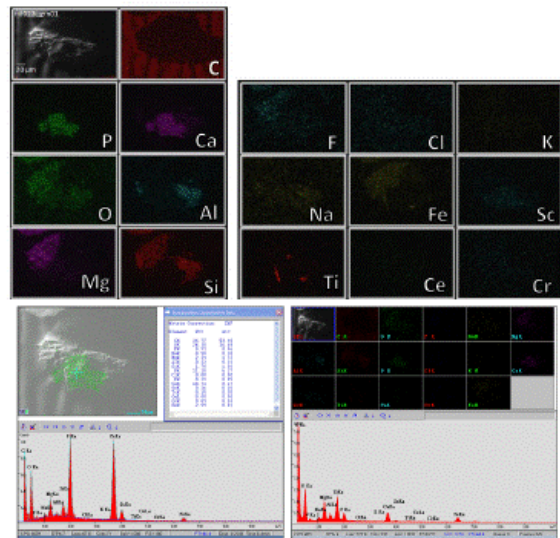
A21-40: fld022_grn01, 63-150 μm



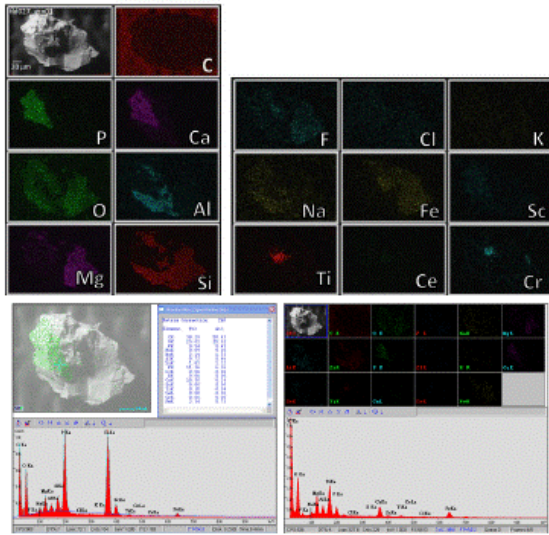
A21-40: fld022_grn02, 63-150 μm



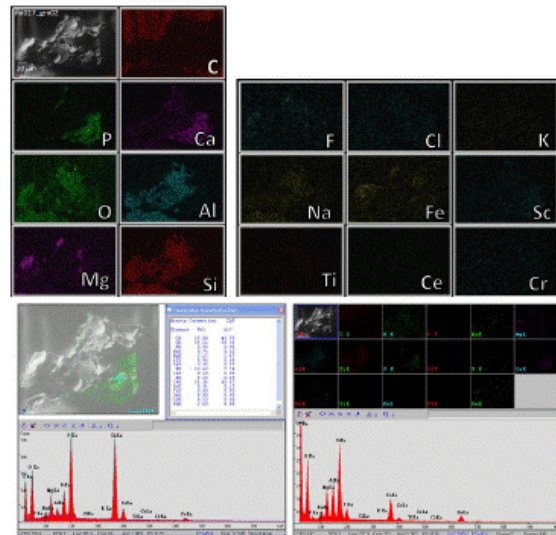
A21-40: fld023_grn01, 63-150 μm



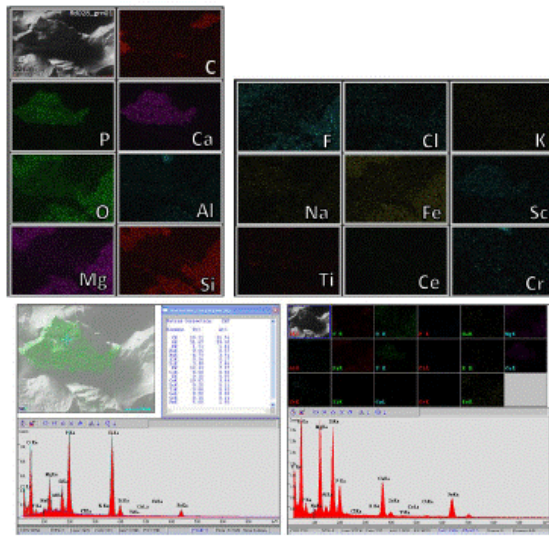
A21-40: fld027_grn01, 63-150 μm



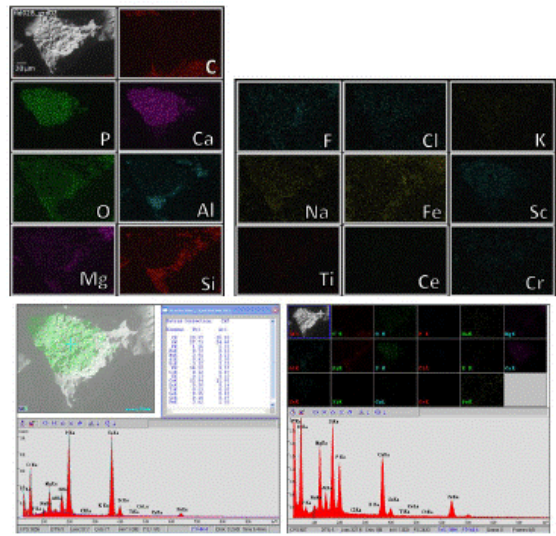
A21-40: fld027_grn02, 63-150 μm



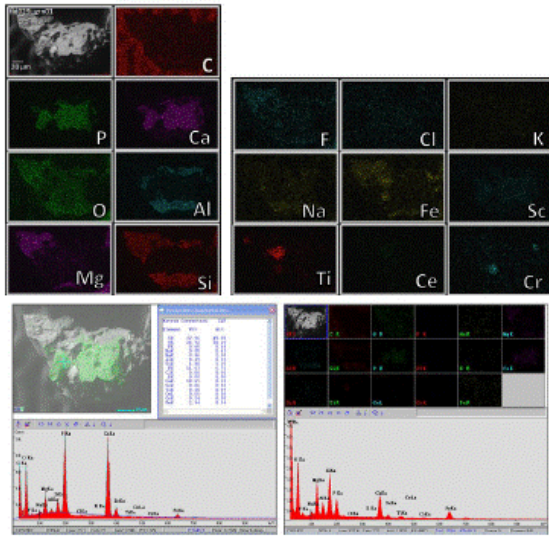
A21-40: fld028_grn01, 63-150 μm



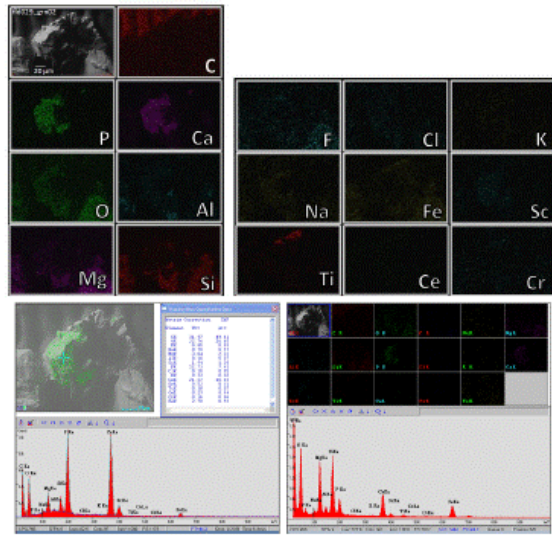
A21-40: fld028_grn02, 63-150 μm



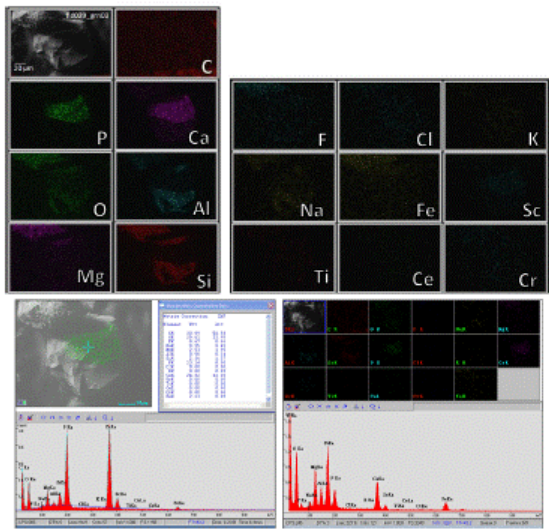
A21-40: fld029_grn01, 63-150 μm



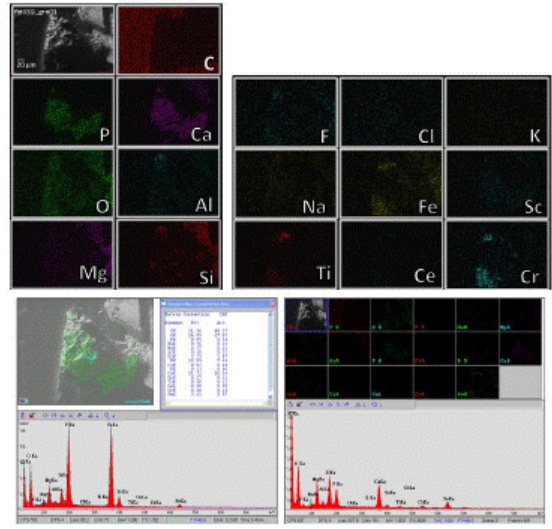
A21-40: fld029_grn02, 63-150 μm



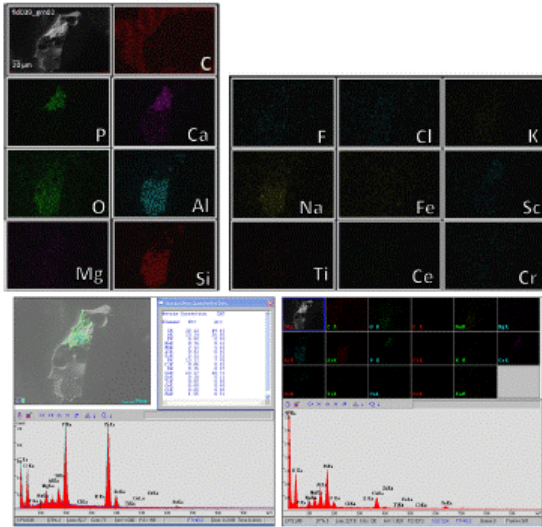
A21-40: fld029_grn03, 63-150 μm



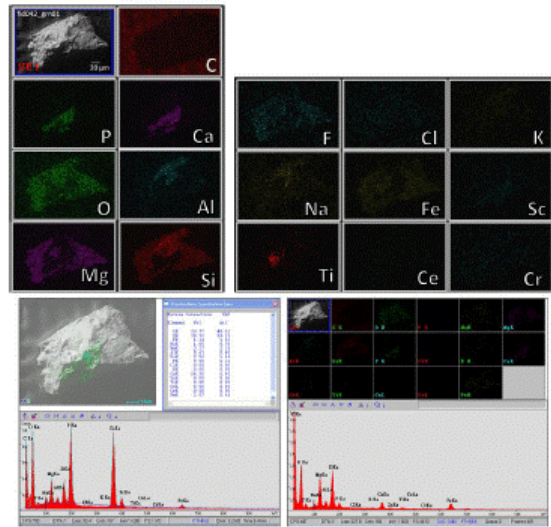
A21-40: fld039_grn01, 63-150 μm



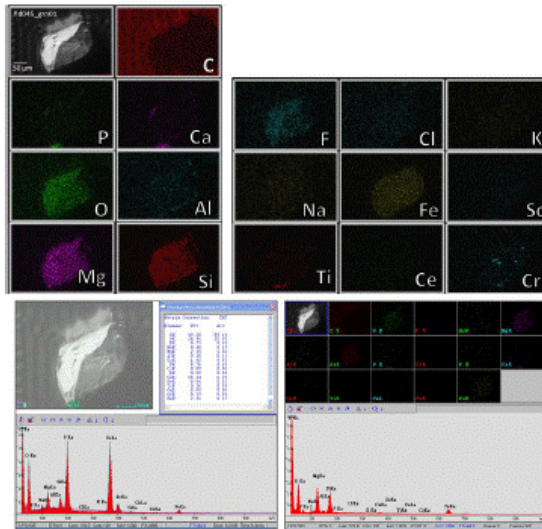
A21-40: fld039_grn02, 63-150 μm



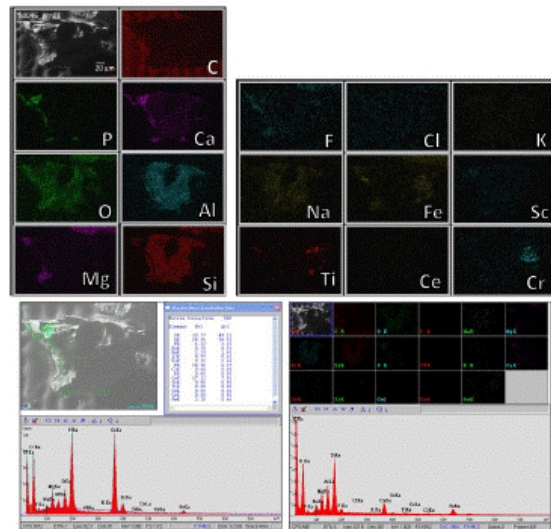
A21-40: fld042_grn01, 63-150 μm



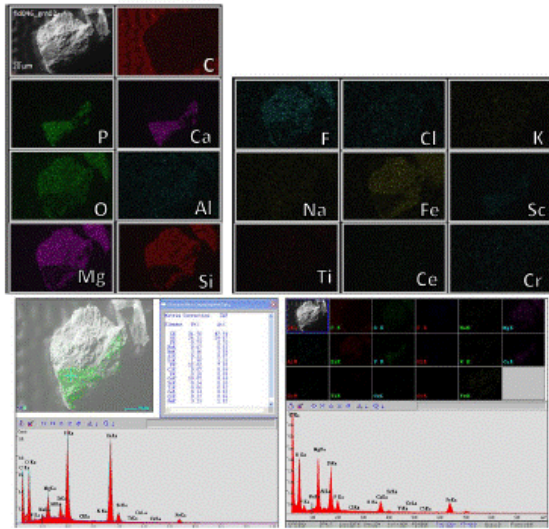
A21-40: fld045_grn01, 63-150 μm



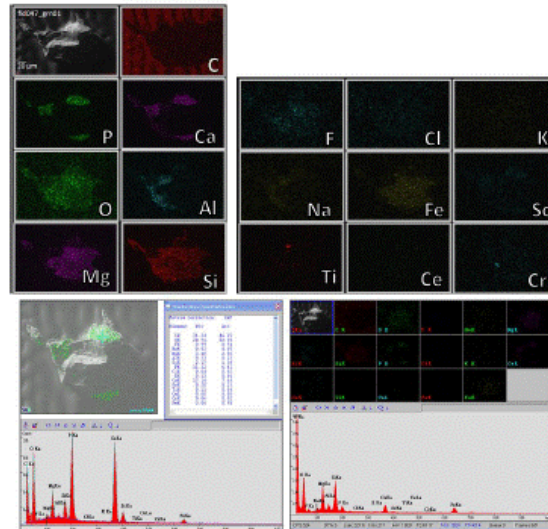
A21-40: fld046_grn01, 63-150 μm



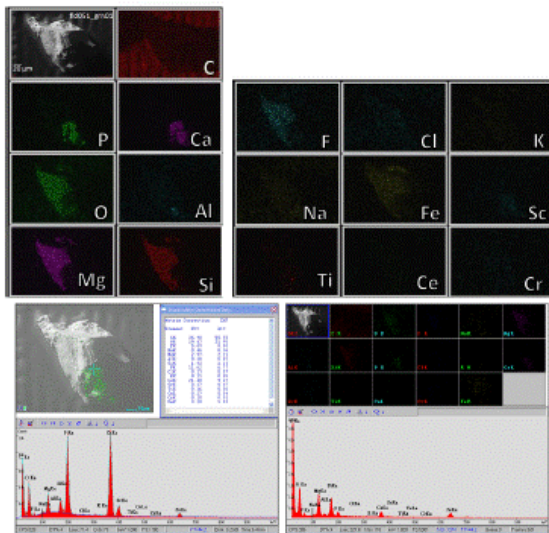
A21-40: fld046_grn02, 63-150 μm



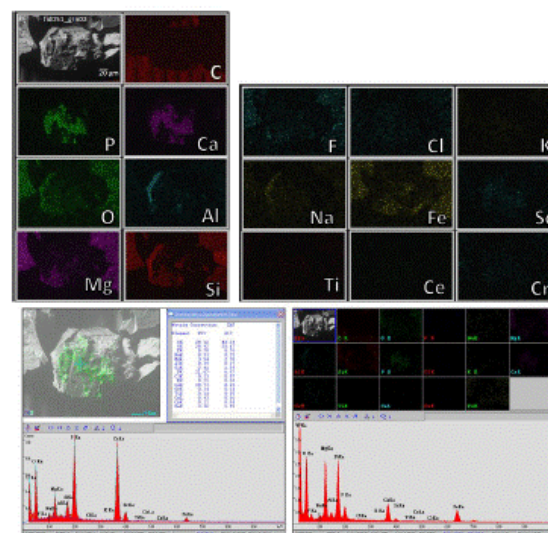
A21-40: fld047_grn01, 63-150 μm



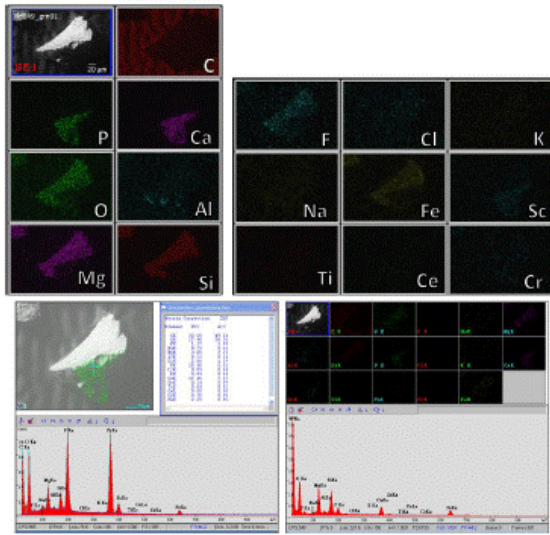
A21-40: fld051_grn01, 63-150 μm



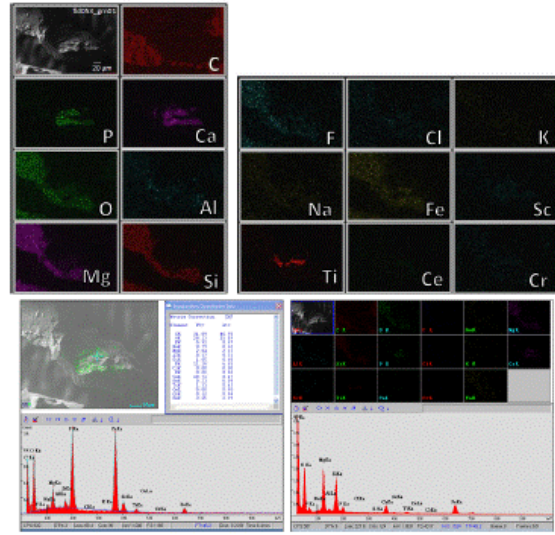
A21-40: fld051_grn02, 63-150 μm



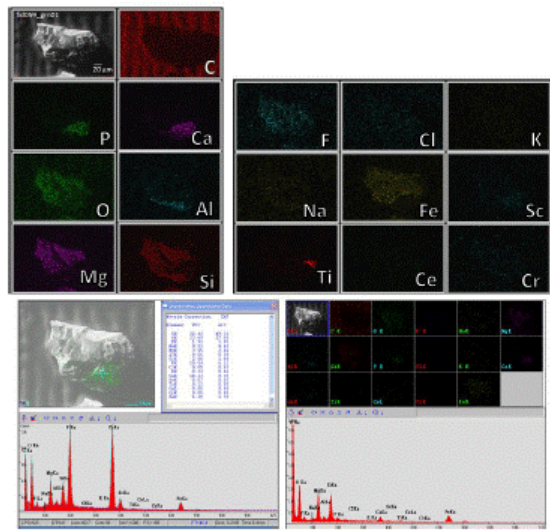
A41-56: fld049_grn01, 63-150 μm



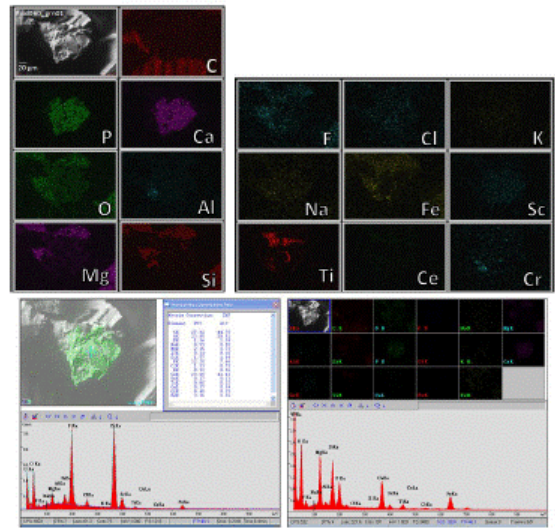
A41-56: fld053_grn01, 63-150 μm



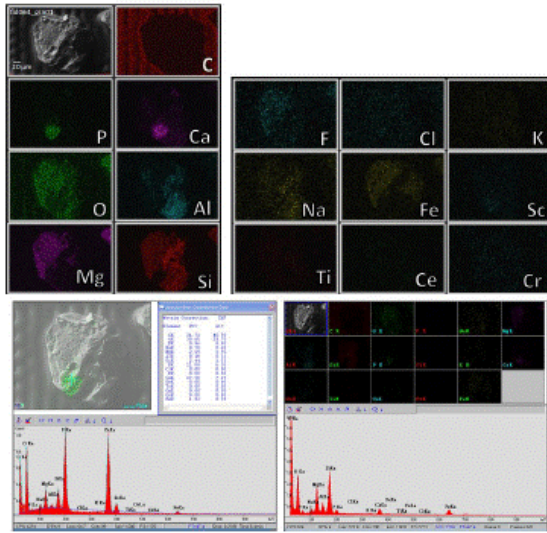
A41-56: fld059_grn01, 63-150 μm



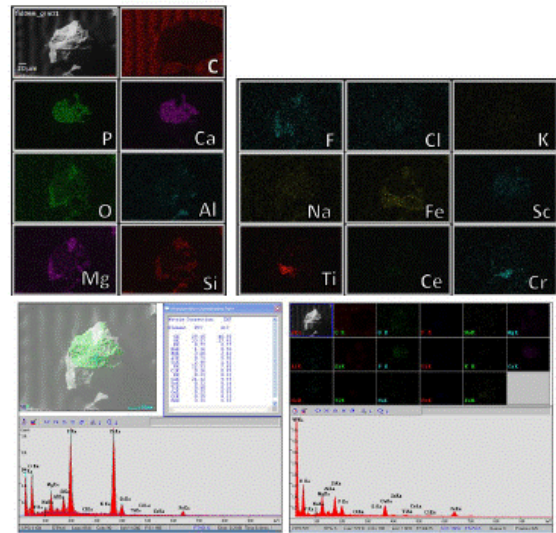
A41-56: fld060_grn01, 63-150 μm



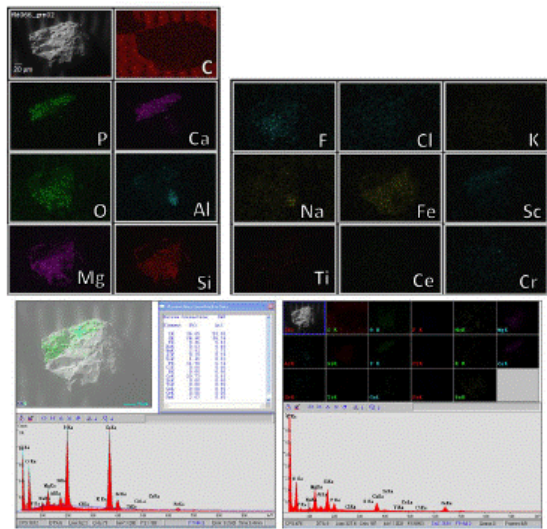
A41-56: fld064_grn01, 63-150 μm



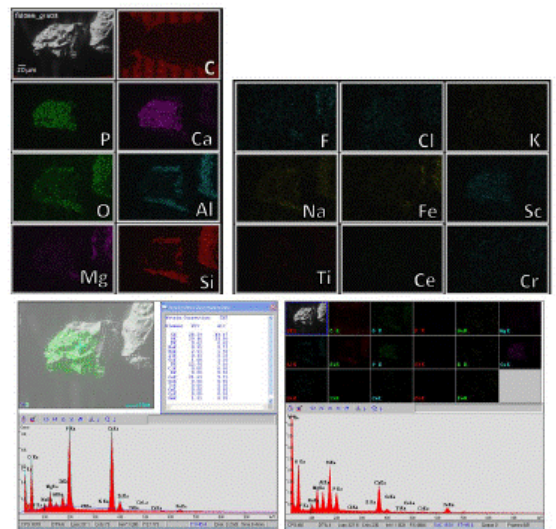
A41-56: fld066_grn01, 63-150 μm



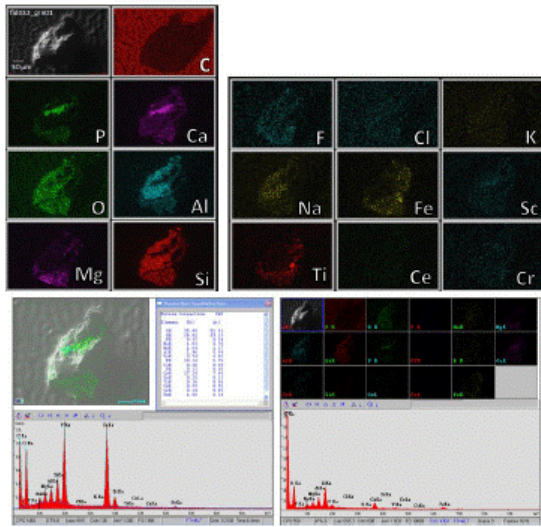
A41-56: fld066_grn02, 63-150 μm



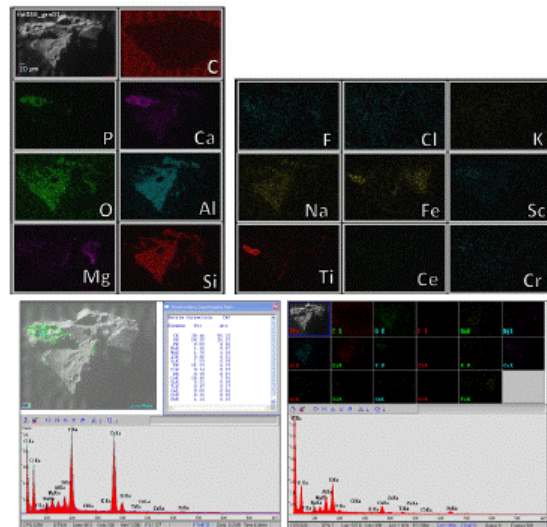
A41-56: fld066_grn03, 63-150 μm



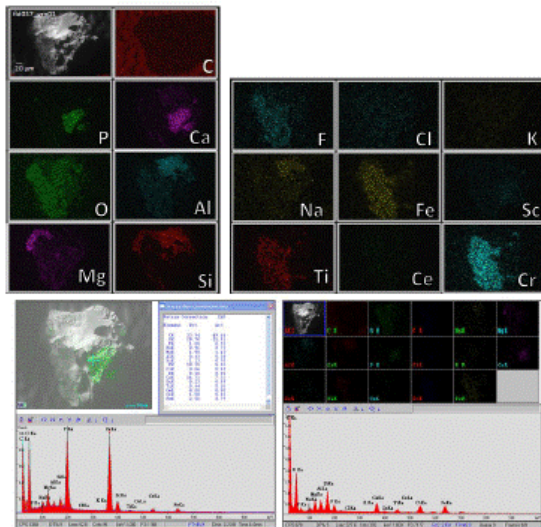
A41-56: fld032_grn01, >180 μm



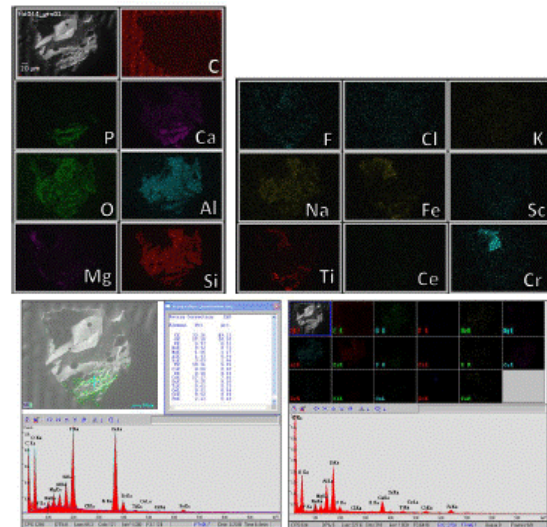
A41-56: fld036_grn01, >180 μm



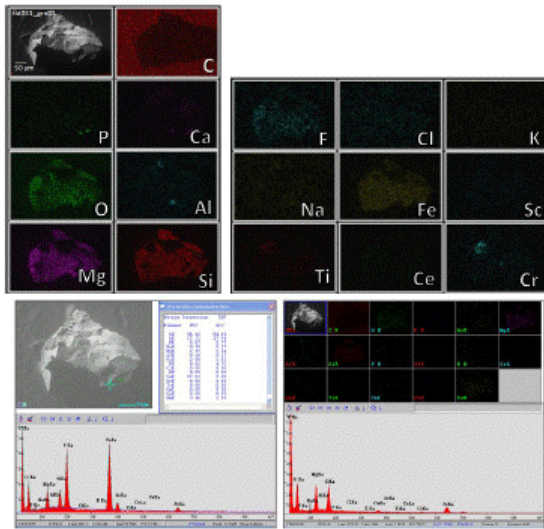
A41-56: fld037_grn01, >180 μm



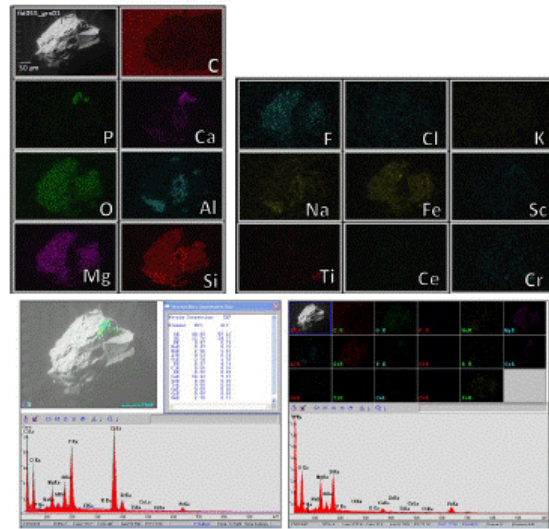
A41-56: fld044_grn01, >180 μm



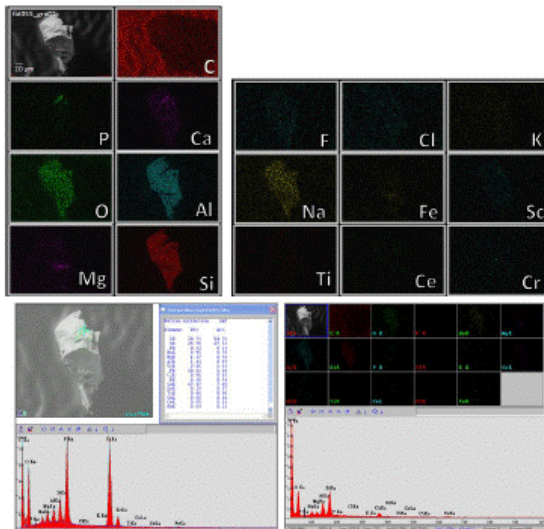
A41-56: fld051_grn01, >180 μm



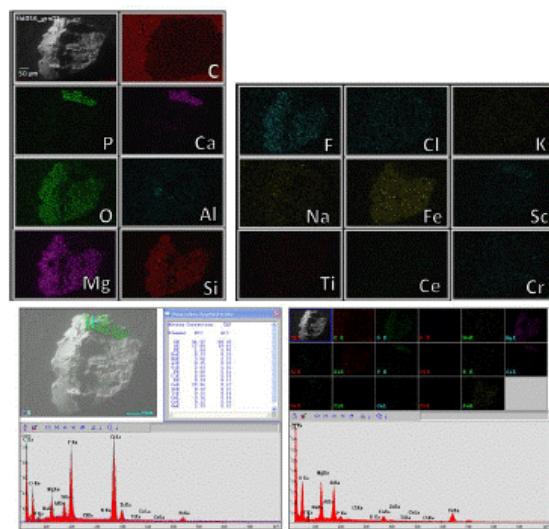
A41-56: fld055_grn01, >180 μm



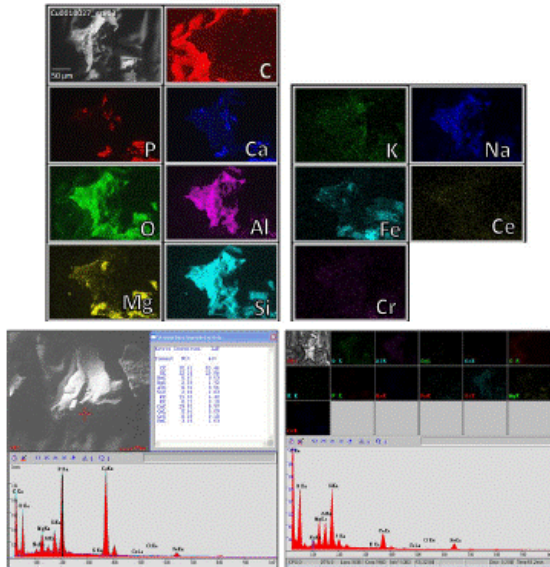
A41-56: fld055_grn02, >180 μm



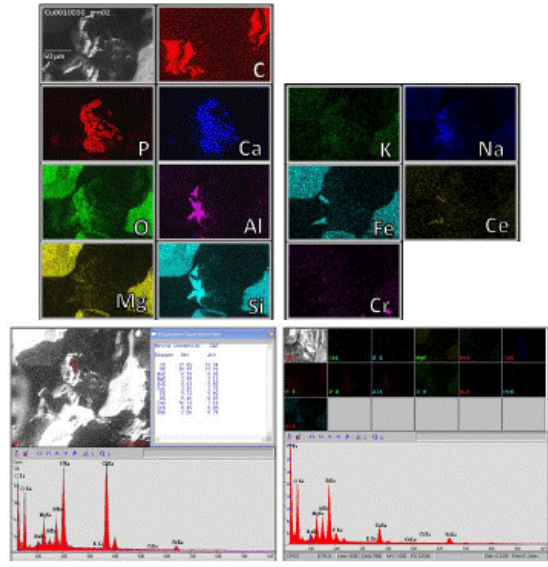
A41-56: fld056_grn01, >180 μm



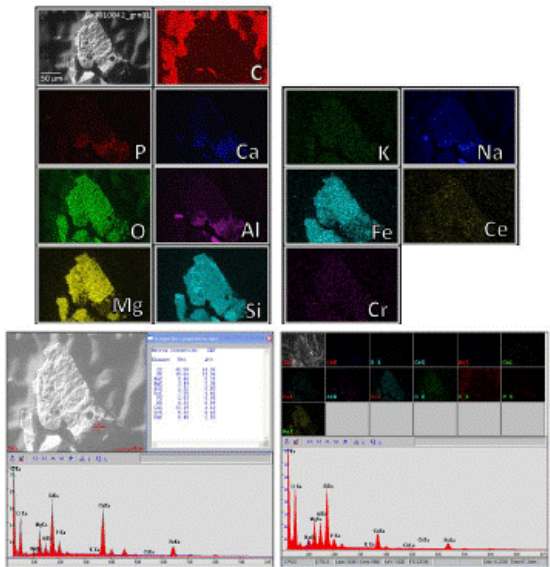
AHp123: Cu0010027_grn03, 63-150 μm



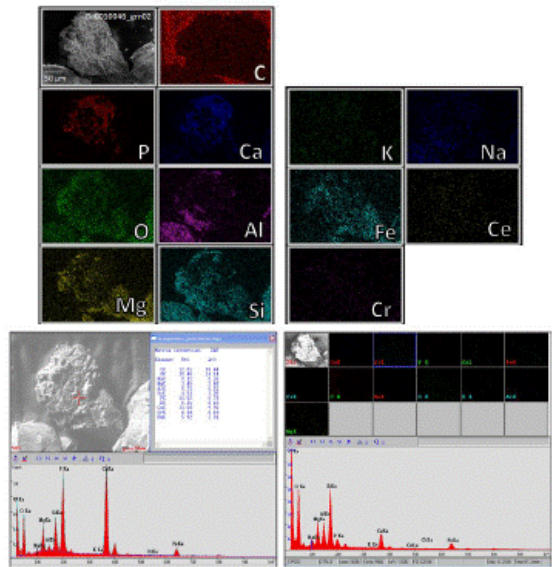
AHp123: Cu0010030_grn02, 63-150 μm



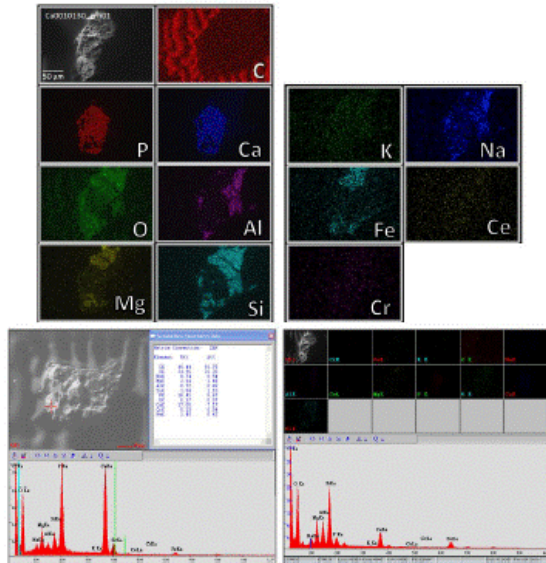
AHp123: Cu0010042_grn01, 63-150 μm



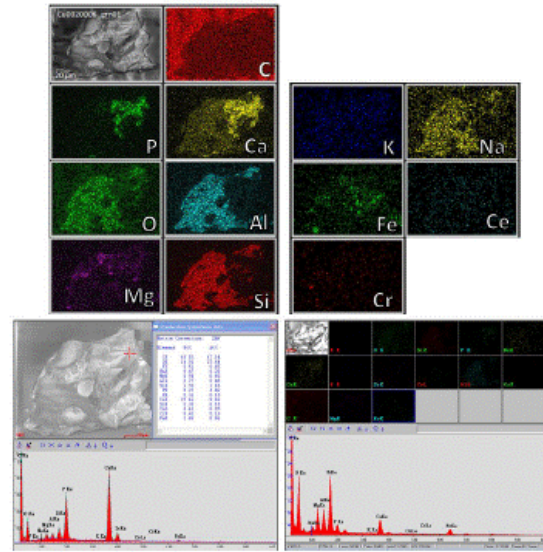
AHp123: Cu0010046_grn02, 63-150 μm



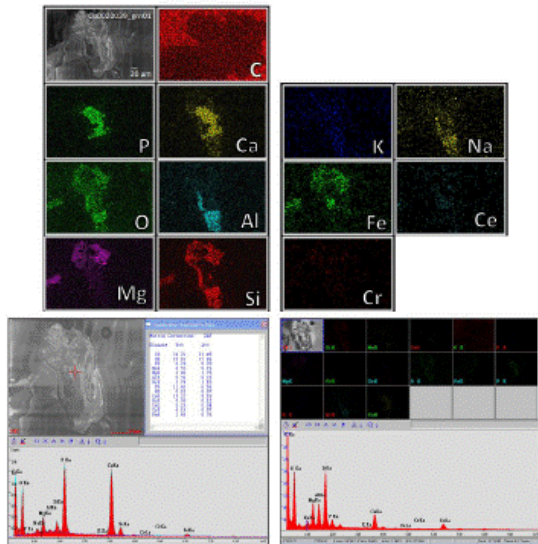
AHp123: Cu0010130_grn01, 63-150 μm



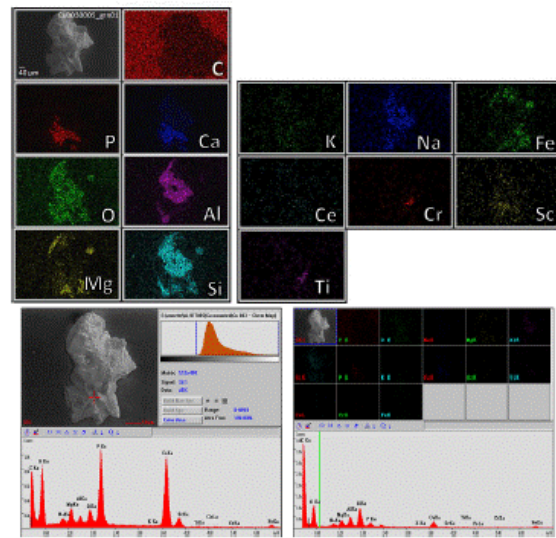
AHp123: Cu0020006_grn01, 150-180 μm



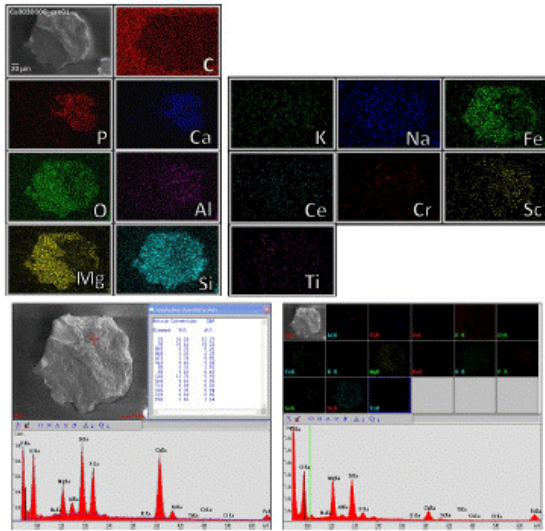
AHp123: Cu0020039_grn01, 150-180 μm



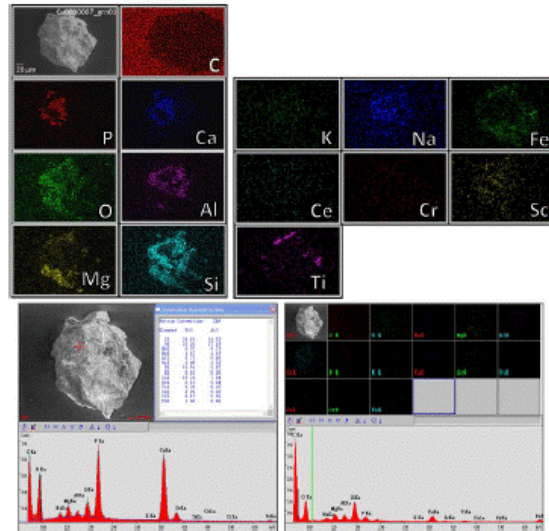
AHp123: Cu0030005_grn01, 150-180 μm



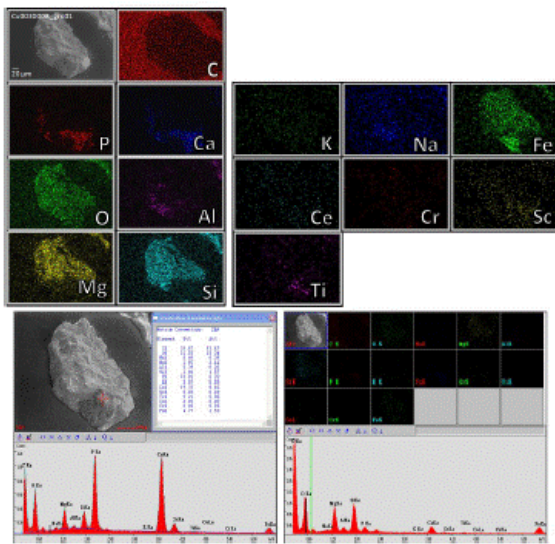
AHp123: Cu0030006_grn01, 150-180 μm



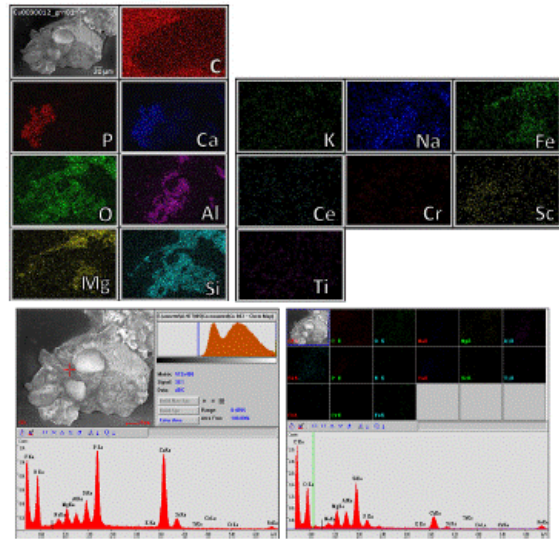
AHp123: Cu0030007_grn01, 150-180 μm



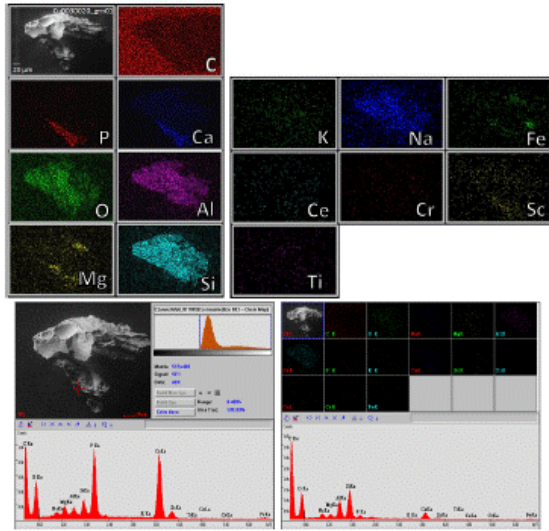
AHp123: Cu0030008_grn01, 150-180 μm



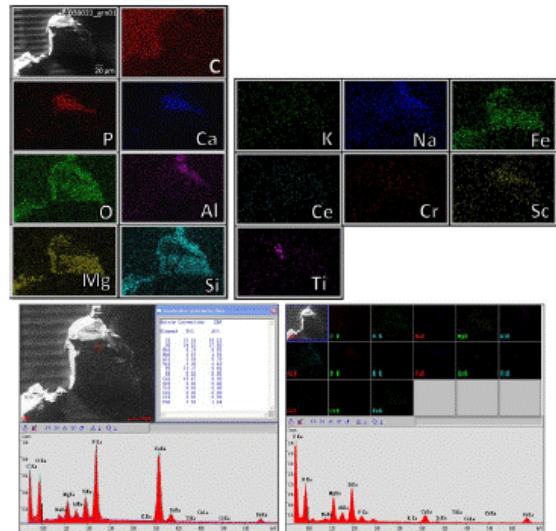
AHp123: Cu0030012_grn01, 150-180 μm



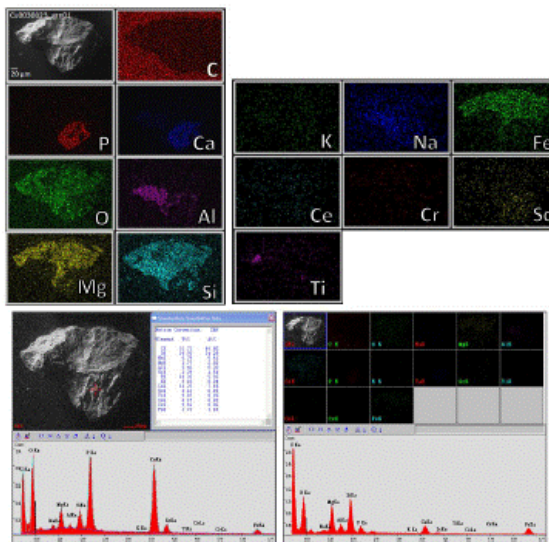
AHp123: Cu0030020_grn01, 150-180 μm



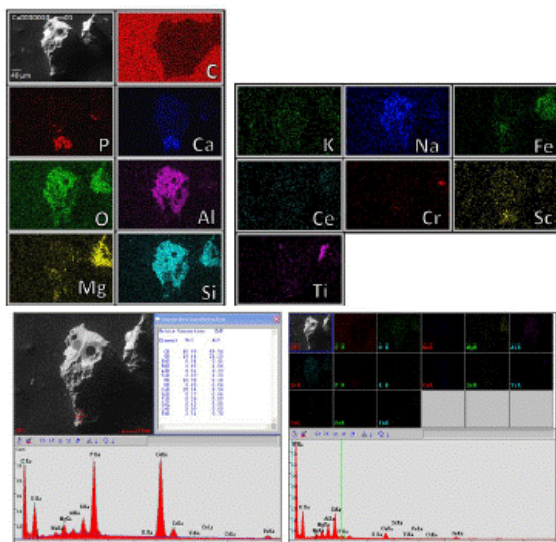
AHp123: Cu0030022_grn01, 150-180 μm



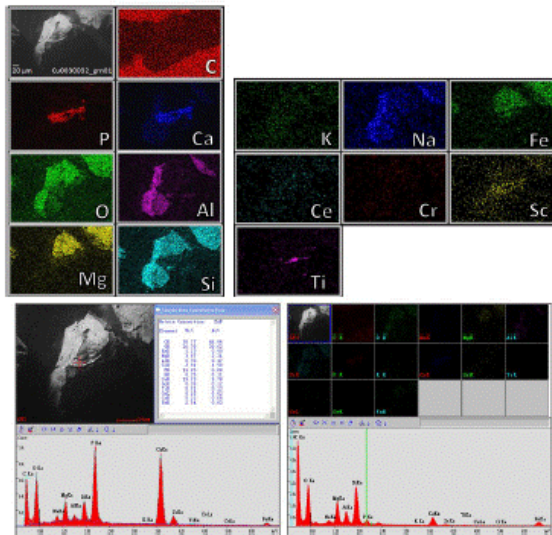
AHp123: Cu0030023_grn01, 150-180 μm



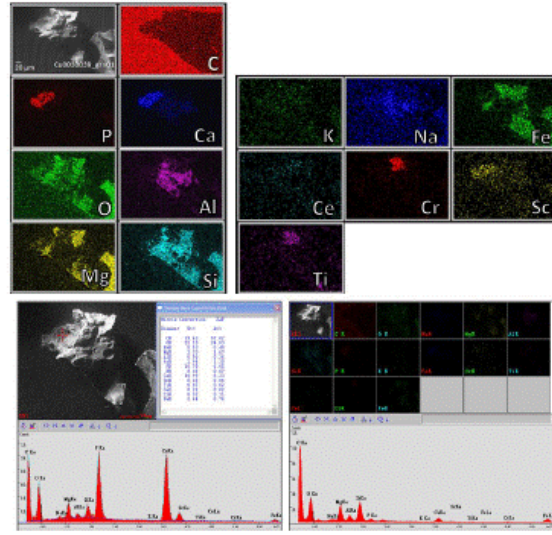
AHp45: Cu0030030_grn01, 150-180 μm



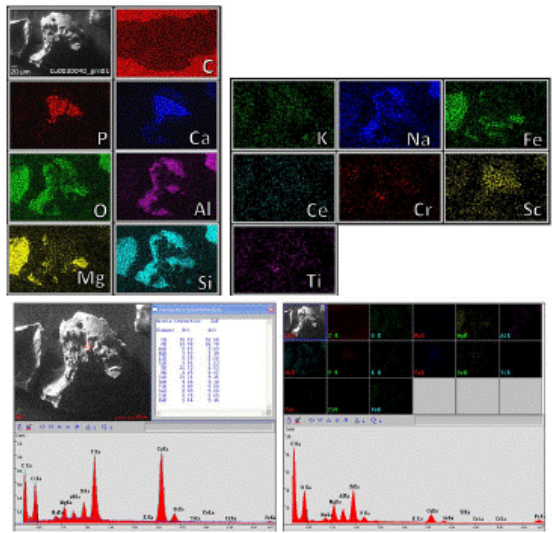
AHp45: Cu0030032_grn01, 150-180 μm



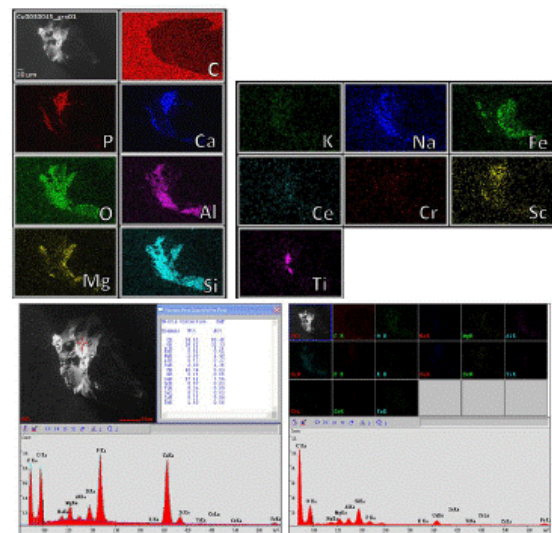
AHp45: Cu0030039_grn01, 150-180 μm



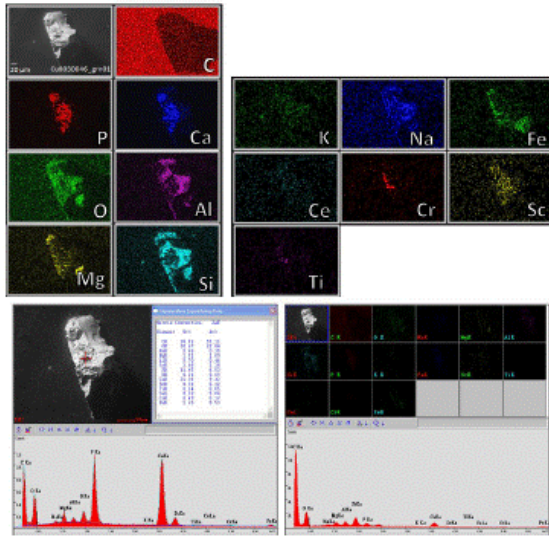
AHp45: Cu0030040_grn01, 150-180 μm



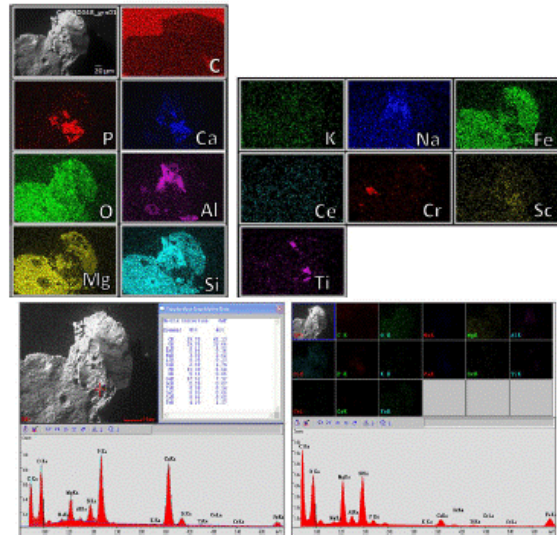
AHp45: Cu0030045_grn01, 150-180 μm



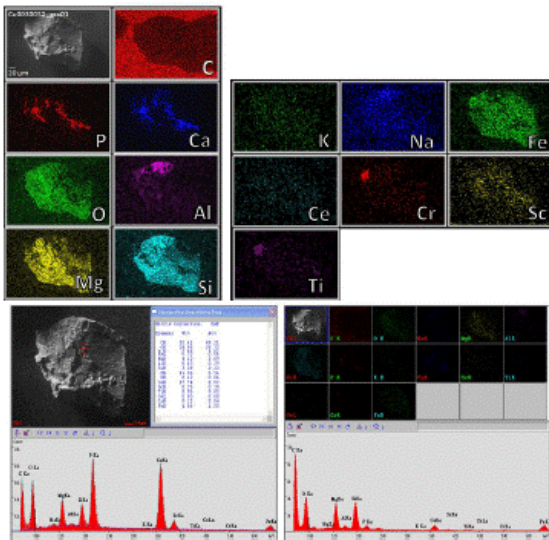
AHp45: Cu0030046_grn01, 150-180 μm



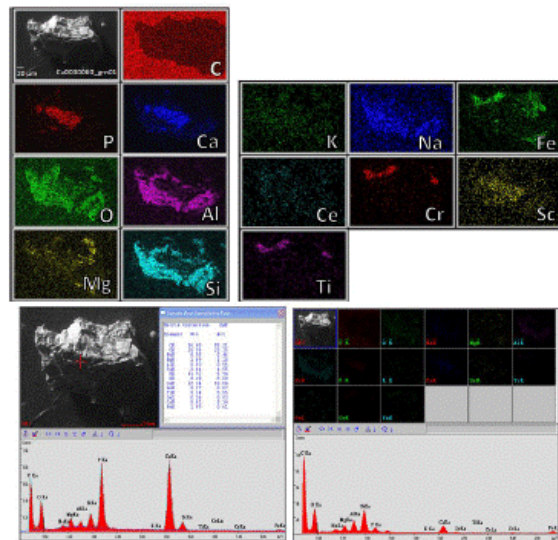
AHp45: Cu0030048_grn01, 150-180 μm



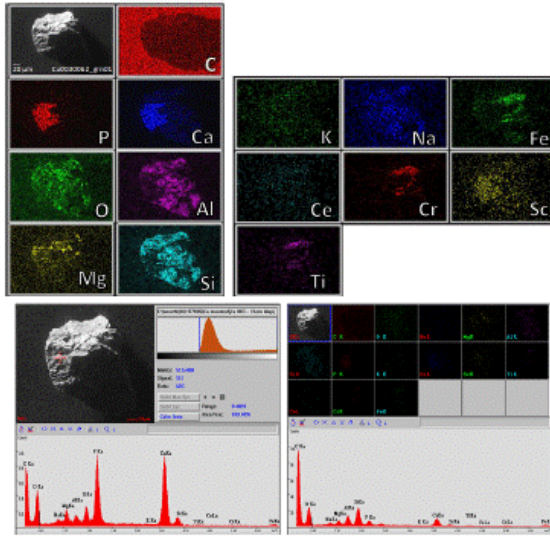
AHp45: Cu0030052_grn01, 150-180 μm



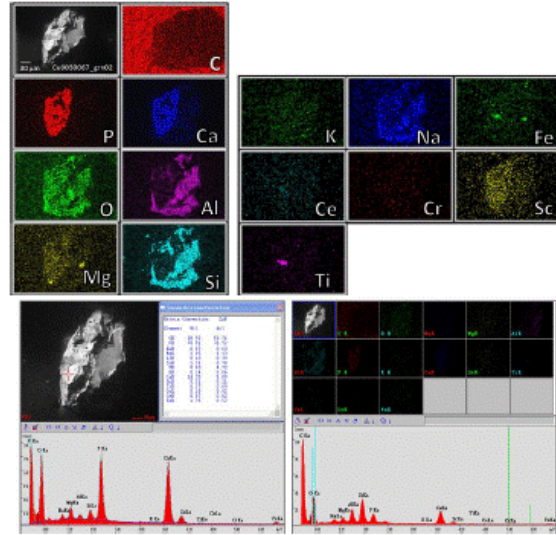
AHp45: Cu0030060_grn01, 150-180 μm



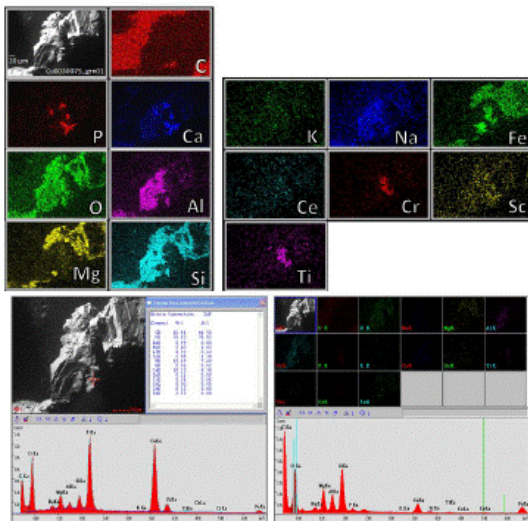
AHp45: Cu0030062_grn01, 150-180 μm



AHp45: Cu0030067_grn02, 150-180 μm

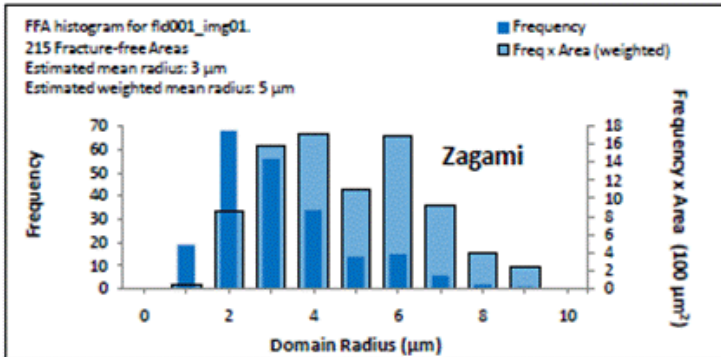
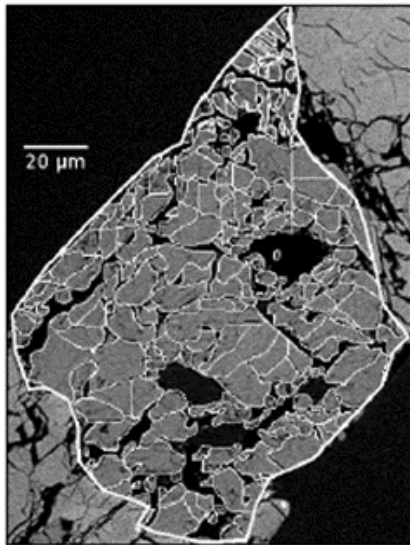


AHp45: Cu0030075_grn01, 150-180 μm

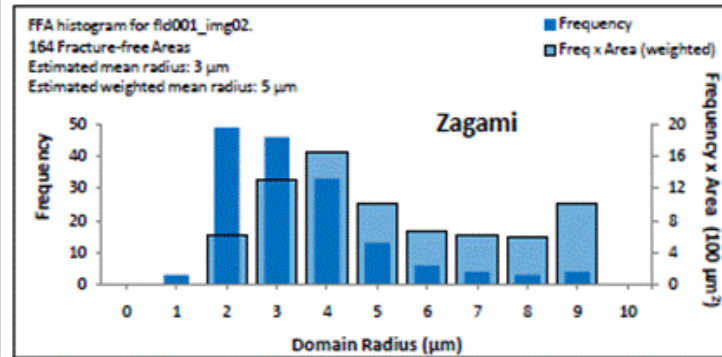
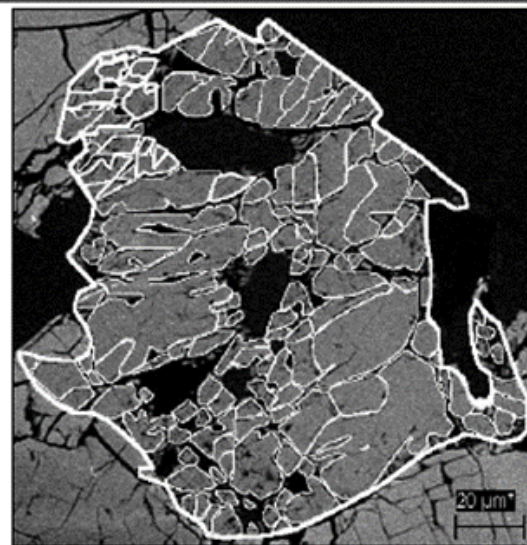


APPENDIX C
TRACED ZAGAMI MERRILLITE PHOSPHATES AND DIFFUSION DOMAIN HISTOGRAMS

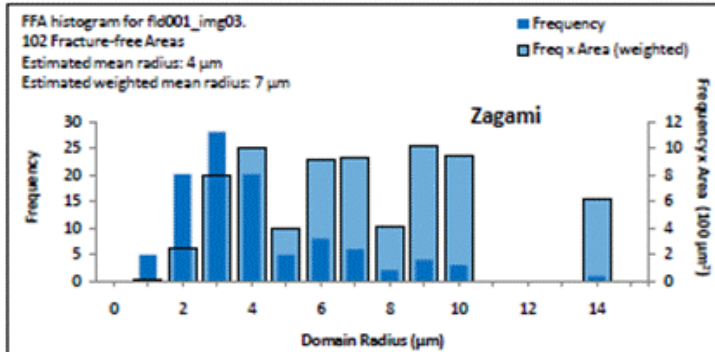
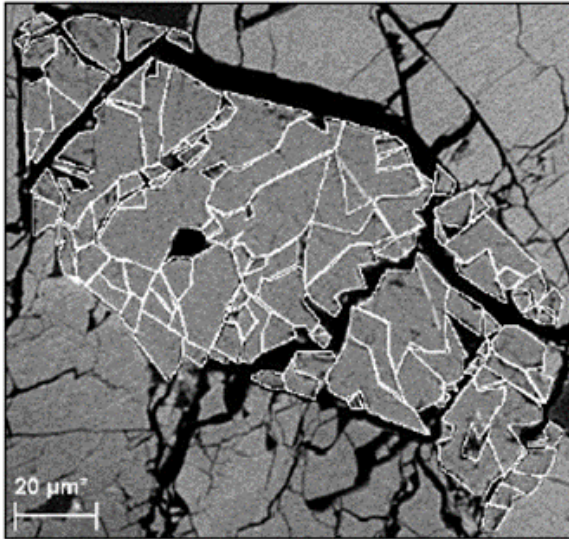
The following BSE images are from thin section Zagami 4709-1 supplied by the American Museum of Natural History, New York, NY. Each thin section image that follows in this appendix shows white traces on the mineral merrillite. The traces mark fracture-free areas (FFA) identified in each mineral. Each histogram shows the radius distribution defined by FFAs from the merrillite thin section. The left axis of each histogram represents the raw frequency of each radius (blue solid bars), and the right axis illustrates the weighted frequency (pale blue bars with borders) of the larger FFAs.



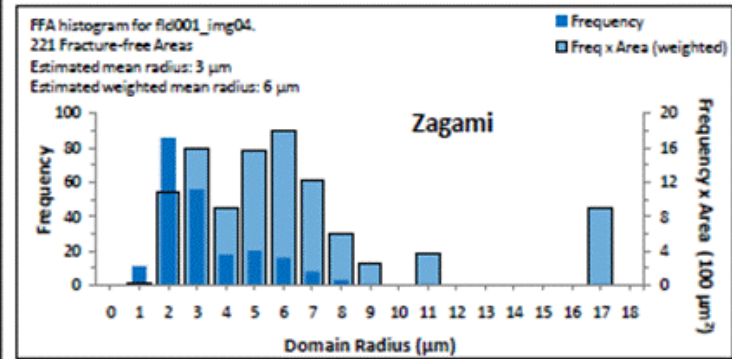
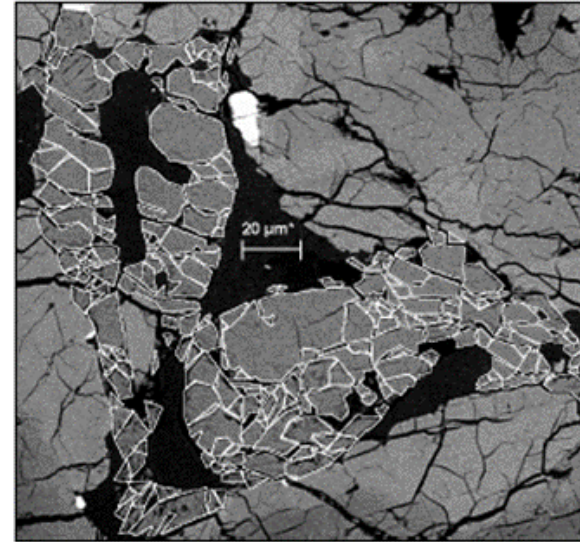
Zagami BSE image fld001_img01 and histogram.
 215 Fracture-free areas.
 Estimated mean radius: 3 μm
 Estimated weighted mean radius: 5 μm



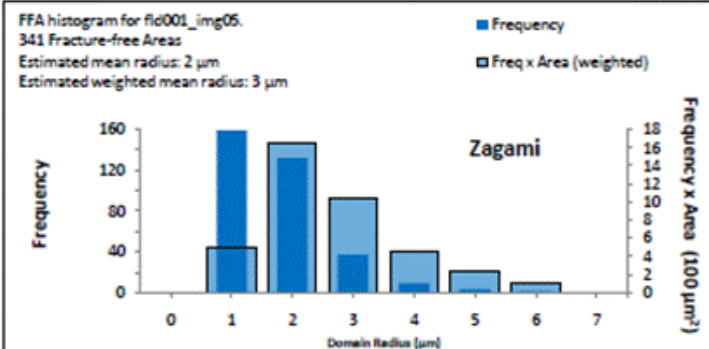
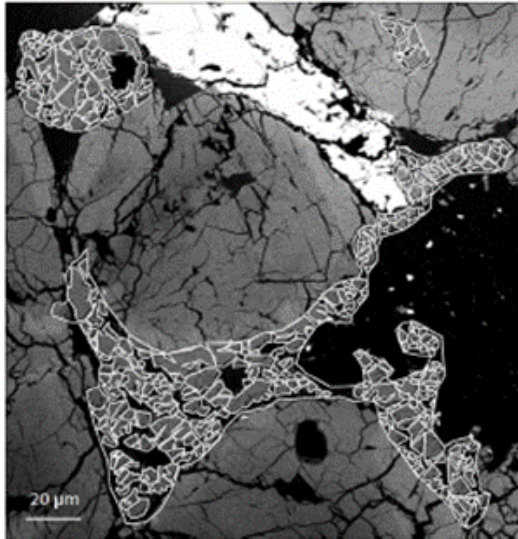
Zagami BSE image fld001_img02 and histogram.
 164 Fracture-free areas.
 Estimated mean radius: 3 μm
 Estimated weighted mean radius: 5 μm



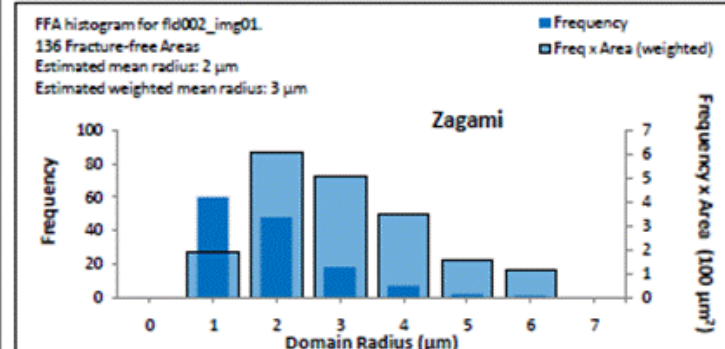
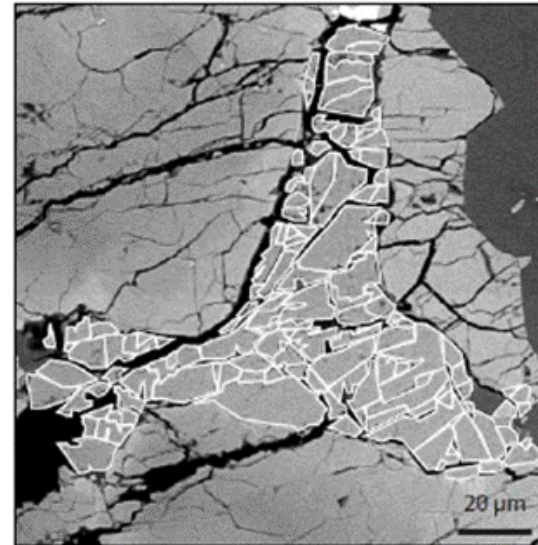
Zagami BSE image fld001_img03 and histogram.
 102 Fracture-free areas.
 Estimated mean radius: 4 μm
 Estimated weighted mean radius: 7 μm



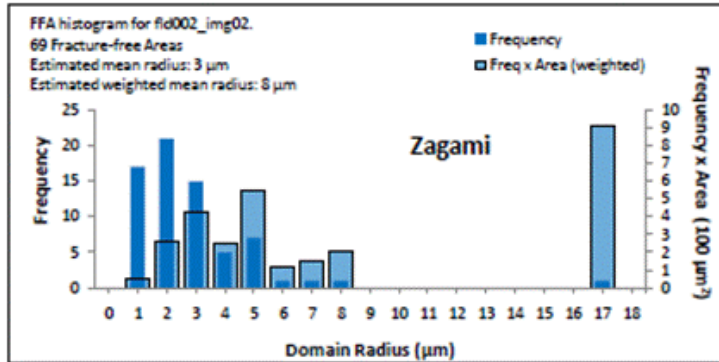
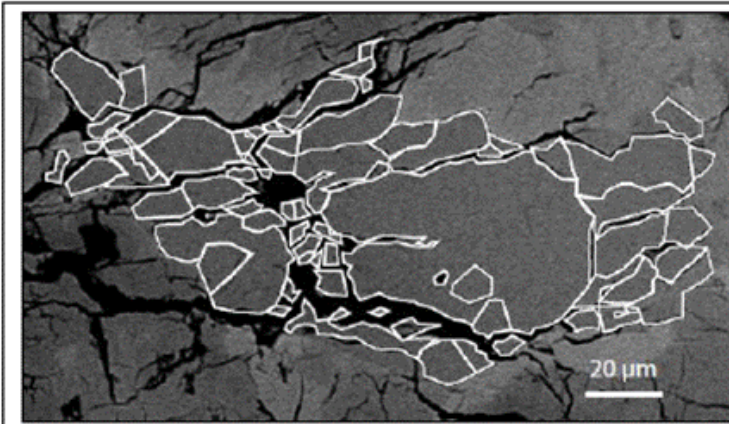
Zagami BSE image fld001_img04 and histogram.
 221 Fracture-free areas.
 Estimated mean radius: 3 μm
 Estimated weighted mean radius: 6 μm



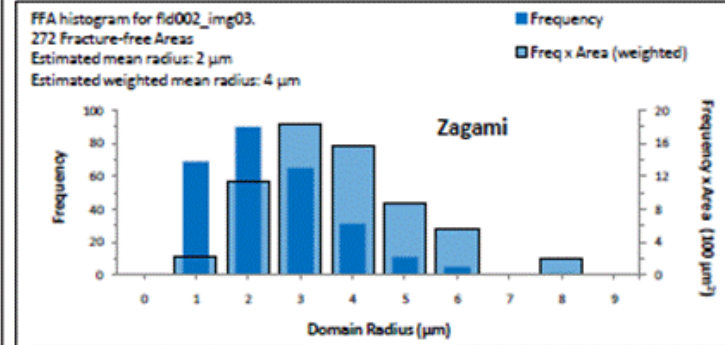
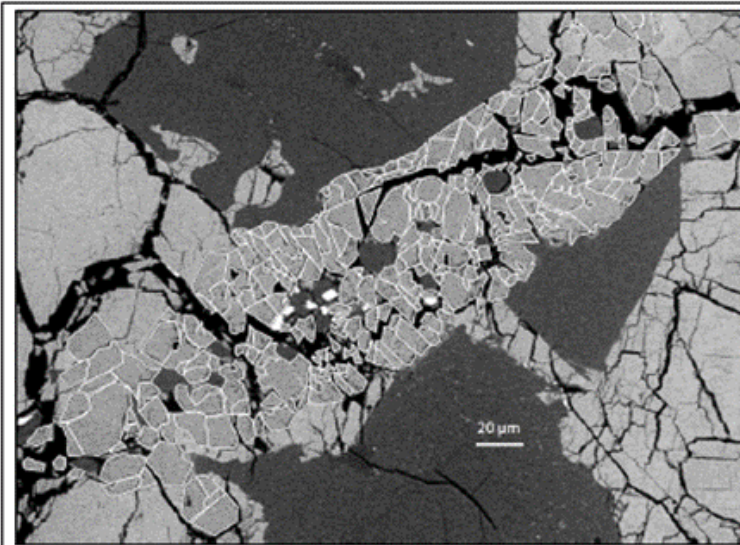
Zagami BSE image fld001_img05 and histogram.
 341 Fracture-free areas.
 Estimated mean radius: 2 μm
 Estimated weighted mean radius: 3 μm



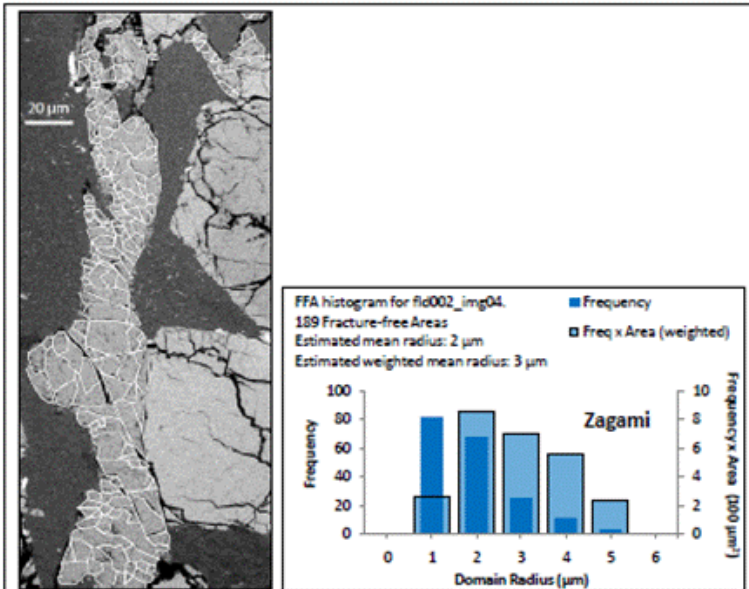
Zagami BSE image fld002_img01 and histogram.
 136 Fracture-free areas.
 Estimated mean radius: 2 μm
 Estimated weighted mean radius: 3 μm



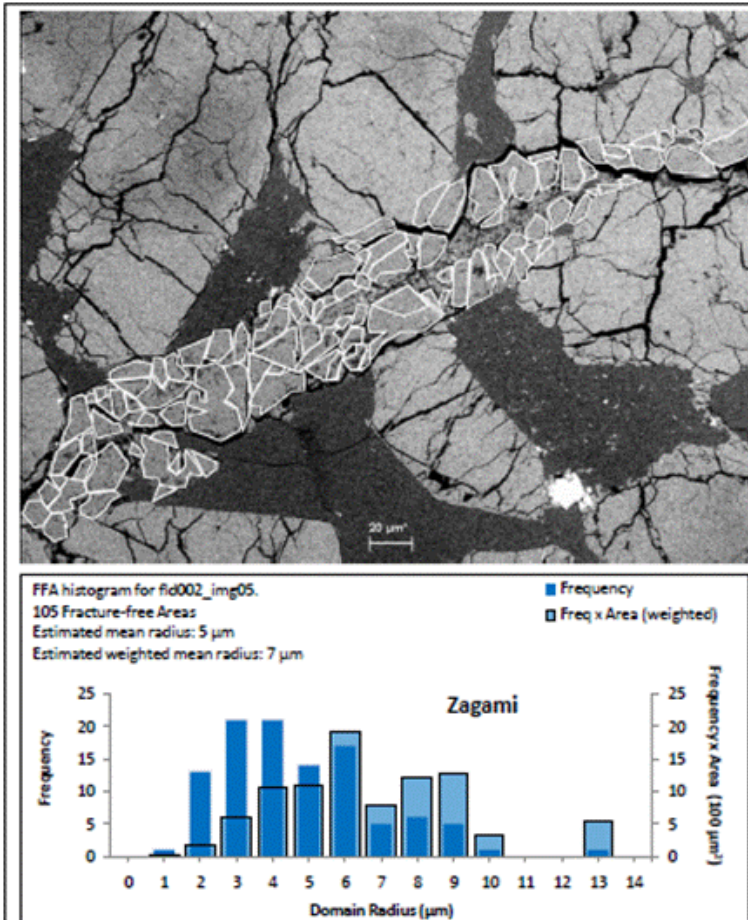
Zagami BSE image fld002_img02 and histogram.
 69 Fracture-free areas.
 Estimated mean radius: 3 μm
 Estimated weighted mean radius: 8 μm



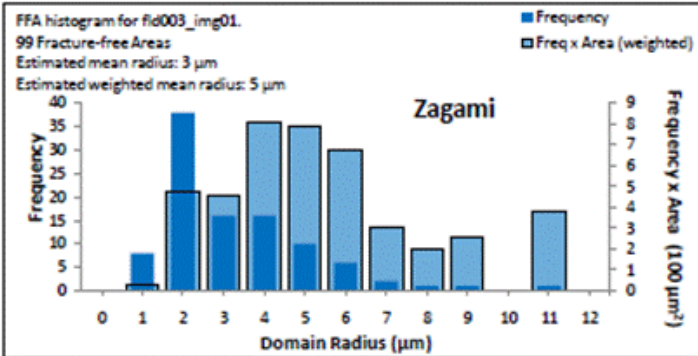
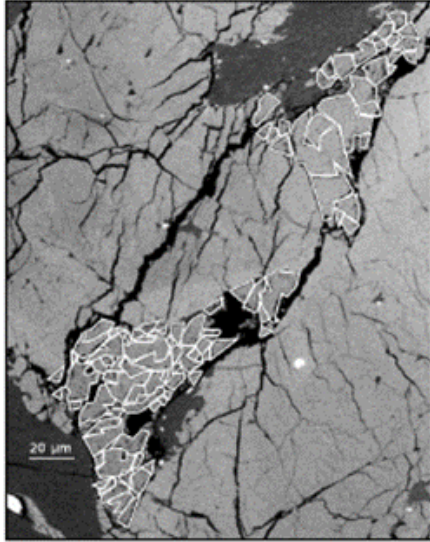
Zagami BSE image fld002_img03 and histogram.
 272 Fracture-free areas.
 Estimated mean radius: 2 μm
 Estimated weighted mean radius: 4 μm



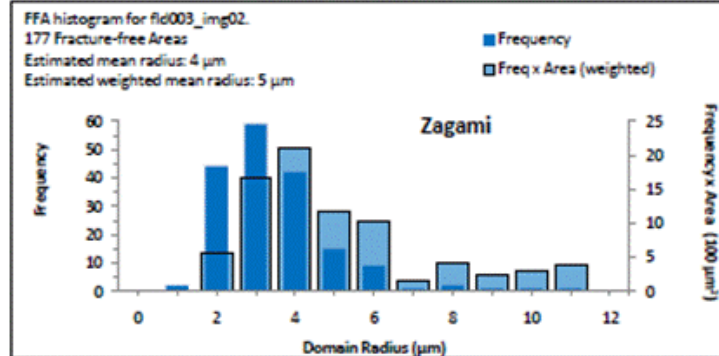
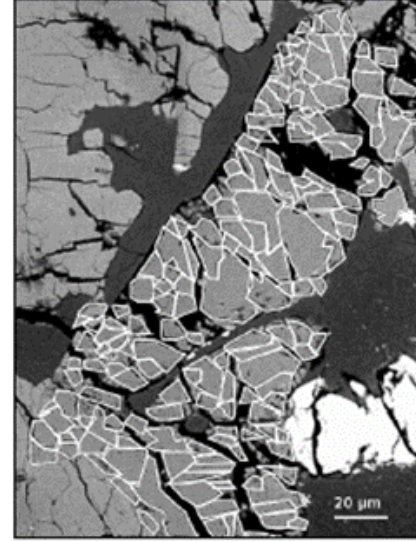
Zagami BSE image fld002_img04 and histogram.
 189 Fracture-free areas.
 Estimated mean radius: 2 μm
 Estimated weighted mean radius: 3 μm



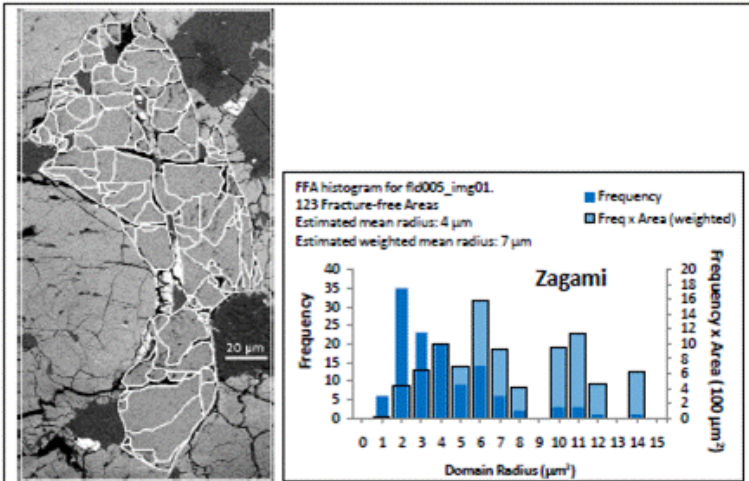
Zagami BSE image fld002_img05 and histogram.
 105 Fracture-free areas.
 Estimated mean radius: 5 μm
 Estimated weighted mean radius: 7 μm



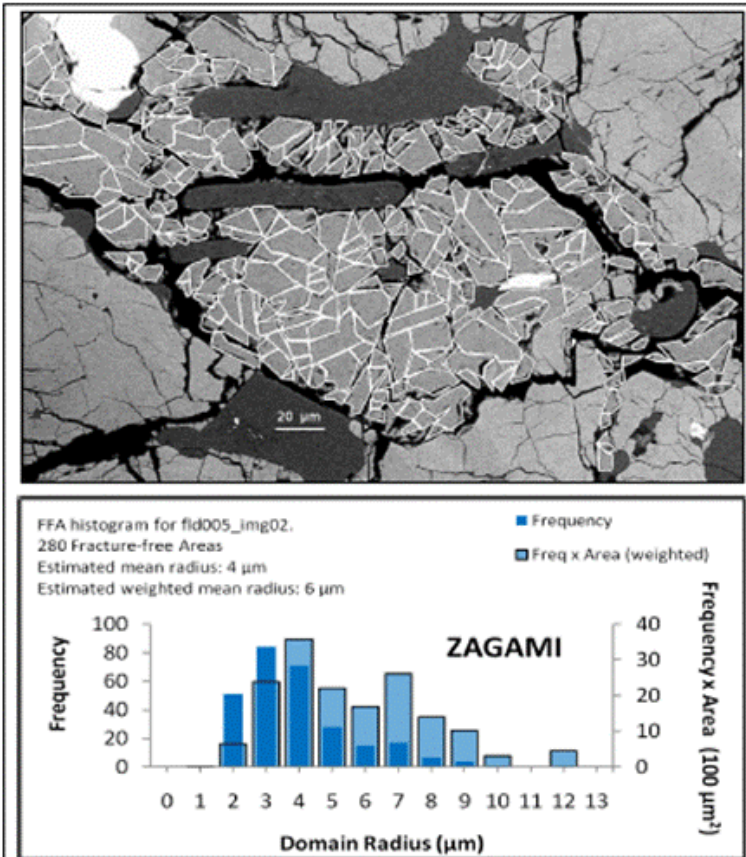
Zagami BSE image fld003_img01 and histogram.
 99 Fracture-free areas.
 Estimated mean radius: 3 μm
 Estimated weighted mean radius: 5 μm



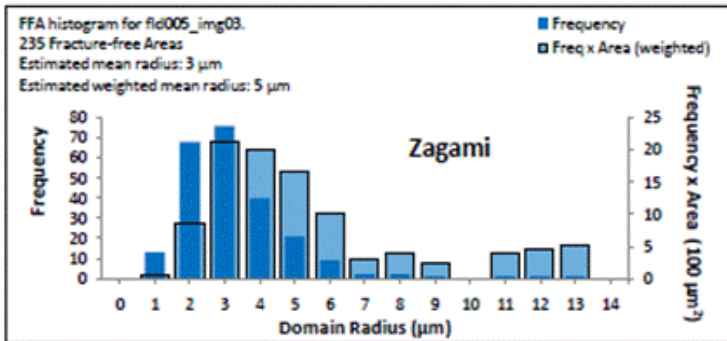
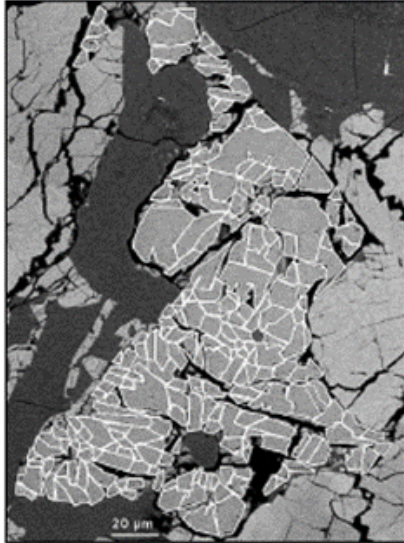
Zagami BSE image fld003_img02 and histogram.
 177 Fracture-free areas.
 Estimated mean radius: 4 μm
 Estimated weighted mean radius: 5 μm



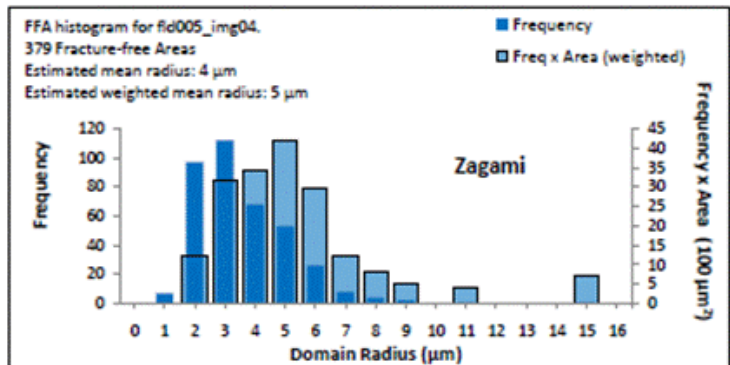
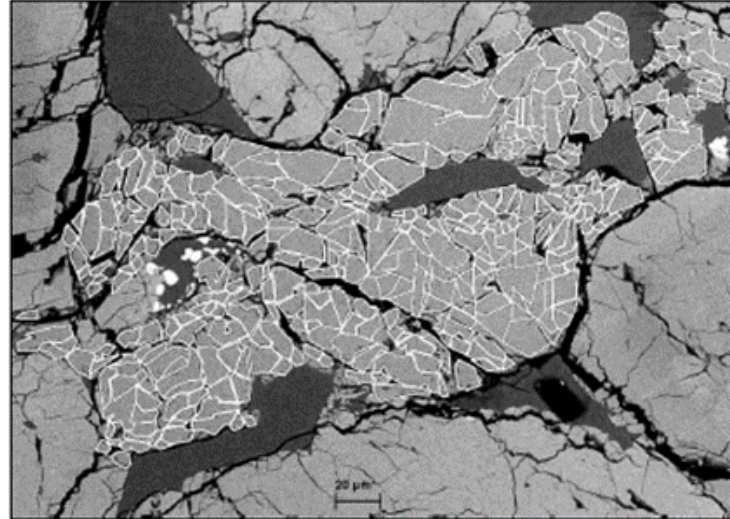
Zagami BSE image fld005_img01 and histogram.
 123 Fracture-free areas.
 Estimated mean radius: 4 μm
 Estimated weighted mean radius: 7 μm



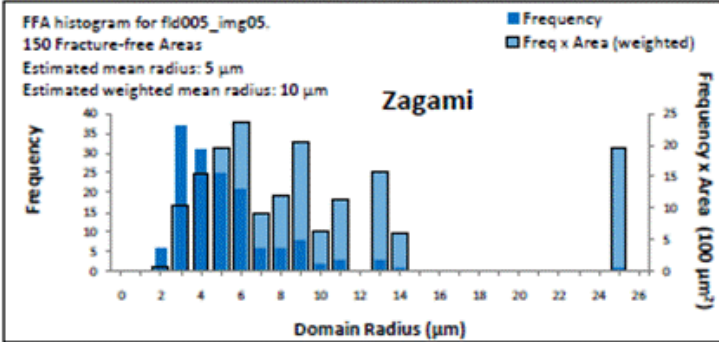
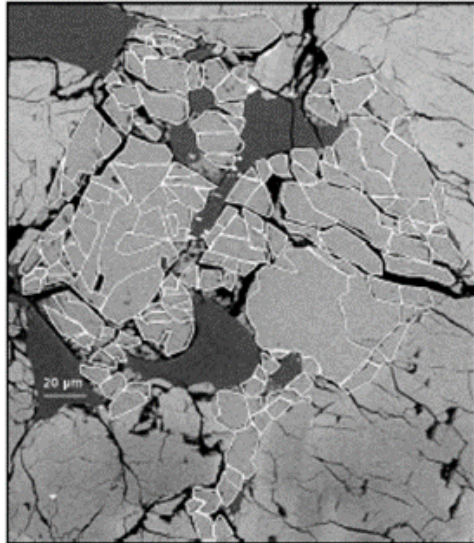
Zagami BSE image fld005_img02 and histogram.
 280 Fracture-free areas.
 Estimated mean radius: 4 μm
 Estimated weighted mean radius: 6 μm



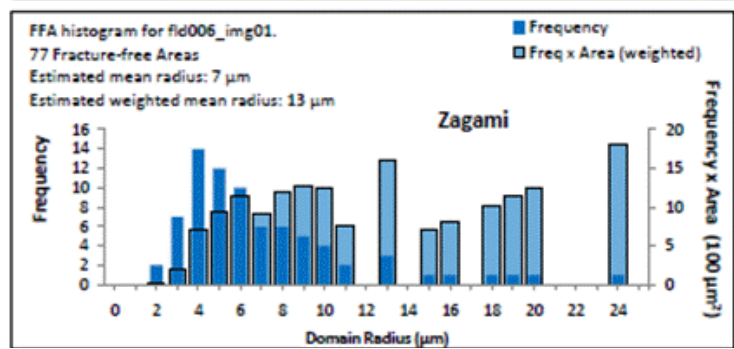
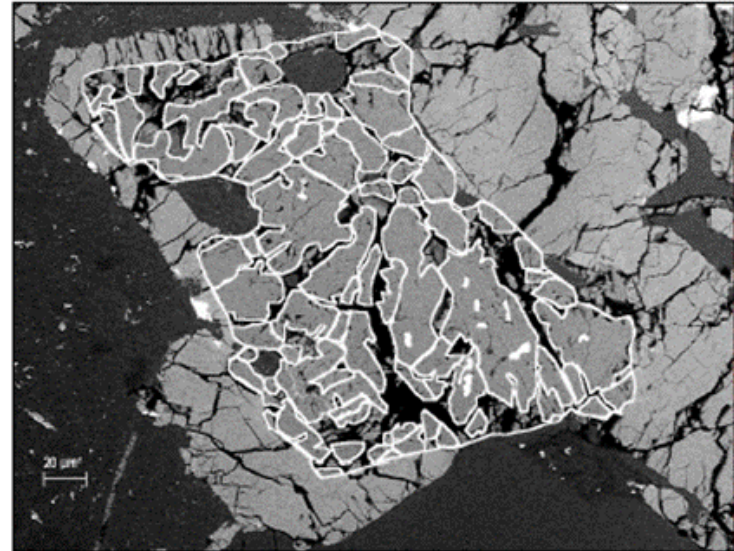
Zagami BSE image fld005_img03 and histogram.
 235 Fracture-free areas.
 Estimated mean radius: 3 μm
 Estimated weighted mean radius: 5 μm



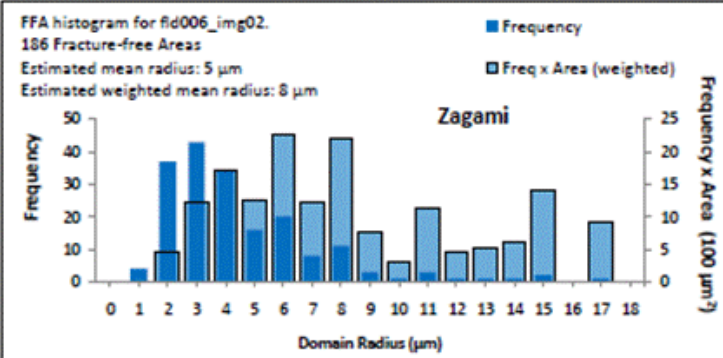
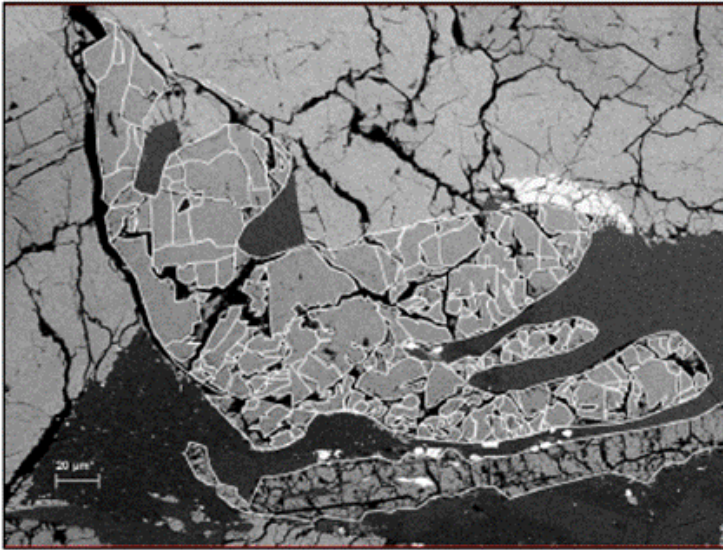
Zagami BSE image fld005_img04 and histogram.
 379 Fracture-free areas.
 Estimated mean radius: 4 μm
 Estimated weighted mean radius: 5 μm



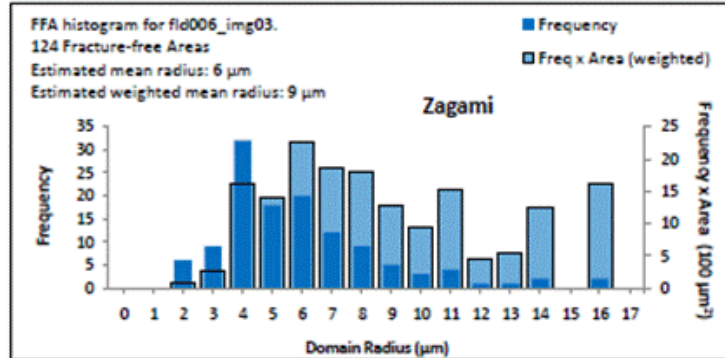
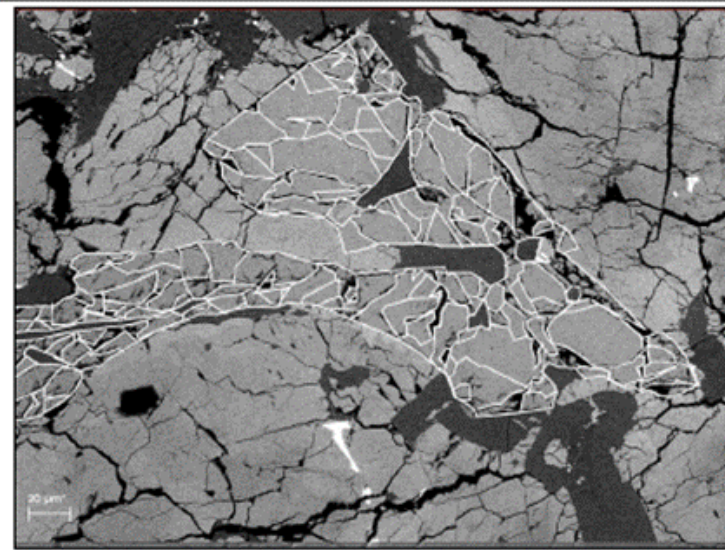
Zagami BSE image fld005_img05 and histogram.
 150 Fracture-free areas.
 Estimated mean radius: 5 μm
 Estimated weighted mean radius: 10 μm



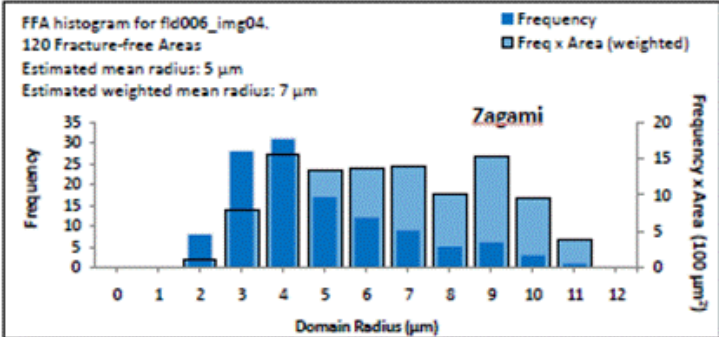
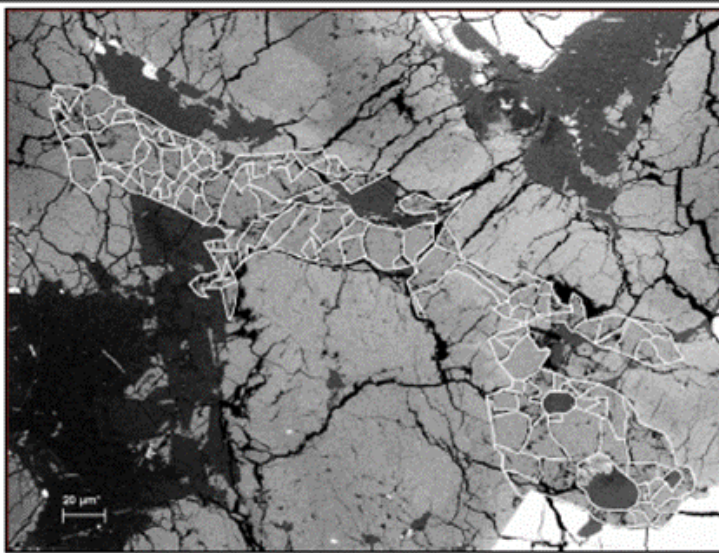
Zagami BSE image fld006_img01 and histogram.
 77 Fracture-free areas.
 Estimated mean radius: 7 μm
 Estimated weighted mean radius: 13 μm



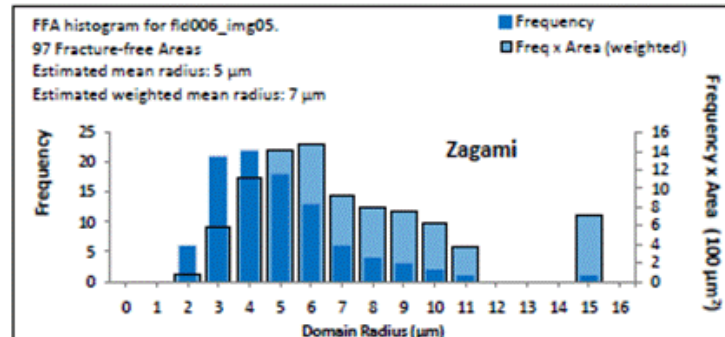
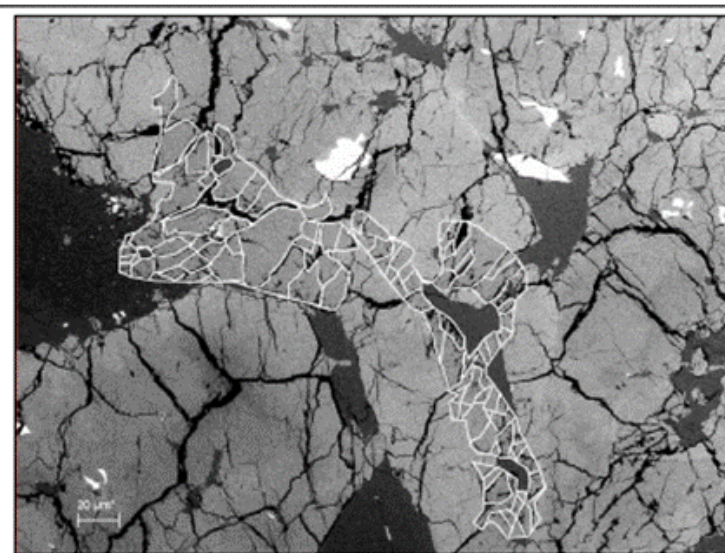
Zagami BSE image fld006_img02 and histogram.
186 Fracture-free areas.
Estimated mean radius: 5 μm
Estimated weighted mean radius: 8 μm



Zagami BSE image fld006_img03 and histogram.
124 Fracture-free areas.
Estimated mean radius: 6 μm
Estimated weighted mean radius: 9 μm



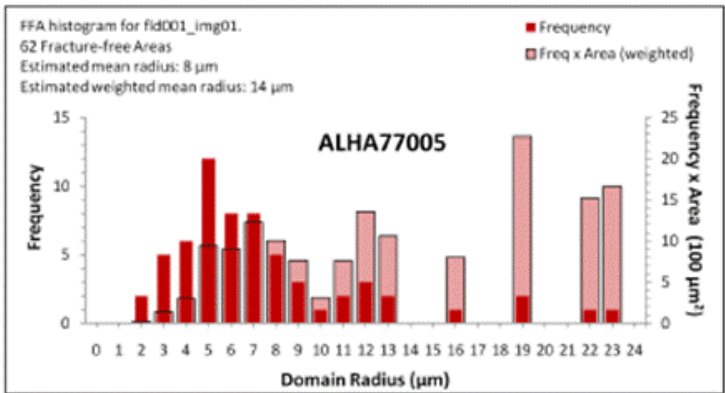
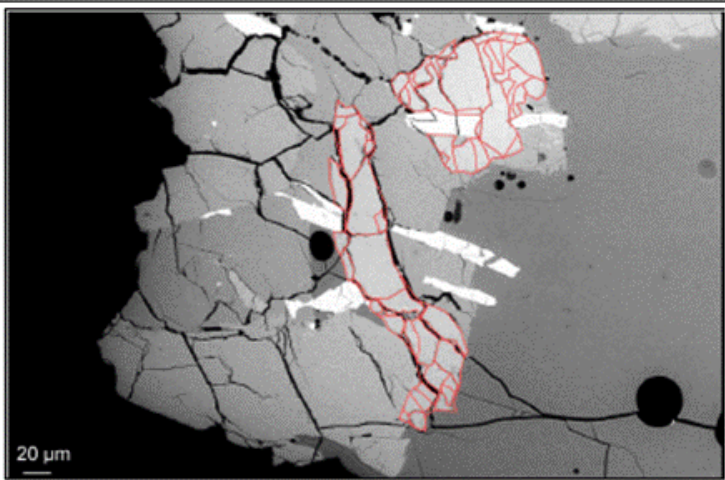
Zagami BSE image fld006_img04 and histogram.
 120 Fracture-free areas.
 Estimated mean radius: 5 μm
 Estimated weighted mean radius: 7 μm



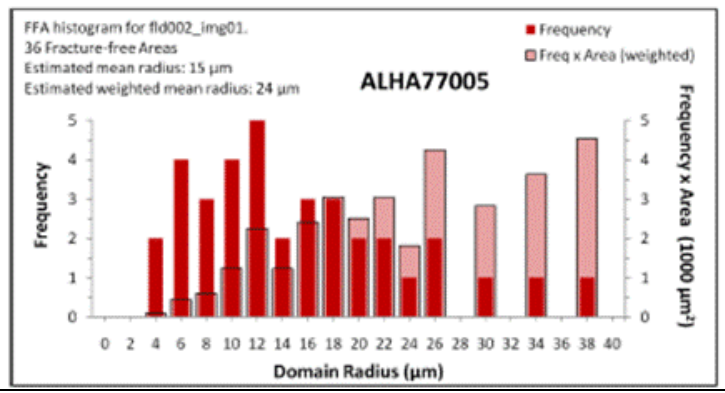
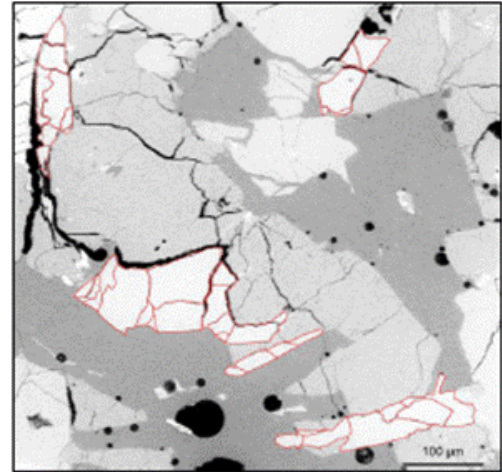
Zagami BSE image fld006_img05 and histogram.
 97 Fracture-free areas.
 Estimated mean radius: 5 μm
 Estimated weighted mean radius: 7 μm

APPENDIX D
TRACED ALHA77005 MERRILLITE PHOSPHATES AND DIFFUSION DOMAIN HISTOGRAMS

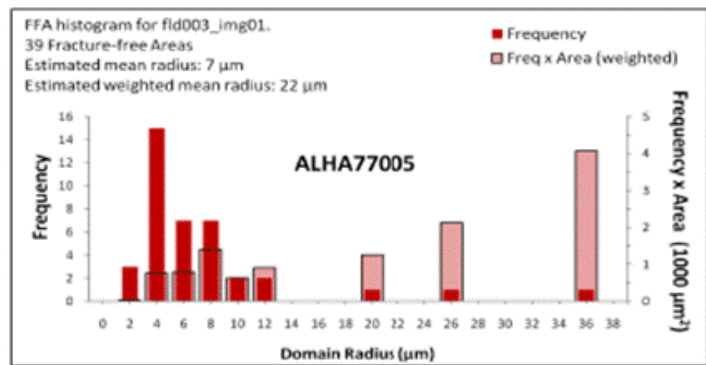
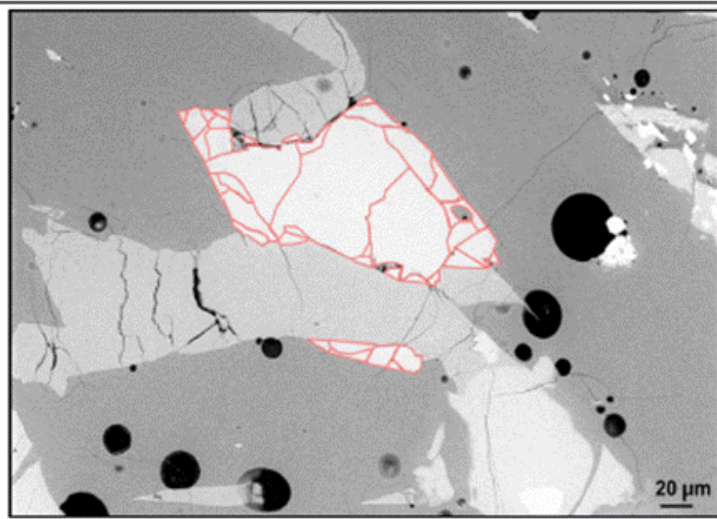
The following BSE images are from thin section ALHA77005 120 supplied by the National Aeronautics and Space Administration (NASA). Each thin section image that follows in this appendix shows red traces on the mineral merrillite. The traces mark fracture-free areas (FFA) identified in each mineral. Each histogram shows the radius distribution defined by FFAs from the merrillite thin section. The left axis of each histogram represents the raw frequency of each radius (red solid bars), and the right axis illustrates the weighted frequency (pale red bars with borders) of the larger FFAs.



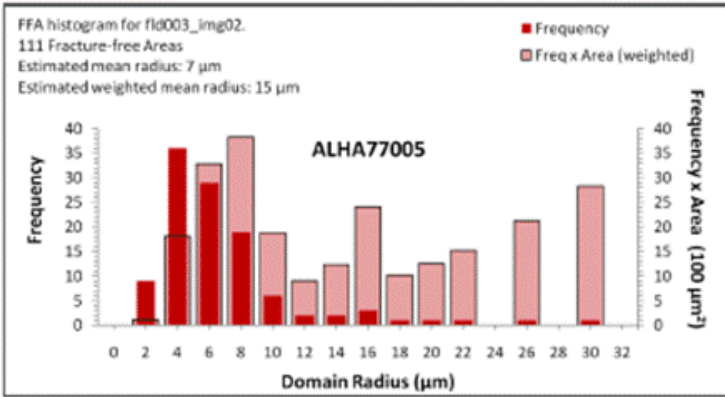
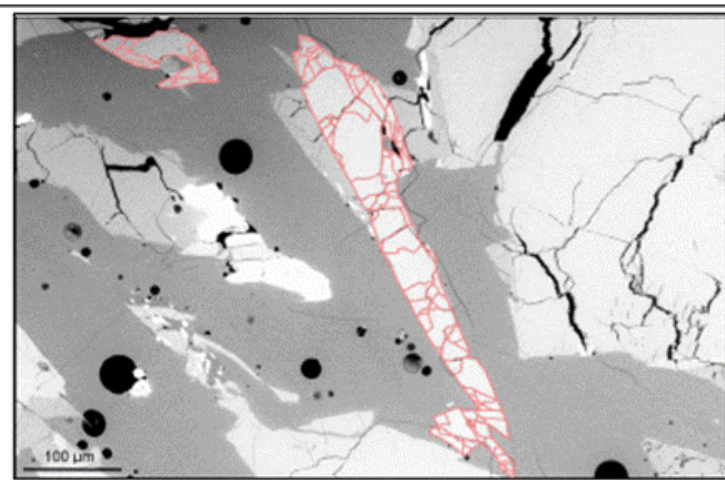
ALHA77005 BSE image fld001_img01 and histogram.
 62 Fracture-free areas.
 Estimated mean radius: 8 μm
 Estimated weighted mean radius: 14 μm



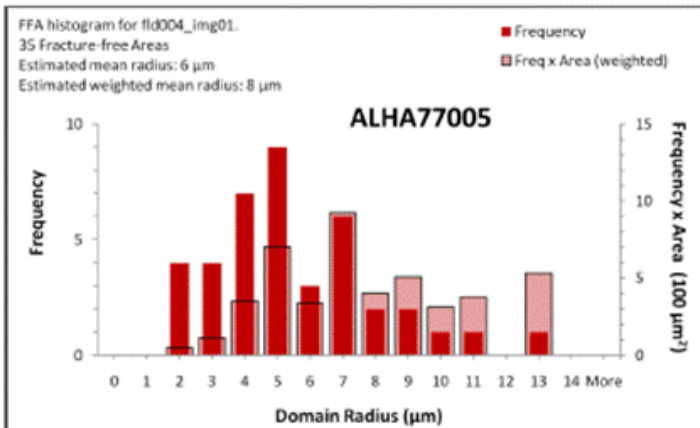
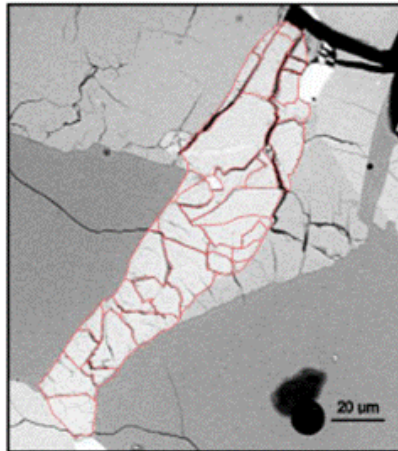
ALHA77005 BSE image fld002_img01 and histogram.
 36 Fracture-free areas.
 Estimated mean radius: 15 μm
 Estimated weighted mean radius: 24 μm



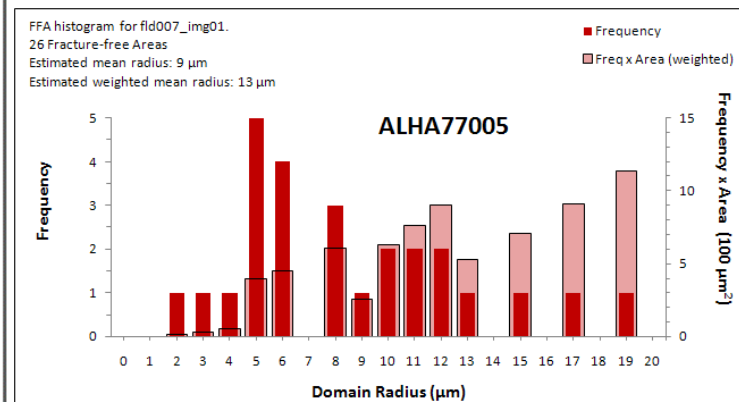
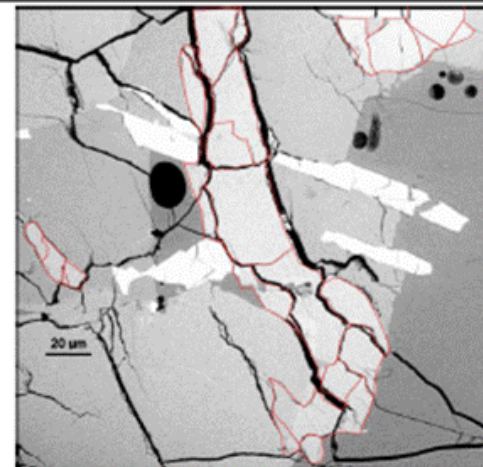
ALHA77005 BSE image fld003_img01 and histogram.
 39 Fracture-free areas.
 Estimated mean radius: 7 μm
 Estimated weighted mean radius: 22 μm



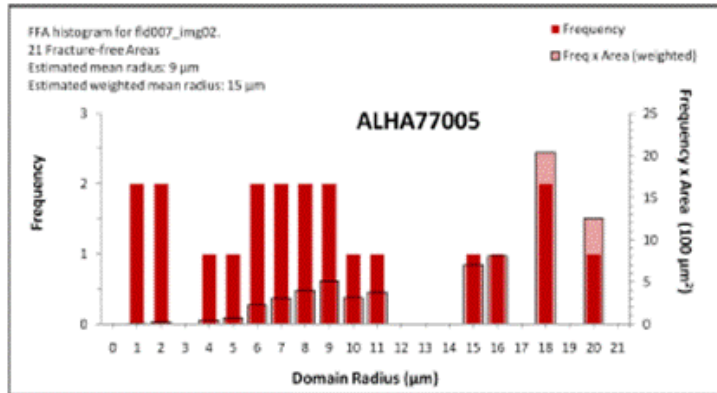
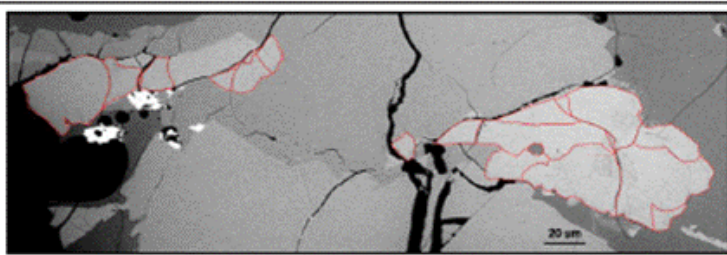
ALHA77005 BSE image fld003_img02 and histogram.
 111 Fracture-free areas.
 Estimated mean radius: 7 μm
 Estimated weighted mean radius: 15 μm



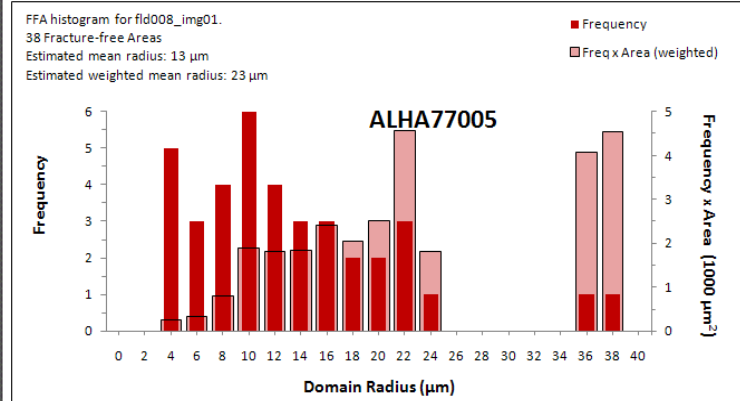
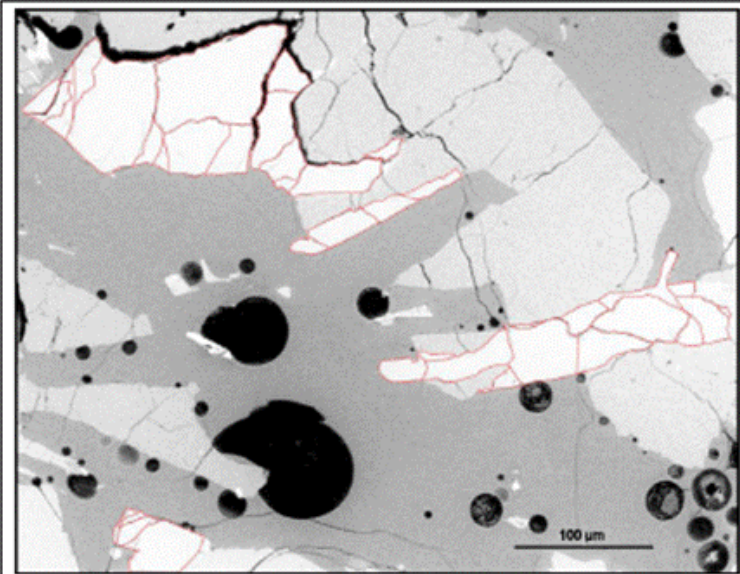
ALHA77005 BSE image fld004_img01 and histogram.
 35 Fracture-free areas.
 Estimated mean radius: 6 μm
 Estimated weighted mean radius: 8 μm



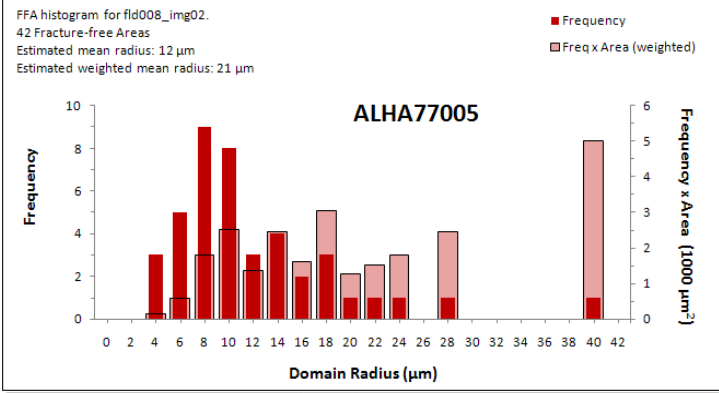
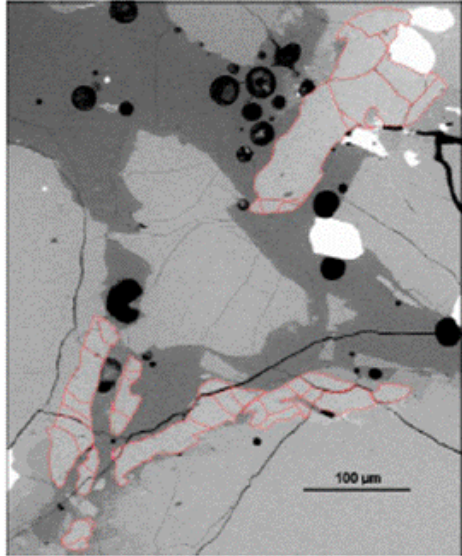
ALHA77005 BSE image fld007_img01 and histogram.
 26 Fracture-free areas.
 Estimated mean radius: 9 μm
 Estimated weighted mean radius: 13 μm



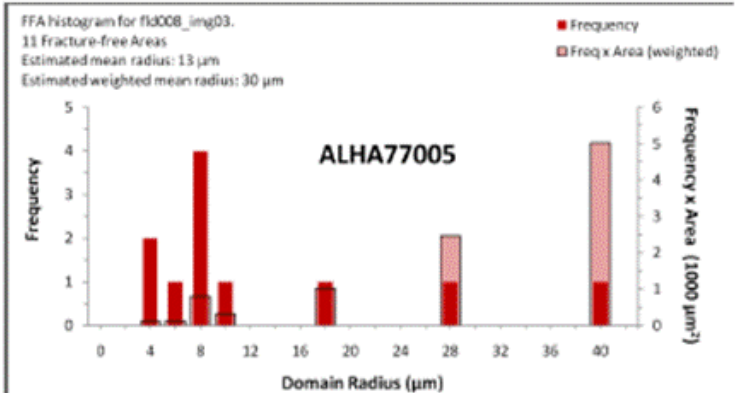
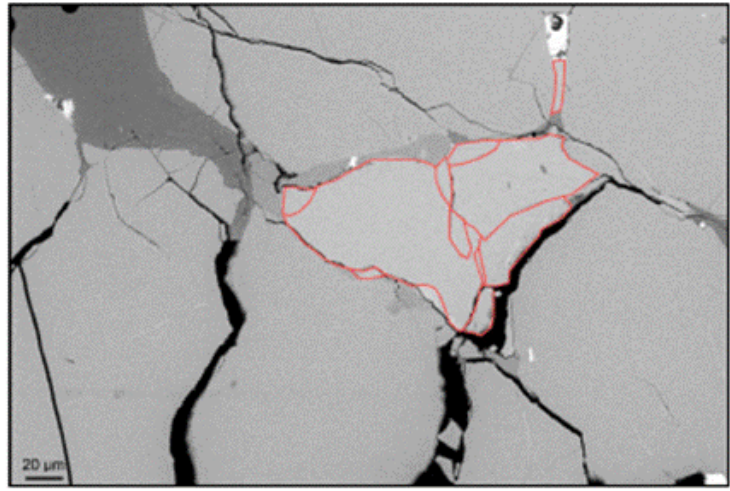
ALHA77005 BSE image fld007_img02 and histogram.
 21 Fracture-free areas.
 Estimated mean radius: 9 μm
 Estimated weighted mean radius: 15 μm



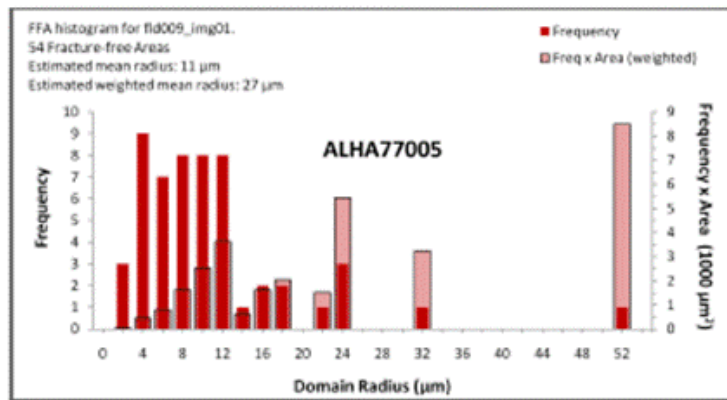
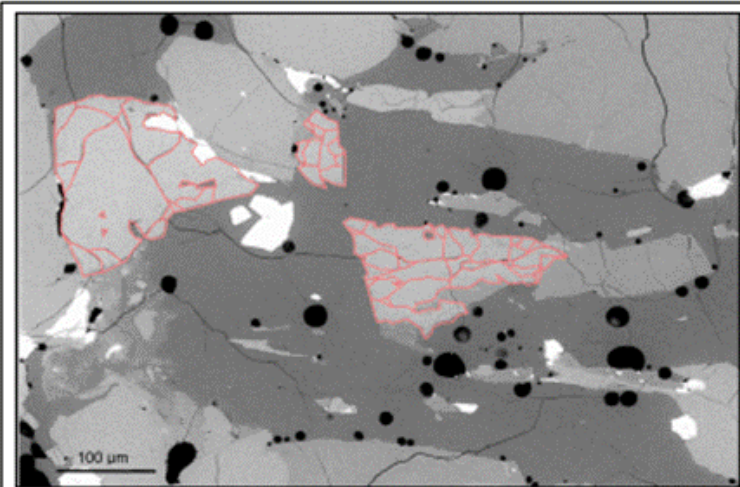
ALHA77005 BSE image fld008_img01 and histogram.
 38 Fracture-free areas.
 Estimated mean radius: 13 μm
 Estimated weighted mean radius: 23 μm



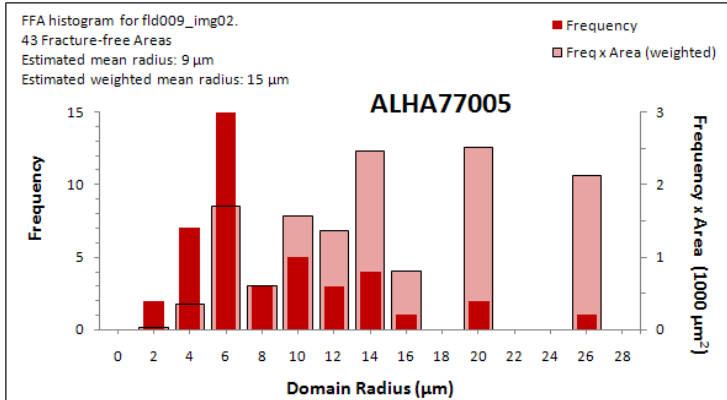
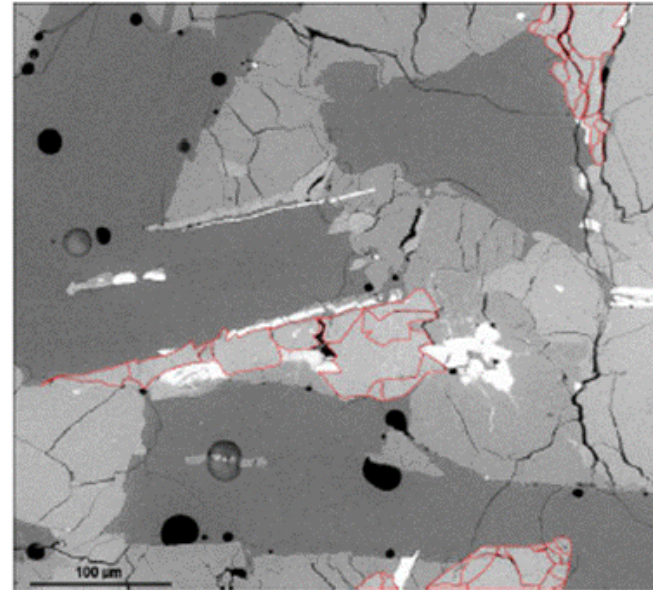
ALHA77005 BSE image fld008_img02 and histogram.
 42 Fracture-free areas.
 Estimated mean radius: 12 μm
 Estimated weighted mean radius: 21 μm



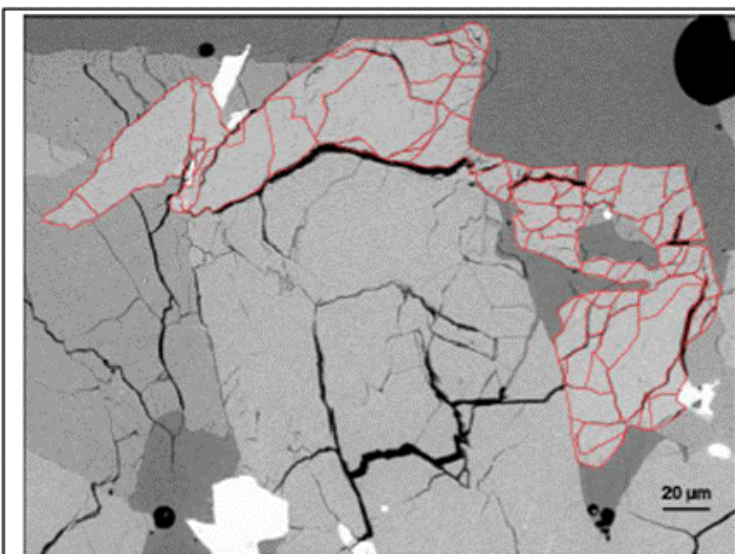
ALHA77005 BSE image fld008_img03 and histogram.
 11 Fracture-free areas.
 Estimated mean radius: 13 μm
 Estimated weighted mean radius: 30 μm



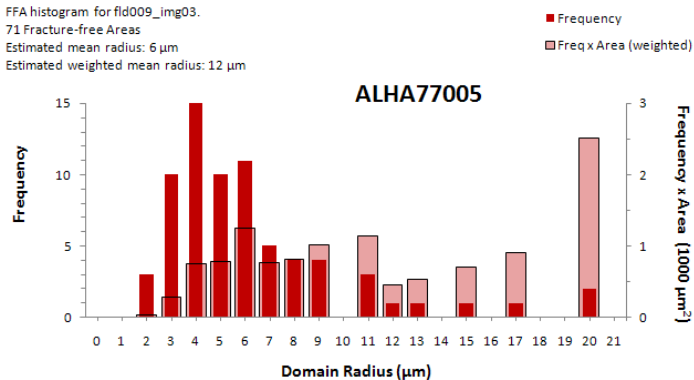
ALHA77005 BSE image fld009_img01 and histogram.
 54 Fracture-free areas.
 Estimated mean radius: 11 μm
 Estimated weighted mean radius: 27 μm



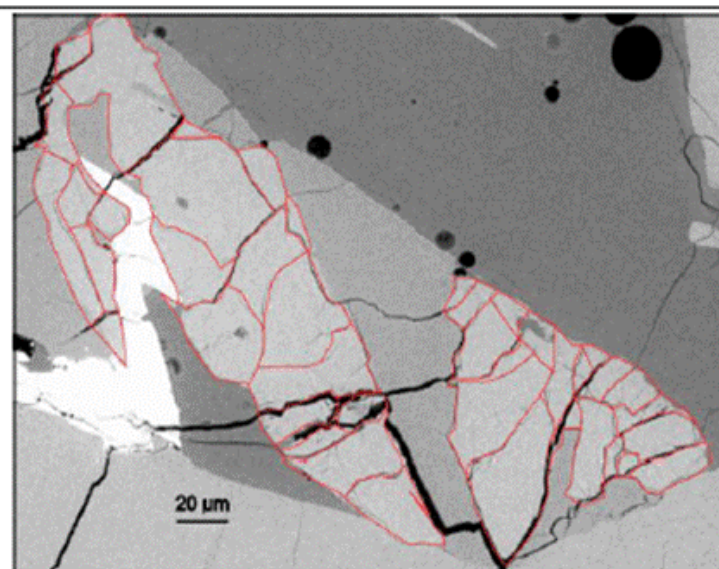
ALHA77005 BSE image fld009_img02 and histogram.
 43 Fracture-free areas.
 Estimated mean radius: 9 μm
 Estimated weighted mean radius: 15 μm



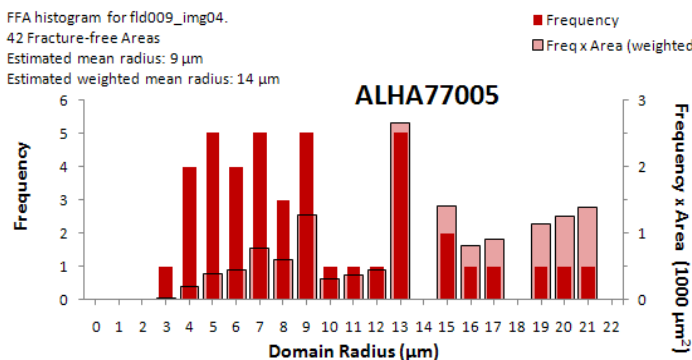
FFA histogram for fld009_img03.
 71 Fracture-free Areas
 Estimated mean radius: 6 μm
 Estimated weighted mean radius: 12 μm



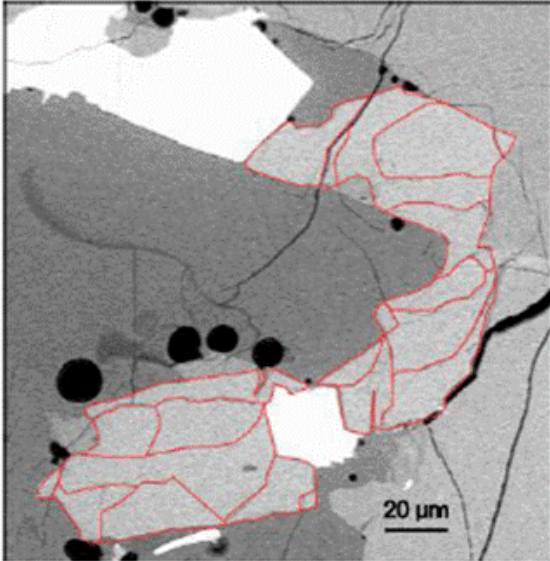
ALHA77005 BSE image fld009_img03 and histogram.
 71 Fracture-free areas.
 Estimated mean radius: 6 μm
 Estimated weighted mean radius: 12 μm



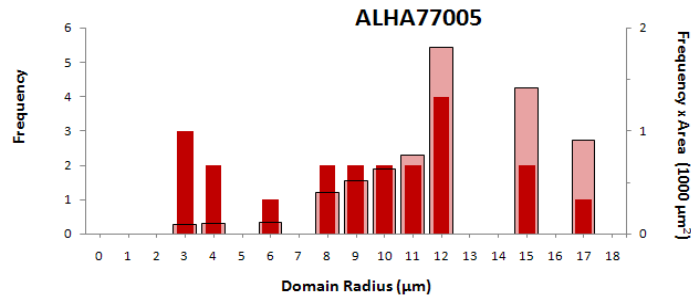
FFA histogram for fld009_img04.
 42 Fracture-free Areas
 Estimated mean radius: 9 μm
 Estimated weighted mean radius: 14 μm



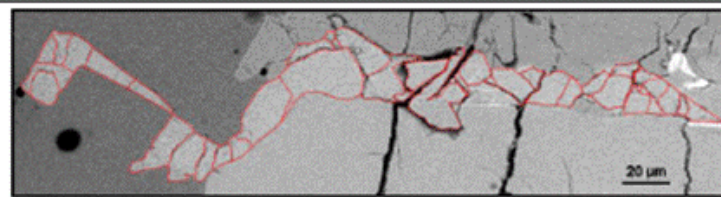
ALHA77005 BSE image fld009_img04 and histogram.
 42 Fracture-free areas.
 Estimated mean radius: 9 μm
 Estimated weighted mean radius: 14 μm



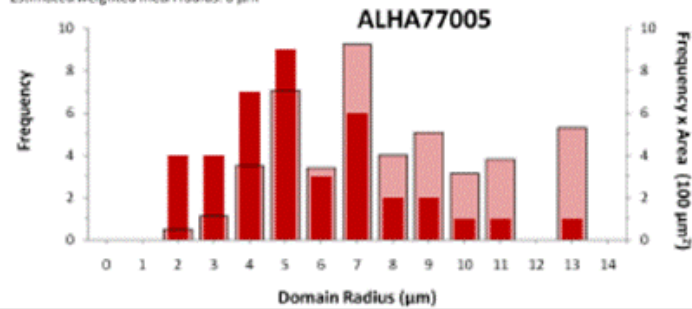
FFA histogram for fld009_img05.
 21 Fracture-free Areas
 Estimated mean radius: 9 μm
 Estimated weighted mean radius: 12 μm



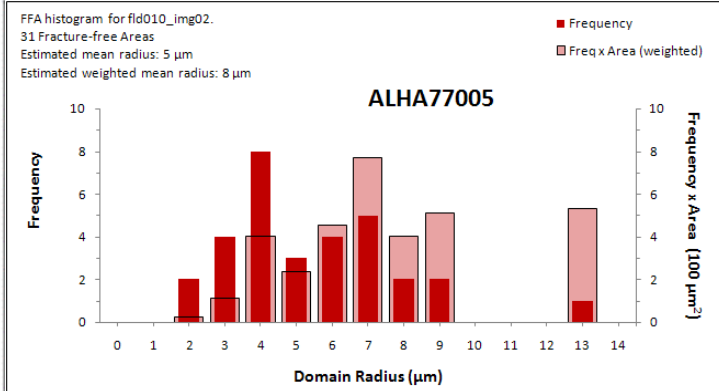
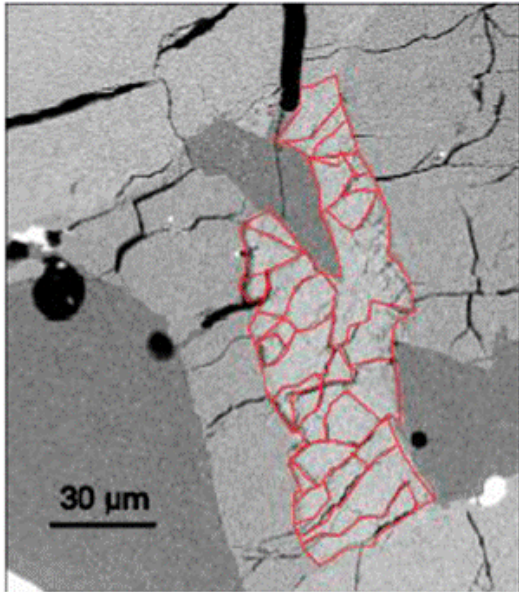
ALHA77005 BSE image fld009_img05 and histogram.
 21 Fracture-free areas.
 Estimated mean radius: 9 μm
 Estimated weighted mean radius: 12 μm



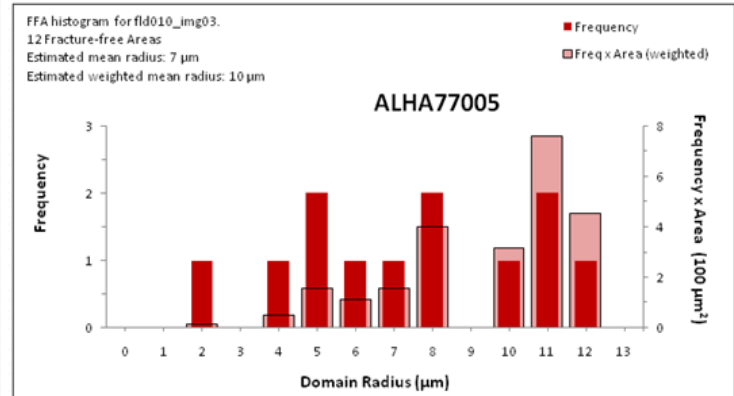
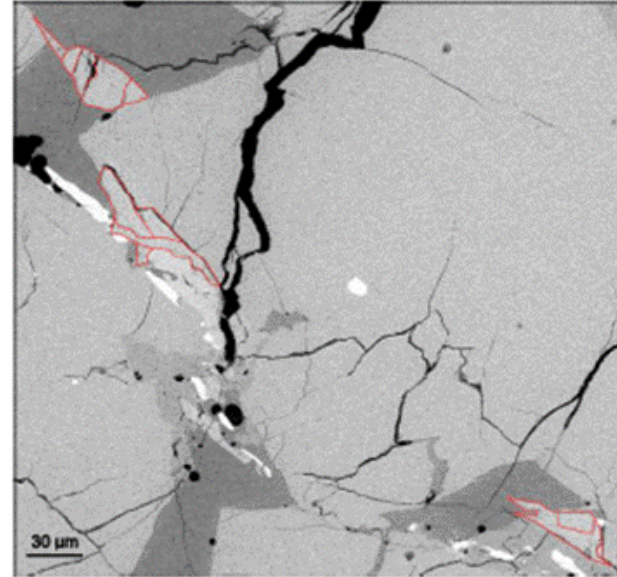
FFA histogram for fld010_img01.
 40 Fracture-free Areas
 Estimated mean radius: 6 μm
 Estimated weighted mean radius: 8 μm



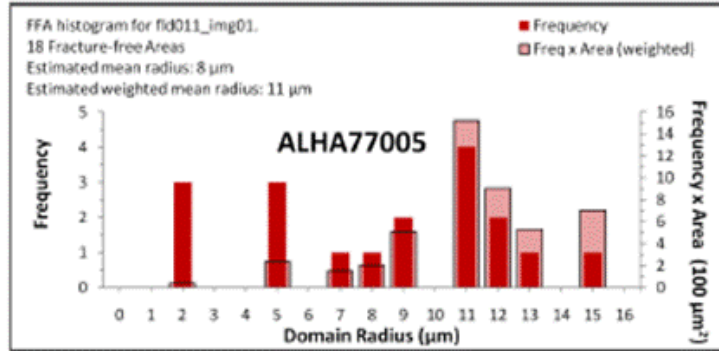
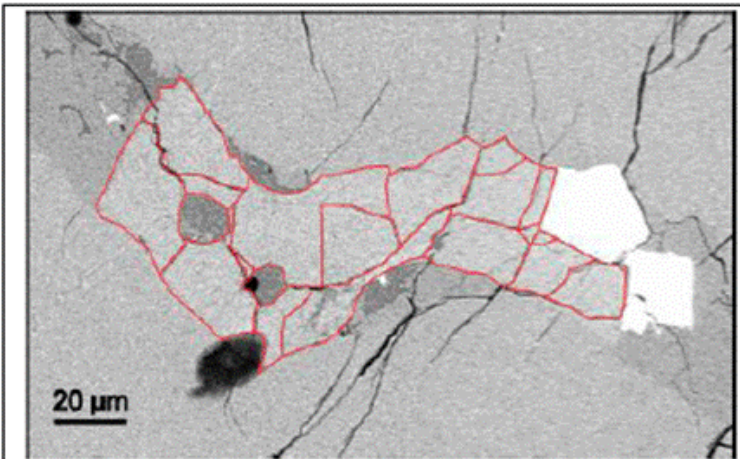
ALHA77005 BSE image fld010_img01 and histogram.
 40 Fracture-free areas.
 Estimated mean radius: 6 μm
 Estimated weighted mean radius: 8 μm



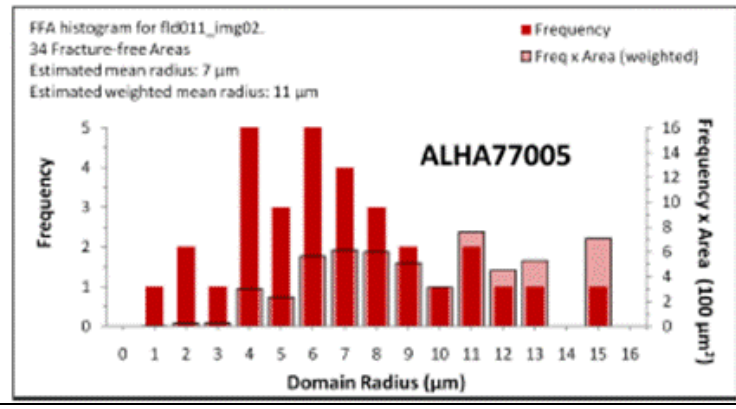
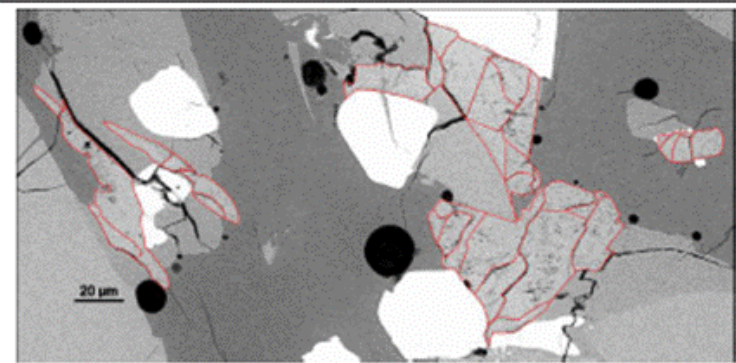
ALHA77005 BSE image fld010_img02 and histogram.
 31 Fracture-free areas.
 Estimated mean radius: 5 μm
 Estimated weighted mean radius: 8 μm



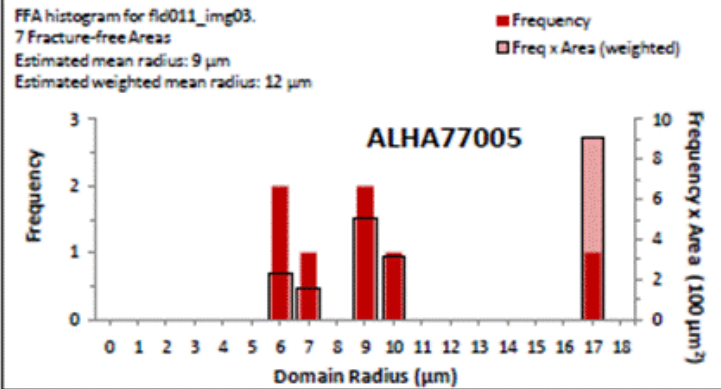
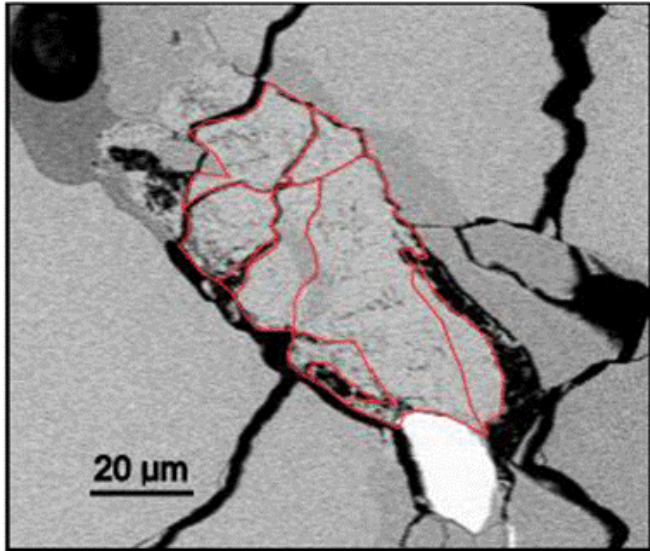
ALHA77005 BSE image fld010_img03 and histogram.
 12 Fracture-free areas.
 Estimated mean radius: 7 μm
 Estimated weighted mean radius: 10 μm



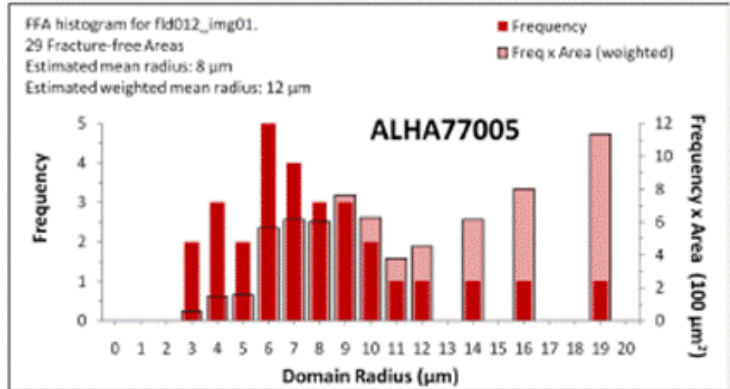
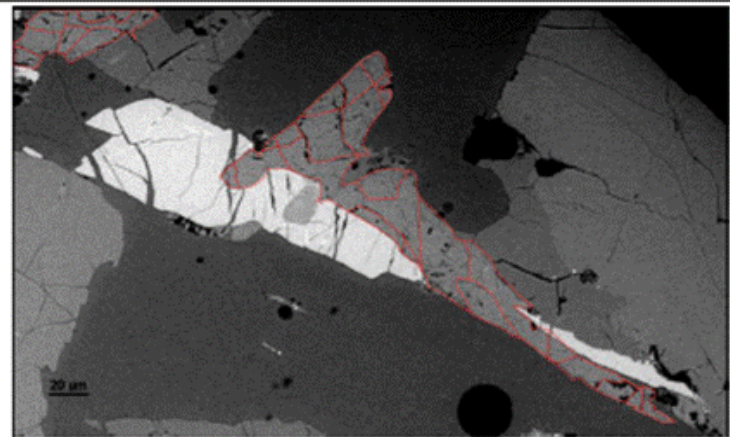
ALHA77005 BSE image fld011_img01 and histogram.
 18 Fracture-free areas.
 Estimated mean radius: 8 μm
 Estimated weighted mean radius: 11 μm



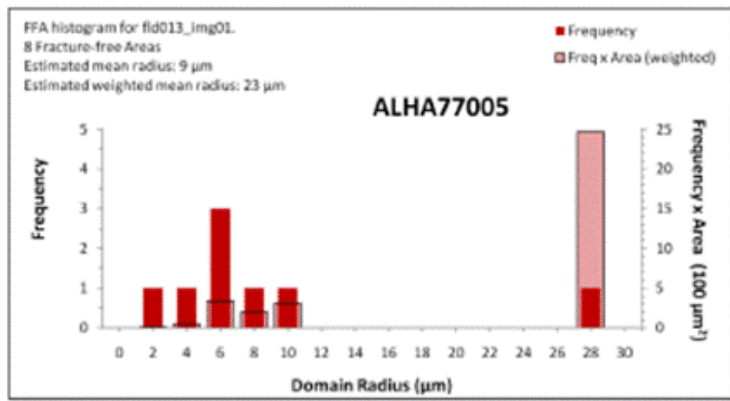
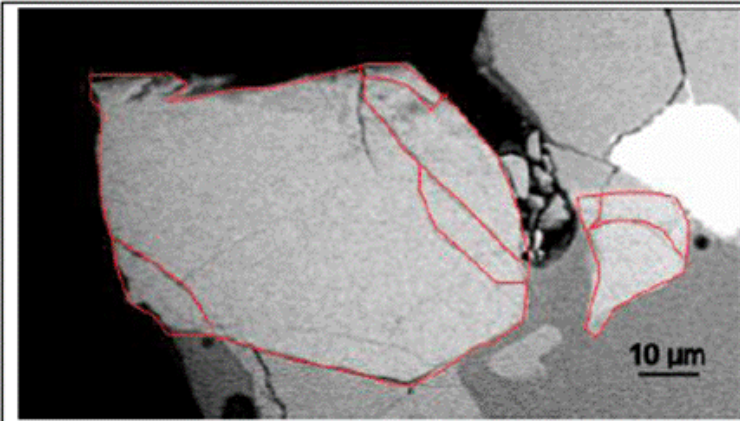
ALHA77005 BSE image fld011_img02 and histogram.
 34 Fracture-free areas.
 Estimated mean radius: 7 μm
 Estimated weighted mean radius: 11 μm



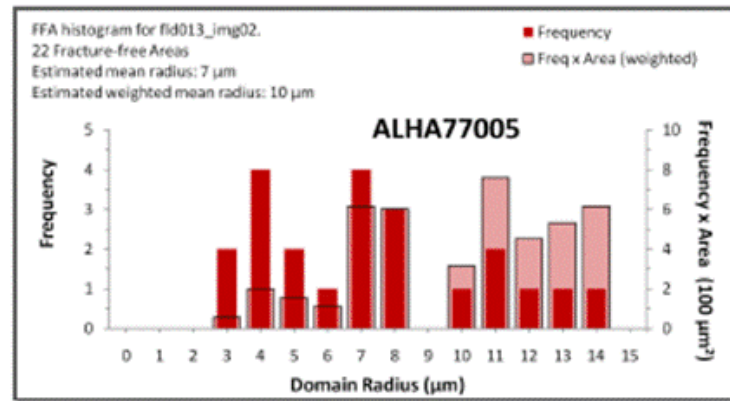
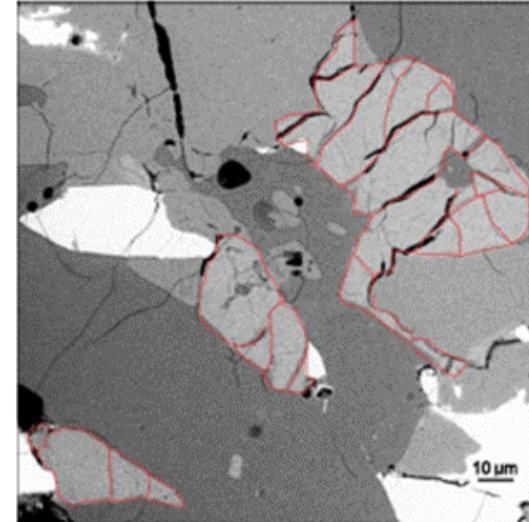
ALHA77005 BSE image fld011_img03 and histogram.
 7 Fracture-free areas.
 Estimated mean radius: 9 μm
 Estimated weighted mean radius: 12 μm



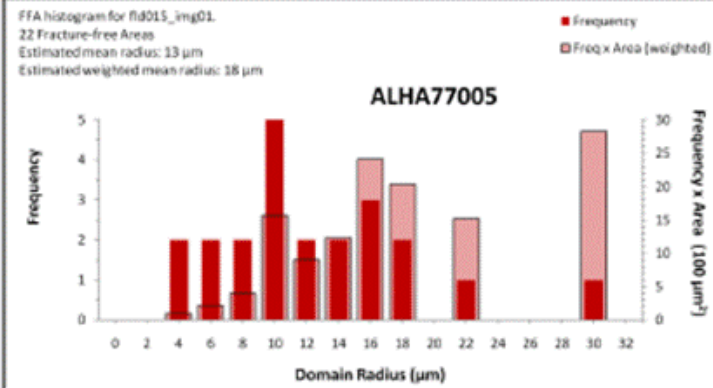
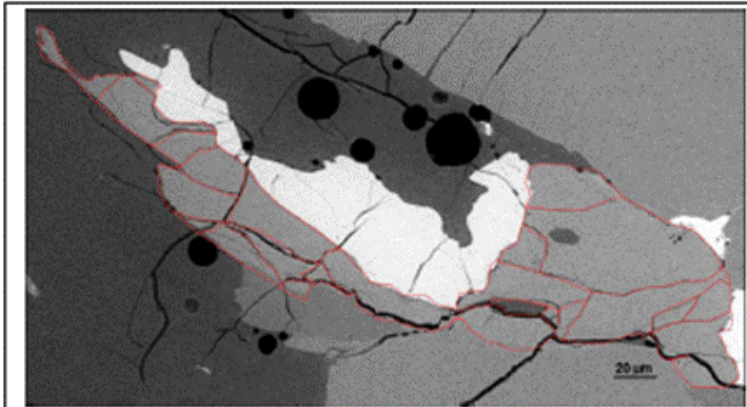
ALHA77005 BSE image fld012_img01 and histogram.
 29 Fracture-free areas.
 Estimated mean radius: 8 μm
 Estimated weighted mean radius: 12 μm



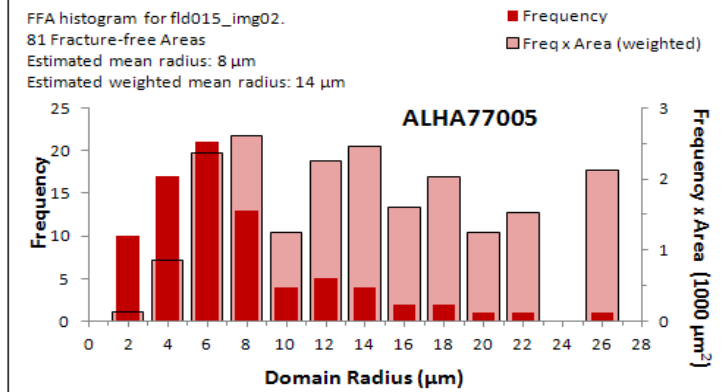
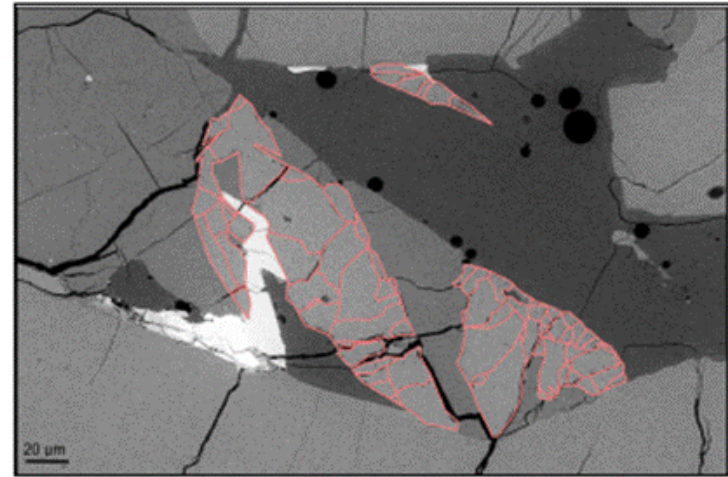
ALHA77005 BSE image fld013_img01 and histogram.
 8 Fracture-free areas.
 Estimated mean radius: 9 μm
 Estimated weighted mean radius: 23 μm



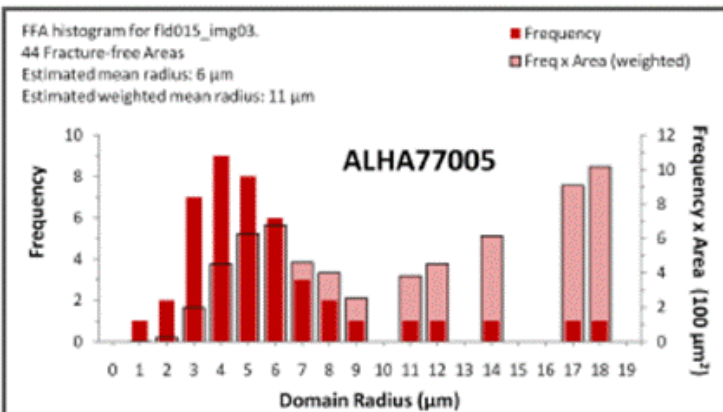
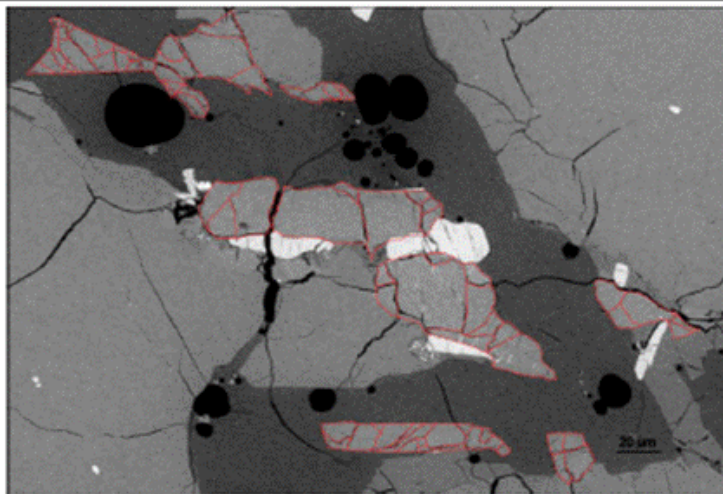
ALHA77005 BSE image fld013_img02 and histogram.
 22 Fracture-free areas.
 Estimated mean radius: 7 μm
 Estimated weighted mean radius: 10 μm



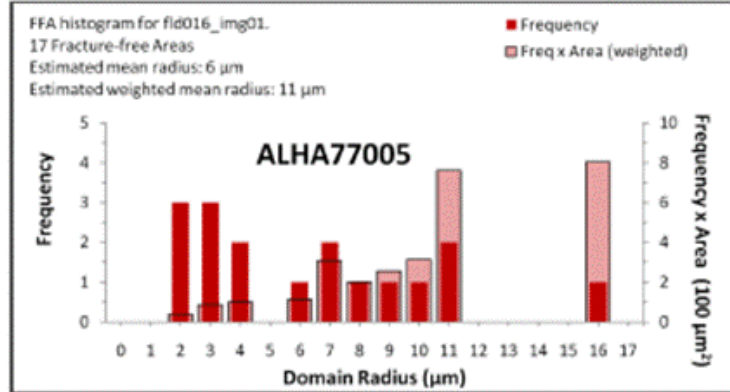
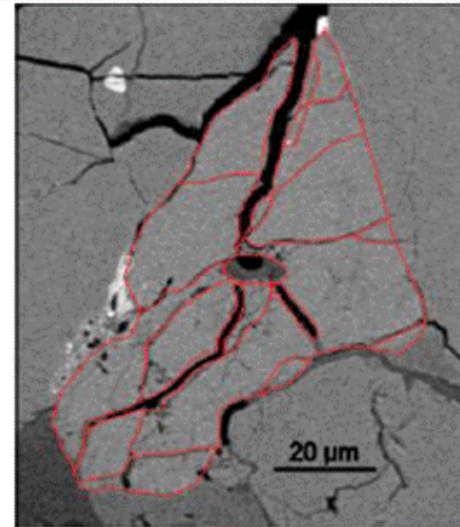
ALHA77005 BSE image fld015_img01 and histogram.
 22 Fracture-free areas.
 Estimated mean radius: 13 μm
 Estimated weighted mean radius: 18 μm



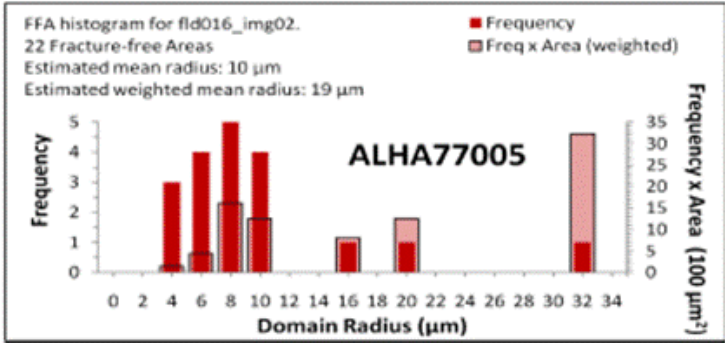
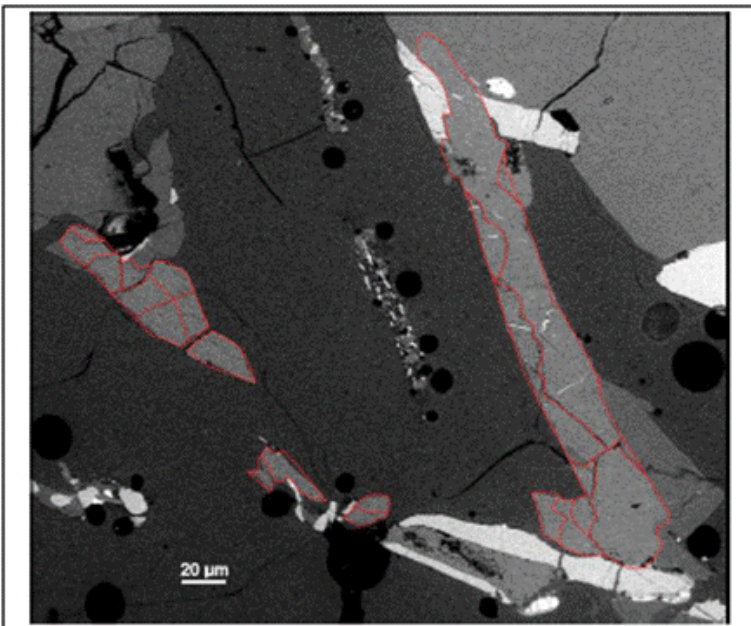
ALHA77005 BSE image fld015_img02 and histogram.
 81 Fracture-free areas.
 Estimated mean radius: 8 μm
 Estimated weighted mean radius: 14 μm



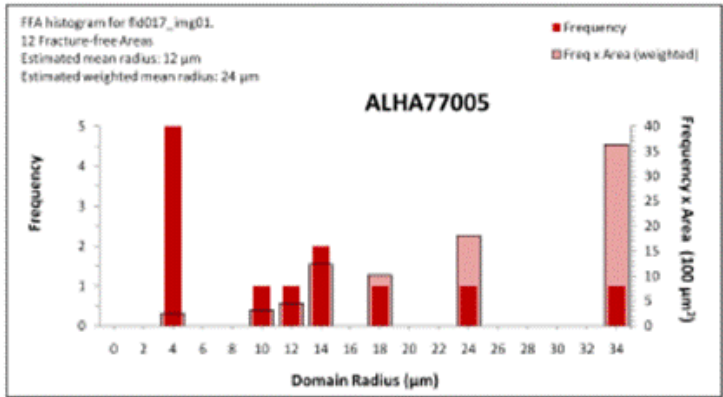
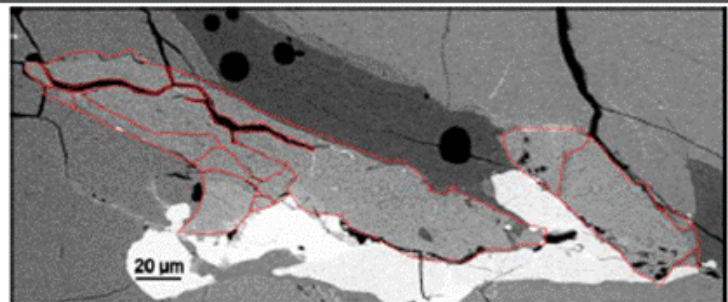
ALHA77005 BSE image fld015_img03 and histogram.
 44 Fracture-free areas.
 Estimated mean radius: 6 μm
 Estimated weighted mean radius: 11 μm



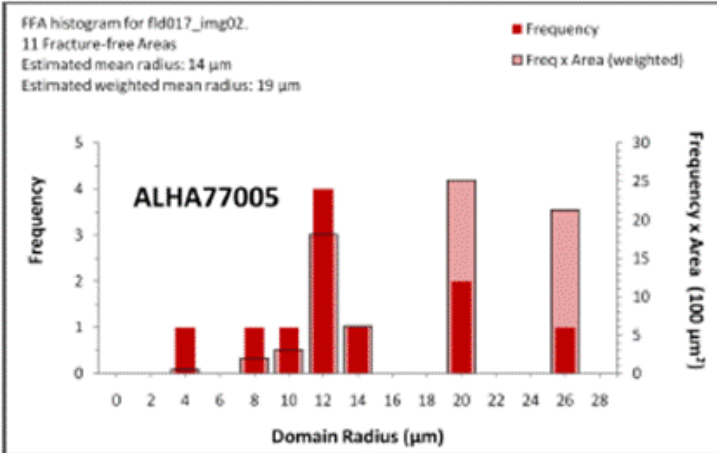
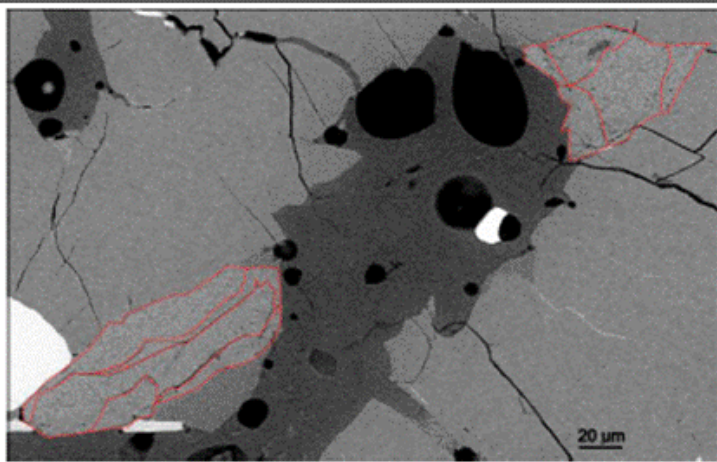
ALHA77005 BSE image fld016_img01 and histogram.
 17 Fracture-free areas.
 Estimated mean radius: 6 μm
 Estimated weighted mean radius: 11 μm



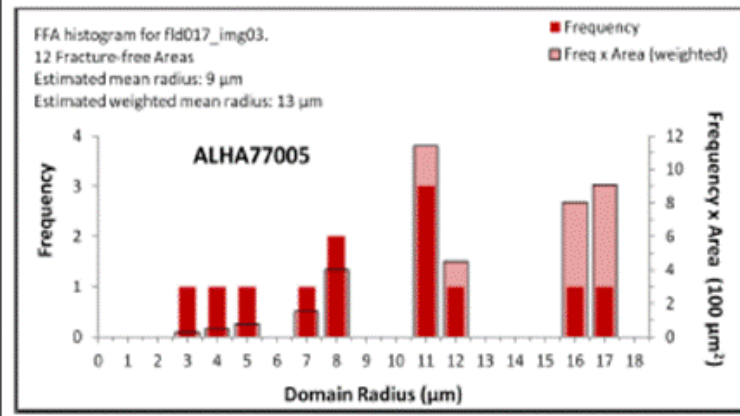
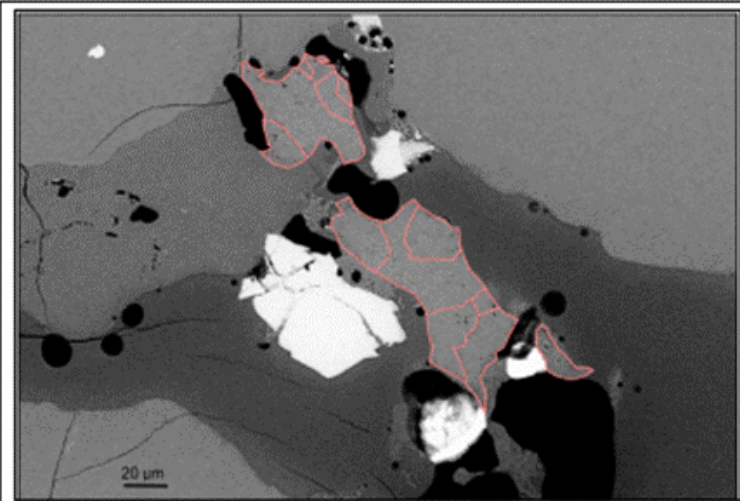
ALHA77005 BSE image fld016_img02 and histogram.
 22 Fracture-free areas.
 Estimated mean radius: 10 μm
 Estimated weighted mean radius: 19 μm



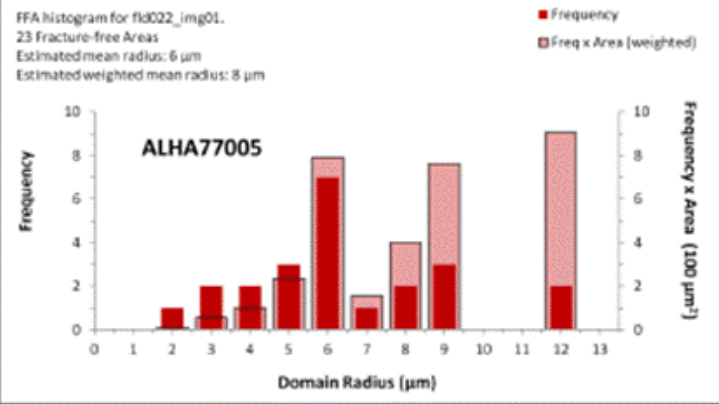
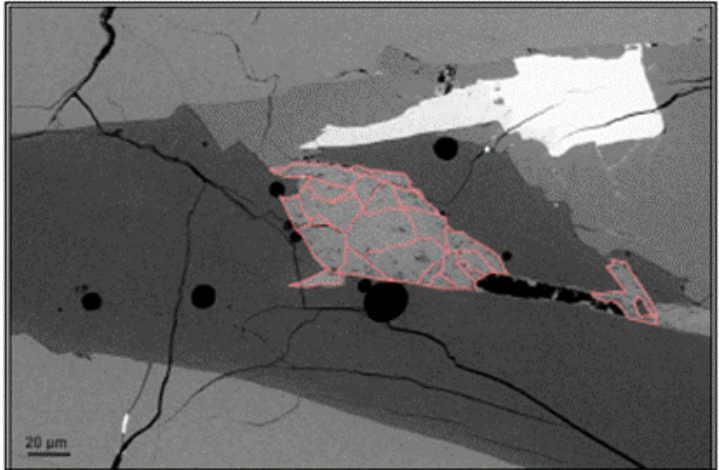
ALHA77005 BSE image fld017_img01 and histogram.
 12 Fracture-free areas.
 Estimated mean radius: 12 μm
 Estimated weighted mean radius: 24 μm



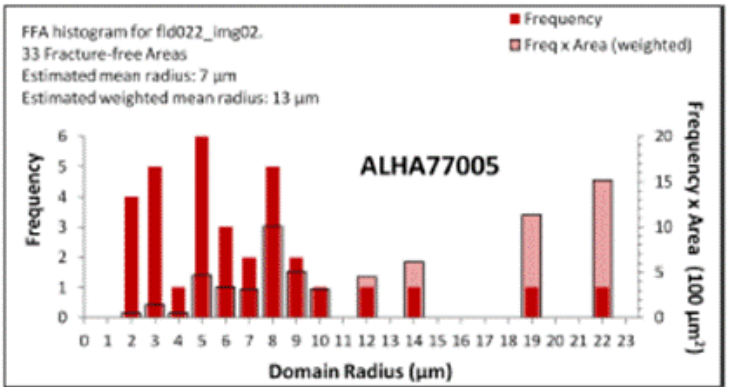
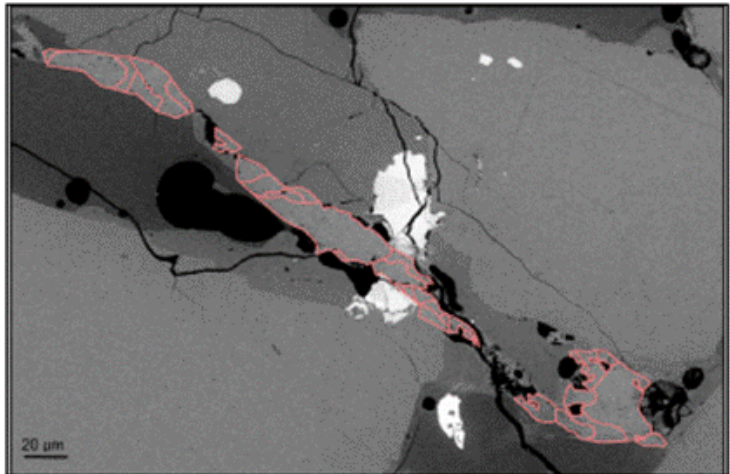
ALHA77005 BSE image fld017_img02 and histogram.
 11 Fracture-free areas.
 Estimated mean radius: 14 μm
 Estimated weighted mean radius: 19 μm



ALHA77005 BSE image fld017_img03 and histogram.
 12 Fracture-free areas.
 Estimated mean radius: 9 μm
 Estimated weighted mean radius: 13 μm



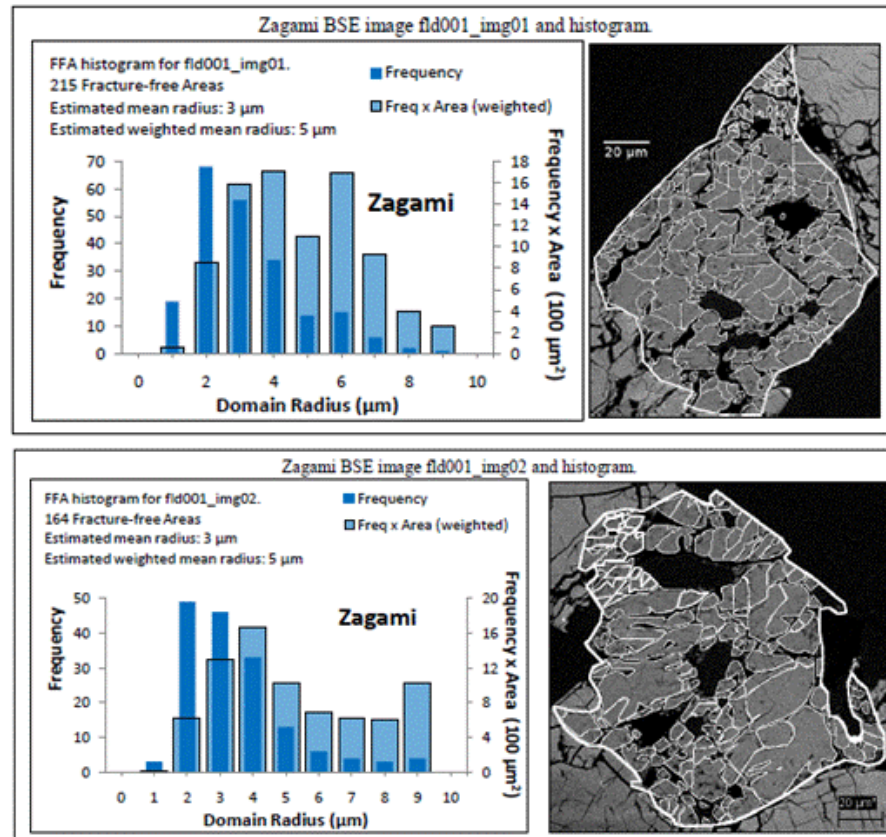
ALHA77005 BSE image fld022_img01 and histogram.
 23 Fracture-free areas.
 Estimated mean radius: 6 μm
 Estimated weighted mean radius: 8 μm

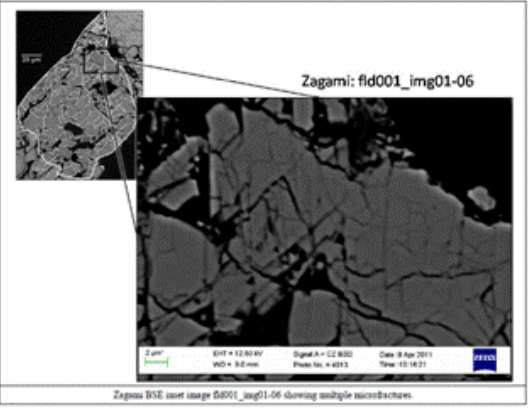
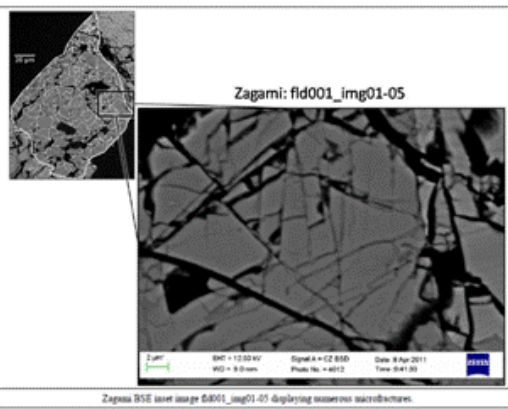
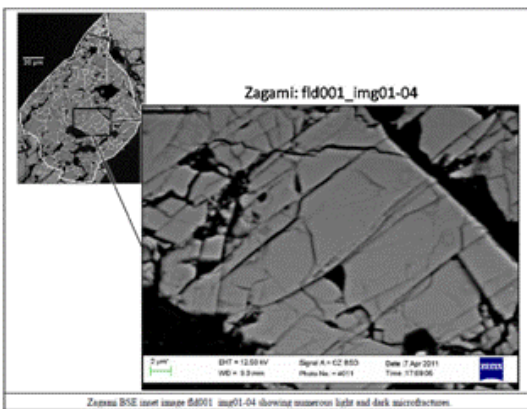
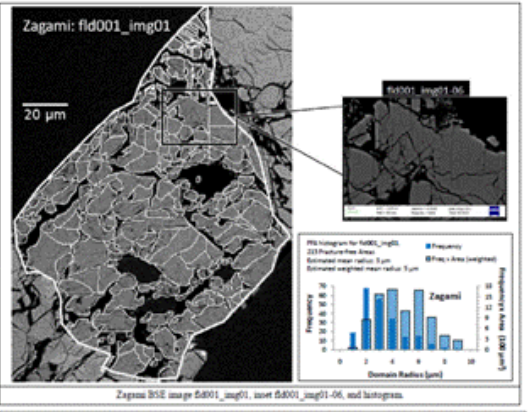
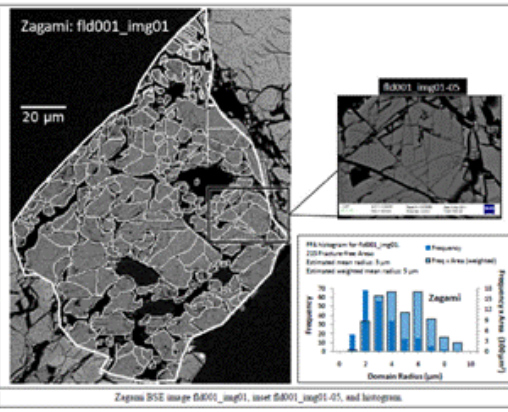
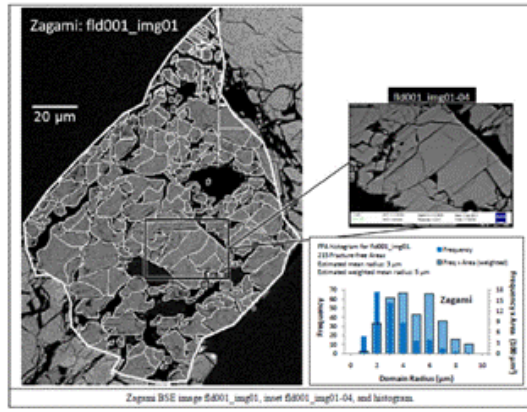


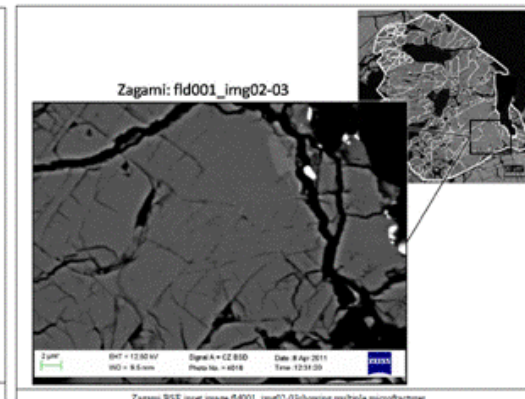
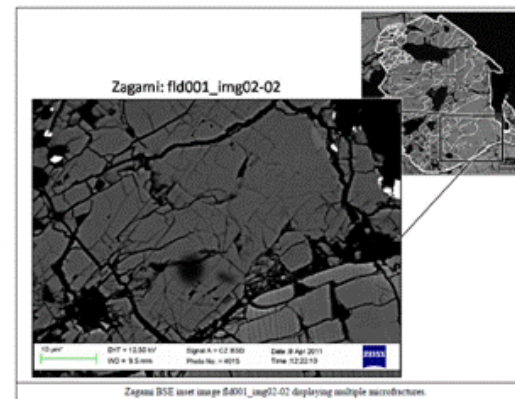
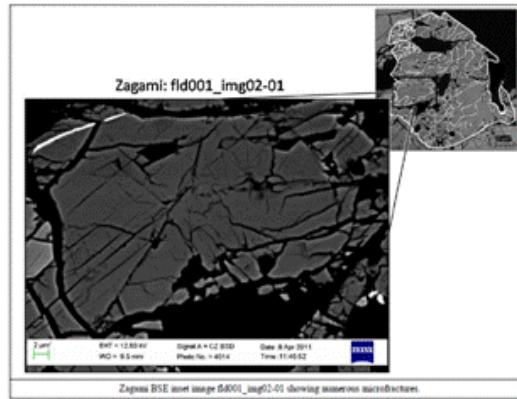
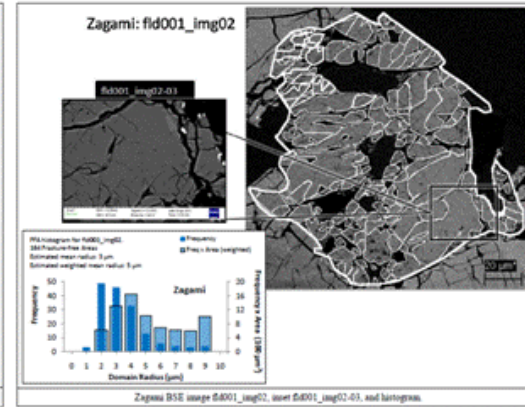
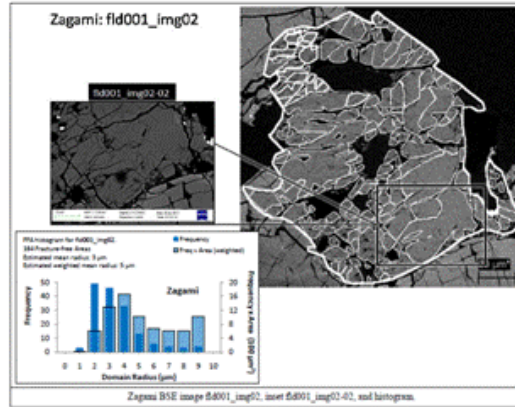
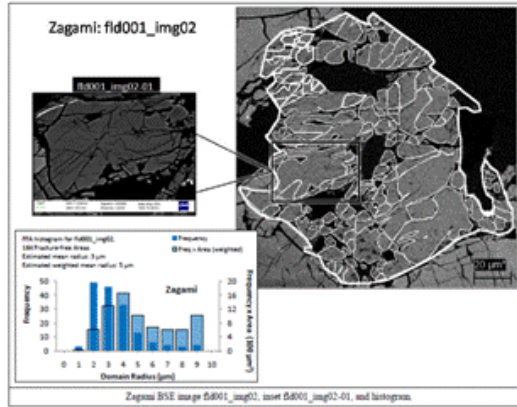
ALHA77005 BSE image fld022_img02 and histogram.
 33 Fracture-free areas.
 Estimated mean radius: 7 μm
 Estimated weighted mean radius: 13 μm

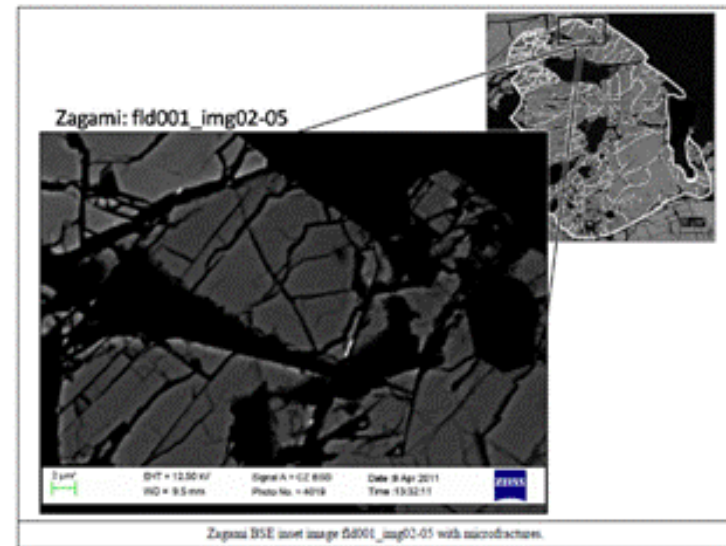
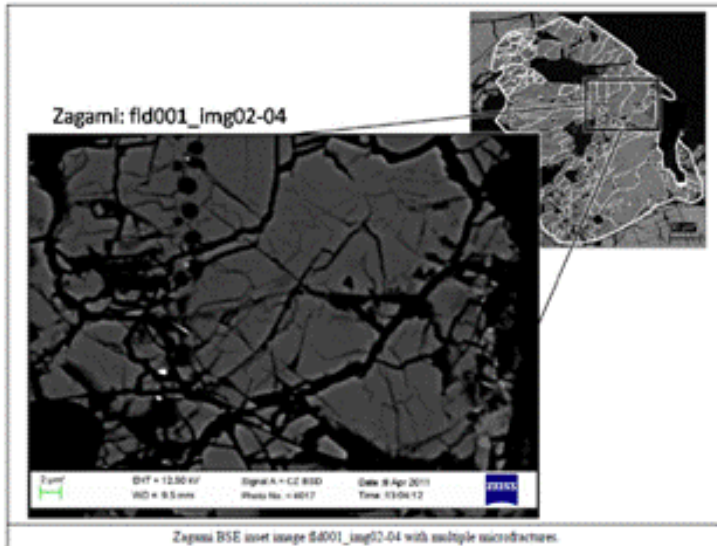
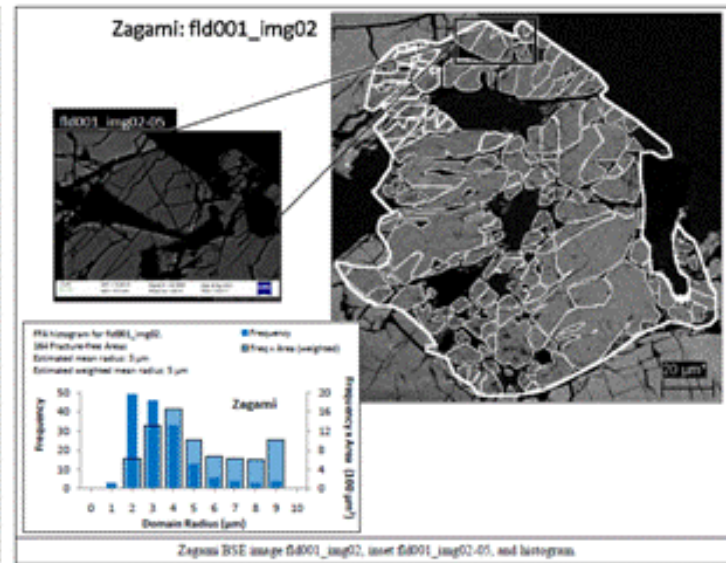
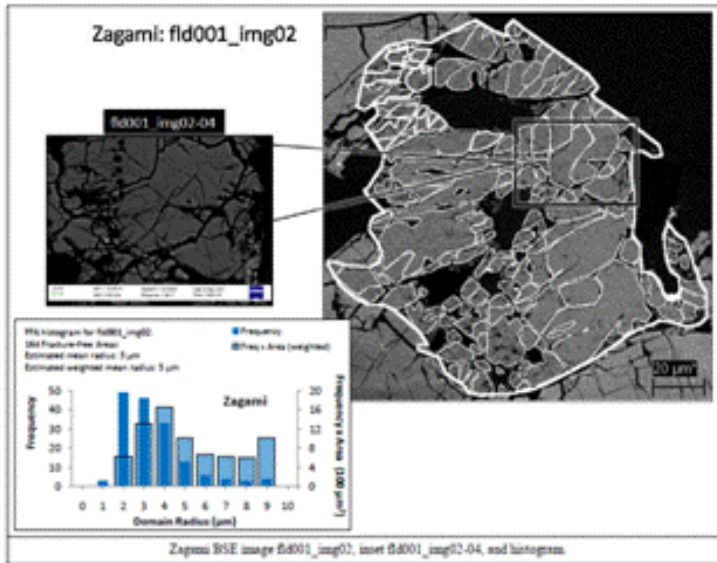
APPENDIX E ZAGAMI MICROFRACTURES

The following images are close-up views of merrillite (phosphate) minerals. White traces on each image represent fracture-free areas (FFA) from each merrillite. All histograms show a radius distribution defined by FFAs for each respective merrillite. Left axis represents the raw frequency of each radius (blue solid bars), and the right axis illustrates the weighted frequency (pale blue bars with borders) of the larger FFAs. All insets display a close-up view of evident microfractures. The appearance of microfractures suggests rapid pathways for helium diffusion. All images were retrieved from thin section (Zagami 4709-1) supplied by the American Museum of Natural History, New York, NY.



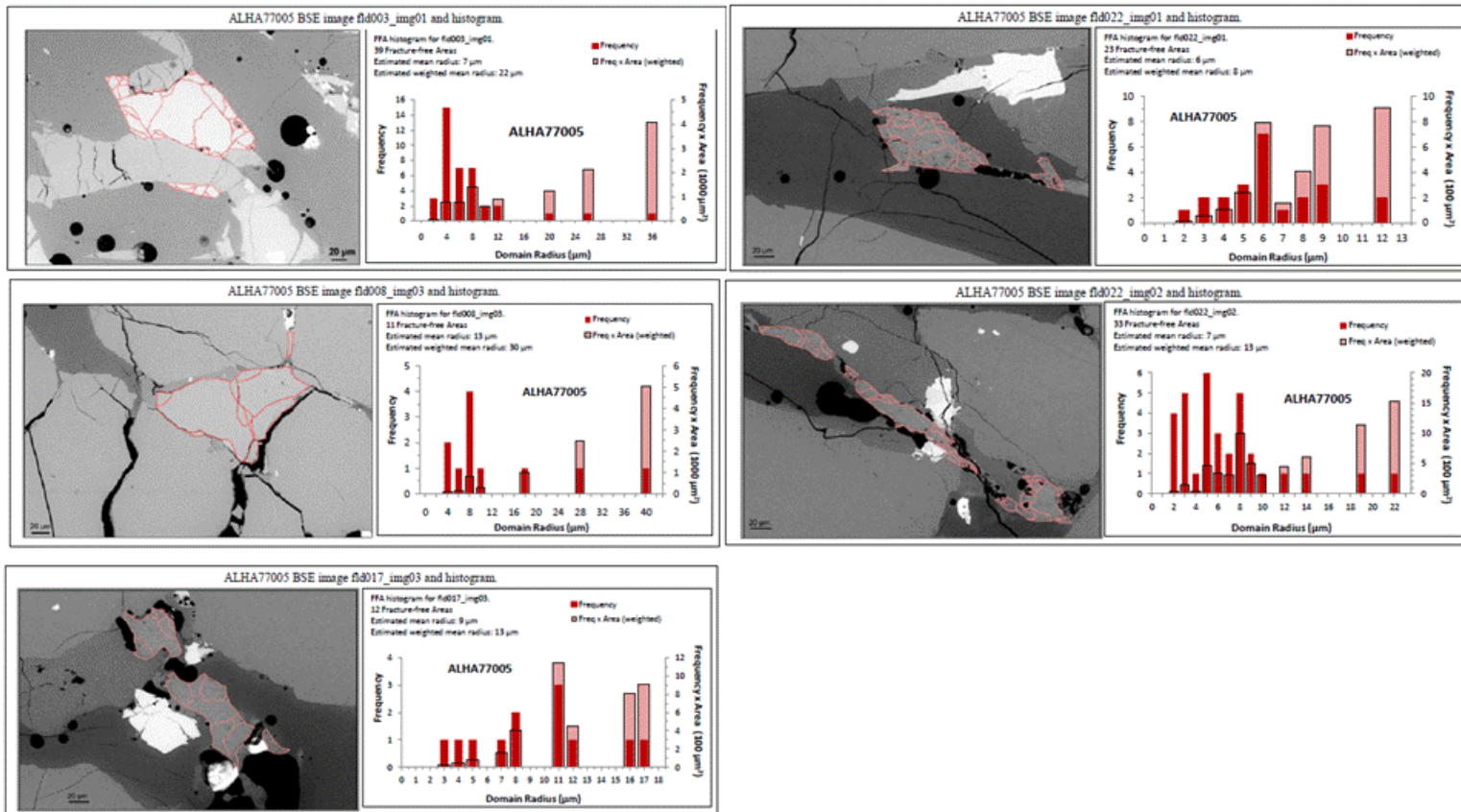


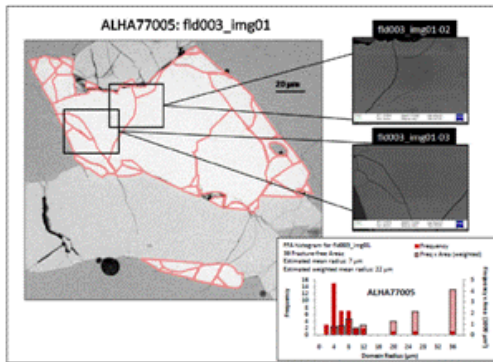




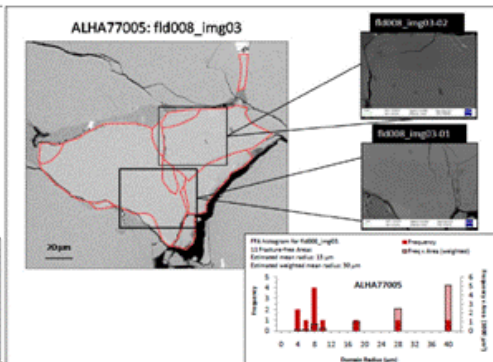
APPENDIX F ALHA77005 MICROFRACTURES

The following images are close-up views of merrillite minerals. Red traces on each image represent fracture-free areas (FFA) from each merrillite. All histograms show a radius distribution defined by FFAs for each respective merrillite. Left axis represents the raw frequency of each radius (red solid bars), and the right axis illustrates the weighted frequency (pale red bars with borders) of the larger FFAs. The appearance of microfractures suggests rapid pathways for helium diffusion. All images were retrieved from thin section (ALHA77005 120) supplied by NASA.

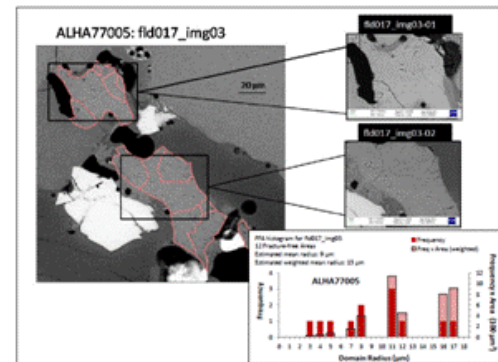




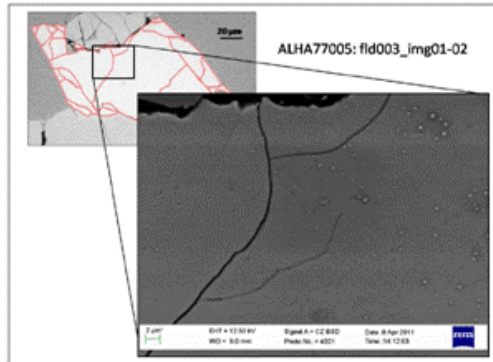
ALHA77005 BSE image f8003_img01 and histogram. Insets f8003_img01-02 and f8003_img01-03 display close-up views of possible macrofractures.



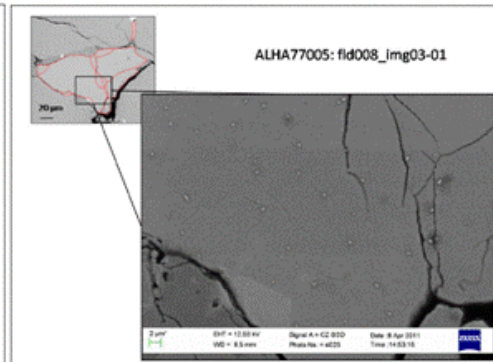
ALHA77005 BSE image f8008_img03 and histogram. Insets f8008_img03-01 and f8008_img03-02 display a close-up view of possible macrofractures.



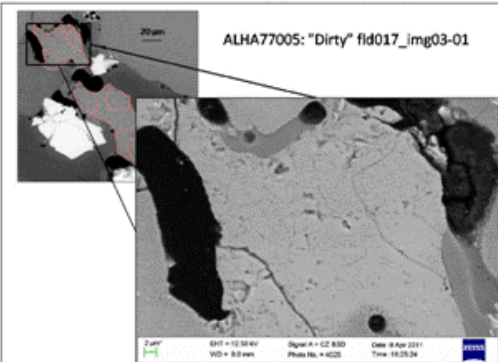
ALHA77005 BSE image f8017_img03 and histogram. Insets f8017_img03-01 and f8017_img03-02 display a close-up view of macrofractures and other features separating between domains.



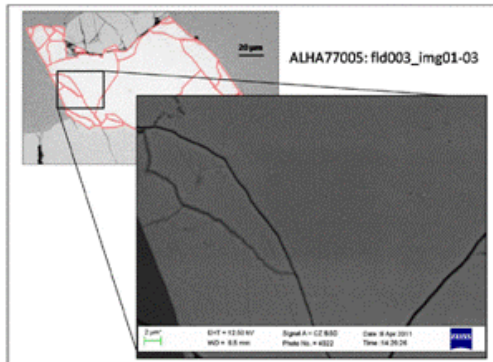
ALHA77005 BSE image f8003_img01-02. Searching for possible macrofractures. Close-up view shows very little evidence of macrofractures.



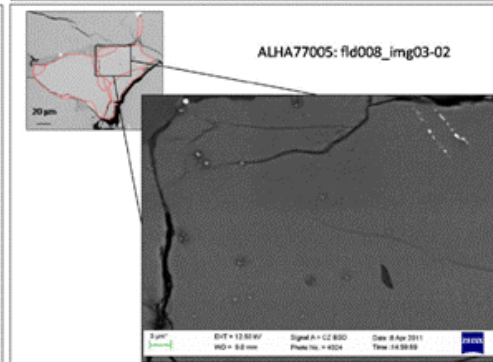
ALHA77005 BSE image f8008_img03-01. Searching for possible macrofractures. Close-up view shows very little evidence of macrofractures.



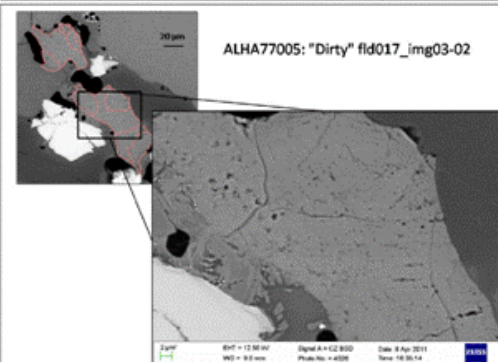
ALHA77005 BSE image f8017_img03-01. Close-up view shows some macrofractures, cracks, and fissures.



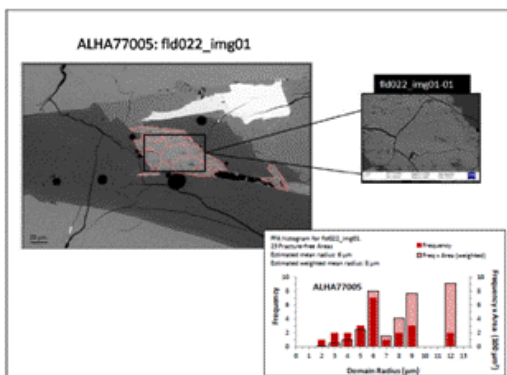
ALHA77005 BSE image f8003_img01-03. Searching for possible macrofractures. Close-up view shows very little evidence of macrofractures.



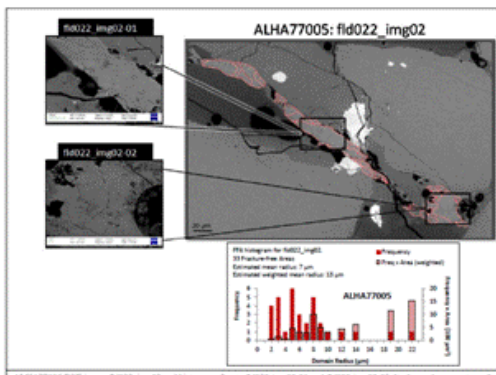
ALHA77005 BSE image f8008_img03-02. Searching for possible macrofractures. Close-up view shows very little evidence of macrofractures.



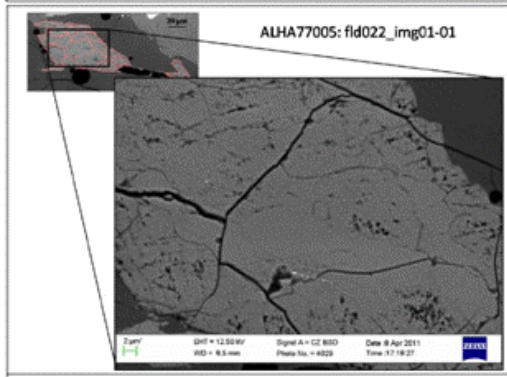
ALHA77005 BSE image f8017_img03-02. Close-up view shows some macrofractures, cracks, and fissures.



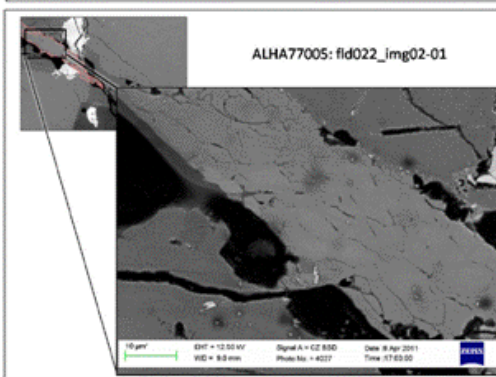
ALHA77005 BSE image fld022_img01 and histogram. Inset fld022_img01-01 displays a close-up view of possible microfractures.



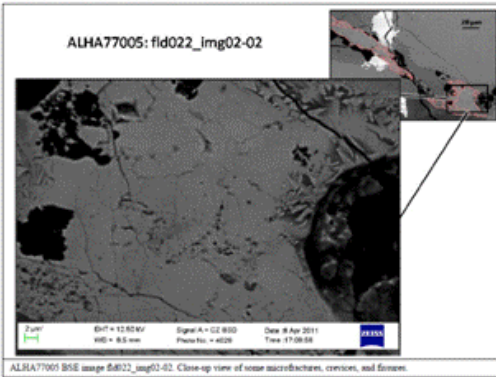
ALHA77005 BSE image fld022_img02 and histogram. Insets fld022_img02-01 and fld022_img02-02 display a close-up view of possible microfractures.



ALHA77005 BSE image fld022_img01-01. Close-up view shows some microfractures, cracks, and fissures.



ALHA77005 BSE image fld022_img02-01. Close-up view of microfractures.



ALHA77005 BSE image fld022_img02-02. Close-up view of some microfractures, cracks, and fissures.

APPENDIX G ZAGAMI THERMAL MODELS

The following thermal modeling simulations for Zagami show the relationship between helium fractional loss and maximum shock temperature at varying diffusion domain radii. Each curve represents the diffusion profile per diffusion domain size (refer to the legend of each graph for the range of radii). One comparison is also made with apatite assuming a radius of 50 μm (Ap50 μm , black solid line) and diffusion properties of apatite: $E_a = 32.9$ kcal/mol, $\ln(D_o/a^2) = 13.44/\text{s}$, and $D_o = 50$ cm^2/s (Farley, 2000).

Diffusion domain sizes are calculated from fracture-free area (FFA) data of Zagami phosphates (merrillite) from thin section (Zagami 4709-1). The light gray box represents the post-shock temperature 220 ± 50 $^\circ\text{C}$ (Nyquist *et al.*, 2001) converted to a peak shock temperature range by applying ambient temperatures of Mars. Two tables follow the simulations at the end of this appendix listing all the shock temperatures as calculated from the thermal modeling of Zagami.

Diffusion properties of merrillite:

$E_a = 32.28$ kcal/mol, $\ln(D_o/a^2) = 5.73/\text{s}$, and $D_o = 0.01$ cm^2/s .

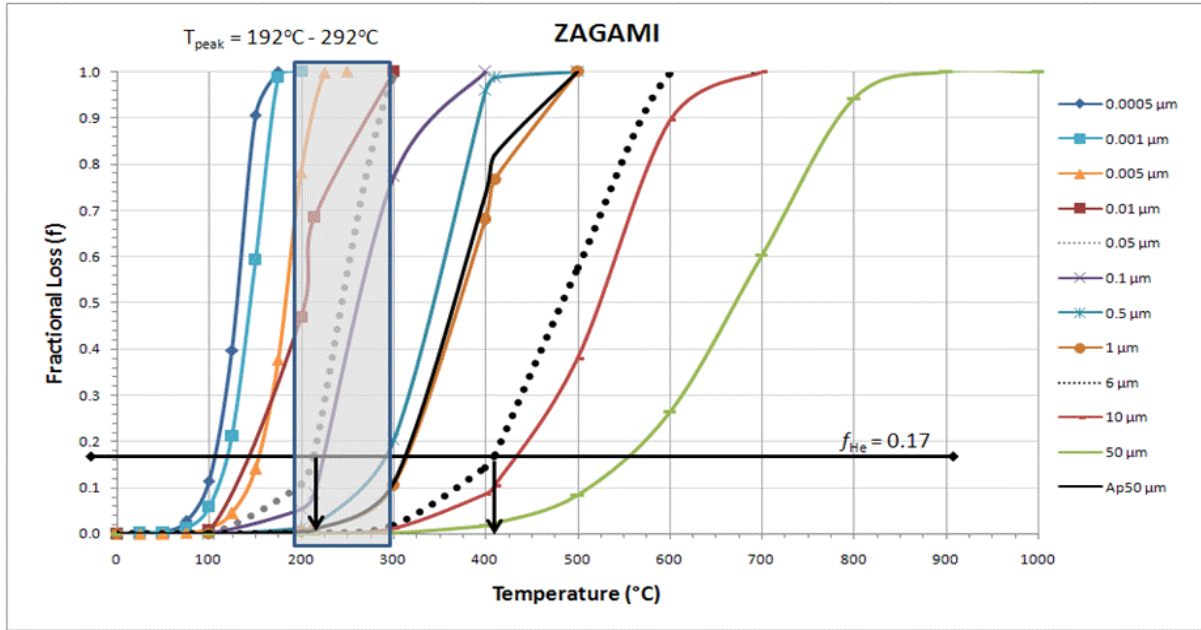
Number of FFAs = 3861 (from 22 phosphates).

Maximum average diffusion domain size = 3.82 μm .

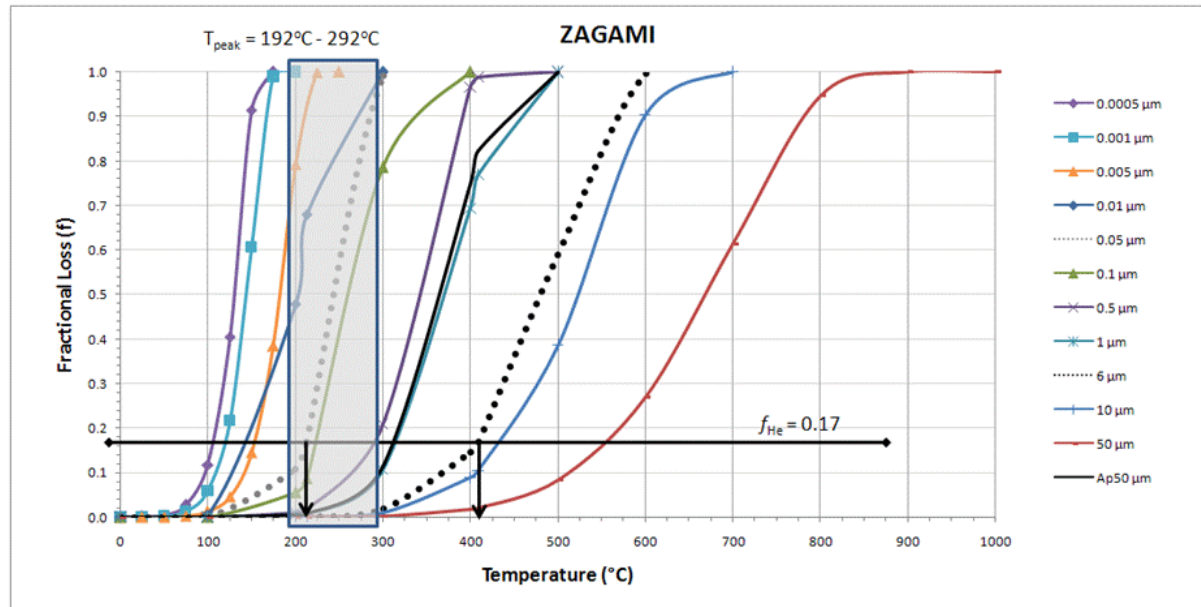
Maximum average weighted diffusion domain size = 6.27 μm (black dotted line).

Diffusion domain size estimate from microfractures = 0.05 μm (light gray dotted line).

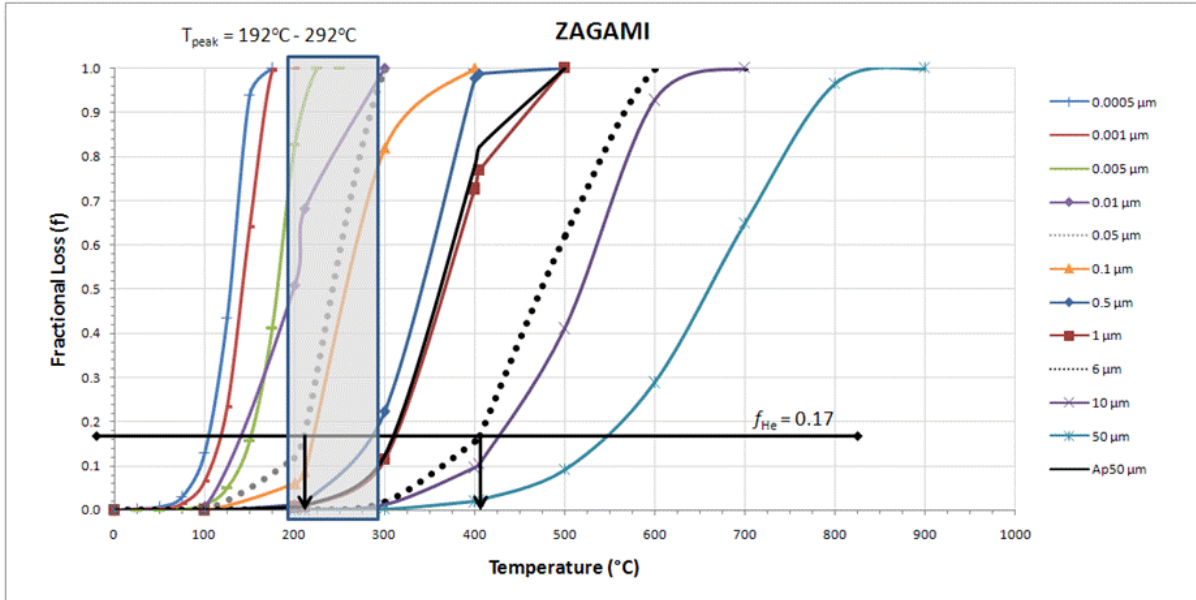
Overall diffusion domain size range for Zagami: 0.05 μm to 6 μm .



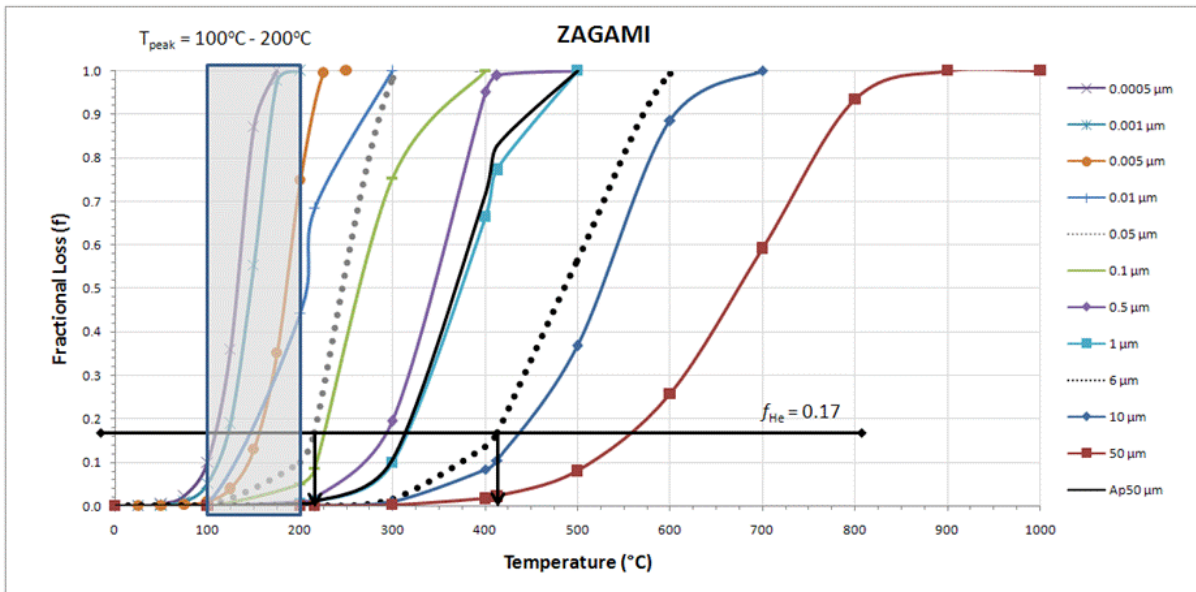
Depth from surface of parent body, $d = 15$ cm.
 Ambient Temperature, $T_s = 21.85^{\circ}\text{C}$. Parent body size, $A = 23$ cm.



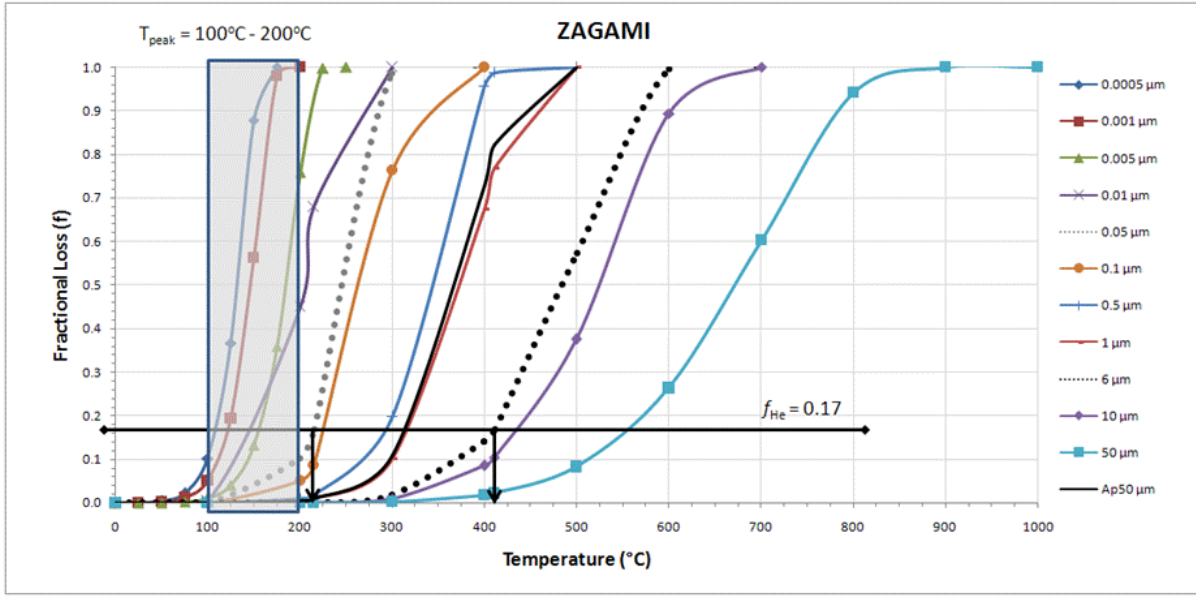
Depth from surface of parent body, $d = 15$ cm.
 Ambient Temperature, $T_s = 21.85^{\circ}\text{C}$. Parent body size, $A = 25$ cm.



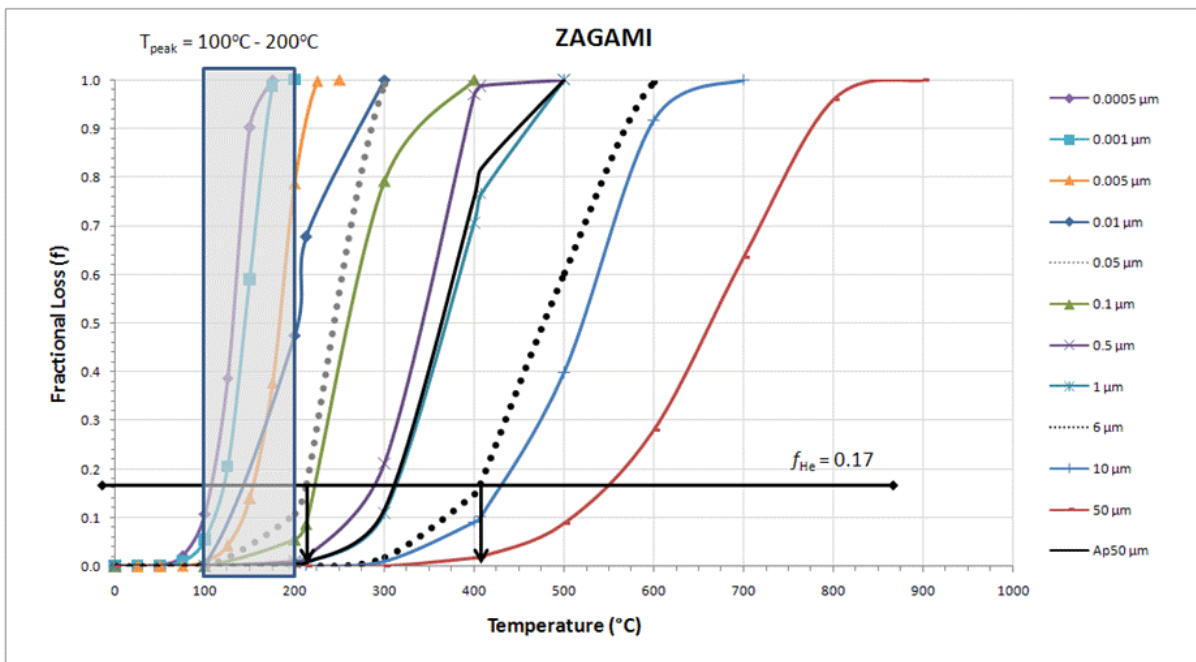
Depth from surface of parent body, $d = 15$ cm.
 Ambient Temperature, $T_s = 21.85^{\circ}\text{C}$. Parent body size, $A = 35$ cm.



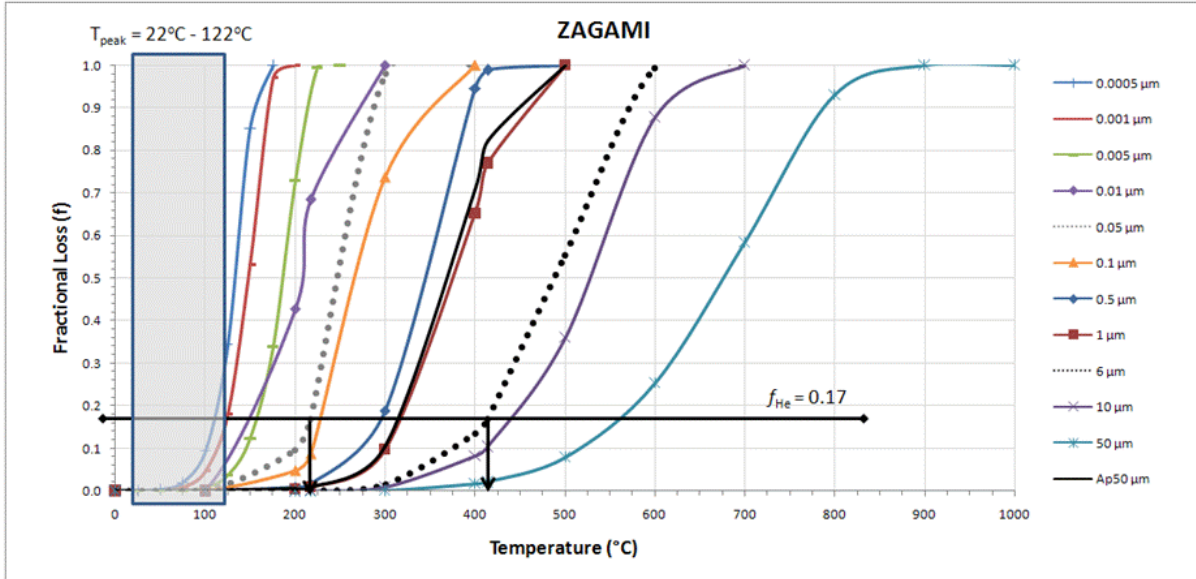
Depth from surface of parent body, $d = 15$ cm.
 Ambient temperature, $T_s = -70^{\circ}\text{C}$. Parent body size, $A = 23$ cm.



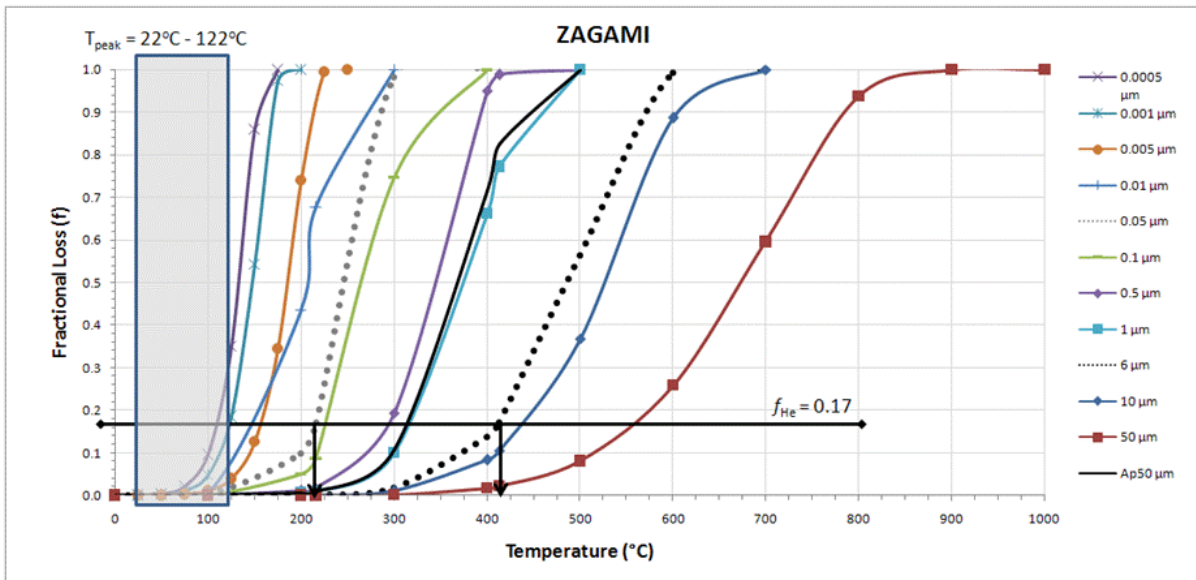
Depth from surface of parent body, $d = 15$ cm.
 Ambient Temperature, $T_s = -70^{\circ}\text{C}$. Parent body size, $A = 25$ cm.



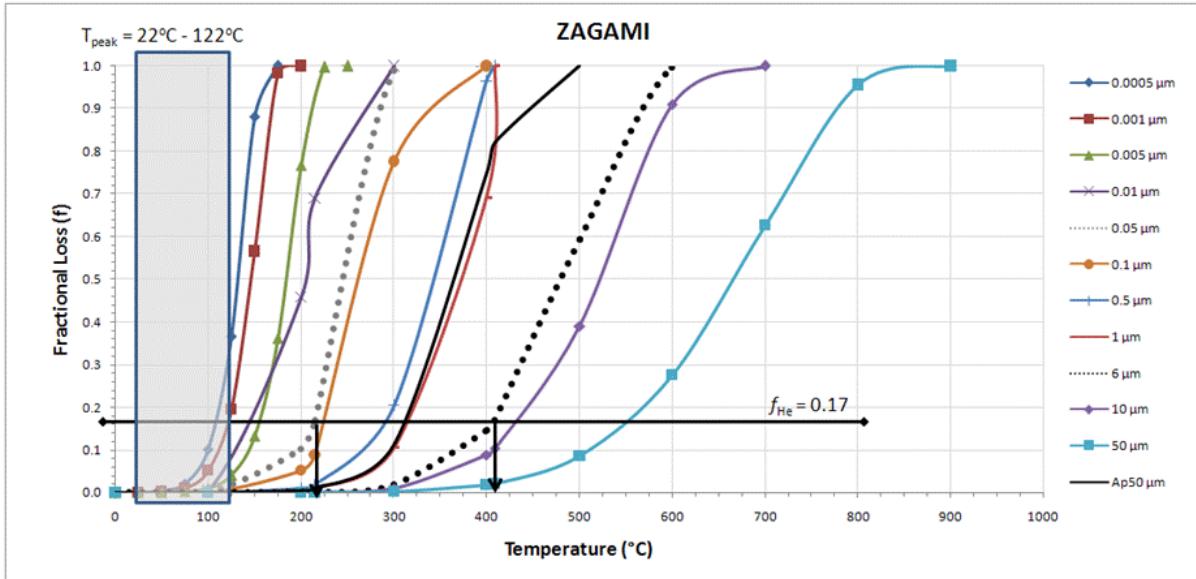
Depth from surface of parent body, $d = 15$ cm.
 Ambient Temperature, $T_s = -70^{\circ}\text{C}$. Parent body size, $A = 35$ cm.



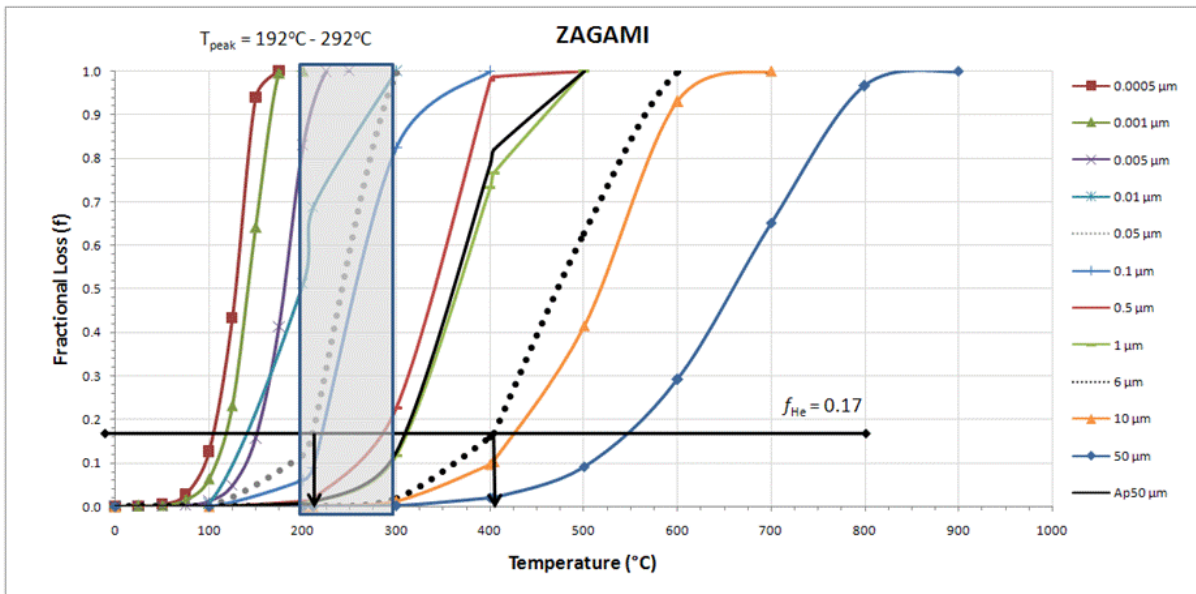
Depth from surface of parent body, $d = 15$ cm.
 Ambient Temperature, $T_s = -148^{\circ}\text{C}$. Parent body size, $A = 23$ cm.



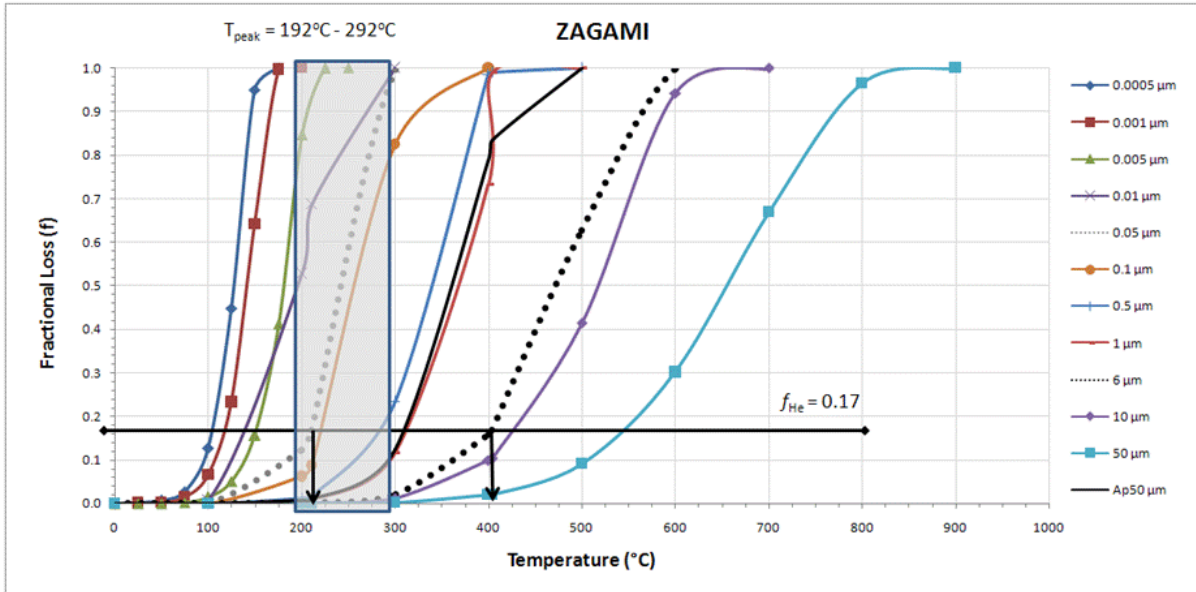
Depth from surface of parent body, $d = 15$ cm.
 Ambient Temperature, $T_s = -148^{\circ}\text{C}$. Parent body size, $A = 25$ cm.



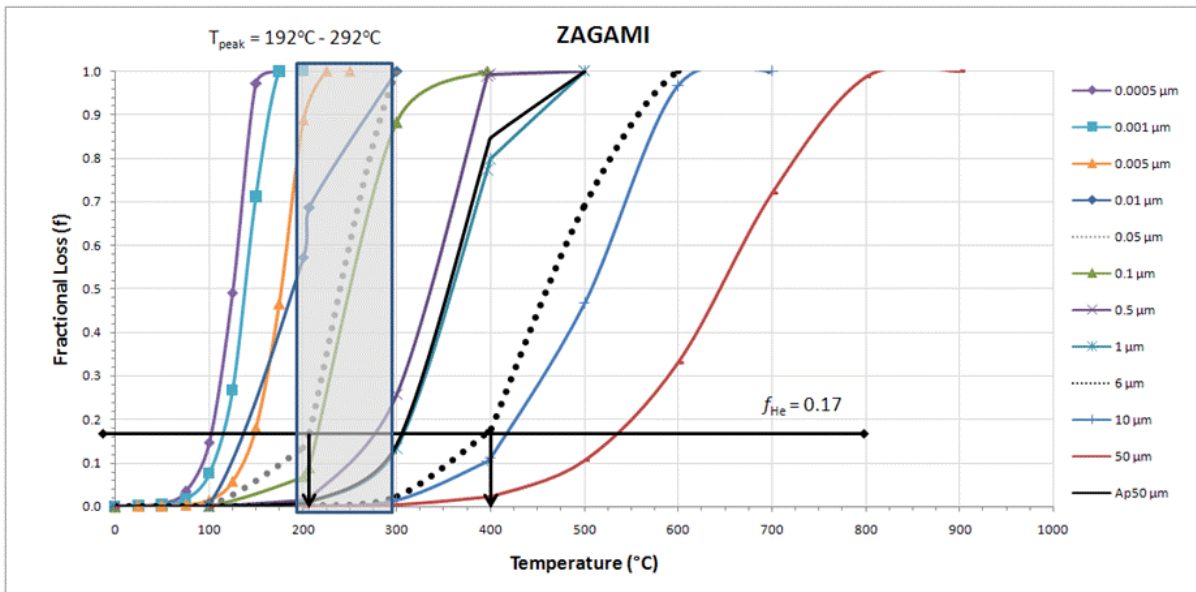
Depth from surface of parent body, $d = 15$ cm.
 Ambient Temperature, $T_s = -148^{\circ}\text{C}$. Parent body size, $A = 35$ cm.



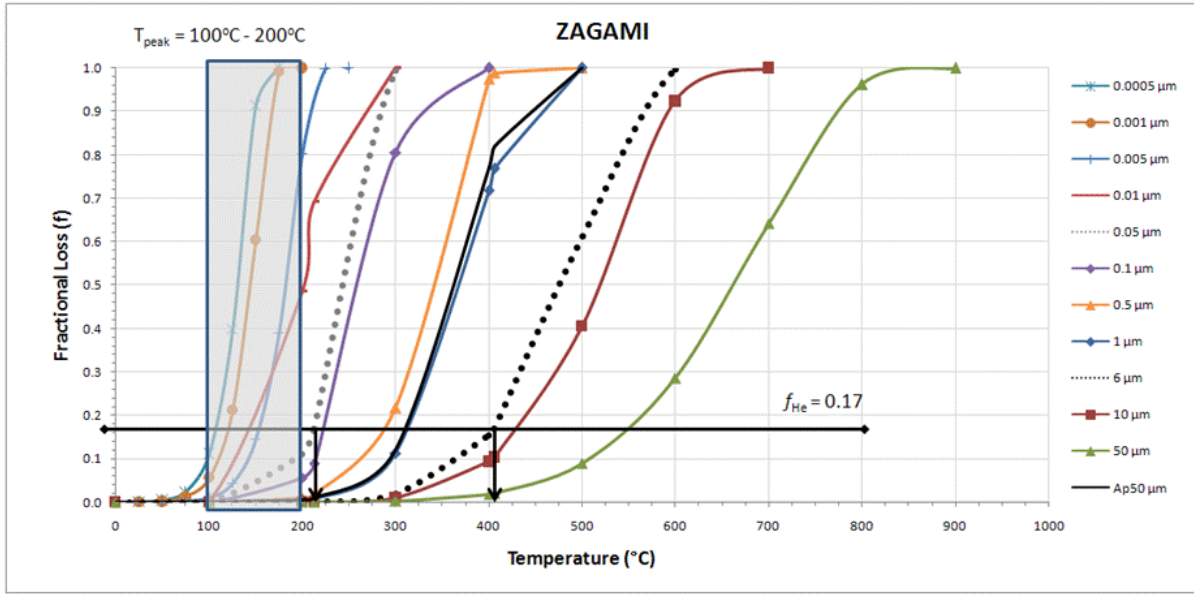
Depth from surface of parent body, $d = 18$ cm.
 Ambient Temperature, $T_s = 21.85^{\circ}\text{C}$. Parent body size, $A = 23$ cm.



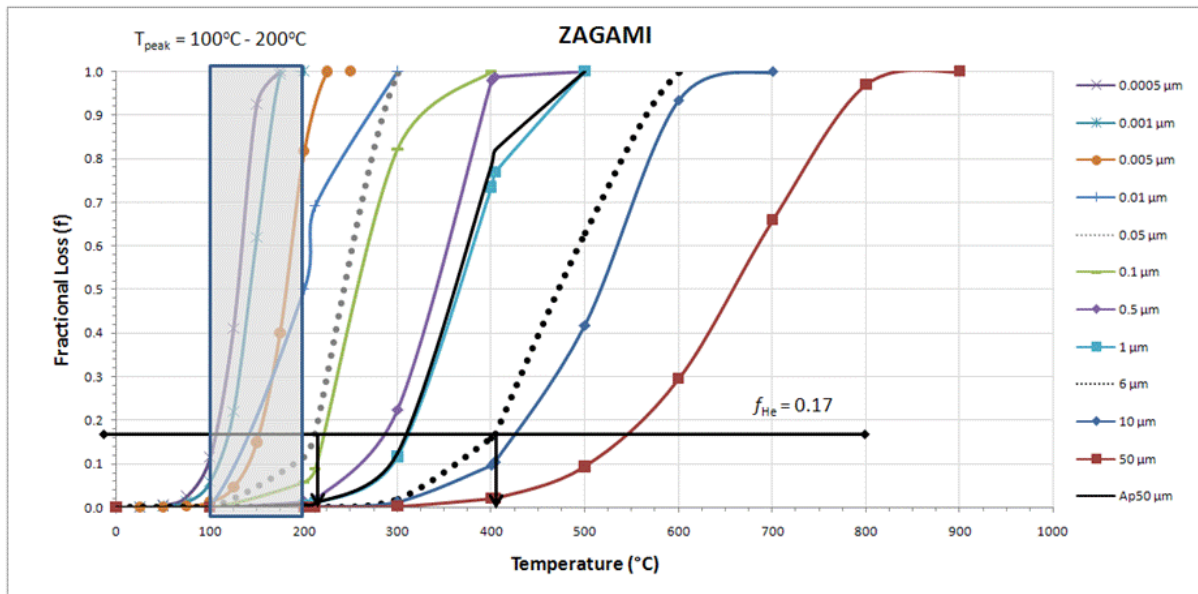
Depth from surface of parent body, $d = 18$ cm.
 Ambient Temperature, $T_s = 21.85^{\circ}\text{C}$. Parent body size, $A = 25$ cm.



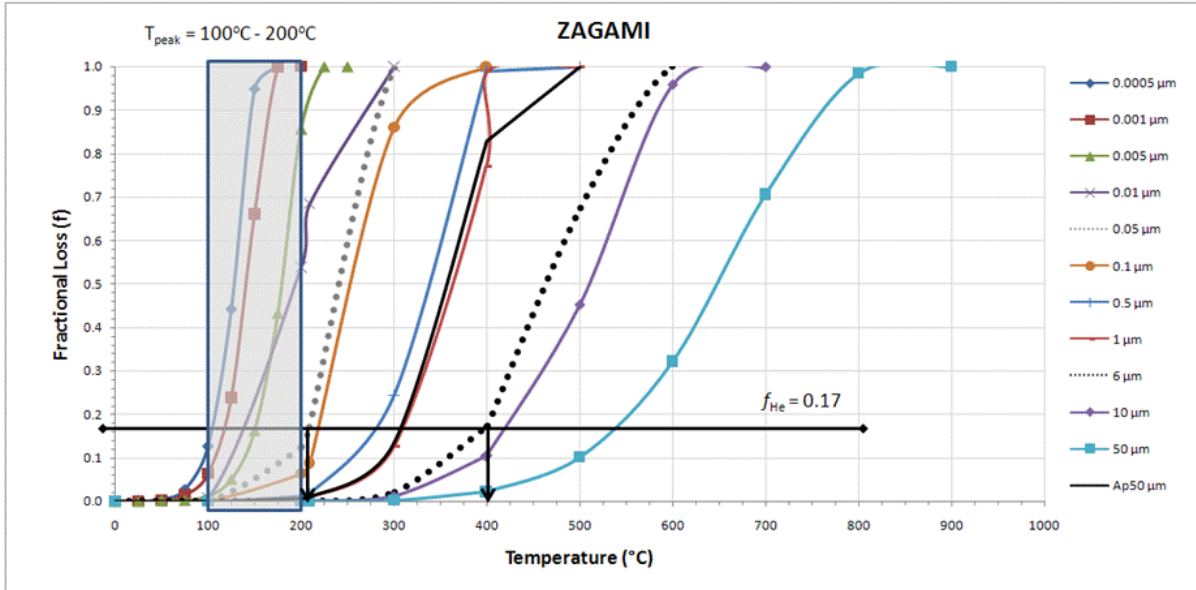
Depth from surface of parent body, $d = 18$ cm.
 Ambient Temperature, $T_s = 21.85^{\circ}\text{C}$. Parent body size, $A = 35$ cm.



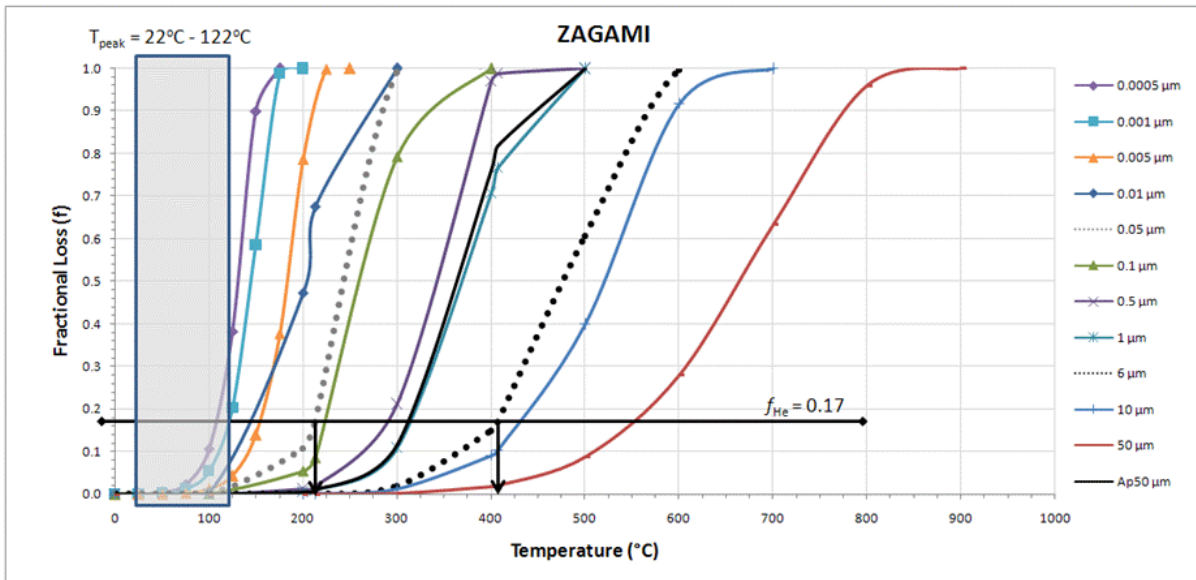
Depth from surface of parent body, $d = 18$ cm.
 Ambient Temperature, $T_s = -70^{\circ}\text{C}$. Parent body size, $A = 23$ cm.



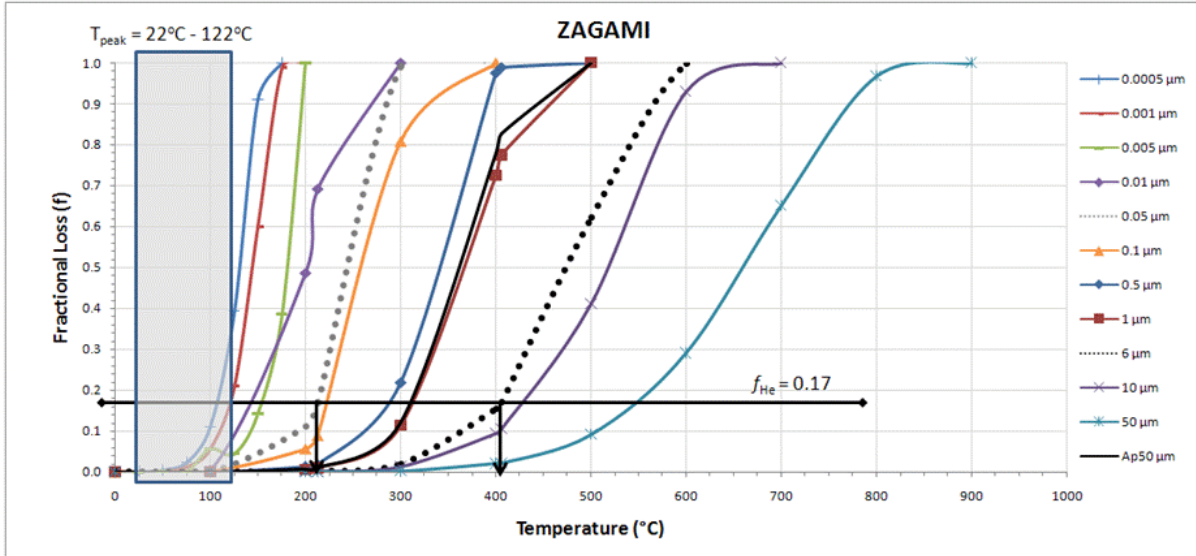
Depth from surface of parent body, $d = 18$ cm.
 Ambient Temperature, $T_s = -70^{\circ}\text{C}$. Parent body size, $A = 25$ cm.



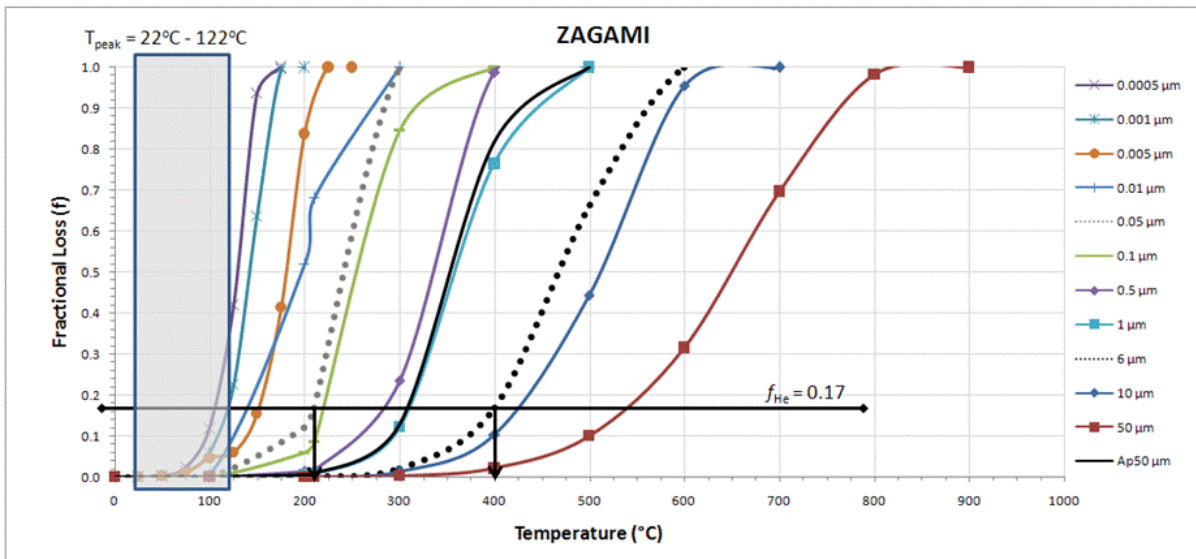
Depth from surface of parent body, $d = 18$ cm.
 Ambient Temperature, $T_s = -70^{\circ}\text{C}$. Parent body size, $A = 35$ cm.



Depth from surface of parent body, $d = 18$ cm.
 Ambient Temperature, $T_s = -148^{\circ}\text{C}$. Parent body size, $A = 23$ cm.



Depth from surface of parent body, $d = 18$ cm.
 Ambient Temperature, $T_s = -148^{\circ}\text{C}$. Parent body size, $A = 25$ cm.



Depth from surface of parent body, $d = 35$ cm.
 Ambient Temperature, $T_s = -148^{\circ}\text{C}$. Parent body size, $A = 35$ cm.

Shock temperatures from thermal modeling at $d = 15$ cm and $d = 18$ cm. d = depth from surface of parent body. T_s = ambient temperature of Mars. A = parent body size. Overall shock temperature averages: $\sim 213^\circ\text{C}$ at $0.05\ \mu\text{m}$ and $\sim 407^\circ\text{C}$ at $6\ \mu\text{m}$.

$d=15$ cm	$T_s = 22^\circ\text{C}$		$T_s = -70^\circ\text{C}$		$T_s = -148^\circ\text{C}$		
	A	$0.05\ \mu\text{m}$	$6\ \mu\text{m}$	$0.05\ \mu\text{m}$	$6\ \mu\text{m}$	$0.05\ \mu\text{m}$	$6\ \mu\text{m}$
23		214	410	216	413	217	414
25		213	409	215	411	216	413
35		211	405	213	407	215	409
avg		212.67	408	214.67	410.33	216	412
std dev		1.53	2.65	1.53	3.06	1	2.65

$d=18$ cm	$T_s = 22^\circ\text{C}$		$T_s = -70^\circ\text{C}$		$T_s = -148^\circ\text{C}$		
	A	$0.05\ \mu\text{m}$	$6\ \mu\text{m}$	$0.05\ \mu\text{m}$	$6\ \mu\text{m}$	$0.05\ \mu\text{m}$	$6\ \mu\text{m}$
23		211	404	213	406	213	407
25		211	404	212	404	213	406
35		207	397	209	399	210	400
avg		209.67	401.67	211.33	403	212	404.33
std dev		2.31	4.04	2.08	3.61	1.73	3.79

APPENDIX H ALHA77005 THERMAL MODELS

The following thermal modeling simulations for ALHA77005 show the relationship between helium fractional loss and maximum shock temperature at varying diffusion domain radii. Each curve represents the diffusion profile per diffusion domain size (refer to the legend of each graph for the range of radii). One comparison is also made with apatite assuming a radius of 50 μm (Ap50 μm , black solid line) and diffusion properties of apatite: $E_a = 32.9$ kcal/mol, $\ln(D_o/a^2) = 13.44/\text{s}$, and $D_o = 50$ cm^2/s (Farley, 2000).

Diffusion domain sizes are calculated from fracture-free area (FFA) data of ALHA77005 phosphates (merrillite) from thin section (ALHA77005 120). The light gray box represents the post-shock temperature 450-600 $^{\circ}\text{C}$ (Nyquist *et al.*, 2001) converted to a peak shock temperature range by applying ambient temperatures of Mars. Two tables follow the simulations at the end of this appendix listing all the shock temperatures calculated from the thermal modeling of ALHA77005.

Diffusion properties of merrillite:

$E_a = 32.28$ kcal/mol, $\ln(D_o/a^2) = 5.73/\text{s}$, and $D_o = 0.01$ cm^2/s .

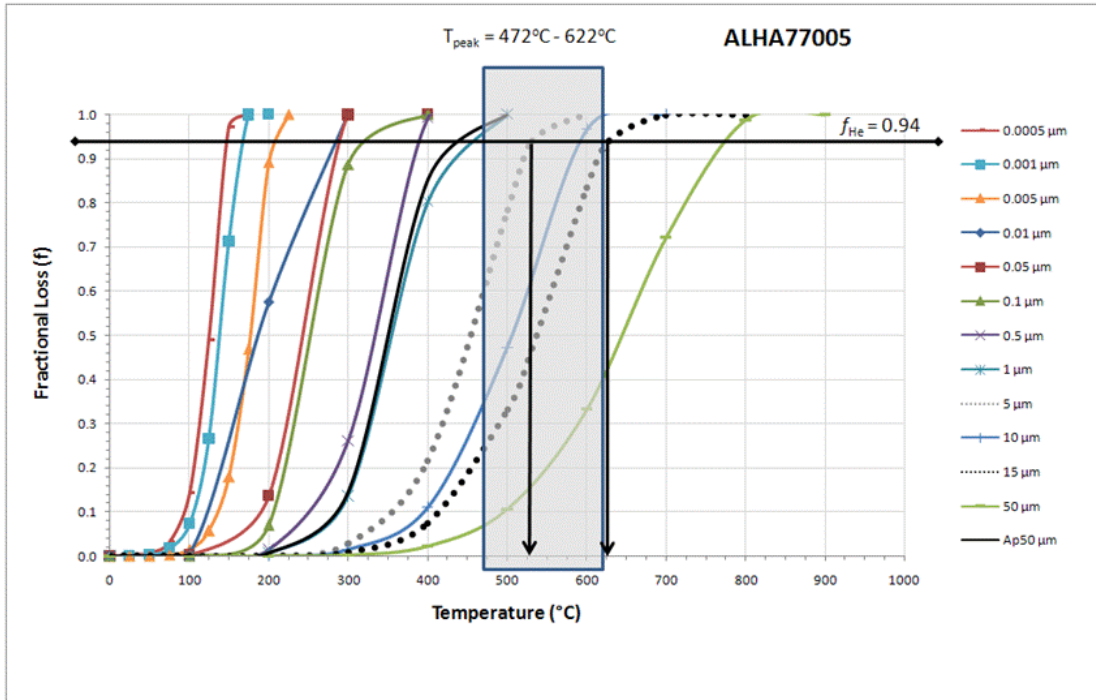
Number of FFAs = 1130 (from 34 phosphates).

Maximum average diffusion domain size = 8.82 μm .

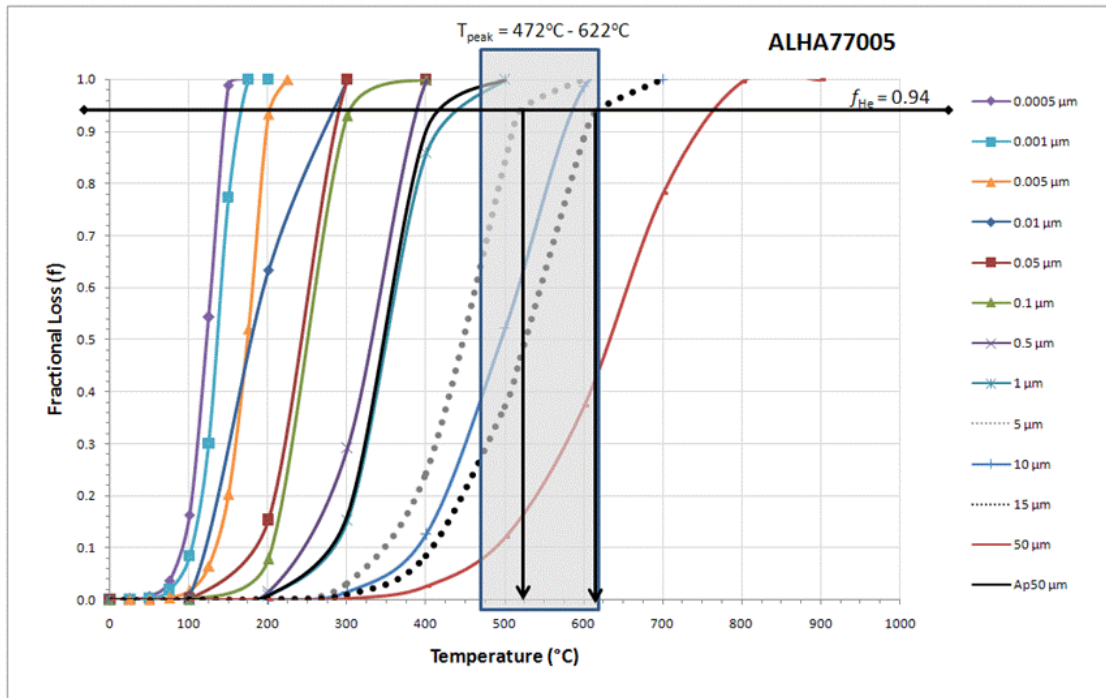
Maximum average weighted diffusion domain size = 15.29 μm (black dotted line).

Diffusion domain size estimate from microfractures = 5 μm (light gray dotted line).

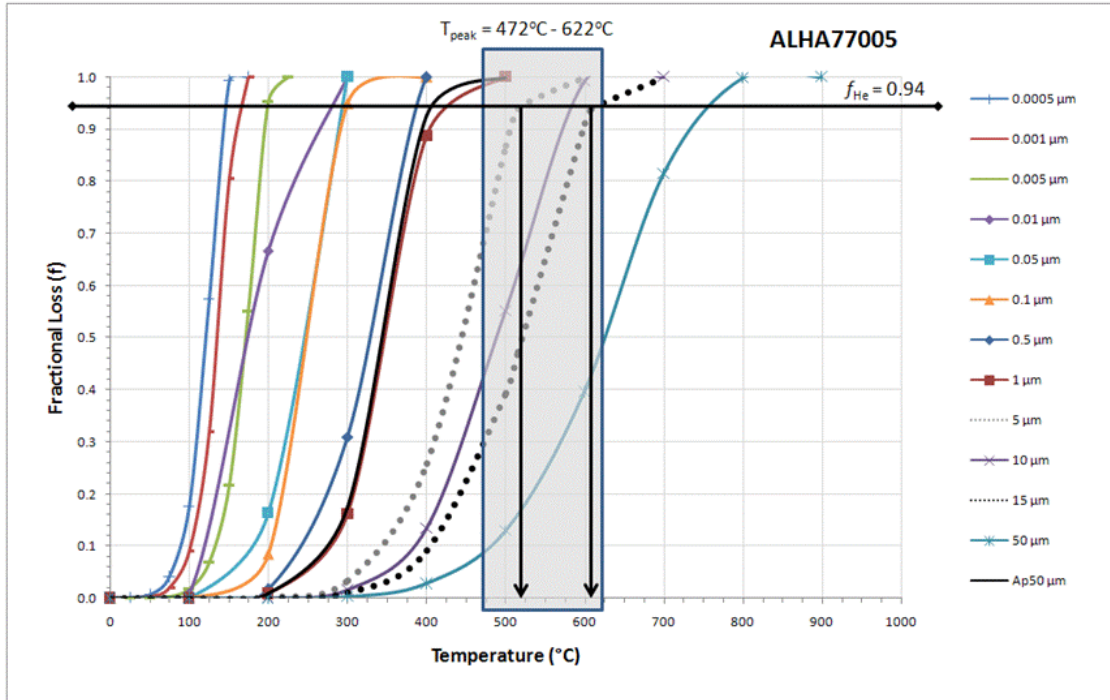
Overall diffusion domain size range for ALHA77005: 5 μm to 15 μm .



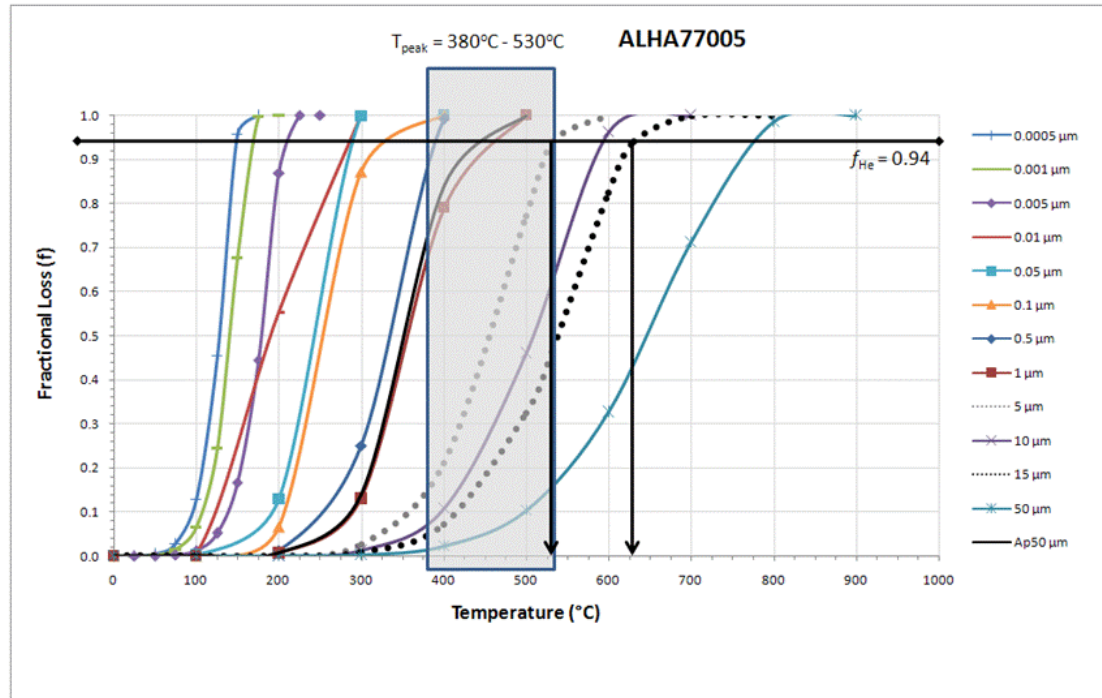
Depth from surface of parent body, $d = 24$ cm.
 Ambient Temperature, $T_s = 21.85^{\circ}\text{C}$. Parent body size, $A = 25$ cm.



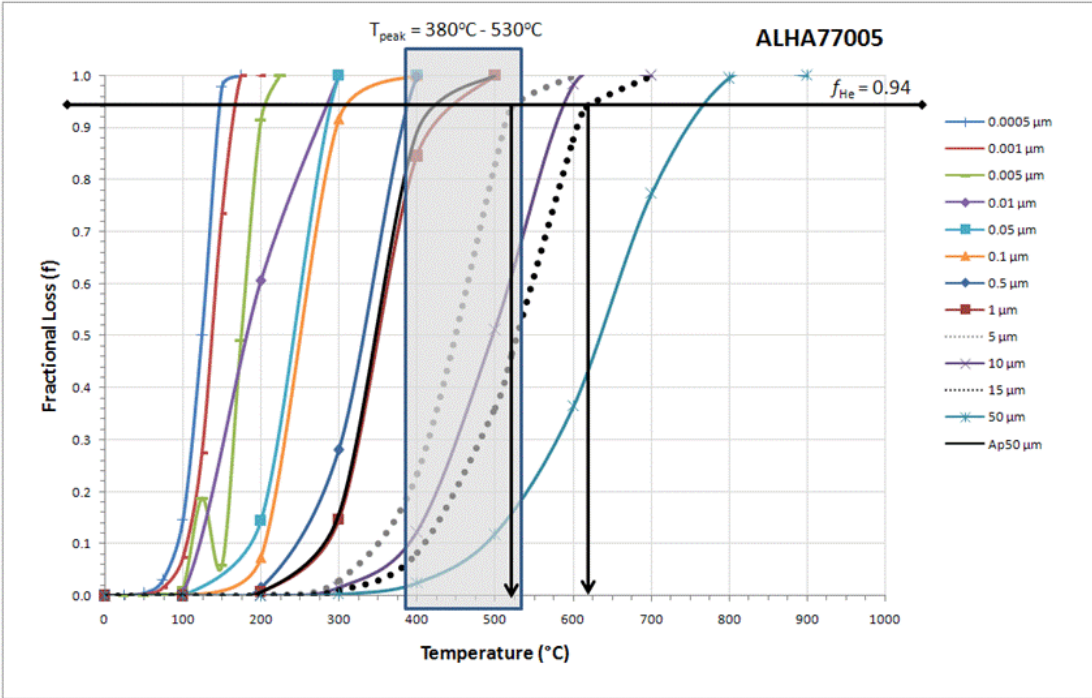
Depth from surface of parent body, $d = 30$ cm.
 Ambient Temperature, $T_s = 21.85^{\circ}\text{C}$. Parent body size, $A = 30$ cm.



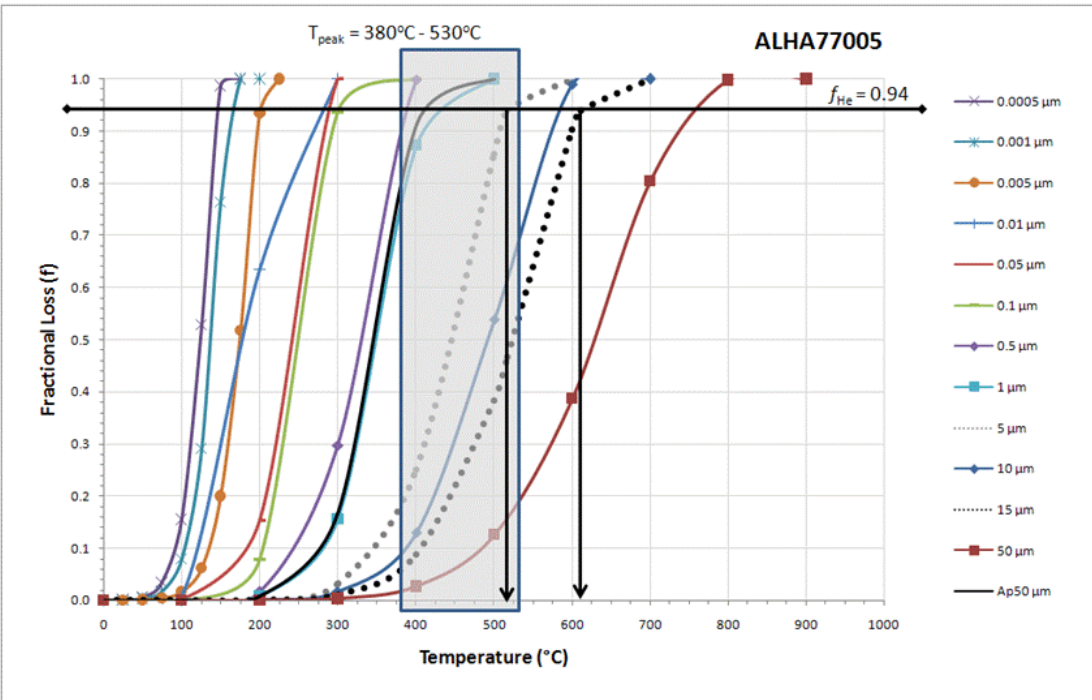
Depth from surface of parent body, $d = 24$ cm.
 Ambient Temperature, $T_s = 21.85^{\circ}\text{C}$. Parent body size, $A = 35$ cm.



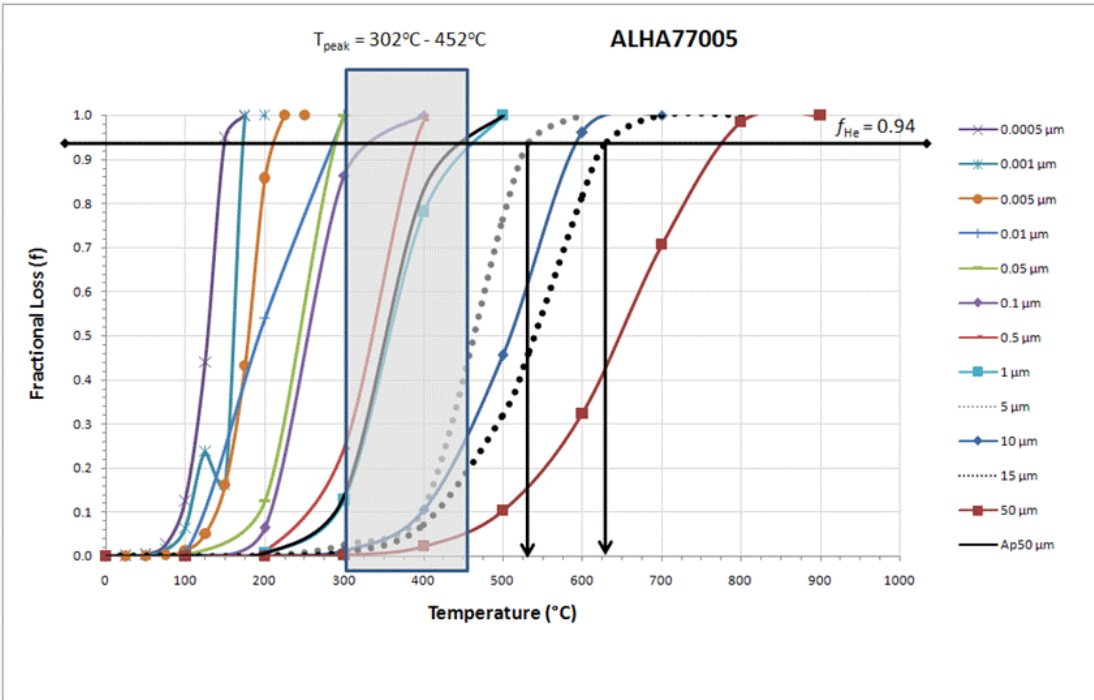
Depth from surface of parent body, $d = 24$ cm.
 Ambient Temperature, $T_s = -70^{\circ}\text{C}$. Parent body size, $A = 25$ cm.



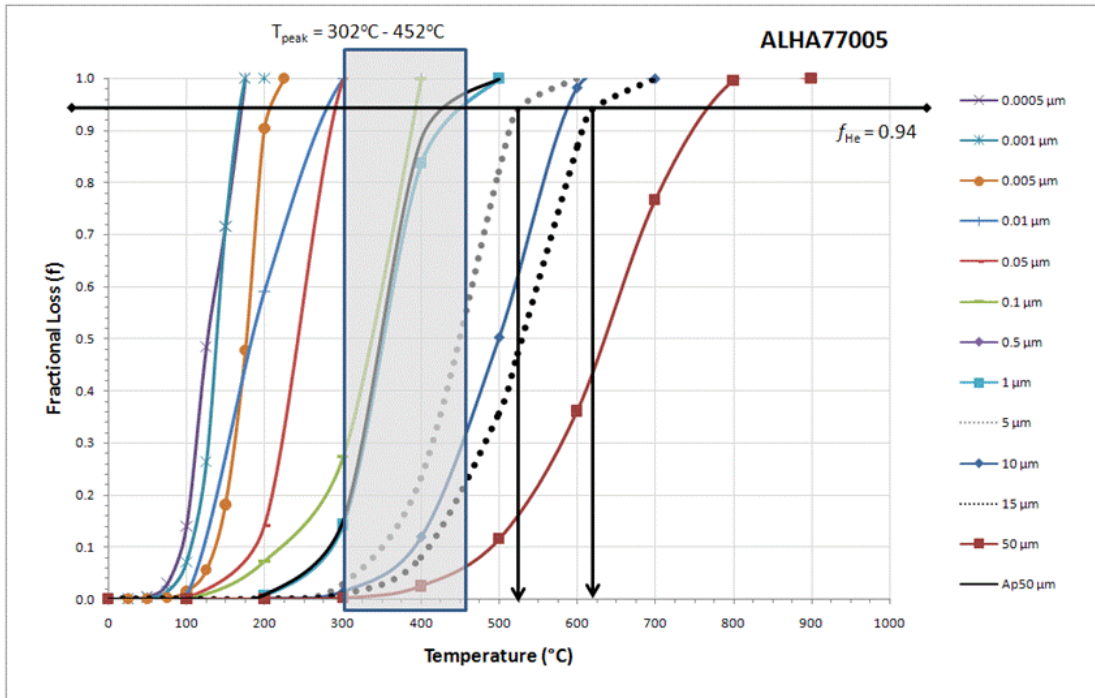
Depth from surface of parent body, $d = 24$ cm.
 Ambient Temperature, $T_s = -70^{\circ}\text{C}$. Parent body size, $A = 30$ cm.



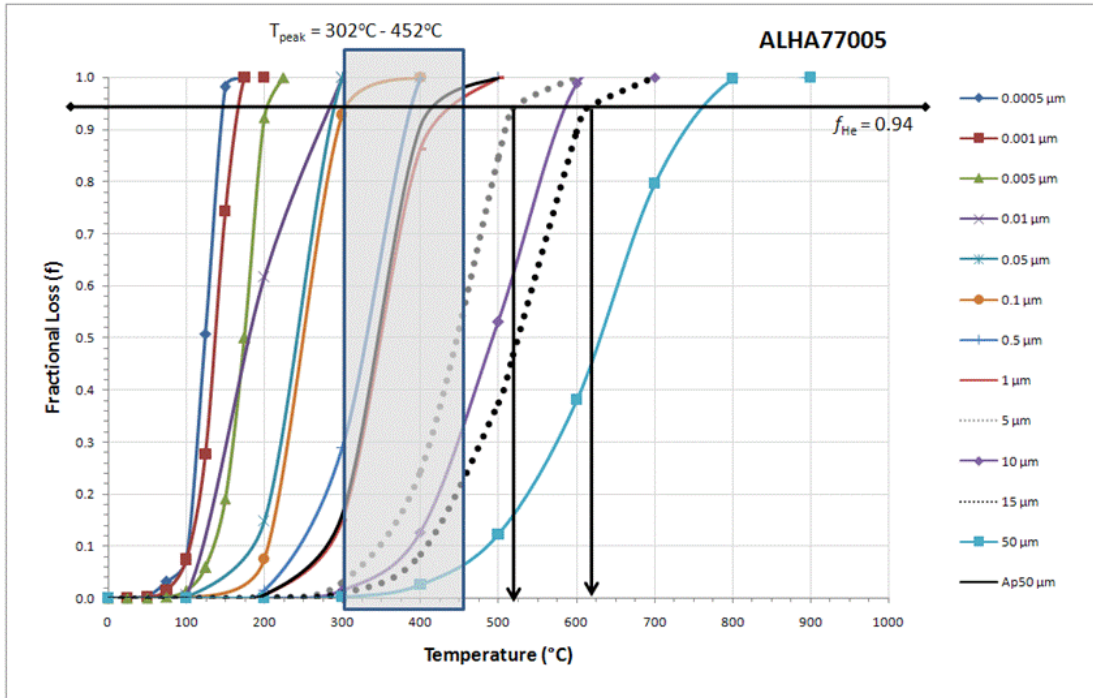
Depth from surface of parent body, $d = 24$ cm.
 Ambient Temperature, $T_s = -70^{\circ}\text{C}$. Parent body size, $A = 35$ cm.



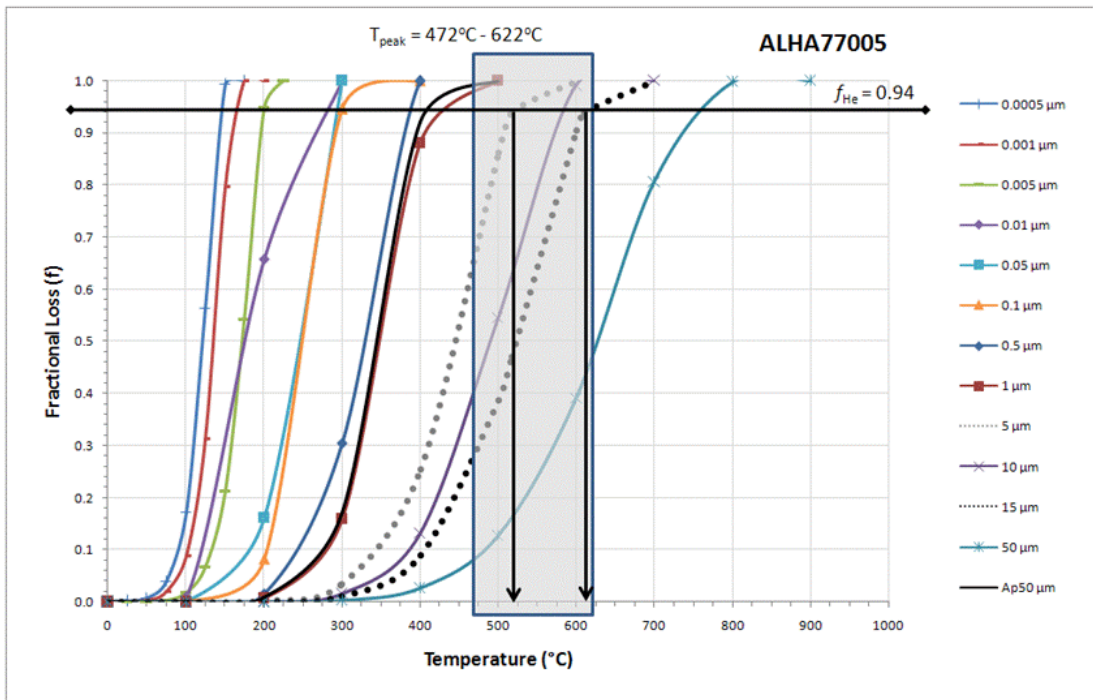
Depth from surface of parent body, $d = 24$ cm.
 Ambient Temperature, $T_s = -148^{\circ}\text{C}$. Parent body size, $A = 25$ cm.



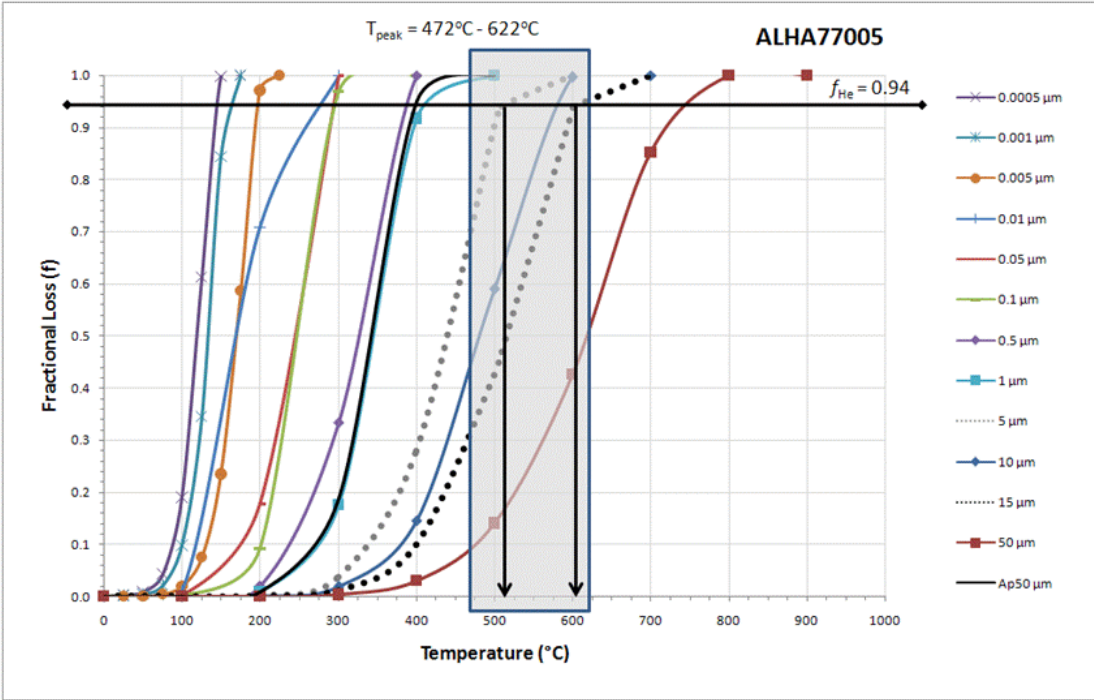
Depth from surface of parent body, $d = 30$ cm.
 Ambient Temperature, $T_s = -148^{\circ}\text{C}$. Parent body size, $A = 30$ cm.



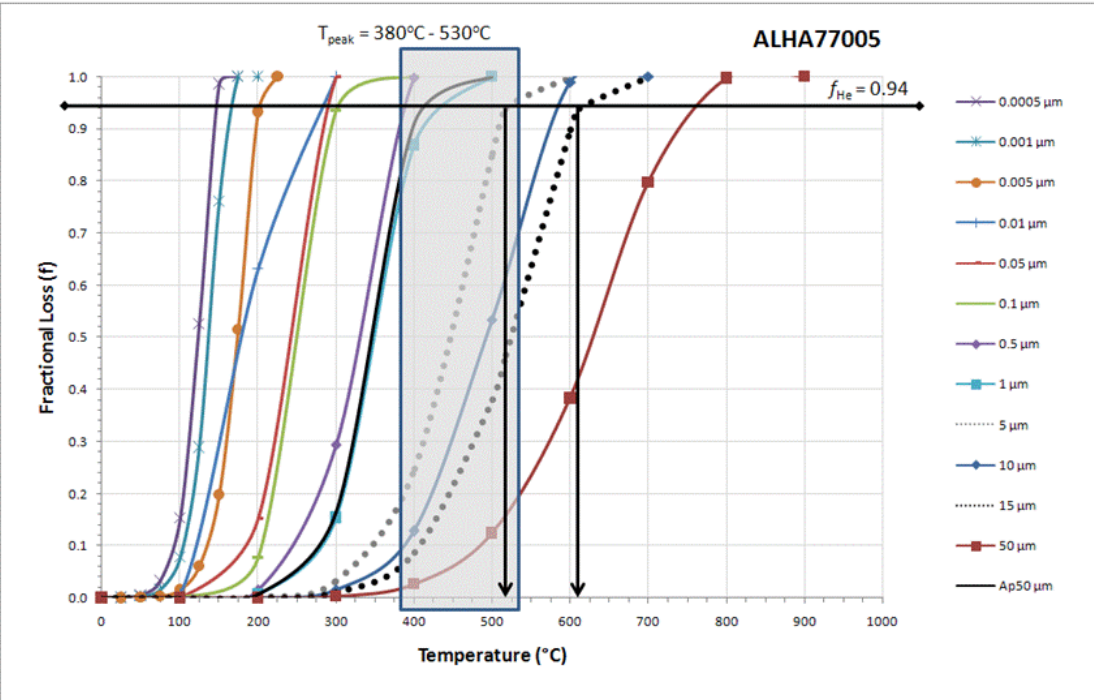
Depth from surface of parent body, $d = 24$ cm.
 Ambient Temperature, $T_s = -148^{\circ}\text{C}$. Parent body size, $A = 35$ cm.



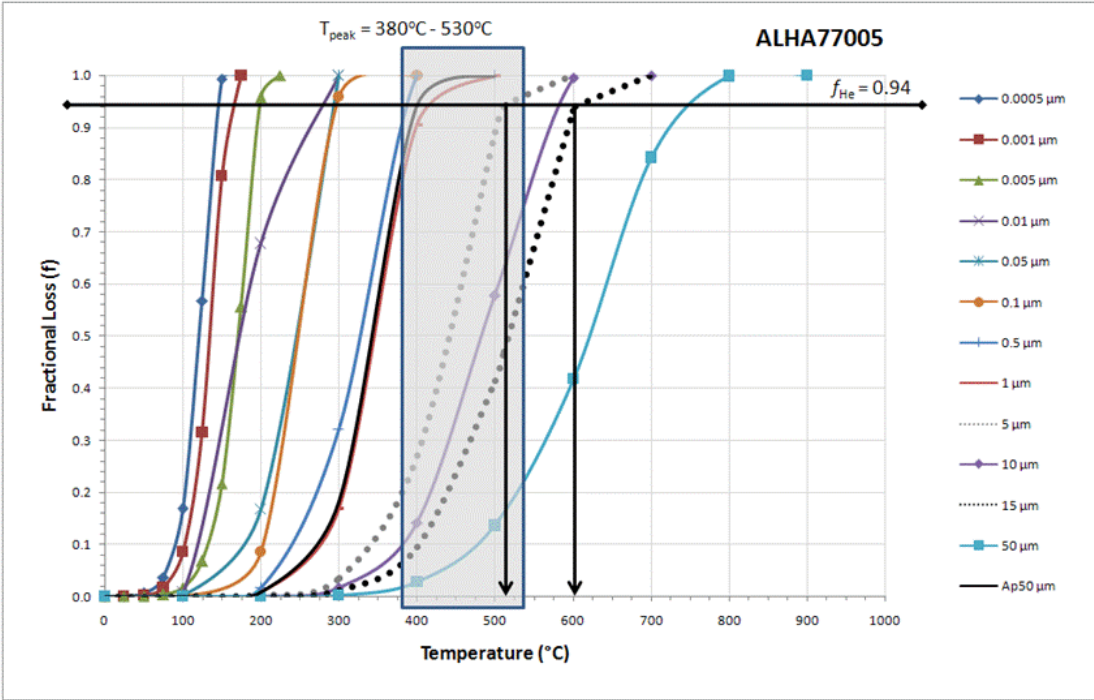
Depth from surface of parent body, $d = 28$ cm.
 Ambient Temperature, $T_s = 21.85^{\circ}\text{C}$. Parent body size, $A = 30$ cm.



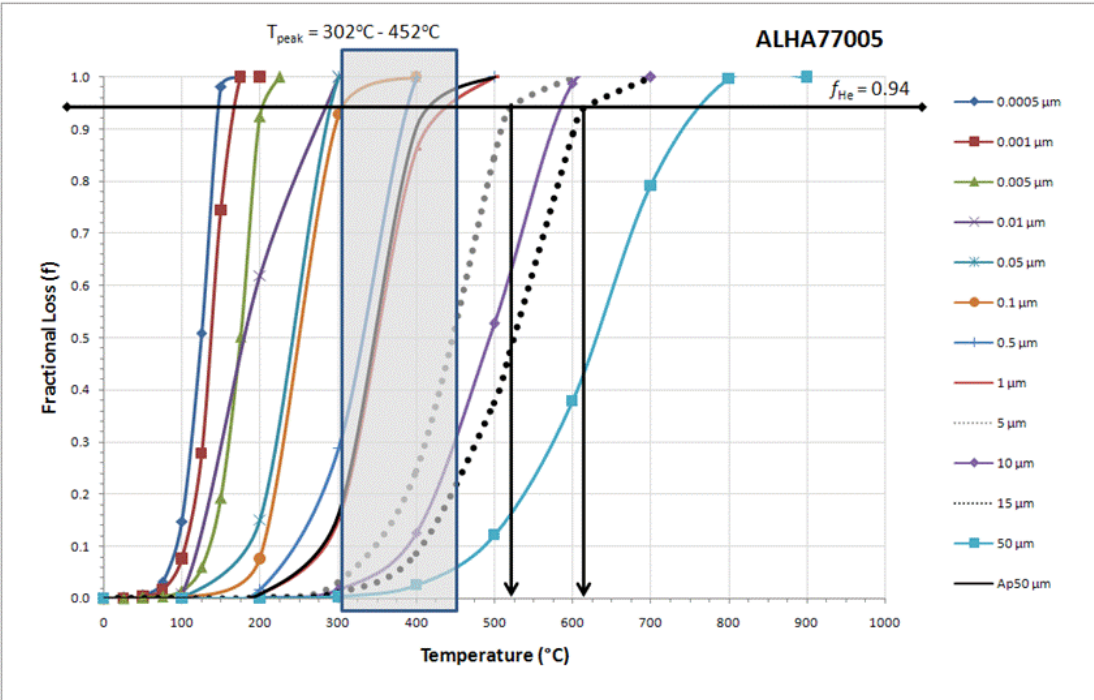
Depth from surface of parent body, $d = 28$ cm.
 Ambient Temperature, $T_s = 21.85^{\circ}\text{C}$. Parent body size, $A = 35$ cm.



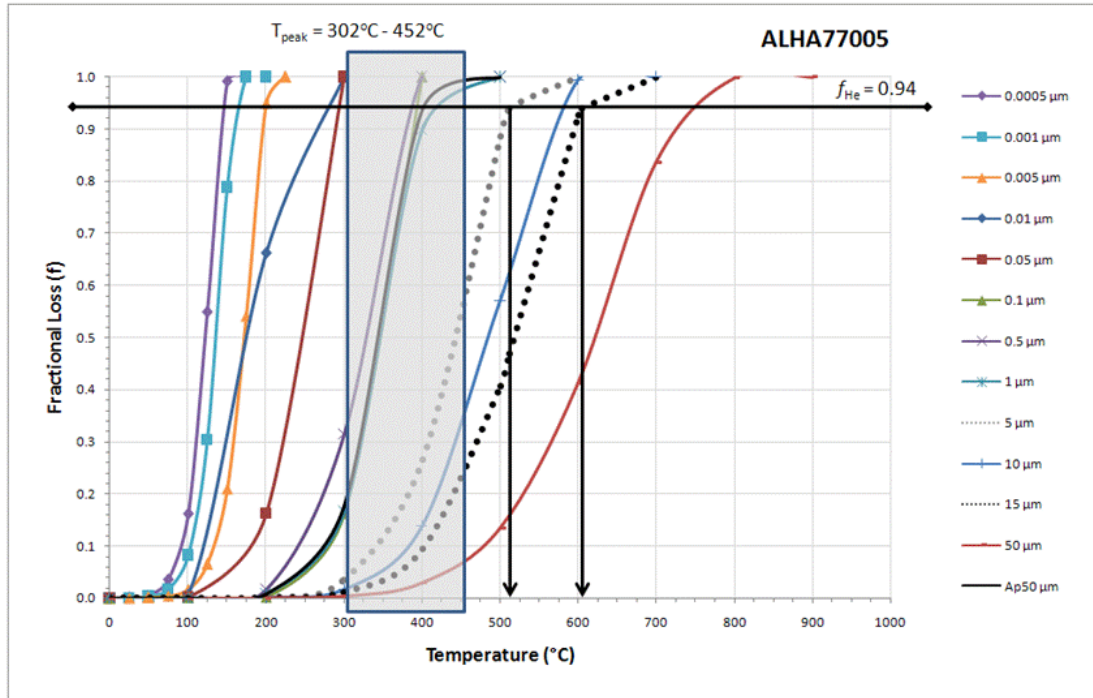
Depth from surface of parent body, $d = 28$ cm.
 Ambient Temperature, $T_s = -70^{\circ}\text{C}$. Parent body size, $A = 30$ cm.



Depth from surface of parent body, $d = 28$ cm.
 Ambient Temperature, $T_s = -70^{\circ}\text{C}$. Parent body size, $A = 35$ cm.



Depth from surface of parent body, $d = 28$ cm.
 Ambient Temperature, $T_s = -148^{\circ}\text{C}$. Parent body size, $A = 30$ cm.



Depth from surface of parent body, $d = 28$ cm.
 Ambient Temperature, $T_s = -148^\circ\text{C}$. Parent body size, $A = 35$ cm.

Shock temperatures from thermal modeling at $d = 24$ cm and $d = 28$ cm. $d =$ depth from surface of parent body. $T_s =$ ambient temperature of Mars. $A =$ parent body size. Overall shock temperature averages: $\sim 520^\circ\text{C}$ at $5 \mu\text{m}$ and $\sim 615^\circ\text{C}$ at $15 \mu\text{m}$.

$d=24\text{cm}$	$T_s = 22^\circ\text{C}$		$T_s = -70^\circ\text{C}$		$T_s = -148^\circ\text{C}$	
	$5 \mu\text{m}$	$15 \mu\text{m}$	$5 \mu\text{m}$	$15 \mu\text{m}$	$5 \mu\text{m}$	$15 \mu\text{m}$
A						
25	531	628	532	630	533	631
30	520	616	522	617	524	619
35	516	609	517	611	519	613
avg	522.33	617.67	523.67	619.33	525.33	621
std dev	7.77	9.61	7.64	9.71	7.09	9.17

$d=28\text{cm}$	$T_s = 22^\circ\text{C}$		$T_s = -70^\circ\text{C}$		$T_s = -148^\circ\text{C}$	
	$5 \mu\text{m}$	$15 \mu\text{m}$	$5 \mu\text{m}$	$15 \mu\text{m}$	$5 \mu\text{m}$	$15 \mu\text{m}$
A						
30	517	610	518	612	520	614
35	509	601	511	603	512	604
avg	513	605.5	514.5	607.5	516	609
std dev	5.66	6.36	4.95	6.36	5.66	7.07

LIST OF REFERENCES

- Alexander C.M. O'D., 2001. Inherited material from the protosolar cloud: composition and origin. *Philosophical Transactions of the Royal Society of London A* 359, 1973-1989.
- Artemieva N. and Ivanov B.A., 2004. Launch of Martian meteorites in oblique impacts. *Icarus* 171, 84-101.
- Ash R.D., Knott S.F., and Turner G., 1996. A 4-Gyr shock age for a martian meteorite and implications for the cratering history of Mars. *Nature* 380, 57-59.
- Baalke R., 2006. Mars Meteorites. National Aeronautics and Space Administration (NASA), Jet Propulsion Laboratory, California Institute of Technology. <<http://www2.jpl.nasa.gov/snc/>>. Accessed 23 March 2011.
- Beck P., Barrat J.A., Gillet Ph., Wadhwa M., Franchi I.A., Greenwood R.C., Bohn M., Cotton J., van de Moortèle B., and Reynard B., 2006. Petrography and geochemistry of the chassignite Northwest Africa 2737 (NWA 2737). *Geochimica et Cosmochimica Acta* 70, 2127-2139.
- Beech M., Nie W., and Coulson I.M., 2008. The pre-atmospheric size of the Martian meteorite ALH 77005 progenitor. *Planetary and Space Science* 56, 320-325.
- Binns R.A., 1967. Stony Meteorites bearing Maskelynite. *Nature* 213, 1111-1112.
- Boctor N.Z., Fei Y., Bertka C.M., D'Alexander C.M.O., and Hauri E., 1999. Shock Metamorphic Effects in Martian Meteorite ALHA 77005. Lunar and Planetary Science Conference XXX abs. #1628.
- Bogard D.D. and Johnson P., 1983. Martian Gases in an Antarctic Meteorite? *Science* 221, 651-654.
- Bogard D., Hörz F., and Johnson P., 1987. Shock effects and argon loss in samples of the Leedey L6 chondrite experimentally shocked to 29-70 GPa pressures. *Geochimica et Cosmochimica Acta* 51, 2035-2044.
- Bogard D.D. and Garrison D.H., 1999. Argon-39-argon-40 'ages' and trapped argon in Martian shergottites, Chassigny, and Allan Hills 84001. *Meteoritics and Planetary Science* 34, 451-473.
- Bogard D.D. and Park J., 2008. ^{39}Ar - ^{40}Ar dating of the Zagami Martian shergottite and implications for magma origin of excess ^{40}Ar . *Meteoritics and Planetary Science* 43, 1113-1126.
- Bogard D.D., 2009. K-Ar dating of rocks on Mars: Requirements from Martian meteorite analyses and isochron modeling. *Meteoritics and Planetary Science* 44, 3-14.

- Bogard D.D., Park J., and Garrison D., 2009. ^{39}Ar - ^{40}Ar ages and origin of excess ^{40}Ar in Martian shergottites. *Meteoritics and Planetary Science* 44, 905-923.
- Borg L.E., Nyquist L.E., Wiesmann H., and Reese Y., 2002. Constraints on the petrogenesis of Martian meteorites from the Rb-Sr and Sm-Nd isotopic systematic of the Iherzolitic shergottites ALH77005 and LEW88516. *Geochimica et Cosmochimica Acta* 66, 2037-2053.
- Borg L.E., Asmerom Y., and Edmunson J.E., 2003. Uranium-Lead isotopic systematics of the Martian meteorite Zagami. *Lunar and Planetary Science Conference XXXIV abs. #1107*.
- Borg L.E., Edmunson J.E., and Asmerom Y., 2005. Constraints on the U-Pb isotopic systematics of Mars inferred from a combined U-Pb, Rb-Sr, and Sm-Nd isotopic study of the Martian meteorite Zagami. *Geochimica et Cosmochimica Acta* 69, 5819-5830.
- Bouvier A., Blichert-Toft J., Vervoort J.D., and Albarède F., 2005. The age of SNC meteorites and the antiquity of Martian surface. *Earth and Planetary Science Letters* 240, 221-233.
- Butler C.P., 1966. Temperatures of Meteoroids in Space. *Meteoritics* 3, 59-70.
- Cassata W. S., Shuster D. L., Renne P. R., and Weiss B. P., 2010. Evidence for shock heating and constraints on Martian surface temperatures revealed by $^{40}\text{Ar}/^{39}\text{Ar}$ thermochronometry of Martian meteorites. *Geochimica et Cosmochimica Acta* 74, 6900-6920.
- Chen J.H. and Wasserburg G.J., 1986. Formation ages and evolution of Shergotty and its parent planet from U-Th-Pb systematics. *Geochimica et Cosmochimica Acta* 50, 955-968.
- Clayton R.N., 1993. Oxygen Isotopes in Meteorites. *Annual Review of Earth and Planetary Sciences* 21, 115-149.
- Clayton R.N. and Mayeda T.K., 1996. Oxygen isotope studies of achondrites. *Geochimica et Cosmochimica Acta* 60, 1999-2017.
- Edmunson J., Borg L.E., Shearer C.K., and Papike J.J., 2005. Defining the mechanisms that disturb the Sm-Nd isotopic systematics of the Martian meteorites: Examples from Dar al Gani 476 and Allan Hills 77005. *Meteoritics and Planetary Science* 40, 1159-1174.
- Ehlers K. and Powell R., 1994. An empirical modification of Dodson's equation for closure temperature in binary systems. *Geochimica et Cosmochimica Acta* 58, 241-248.

- Ehlers T.A. and Farley K.A., 2003. Apatite (U-Th)/He thermochronometry: methods and applications to problems in tectonic and surface processes. *Earth and Planetary Science Letters* 206, 1- 14.
- El Goresy A., Chen M., Gillet Ph., and Dubrovinsky L.S., 2000a. Shock-induced high-pressure phase transition of Labradorite to Hollandite in Zagami and the assemblage Hollandite + Jadeite in L Chondrites: Constraints to peak shock pressures. *Meteoritics and Planetary Science* 35, A51 (Abstract).
- El Goresy A., Dubrovinsky L., Sharp T.G., Saxena S.K., and Chen M., 2000b. A monoclinic post-stishovite polymorph of silica in the Shergotty meteorite. *Science* 288, 632-634.
- Eugster O., 1988. Cosmic-ray production rates for ^3He , ^{21}Ne , ^{38}Ar , ^{83}Kr , and ^{126}Xe in chondrites based on ^{81}Kr -Kr exposure ages. *Geochimica et Cosmochimica Acta* 52, 1649-1662.
- Eugster O., Weigel A., and Polnau E., 1997. Ejection times of Martian meteorites. *Geochimica et Cosmochimica Acta* 61, 2749-2757.
- Eugster O., Busemann H., Lorenzetti S., and Terribilini D., 2002. Ejection ages from krypton-81-krypton-83 dating and pre-atmospheric sizes of martian meteorites. *Meteoritics and Planetary Science* 37, 1345-1360.
- Eugster O., 2003. Cosmic-ray Exposure Ages of Meteorites and Lunar Rocks and Their Significance. *Chemie der Erde Geochemistry* 63, 3-30.
- Farley K.A., Wolf R.A., and Silver L.T., 1996. The effects of long alpha-stopping distances on (U-Th)/He ages. *Geochimica et Cosmochimica Acta* 60, 4223-4229.
- Farley K.A., 2000. Helium diffusion from apatite: General behavior as illustrated by Durango fluorapatite. *Journal of Geophysical Research* 105, 2903-2914.
- Farley K., 2002. (U-Th)/He Dating: Techniques, Calibrations, and Applications. *Reviews in Mineralogy and Geochemistry* 47, 819-844.
- Fritz J., Artemieva N., and Greshake A., 2005a. Ejection of Martian meteorites. *Meteoritics and Planetary Science* 4, 1393-1411.
- Fritz J., Greshake A., and Stöffler D., 2005b. Micro-Raman spectroscopy of plagioclase and maskelynite in Martian meteorites: Evidenced of progressive shock metamorphism. *Antarctic Meteorite Research* 18, 96-116.
- Gladman B., 1997. Destination: Earth. *Martian Meteorite Delivery*. *Icarus* 130, 228-246.
- Haag R., 2010. Robert A. Haag Private Meteorite Collection - Mars Rocks. Copyright 1996-2010. The MeteoriteMan. Accessed 6 November 2010. <<http://meteoriteman.com/collection/zagami.htm>>.

- Harrison T.M. and Zeitler P.K., 2005. Fundamentals of Noble Gas Thermochronometry. *Reviews in Mineralogy and Geochemistry* 59, 123-149.
- Hartmann W.K. and Neukum G., 2001. Cratering chronology and the evolution of Mars. *Space Science Review* 96, 165-194.
- Harvey R., 2003. The Origin and Significance of Antarctic Meteorites. *Chemie der Erde Geochemistry* 63, 93-147.
- Head J.N., Melosh J.H., and Ivanov B.A., 2002. Martian meteorite launch: high-speed ejecta from small craters. *Science* 298, 1752-1756.
- Hourigan J.K., Reiners P.W., and Brandon M.T., 2005. U-Th zonation-dependent alpha-ejection in (U-Th)/He chronometry. *Geochimica et Cosmochimica Acta* 69, 3349-3365.
- Hughes J.M., Jolliff B.L., and Rakovan J., 2008. The crystal chemistry of whitlockite and merrillite and the dehydrogenation of whitlockite to merrillite. *American Mineralogist* 93, 1300-1305.
- Hutchison R., 2004. *Meteorites: A Petrologic, Chemical and Isotopic Synthesis*. First edition. Cambridge, United Kingdom: Cambridge University Press.
- Ikeda Y., 1994. Petrography and petrology of the ALHA77005 shergottite. *Proceedings of the NIPR Symposium on Antarctic Meteorites 7th*, National Institute of Polar Research, Tokyo 9-29.
- Jagoutz E., 1989. Sr and Nd isotopic systematics in ALHA77005: Age of shock metamorphism in shergottites and magmatic differentiation on Mars. *Geochimica et Cosmochimica Acta* 53, 2429-2441.
- Jagoutz E., Sorowka A., Vogel J.D. and Wänke H., 1994. ALHA84001: Alien or Progenitor of the SNC Family? *Meteoritics* 29, 478-479 (Abstract).
- Jolliff B.L., Hughes J.M., Freeman J.J., and Ziegler R.A., 2006. Crystal chemistry of lunar merrillite and comparison to other meteoritic and planetary suites of whitlockite and merrillite. *American Mineralogist* 91, 1583-1595.
- Langenhorst, F., Stöffler D., and Klein D., 1991. Shock metamorphism of the Zagami achondrite. *Lunar and Planetary Science Conference XXII*, 779-780 (Abstract).
- Langenhorst F. and Poirier J-P., 2000a. Anatomy of black veins in Zagami: clues to the formation of high-pressure phase. *Earth and Planetary Science Letters* 184, 37-55.
- Langenhorst F. and Poirier J-P., 2000b. Eclogitic minerals in a shocked basaltic meteorite. *Earth and Planetary Science Letters* 176, 259-265.

- Lorenzetti S., Eugster O., Busemann H., Marti K., Burbine T.H., and McCoy T., 2003. History and origin of aubrites. *Geochimica et Cosmochimica Acta* 67, 557–571.
- Ma M.-S., Laul J.C., and Schmitt R.A., 1981. Complementary rare earth element patterns in unique achondrites, such as ALHA77005 and shergottites, and in the earth. In: Lunar and Planetary Science Conference, 12th, Houston, Texas, USA. Proceedings of the Lunar and Planetary Science Conference 12B, 1349-1358.
- MacPherson G., 1985. In: Antarctic Meteorite Newsletter 8 (2) 5. Curation Astromaterials Acquisition and Curation Office, NASA Johnson Space Center, Houston, Texas, USA.
- Malavergne V., Guyot F., Benzerara K., and Martinez I., 2001. Descriptions of new shock-induced phases in the Shergotty, Zagami, Nakhla and Chassigny meteorites. *Meteoritics and Planetary Science* 36, 1297-1305.
- Mason B., 1981. Antarctic Meteorite Newsletter 4 (1) 12 Curation Astromaterials Acquisition and Curation Office, NASA Johnson Space Center, Houston, Texas, USA.
- McCoy T.J., Taylor G.J., Keil K., and Noll Jr. P.D., 1991. Zagami: Product of a Two-Stage Magmatic History. Lunar and Planetary Science Conference XXII, 867-868.
- McCoy T.J., Taylor G.J., and Keil K., 1992. Zagami: Product of a Two-Stage Magmatic History. *Geochimica et Cosmochimica Acta* 56, 3571-3582.
- McCoy T.J., Keil K., and Taylor, G.J., 1993. The dregs of crystallization in Zagami. Lunar and Planetary Science Conference XXIV, 947-948.
- McCoy T.J., Wadhwa M., and Keil K., 1999. New lithologies in the Zagami meteorite: Evidence for fractional crystallization of a single magma unit on Mars. *Geochimica et Cosmochimica Acta* 63, 1249-1262.
- McDougall I. and Harrison T.M., 1999. *Geochronology and Thermochemistry by the ⁴⁰Ar/³⁹Ar Method*. Second edition. Oxford, New York: Oxford University Press.
- McSween H.Y., Taylor L.A., and Stolper E.M., 1979a. Allan Hills 77005: A new meteorite type found in Antarctica. *Science* 204, 1201-1203.
- McSween H.Y., Stolper E.M., Taylor L.A., Muntean R.A., O'Kelley G.D., Eldridge J.S., Biswas S., Ngo H.T., and Lipschutz M.E., 1979b. Petrogenetic relationship between Allan Hills 77005 and other achondrites. *Earth and Planetary Science Letters* 45, 275-284.
- McSween H.Y. and Stöffler D., 1980. Shock Metamorphic Features in Allan Hills 77005 Meteorite. Lunar and Planetary Science Conference XI, 717-719.

- McSween H.Y., 1984. SNC meteorites: Are they Martian rocks? *Geology* 12, 3-6.
- McSween H.Y., 1985. SNC Meteorites: Clues to Martian Petrologic Evolution. *Reviews of Geophysics* 23, 391-416.
- McSween H.Y., 1994. What we have learned about Mars from SNC meteorites. *Meteoritics* 29, 757-779.
- The Meteoritical Society (2002) Meteoritical Bulletin Database. Lunar and Planetary Institute, The Meteoritical Society: International Society for Meteoritics and Planetary Science. Modified 1 March 2011. <<http://www.lpi.usra.edu/meteor/metbull.php>>. Accessed 23 March 2011.
- Melosh H.J., 1985. Ejection of rock fragments from planetary bodies. *Geology* 13, 144-148.
- Melosh H.J., 1995. Cratering dynamics and the delivery of meteorites to the Earth. *Meteoritics* 30, 545-546.
- Meyer C., 2003. The Mars Meteorite Compendium. National Aeronautics and Space Administration (NASA); Astromaterials Research & Exploration Science (ARES); Lyndon B. Johnson Space Center, Houston, Texas, USA. Modified 29 April 2011. <<http://curator.jsc.nasa.gov/antmet/mmc/index.cfm>>. Accessed 7 June 2011.
- Mikouchi T., Miyamoto M., and McKay G.A., 1998. Mineralogical Characterization of Heated 'Maskelynite' Plagioclase Glass in the Zagami Martian Meteorite. *Meteoritics and Planetary Science* 33, Supplement A109.
- Min K., Farley K.A., Renne P.R., and Marti K., 2003. Single grain (U-Th)/He ages from phosphates in Acapulco meteorite and implications for thermal history. *Earth and Planetary Science Letters* 209, 323-337.
- Min K., Reiners P.W., Nicolescu S., and Greenwood J.P., 2004. Age and temperature of shock metamorphism of Martian meteorite Los Angeles from (U-Th)/He thermochronology. *Geology* 32, 677-680.
- Min K., 2005a. Low-temperature thermal history of Martian meteorite ALH84001 from (U-Th)/He thermochronometry. *Lunar and Planetary Science Conference XXXVI* abs. #2214.
- Min K., 2005b. Low-Temperature Thermochronometry of Meteorites. *Reviews in Mineralogy and Geochemistry* 59, 567-588.
- Min K. and Reiners P.W., 2007. High-temperature Mars-to-Earth transfer of meteorite ALH84001. *Earth and Planetary Science Letters* 260, 72-85.

- Min K., Reiners P.W., and Shuster D.L., 2011. Low-T Thermochronology of St. Severin LL6 Chondrite Revealed From Single-Grain Phosphate (U-Th)/He Ages. 42nd Lunar and Planetary Science Conference abs. #2683.
- Mitchell S.G. and Reiners P.W., 2003. Influence of wildfires on apatite and zircon (U-Th)/He ages. *Geology* 31, 1025-1028.
- Mittlefehldt D.W., 2003. ALH84001, a cumulate orthopyroxenite member of the martian meteorite clan. *Meteoritics* 29, 214-221.
- Miura Y.N., Nagao K., Sugiura N., Sagawa H., and Matsubara K., 1995. Orthopyroxenite ALHA84001 and Shergottite ALHA77005: Additional Evidence for a Martian Origin from Noble Gases. *Geochimica et Cosmochimica Acta* 59, 2105-2113.
- Nishiizumi K., Klein J., Middleton R., Elmore D., Kubik P.W., and Arnold J.R., 1986. Exposure history of shergottites” *Geochimica et Cosmochimica Acta* 50, 1017-1021.
- Nyquist L.E., Bansal B., Wiesmann H., and Shih C.-Y., 1995. Martians young and old: Zagami and ALH84001. *Lunar and Planetary Science Conference XXVI*, 1065-1066.
- Nyquist L.E., Bogard D.D., Shih C.-Y., Greshake A., Stöffler D., and Eugster O., 2001. Ages and Geologic Histories of Martian Meteorites. *Space Science Review* 96, 105-164.
- Nyquist L.E., Shih C.-Y., and Reese Y.D., 2006. Initial Isotopic Heterogeneities In Zagami: Evidence Of A Complex Magmatic History. 69th Annual Meteoritical Society Meeting Abstract #5143, Eth Zurich, Switzerland.
- O’Neill C.O., Ikeda Y., and Delaney J.S., 1987. The Compositional Zoning of Feldspathic Phases in Allan Hills 77005, 32. *Lunar and Planetary Science XVIII*, 750-751.
- Paneth F.A. and Reasbeck P., 1952. Helium 3 content and age of meteorites. *Geochimica et Cosmochimica Acta* 2, 300-303.
- Reiners P.W. and Farley K.A., 1999. Helium diffusion and (U-Th)/He thermochronometry of titanite. *Geochimica et Cosmochimica Acta* 63, 3845-3859.
- Reiners P.W., 2002. (U-Th)/He Chronometry Experiences a Renaissance. *Eos, Transactions, American Geophysical Union* 83, 21, 26-27.
- Reiners P.W. and Ehlers T.A., 2005. Low-Temperature Thermochronology: Techniques, Interpretations, and Applications. *Reviews in Mineralogy and Geochemistry, Mineralogical Society of America*: 58, 622 pages.

- Reiners P.W., 2005. Zircon (U-Th)/He Thermochronometry. Low-Temperature Thermochronology: Techniques, Interpretations, and Applications. *Reviews in Mineralogy and Geochemistry* 58, 151-179.
- Reiners P.W., Thomson S.N., McPhillips D., Donelick R.A., and Roering J.J., 2007. Wildfire thermochronology and the fate and transport of apatite in hillslope and fluvial environments. *Journal of Geophysical Research* 112, 1-29.
- Reiners P.W. and Shuster D.L., 2009. Thermochronology and landscape evolution. *Physics Today*. American Institute of Physics 62, 31-36.
- Schaeffer O.A. and Warasila R., 1981. ^{39}Ar - ^{40}Ar study of Allan Hills meteorite A77005, A unique achondrite. *Lunar and Planetary Science Conference XII*, 932-933.
- Schnabel C., Ma P., Herzog G.F., Faestermann T., Knie K., and Korschinek G., 2001. ^{10}Be , ^{26}Al , and ^{53}Mn in Martian Meteorites. *32nd Lunar and Planetary Science Conference abs. #1353*.
- Schultz, L. and Franke, L., 2004. Helium, neon, and argon in meteorites: A data collection. *Meteoritics and Planetary Science* 39, 1889-1890.
- Schwenzer S.P., Fritz J., Stöffler D., Trieloff M., Amini M., Greshake A., Herrmann S., Herwig K., Jochum K.P., Mohapatra R.K., Stoll B., and Ott U., 2008. Helium loss from Martian meteorites mainly induced by shock metamorphism: Evidence from new data and a literature compilation. *Meteoritics and Planetary Science* 43, 1841-1859.
- Score R., Schwarz C.M., King T.V.V., Mason B., Bogard D.D., and Gabel E.M., eds., 1981. *Antarctic Meteorite Newsletter 4 (1) Curation Astromaterials Acquisition and Curation Office, NASA Johnson Space Center, Houston, Texas, USA*.
- Sharp T.G., El Goresy A., Wopenka B., and Chen M., 1999. A Post-Stishovite SiO_2 Polymorph in the Meteorite Shergotty: Implications for Impact Events. *Science* 284, 1511-1513.
- Sharp T.G. and de Carli, P.S., 2006. Shock Effects in Meteorites. In *Meteorites and the Early Solar System II*, Eds. D.S. Lauretta and H.Y. McSween Jr., The University of Arizona Press, Tucson, 943 p., 653-677.
- Shearer C.K., Burger P.V., Papike J.J., and Karner J., 2009. Comparisons between RBT 04262 and Iherzolitic shergottites (ALHA77005 and LEW 88516). *40th Lunar and Planetary Science Conference abs. #1300*.
- Shih C-Y, Nyquist L.E., Bogard D.D., McKay G.A., Wooden J.L., Bansal B.M., and Wiesmann H., 1982. Chronology and petrogenesis of young achondrites, Shergotty, Zagami, and ALHA77005: Late magmatism on a geologically active planet. *Geochimica et Cosmochimica Acta* 46, 2323-2344.

- Shirley J.H. and Fairbridge R.W., 1997. *Encyclopedia of Planetary Sciences*. First edition. London, United Kingdom: Chapman and Hall.
- Shu F.H., Shang H., Gounelle M., Glassgold A.E., and Lee T., 2001. The Origin of Chondrules and Refractory Inclusions in Chondritic Meteorites. *The Astrophysical Journal* 548, 1029-1050.
- Shuster D.L. and Farley K.A., 2003. $^4\text{He}/^3\text{He}$ Thermochronometry. *Earth and Planetary Science Letters* 217, 1-17.
- Shuster D.L. and Weiss P.B., 2005. Martian Surface Paleotemperatures from Thermochronology of Meteorites. *Science* 309, 594-597.
- Soffen G.A., 1976. Scientific Results of the Viking Missions. *Science* 194, 1274-1276.
- Spanovich N., Smith M.D., Smith P.H., Wolff M.J., Christensen P.R., and Squyres S.W., 2006. Surface and near-surface atmospheric temperatures for the Mars Exploration Rover landing sites. *Icarus* 180, 314-320.
- Stockli D.F., 2005. Application of Low-Temperature Thermochronometry to Extensional Tectonic Settings. *Low-Temperature Thermochronology: Techniques, Interpretations, and Applications. Reviews in Mineralogy and Geochemistry* 58, 411-448.
- Stöffler D., Ostertag R., Jammes C., and Pfannschmidt G., 1986. Shock metamorphism and petrography of the Shergotty achondrite. *Geochimica et Cosmochimica Acta* 50, 889-903.
- Stöffler, D., Bischoff, A., Buchwald, V., and Rubin, A.E., 1988. Shock Effects in Meteorites. In *Meteorites and the Early Solar System*, Eds. J.F. Kerridge and M.S. Matthews, The University of Arizona Press, Tucson, 1269 p., 165-202.
- Stöffler D., 2000. Maskelynite confirmed as diaplectic glass: Indication for peak shock pressures below 45 GPa in all Martian meteorites. *Lunar and Planetary Science Conference XXXI abs. #1170*.
- Swindle T.D., Grier J.A., and Burkland M.K., 1995. Noble gases in orthopyroxenite ALH84001: A different kind of martian meteorite with an atmospheric signature. *Geochimica et Cosmochimica Acta* 59, 793-801.
- Treiman A.H., McKay G.A., Bogard D.D., Mittlefehldt D.W., Wang M.-S., Keller L., Lipschultz M.E., Lindstrom M.M., and Garrison D., 1994. Comparison of the LEW88516 and ALHA77005 Martian Meteorites: Similar but distinct. *Meteoritics* 29, 581-592.
- Treiman A.H., 1995. A petrographic history of martian meteorite ALH84001: Two shocks and an ancient age. *Meteoritics* 30, 294-302.

- Treiman A.H., 1998. The history of Allan Hills 84001 revised: Multiple shock events. *Meteoritics and Planetary Science* 33, 753-764.
- Treiman A.H., Gleason J.D., and Bogard D.D., 2000. The SNC meteorites are from Mars. *Planetary and Space Science* 48, 1213-1230.
- Trielloff M., Jessberger E.K., Herrwerth I., Hopp J., Fiéni C., Ghélis M., Bourot-Denise M., and Pellas P., 2003. Structure and thermal history of the H-chondrite parent asteroid revealed by thermochronometry. *Nature* 422, 502-506.
- Turner G., Huneke J.C., Podosek F.A., and Wasserburg G.J., 1971. ^{40}Ar - ^{39}Ar ages and cosmic ray exposure ages of Apollo 14 samples. *Earth and Planetary Science Letters* 12, 19-35.
- Turner G., Enright M.C., and Cadogan P.H., 1978. The early history of chondrite parent bodies inferred from ^{40}Ar - ^{39}Ar ages. *Proceedings of the Lunar and Planetary Science Conference 9th*, 989-1025.
- Turner G., Knott S.F., Ash R.D., and Gilmour J.D., 1997. Ar-Ar chronology of the Martian meteorite ALH84001: Evidence for the timing of the early bombardment of Mars. *Geochimica et Cosmochimica Acta* 61, 3835-3850.
- Vistisen L., Petersen D., and Madsen M.B., 1992. Mössbauer spectroscopy showing large-scale inhomogeneity in the presumed Martian meteorite Zagami. *Physica Scripta* 46, 94-96.
- Wadhwa M., McSween H.Y., and Crozaz G., 1994. Petrogenesis of shergottite meteorites inferred from minor and trace element microdistributions. *Geochimica et Cosmochimica Acta* 58, 4213-4229.
- Wang A., Jolliff B.L., and Haskin L.A., 1999. Raman spectroscopic characterization of a Martian SNC meteorite: Zagami. *Journal of Geophysical Research* 104 (E4) 8509-8519.
- Watson J.T and Wang S., 1991. The histories of ordinary chondrite parent bodies: U,Th-He age distributions. *Meteoritics* 26, 161-167.
- Weiss B.P., Shuster D.L., and Stewart S.T., 2002. Temperature on Mars from $^{40}\text{Ar}/^{39}\text{Ar}$ thermochronology of ALH84001. *Earth and Planetary Science Letters* 201, 465-472.
- Wolf R.A., Farley K.A., and Silver L.T., 1996. Helium diffusion and low-temperature thermochronometry on apatites. *Geochimica et Cosmochimica Acta* 60, 4231-4240.
- Wooden J., Shih C.-Y., Nyquist L., Bansal B., Wiesmann H., and McKay G., 1982. Rb-Sr and Sm-Nd Isotopic Constraints on the Origin of EETA 79001: A Second Antarctic Shergottite. *Lunar and Planetary Science Conference XIII*, 879-880.

Yanai K., 1981. Photographic Catalog of the Selected Antarctic Meteorites. First edition. Tokyo, Japan: National Institute of Polar Research.

Zeitler P.K., Herczeg A.L., McDougall I., and Honda M., 1987. U-Th-He dating of apatite: A potential thermochronometer. *Geochimica et Cosmochimica Acta* 51, 2865-2868.

BIOGRAPHICAL SKETCH

Annette Emily Farah received a Bachelor of Science degree in geology, Bachelor of Arts degree in mathematics and a minor in physics from the University of South Florida (Tampa, FL) in 2003. After graduation, Annette worked as a Web Content Developer in 2003 and as a Geologist in 2006. During this time, she saved enough money for her move to Gainesville and attend graduate school in August 2008. She will receive a Master of Science degree in geology from the University of Florida in August 2011. Annette will continue to follow her interests in the sciences by enrolling in a PhD program or pursuing a career in the industry.